6-19-2014

Effect of Variation of Silicon Nitride Passivation Layer on Electron Irradiated Aluminum Gallium Nitride/ Gallium Nitride HEMT Structures

Helen C. Jackson

EFFECT OF VARIATION OF SILICON NITRIDE PASSIVATION LAYER ON ELECTRON IRRADIATED ALUMINUM GALLIUM NITRIDE/GALLIUM NITRIDE HEMT STRUCTURES

DISSERTATION

Helen C. Jackson, Civilian, USAF
AFIT- ENP-DS-14-J-17

DEPARTMENT OF THE AIR FORCE
AIR UNIVERSITY

AIR FORCE INSTITUTE OF TECHNOLOGY

Wright-Patterson Air Force Base, Ohio

AFIT- ENP-DS-14-J-17

EFFECT OF VARIATION OF SILICON NITRIDE PASSIVATION LAYER ON ELECTRON IRRADIATED ALUMINUM GALLIUM NITRIDE/GALLIUM NITRIDE HEMT STRUCTURES

DISSERTATION

Presented to the Faculty
Department of Engineering Physics
Graduate School of Engineering and Management
Air Force Institute of Technology
Air University
Air Education and Training Command
In Partial Fulfillment of the Requirements for the
Degree of Doctor of Philosophy in Applied Physics

Helen C. Jackson, MS

Civilian, USAF

June 2014

AFIT- ENP-DS-14-J-17

EFFECT OF VARIATION OF SILICON NITRIDE PASSIVATION LAYER ON ELECTRON IRRADIATED ALUMINUM GALLIUM NITRIDE/GALLIUM NITRIDE HEMT STRUCTURES

Helen C. Jackson, MS

Civilian, USAF

Approved:

_____//signed//_____	_30 May 2014
Nancy C. Giles (Chair)	Date
_____//signed//_____	_30 May 2014
Robert D. Loper, Jr. (Member)	Date
_____//signed//_____	_30 May 2014
Donald L. Dorsey (Member)	Date

Accepted:

_____//signed//_____	_5 June 2014
Adedeji B. Badiru Dean, Graduate School of Engineering and Management	Date

Abstract

Silicon nitride (Si_3N_4) passivation layers on AlGaN/GaN heterojunction devices can significantly improve performance by reducing electron traps at the surface. The radiation hardness of Si_3N_4 is important to understand in order to obtain further technology developments. This research studies the effect of displacement damage caused by 1.0 MeV electron irradiation on AlGaN/GaN HEMTs as a function of passivation-layer thickness for two types of heterostructure layers. Passivation layer thicknesses of 0, 20, 50, and 120 nanometers were explored for the AlGaN/GaN test structures with either an AlN nucleation layer or a GaN cap structure. Hall effect, photoluminescence (PL), and deep-level transient spectroscopy (DLTS) measurements were made on the test structures before and immediately after 1.0 MeV electron irradiations at fluences of 10^{16} cm^{-2}. Changes in carrier mobility, carrier concentration, and conductivity were monitored as a function of Si_3N_4 thickness. Models were developed that relate the device structure and passivation-layer thickness to changes observed in PL and DLTS measurements. A software model is developed to determine the production rate of defects from 1.0 MeV electrons that can be used for other electron energies and other materials. The presence of either the 50- or 120-nm Si_3N_4 passivation layer preserved the channel current for both structures and appears to be in the optimal range to preserve radiation hardness.

AFIT- ENP-DS-14-J-17

I want to acknowledge my deceased husband, a brilliant scientist, engineer and inventor who was never valued for his true worth and who would have been excited with my research. And above all, I acknowledge and thank my God and my savior Jesus Christ, the source of my hope, strength and wisdom.

Acknowledgments

I would like to express my sincere appreciation to my current and previous advisor and all who gave technical advice and guidance at AFIT. I would like to thank my very patient AFRL sponsor, Dr. Donald Dorsey. I am very grateful to the technicians like Timothy Cooper, Wally Rice and Douglas McFarland. I am so thankful for physicist Dr. Gary Farlow, Dr. David Look and Z. Fang, without whom this research effort could not have happened.

Helen C. Jackson

Table of Contents

Page

Abstract iv

Dedication v

Acknowledgements vi

Table of Contents vii

List of Figures xi

List of Tables xxi

I. Introduction 1
- 1.1. General Issue 1
- 1.2. Research Objective 6
- 1.3. Investigative Questions 7
- 1.4. Methodology 7
- 1.5. Key Results Summary 8
- 1.6. Preview 9

II. AlGaN/GaN Characterization Physics 12
- 2.1. AlGaN/GaN HEMT physics 12
  - 2.1.1. Device Structure 12
  - 2.1.2. Charge Balance 13
  - 2.1.3. Two dimensional electron gas (2DEG) 17
  - 2.1.4. Polarization: AlGaN/GaN Surface and 2DEG 18
  - 2.1.5. Device Behavior 23
  - 2.1.6. The Purpose and Effect of Passivation 24
- 2.2. Characterization Overview 28
  - 2.2.1. The Hall System 28
  - 2.2.2. Mobility and Scattering Mechanisms 31
  - 2.2.3. Hall Mobility and Carrier Density as a Function of Device Structure 36
  - 2.2.4. Carrier Density 39
  - 2.2.5. Conductivity 41
- 2.3. Photoluminescence physics 42
  - 2.3.1. The Photoluminescence Peak 42
    - 2.3.1.1. DX Centers 44
    - 2.3.1.2. Excitons 45
  - 2.3.2. The Yellow Line Emission 50
  - 2.3.3. The Blue Line 51

2.4. Deep Level Transient Spectroscopy 51
2.5. Defects, Donors, Traps 53
2.6. The physics and numerical methods behind simulations 56
2.6.1. Schrodinger Poisson: Self-consistent Solution of Schrodinger's Equation 56
2.6.2. CASINO 59

III. Overview of 1-MeV Electron Irradiation Effects 62
3.1. Introduction 62
3.2. MeV Electron Radiation Effects 63
3.3. Previous 1-MeV Electron Irradiation Studies on AlGaN/GaN HEMTs ... 73

IV. Experimental Equipment and Procedures 84
4.1. Introduction 84
4.2. Device Preparation 84
4.3. Design of Experiment 89
4.4. Electron Irradiation Experiments 89
4.5. Characterization Experiments 90
4.5.1. Hall Characterization 91
4.5.2. Electrical Characterization for Gate (Schottky) Leakage Current and Capacitance 91
4.5.3. Deep Level Transient Spectroscopy 92
4.5.4. Optical Characterization: Photoluminescence 94

V. Experimental and Analytical Results for Electron Transport Characterization 96
5.1. Effect of Structure and Silicon Nitride Passivation Layer Thickness on Electron Transport Properties in Electron Irradiated AlGaN/GaN 97
5.2. Room Temperature Mobility Results 98
5.2.1. Mobility as a Function of Scattering Mechanisms and Centers ... 99
5.2.2. Modeled Scattering Mechanisms for the Two Different Structures 105
5.2.3. Experimental Carrier Densities 111
5.2.4. Modeled Conduction Bands as a Function of Structure and 2DEG Electron Densities 115
5.2.5. Experimental Conductivity Results 121
5.2.6. Additional Effects of Silicon Nitride Passivation 122
5.2.7. Temperature-Dependent Mobility and Carrier Density 125
5.3. Photoluminescence Measurements for Spatial Localization of Defects 129
5.3.1. Initial Look at Effect of Si_3N_4 Thickness on PL from Deep Centers 131
5.3.2. GaN PL Signatures and Defect Trap Locations 132
5.3.3. Effect of Variation of Si_3N_4 Passivation on Deep Center and Near Band Edge 134
5.3.4. Effect of 1-MeV Electron Irradiation and Si_3N_4 Passivation 138

5.4. Radiation Effects: Analytical and Monte Carlo Models of Radiation Damage and Defect Production 142
5.4.1. Modeled Defect Production Algorithm Results 143
5.4.2. Location and Distribution of Damage: From CASINO 148
5.5. Preliminary Conclusions and Investigative Questions Answered 152

VI. Characterization of Variation of Silicon Nitride Passivation Thickness on Electron Irradiated AlGaN/AlN/GaN and GaN/AlGaN/GaN Electrical Properties 153
6.1. Introduction 153
6.2. Effect of Structure, Passivation and 1 MeV Irradiation on Gate Leakage Current and Gate Capacitance 154
6.2.1. Leakage Current I_g-V_g 154
6.2.2. Capacitance Voltage C_g-V_g 166
6.2.2.1. Post Radiation Effects Results 172
6.3. Transconductance and Diode Measurements 181
6.4. Deep Level Transient Spectroscopy 184

VII. Analysis and Discussion 197
7.1. Conclusions on the Radiation Effects on Si_3N_4 Thickness on Hall Transport Mechanisms 201
7.1.1. Modeled Sheet Carrier Density and Electric Field Height 201
7.1.2. Charge Balance Model for Sheet Carrier Density 205
7.1.3. Mobility Analysis 207
7.1.3.1. Mobility Fits and Modeled Scattering 211
7.1.4. Overall Hall Carrier Transport Measurement Analysis 213
7.2. Conclusions and Model for Radiation Effects Shown in Photoluminescence 218
7.3. Radiation Effects on Variation of Si_3N_4 Thickness on Schottky Leakage Current and Related Measurements 223
7.4. Radiation Effects on Si_3N_4 Thickness Variation on Capacitance Voltage and Related Measurements 224
7.4.1. Changes in Threshold Voltage and Barrier Height and Tunneling Effects 229
7.5. Trap Analysis and Radiation Effects from Deep Level Transient Spectroscopy 234
7.6. Bethe Bloche Electron Damage Models 237
7.7. Summary of Damage Path by 1 MeV Electron Irradiation Area Models for Radiation Damage with Variation of Si_3N_4 239
7.8. Conclusions and Investigative Questions Answered 241

VIII. Conclusion 247
8.1. Significance of Research 249
8.2. Recommendations for Future Research 250

Bibliography 251

List of Figures

Figure Page

2.1. The AlGaN/AlN/GaN (left) and the GaN/AlGaN/GaN (right) device structures used in this research …… 13

2.2. A conduction band diagram for AlGaN/GaN with abrupt interface …… 14

2.3. AlGaN/GaN band diagram showing polarization charges …….. 15

2.4. Crystal structure of GaN and AlN …… 21

2.5. A simplified HEMT structure containing an AlGaN Schottky or donor contact layer, which serves as a source of electrons and a spacer layer ……. 23

2.6. Channel depletion (left). With more negative bias, space charge increases. Channel nears pinch off (right) ……... 24

2.7. Depiction of Si_3N_4 K-center ……... 26

2.8. Set up for Hall measurement showing van der Pauw arrangement ……. 29

2.9. Polar modes for optical phonons ……. 34

2.10. Band diagram comparisons for structure with an AlN interlayer on the left and without the interlayer on the right ……. 37

2.11. Band diagram of a GaN/AlGaN/GaN structure with a 7 nm GaN cap ……. 38

2.12. Temperature-dependent Hall data from an unpassivated sample showing that as carrier density (x-axis) increases, mobility decreases (y-axis) …….. 41

2.13. Depictions of some of the light-driven processes in a semiconductor …… 47

2.14. Hydrogen atom showing its Bohr radius …….…….…….…….……. 47

2.15. The exciton–Bohr radius is depicted …….. 48

2.16. Allowed energy states vs. box size for confined system …… 49

2.17. Donor-acceptor pair transition occurring in PL …….. 51

2.18. Change in capacitance ΔC with time, t ……...…… 52

2.19. Formation of DLTS peak …… 52

2.20. Nextnano simulations used to compare mobility and sheet carrier densities with the observed experimental results from the HEMT epi-stack structures follow this flow chart …….. 59

2.21. Casino's Monte-Carlo simulation of electron paths through a HEMT sample going through the Si_3N_4 passivation ……... 60

2.22. X-ray intensity for Nitrogen in a HEMT sample with 1-keV electrons and 200 electrons trajectories …… 61

3.1. Particles scattered out of the quantum well to nearby layers of AlGaN or GaN ... 70

3.2. Effect of 1-MeV electrons on I-V-T characteristics (1-MeV electrons with dose of $5x10^{15}$ cm^{-2} at room temperature ……... 74

3.3. Effect of 1-MeV electrons on C-V-T characteristics …….. 75

3.4. Effect of 0.5-MeV electrons on deep traps in a SBD with a large Schottky contact ……..... 76

3.5. Three Schottky barrier diodes were compared: irradiated and non-irradiated AlGaN/GaN Schottky barrier diodes, along with an irradiated GaN-Schottky barrier diode ……....77

3.6. ODLTS spectra measured in the AlN/GaN sample before (solid line) and after (dashed line) irradiation with 10^{16} cm^{-2} 10-MeV electrons ……... 80

3.7. C_g-V_g characteristics measured on the AlGaN/GaN MOCVD sample HEMT before and after irradiation with electron doses of 10^{14}, 10^{15}, 1.5×10^{16}, 4.5×10^{16}, 9×10^{16} cm^{-2}…….. 81

4.1. Three stage mask design…….. 86

4.2. The layout of the Si_3N_4 deposition per wafer quadrant and a sample mounted for irradiation on the right …… 87

4.3. Device structures for AlGaN/AlN/GaN and GaN/AlGaN/GaN …… 88

4.4. High Voltage Engineering Van de Graff accelerator at Wright State University (Dayton, OH) …… 90

4.5. Setup used in for I_g-V_g, C_g-V_g and DLTS studies ……..... 92

4.6. Accent DL8000 digital DLTS system (with both LN_2 and LHe cryostats) …… 93

4.7. Hole-like traps in AlGaN/GaN from DLTS …… 94

4.8. PL setup for AlGaAs …… 95

4.9. Orientation of the beam for PL measurements …… 95

5.1. Comparison of 300 K mobility pre- (E0) and post- (E1) the 1-MeV irradiation for AlN (left) and GaN (right) cap structures …… 98

5.2. Microscopic view of distorted crystal threading dislocations …… 101

5.3. Mobility as a function of carrier density and Si_3N_4 thickness in a GaN cap sample with its carrier density saturating at 20 nm …… 103

5.4. The approximately inversely proportional relationship between mobility and carrier density is shown …… 104

5.5. AlGaN/AlN/GaN modeled scattering mechanisms 0 to 320 K …… 107

5.6. Model of AlGaN/GaN with AlN spacer layer, showing the ionized background scattering which is due to residual impurity scattering ……. 107

5.7. AlN structure with 50 nm Si_3N_4 scattering mechanisms 0 to 320 K……108

5.8. GaN cap structure scattering mechanisms from 0 to 350 K…… 108

5.9. GaN cap structure with 50 nm Si_3N_4 scattering mechanisms from 0 to 320 K …109

5.10. The modelled alloy potential and scattering as a function of region ……. 110

5.11. Pre-irradiation (E0) comparison of (left) AIN vs. GaN cap carrier density and the pre- and post-irradiation (E1) Carrier density comparison of both structures ……. 112

5.12. Averaged 300-K results over the sample sets show that the AlGaN/AlN/GaN structure has a higher carrier density prior to irradiation than a structure without an interlayer ……. 113

5.13. The pre- (E0) and post- (E1) irradiation 300-K carrier density and mobility for the GaN cap structure ……. 114

5.14. The pre- (E0) and post- (E1) irradiation 300-K carrier density for the structure with an AlN interlayer ……..... 114

5.15. The 2 DEG sub-band mobility and carrier density…… 117

5.16. Modelled first sub-band energy and conduction band for AlN (1 nm) $Al_{0.25}Ga_{0.75}N$/GaN ……118

5.17. Modeled first sub-band energy and conduction band for Si_3N_4 (50 nm) and AlN (1 nm) $Al_{0.25}Ga_{0.75}N$/GaN(left) along with zoom of the area showing the electron density ……..... 118

5.18. The electron density function for the AlGaN/GaN/GaN structure with 50 nm of Si_3N_4…….…… 119

5.19. Modeled conduction band for GaN (2 nm)/AlGaN/GaN (left) with enlarged view of the cap area ….…… 119

5.20. Modeled conduction band for Si_3N_4 (50 nm)/GaN (2 nm) $Al_{0.25}Ga_{0.75}N$/GaN (left) and enlarged view of cap area (right)…… 120

5.21. Modeled electron density for Si_3N_4 (50 nm)/GaN (2 nm) $Al_{0.25}Ga_{0.75}N$/GaN between the edge of the Si_3N_4 and the front boundary of the GaN …….…..….. 120

5.22. The first electron wave function in the 2DEG area of the GaN cap structure...121

5.23. Comparison of 300 K conductivity pre- (E0) and post- (E1) 1-MeV irradiation on AlN (left) and GaN (right) cap structures ……..... 122

5.24. Temperature dependent mobility as a function of Si_3N_4 thickness for AlGaN/AlN/GaN structure before (E0) and after (E1) 1-MeV electron irradiation …….. 126

5.25. Temperature dependent mobility as a function of Si_3N_4 thickness for GaN/AlGaN/GaN before (E0) and after (E1) 1-MeV electron irradiation ……. 126

5.26. Temperature-dependent carrier density for AlGaN/AlN/GaN shows a higher carrier density than the GaN cap structure; there is little change in the pre- and post-radiation unpassivated carrier density (red), until room temperature …… 127

5.27. Temperature-dependent carrier densities for GaN/AlGaN/GaN show the unpassivated carrier density does change pre- and post-radiation, but is opposite the passivated samples with an increase in carriers post irradiation, until room temperature when the effect is slightly reversed ……..... 127

5.28. Volumetric dislocation on the left on a point defect on the right……. 130

5.29. Radiation producing centers change the PL peak intensities indicating change in acceptor defect population leading to the 2.2 eV deep center PL ……..... 131

5.30. The unpassivated, pre–irradiation spectrum excited using a HeCd laser …..... 132

5.31. PL spectra from 3.25 to 3.50 eV, showing the dominant D^oX peak and the non-radiatively produced phonon replica peaks ……..... 133

5.32. E0 Deep center PL with variation of Si_3N_4 thickness, showing the YL peak at 2.3 eV and the BL peak at 3.0 eV……..... 135

5.33. Near band edge showing a mono-atomic attenuation of the PL light with Si_3N_4 thickness. …… 135

5.34. Linear attenuation of the PL light with increase in Si_3N_4 thickness .....…..... 136

5.35. PL from unpassivated samples after 1-MeV irradiation. Deep centers are not affected as much as shallow centers by irradiation ……..... 138

5.36. PL from sample with 50-nm passivation layer after 1-MeV irradiation. Deep centers are not affected as much as shallow centers by irradiation …..... 139

5.37. PL taken after 1-MeV irradiation showing deep center to NBE region …….. 139

5.38. PL taken after 1-MeV irradiation for the emission region from 3.20 to 3.60 eV, which includes the near band edge ……..... 141

5.39. The pre- and post-1-MeV radiation deep center PL for the sample variation range ……. 142

5.40. Modeled mean free path depth of 1-MeV electron through Si_3N_4 (left), through AlGaN (right), and through GaN (bottom) as a function of kinetic energy …….…….. 143

5.41. A cartoon scenario of the results from CASINO; the red lines on the upper right plot are the backscattered electrons ……..... 149

5.42. CASINO Monte Carlo simuations of 1-MeVelectron irradiation in AlGaN/AlN/GaN sample with 50 nm of Si_3N_4 passivation…… 150

5.43. XY radial energy as a function of position, showing the locus of energy distribution…….…… 151

5.44. Normalized hits by 10 MeV electrons at a fluence of 10^8 nm^{-3} as a function of Si_3N_4 thickness on AlGaN (18nm)/AlN (1nm)/GaN (1700 nm)……..... 152

6.1. Room temperature comparison of Si_3N_4 passivation variation (0, 20, 50, 120 nm) for AlGaN/AlN/GaN……...…..…..……... 155

6.2. Room temperature comparison of Si_3N_4 passivation variation (0, 20, 50, 120 nm) for GaN/AlGaN/GaN……...….. 156

6.3. Temperature dependent I_g-V_g -T for unpassivated GaN cap sample. There is little temperature dependence in reverse bias, where I_g is nearly constant after pinch off …….…….…….…….…….…….…….…….…….…..…..... 157

6.4. Capacitance transients for the unpassivated GaN cap sample showing its electric field dependence for voltage sweep from -3.0 to -3.4 V at 300 K 158

6.5. Temperature dependence of I_g-V_g after 1-MeV electron irradiation for unpassivated GaN/AlGaN/GaN …….…….…..... 160

6.6. Pre(E0) and post(E1)irradiation, 50 nm Si_3N_4 passivated AlGaN/AlN/GaN, showing the increase in post radiation leakage current……..160

6.7. The pre (E0) and post(E1) radiation leakage current of both the AlN structure and the GaN cap structure for a 50 nm passivation layer thickness, showing that the GaN cap structure has less leakage…….....161

6.8. Si_3N_4 thickness variation with GaN cap pre (E0) and post (E1) radiation leakage current comparison showing a shift right E1 for the passivated structures.……..……..162

6.9. Temperature dependent Ideality factor vs. Barrier Height. The barrier height, øb, and the ideality factor, n, as a function of temperature for the (Ni/Au)/AlGaN/GaN/SiC Schottky barrier diode……..164

6.10. C_g-V_g from an unpassivated sample showing the accumulation and depletion and residual capacitance areas ……...… 167

6.11. Temperature-dependent (100, 200, 300, 400K) unpassivated C_g-V_g GaN/AlGaN/GaN with Ni/Au SBD. V_{th} shifts positive with decreasing temperature as device cuts off…….167

6.12. Comparison of Si_3N_4/AlGaN/AlN/GaN (IQ 15) with Si_3N_4/GaN/AlGaN/GaN (IQ 13) room temperature C_g-V_g (left). The unpassivated AlN structure has a higher saturation capacitance, but the opposite is true for the GaN cap structure…….…..170

6.13. Generic AlGaN/GaN structure (not to scale) showing where some of the channel lies under the SBD and some is ungated …….. 170

6.14. The pre- (E0) and post- (E1) irradiation C_g-V_g of 50 nm passivation layer thickness on the AlN and GaN cap structures shows a decrease in capacitance for both structures ……. 173

6.15. Post(E1) C_g-V_g -T for unpassivated GaN/AlGaN/GaN……..... 174

6.16. E1 C_g-V_g -T 50 nm with annealing effects, AlN sample at room temperature ……175

6.17. GaN cap sample at room temperature; C_g-V_g comparison of pre- and post-irradiation on unpassivated (left) and AlN vs. GaN cap pre- and post irradiation and on 50 nm SiN passivated structures (right) …….. 176

6.18. 300 K comparison of C-V showing effect of variation of Si_3N_4 thickness before and after 1 MeV electron irradiation on GaN/AlGaN/GaN…….177

6.19. Comparison of S_3iN_4/AlGaN/AlN/GaN with Si_3N_4/GaN/AlGaN/GaN room temperature Hall carrier density. The unpassivated GaN cap structure (red curve at 0) has a significantly smaller carrier density than the passivated structures…….....178

6.20. The figures above are referred to in the text and are used to explain why sheet carrier density and capacitance changes with a thin GaN cap (lower), as opposed to not having a cap layer (upper) …… 179

6.21. GaN/AlGaN/GaN with 120 nm passivation; Transconductance…… 182

6.22a. Post irradiation for AlGaN/GaN/GaN structure with 20 nm passivation Transconductance……...183

6.22b. Post radiation AlGaN/GaN/GaN structure with 50 nm Passivation Transconductance……...183

6.23. Process used in obtaining DLTS trap peaks……184

6.24. Band diagram of the tunneling from surface states……186

6.25. Trap sites and hopping in AlGaN/GaN……...……186

6.26. Left: Temperature dependent GaN /AlGaN/GaN DLTS as a function of Si_3N_4, showing the persistence of "hole like" traps. Right: Temperature dependent GaN/AlGaN/GaN DLTS spectra as a function of a filling pulse for an unpassivated sample with variation of the applied field from 0.5 V to -2.0 V …… 188

6.27. Pre –irradiated, unpassivated DLTS GaN/AlGaN/GaN structure for which the contacted ohmics where varied, as well as the reverse bias…….....189

6.28. H_1 hole trap that to be the cause of tunneling at the Schottky Ni/AlGaN interface…….……190

6.29. AlGaN/AlN/GaN Pre-irradiation (E0) vs. post irradiation (E1) DLTS for 50 nm Si_3N_4 passivation showing radiation induced traps…….. 191

6.30. Same sample as above, E1, 50 nm, RT annealed, showing observation of traps is affected by starting conditions. Change in DLTS features at low temperature (4^{th} run), showing clear D trap and part of E trap……. 192

6.31. The persistence of the A and D trap in irradiated 50 nm passivated after a 1 week room temperature anneal for AIN sample, through multiple runs and ohmic configurations……... 193

6.32. Dependence of DLTS signal on the tp, which indicates an association of these traps (A_x and D) with extended effects……194

6.33. Unpassivated GaN/AlGaN/GaN E1 showing what is believed to be the radiation induced nitrogen interstitial at A_x…….....195

6.34. Unpassivated GaN cap E0 and E1 comparison showing radiation induced nitrogen interstitial at A_x…….....196

7.1. Modeled electric field is higher at the AlGaN/GaN interface for the AlN structure on the left and the GaN cap structure on the right resulting in a higher 2DEG sheet charge density ……..... 202

7.2. Carrier density as a function of temperature before (E0) experimental and modeled on the left the post irradiation (E1) on the right …… 203

7.3. The first and second modeled 2DEG wavefunctions …… 209

7.4. The comparison between pre and post radiation in a GaN cap sample, showing at 50 nm passivation thickness the sample has mobility of ~1500 cm^2/V-S post radiation …….. 210

7.5. E0 mobility, modelled vs. experimental mobility for AlGaN/AlN/GaN on the top, the E1 total mobility as a function of scattering mechanisms on the bottom ……..... 211

7.6. RT Changes in (a) mobility, (b) carrier density and (c) conductivity as a function of silicon nitride thickness before (E0) and after 1 MeV electron radiation (E1) ……..... 214

7.7. Simplified damage model for electron irradiation effects on AlGaN\GaN …… 217

7.8. Model for radiation damage explaining PL peak changes and change in the Nitrogen and Gallium donor and acceptor populations …… 219

7.9. C_g-V_g showing threshold voltage shifts due to both radiation (dashed lines) and passivation thickness in GaN/AlGaN/GaN ……. 225

7.10. For these 50nm passivated samples, there is a threshold voltage shift right the GaN cap structure E1, corresponding to a decrease in carrier density, but for the AlN there is first right and as it stretches out in the depletion area due to N_{it} more of a negative bias is required for depletion …..…..…..…..…..….. 226

7.11. Figure showing the decrease in barrier height due to trap assisted tunneling, ϕ_B …….. 229

7.12. Si_3N_4 changes barrier height for AlGaN/AlN/GaN pre irradiation ……..... 230

7.13. The barrier height differences due to structure as a function of passivation thickness, showing that before irradiation 50 nm and above increase the barrier height in AlGaN/AlN/GaN but first decrease it in GaN/AlGaN/GaN and then it climbs back up……. 230

7.14. The degradation in barrier height with 1 MeV radiation for GaN/AlGaN/GaN, showing it is least for 50 nm passivation thickness…….. 231

7.15. The relative effects of the changes due to 1 MeV irradiation on barrier height, carrier density and threshold voltage shifts as a function of Si_3N_4 thickness……. 233

7.16. Effect of radiation induced N_A to the change in threshold voltage per thickness of Si_3N_4 ……. 233

7.17. Correspondence to Figure 7.16 changes in E0E1 threshold voltage shift as a function of passivation layer thickness …….. 234

7.18. Figure showing the 2 separate traps ED1 and ED2 that make up trap E …….. 235

7.19. Cross section as a function of kinetic energy in AlGaN for Gallium (red), Nitrogen (blue) and Aluminum (green) …… 239

7.20. Pictorial model that summarizes the 1 MeV electron irradiation damage in the channel and in with the Schottky controlled measurements ……... 240

List of Tables

Table		Page
4.1.	Dimensions of AlGaN/GaN device layers …….	85
4.2.	Hall and PL Experimental Overview…….……	87
5.1.	Scattering mechanisms used in Nextnano models ……	106
5.2.	Material Parameters used in mobility scattering models…….	106
5.3.	Trap location summary…….……	130
5.4.	Table is based on defect production algorithm model, showing that the highest production rate for damage is for lattice atoms gallium, nitrogen, aluminum and silicon ……...……...……...……...…..	147
6.1.	Pre-irradiation (E0) and post radiation (E1) GaN cap Ideality and Barrier heights for GaN/AlGaN/GaN……...165	
7.1.	Summarizing averaged Hall system results radiation effects on the AlN structure……	215
7.2.	Summarizing averaged Hall system results radiation effects on the GaN Cap structure…….216	
7.3.	Loss of sheet carrier concentration post radiation…….217	
7.4.	Pl Peaks for AlGaN/AlN/GaN, summary of the defect peaks…….	222
7.5.	Experimental changes in pre and post radiation threshold voltage shift, carrier density and barrier heights…….232	
7.6.	Observed DTLS traps and their possible effects in samples…….....	237

EFFECT OF VARIATION OF SILICON NITRIDE PASSIVATION LAYER ON ELECTRON IRRADIATED ALUMINUM GALLIUM NITRIDE/GALLIUM NITRIDE HEMT STRUCTURES

I. Introduction

1.1. General Issue

Type III-V devices are widely deployed in DOD RF systems, particularly space systems. Reproducing the space environment in which these devices will operate can show how they would perform under real-world conditions. With the expanding US Air Force's use of emerging GaN High-Electron-Mobility-Transistor (HEMT) technologies, there is a need for a better understanding of the materials and device behaviors in such an environment. AlGaN/GaN structures are known to be preferred materials for the manufacture of fast transistors. This present research is directed at a study of the radiation induced changes and damage such AlGaN/GaN devices would encounter in space.

Over the past few years, several factors have emerged as playing major roles in the developing electronics market. The DOD, in general, and the aerospace industry in particular, are users of a small part of an electronics market that is now dominated by commercial interests and profits. In the 1990's, military standards were replaced by their commercial counterparts. To complicate matters further, failure mechanisms are now more complex with more sophisticated and less-proven semiconductors. The available body of knowledge for AlGaN\GaN devices is much more limited as compared to that for silicon and the existing lifetime data for the devices does not match the expected

capability. This points to a need for further basic studies of device structures, especially those studies including operating and environmental conditions. By studying the effects of displacement damage created by electron irradiation levels comparable to that found in Air Force space-borne operational environments, we can better predict the effects on device performance metrics and radiation hardness. Studies are needed that include structures with and without passivation layers, so that the effects of passivation layers on radiation hardness as a function of layer thickness can be determined.

For satellite payloads, weight, area, and volume are critical considerations and translate directly to cost. However, the addition of very thin silicon nitride layers on already fabricated devices adds very little in terms of weight, area, and volume, and requires no modification of device geometry. This same consideration allows for miniaturization of electronic instruments used in other radiation environments. Clearly, this solution to the radiation hardness problem is preferable to one that requires the addition of heavy shielding or the use of lower-performance devices that have better natural radiation hardness.

Other AlGaN/GaN HEMT problem areas that have been identified recently include (i) impact ionization and channel breakdown, (ii) gate-tunnel leakage and surface traps, and (iii) charge-dipole domain and electric field-breakdown. Normal gate leakage results in surface conduction, which can accumulate as a virtual gate and lead to performance degradation and at a critical electric field, a conducting path to the channel can be formed.

High-energy particles such as electrons and protons produce both displacement and ionization damage. Decades of research have identified the primary concern for

AlGaN/GaN to be displacement damage. Such damage occurs when the incident particle has enough energy to move the atom from its normal lattice position. According to Johnston (Johnston, 2010), who analyzed space electronics involving silicon and AlGaAs/GaAs devices, radiation induced traps are affected by hydrogen, which is introduced during the processing steps of the devices. Due to the migration of these hydrogen related species, devices using silicon nitride had a lower sensitivity to radiation than those using other passivation materials, such as silicon carbide or other deposited oxides.

Numerous papers (Atwater, 2007; Moran et al, 2009; Tsurumi et al, 2008; Ohno et al, 2004; Arulkumaran et al, 2004) have documented the use of Si_3N_4 passivation layers in various device structures, including AlGaAs/GaAs high electron mobility transistors (HEMTs). Their use on the gate-source and gate-drain recess regions of these structures has also been documented by Chou *et al.* (Chou et al, 2002). Also, Si_3N_4 passivation of AlGaAs/GaAs and InP/InGaAs heterojunction bipolar transistors (HBTs) were investigated for reducing surface recombination and improving current gain. However, none of these prior studies addressed the improvement of radiation resistance. It is emphasized that these electronic benefits depend on the Si_3N_4 deposition method. However, the use of Si_3N_4 passivation layers for radiation hardness is not documented to the author's knowledge.

Silicon devices are poor candidates for high power, high frequency space electronics, but attempts to improve their performance in such environments have been done. Devices such as silicon MOSFETS have used silicon dioxide for passivation. As early as the 1980s, use of a Si_3N_4 layer on silicon operational amplifiers to achieve

radiation resistant circuits was discussed. There now exists a need for improved life time and reliability for AlGaN\GaN HEMTs as well as for documentation of its progression for space environments.

AlGaN/GaN heterostructures have great promise in a variety of high power and fast switching applications. Much of this is owing to the high electron mobility (generally accepted value of 1880 $cm^2/(V \cdot s)$) of the 2DEG. Comparable GaN transistors have been shown to have resistances lower than silicon by orders of magnitude. Devices used in space-borne applications experience both protons and electrons from the earth's radiation belt. The space environment in which these AlGaN\GaN High Electron Mobility Transistors (HEMTs) need to operate requires that they be operational under the equivalent of 1.0 MeV electron irradiation (ICRU Report No. 37, 1984). Such high-energy particles cause displacement damage, which can become deep electron or hole traps; more rarely, they cause shallow donors or acceptors. For 1.0 MeV electron irradiation, a dominant defect that is produced is a 0.06 eV donor, and which was identified using Hall Effect measurements as a nitrogen vacancy (Look et al, 1997). Previous studies used electron irradiation on RF GaN HEMTs and characterized their degradation (Kalavagunta, 2009). Other studies have examined the role of bulk traps in device degradation (Meyer, 2008; Fang et al, 2011; Polyakov et al, 2008). None of these studies, however, focused on the role of the Si_3N_4 thickness in the formation of the surface states, either prior to or following 1.0 MeV electron irradiations.

It is believed that in the presence of irradiation, Si_3N_4 passivation reduces the surface donor states which cause trapping in the device, and thus offsets the damage. With the use of Si_3N_4 passivation on AlGaN\GaN heterojunction devices, it may be

possible to achieve improvements in device performance and also radiation hardness, while concurrently preserving its reliability and performance (Jackson et al, 2013). Furthermore, Hall carrier density data indicates the surface states are donors. Such measurements indicate the degree of preservation of mobility and conductivity as a function of Si_3N_4 thickness.

The use of Si_3N_4 in mitigating traps that cause gate lag, virtual gates, and "the how and what" of passivation on the device will be discussed and modeled in this present work. The scattering mechanisms known to exist in these structures have been incorporated in the models and are shown to change with variation of Si_3N_4 thickness. Experimental data show changes in carrier density with both Si_3N_4 thickness, structure and electron irradiation. As far as temperature dependence, the carrier density curves are statistically flat over the temperature range of 10-300 K. The effect of structure variations as well as the differences pre- and post-irradiation on the transport properties will be shown in the experimental results sections. Photoluminescence reveals intrinsic as well as extrinsic impurities, and traps in as-grown and irradiated samples, thereby giving a window to look at the changes in electron transport. The capacitance-voltage experiments show the stretch out-of-gate (Schottky) capacitance (C_g-V_g) curves due to interface traps. Electron irradiation creates acceptor type defects. These displacement damage defects, a dominant concern in device degradation, are charged. Electrically active traps in the area of the gate profoundly affect device characteristics. Not treated in this study, but of critical importance to future work, are stress and device self-heating.

Although Si_3N_4 is currently used for passivation, the thickness range employed in this research has not been published to date. Also, studies have not been carried out on

the effect of the variation of the thickness of the Si_3N_4 passivation layer on HEMT structures subjected to 1.0 MeV electron irradiation. For AlGaN/GaN, there is no true consensus on the location and energy of the post radiation defects, but many researchers have predicted these in similar materials based on DLTS, PL, and Hall measurements.

1.2. Research Objective

This research will determine the effect of the thickness of a Si_3N_4 passivation layer on the properties of two different HEMT structures, specifically AlGaN/AlN/GaN and GaN/AlGaN/GaN. Structures were measured both before and after 1.0 MeV electron irradiations. HEMT performance metrics will be determined through measurements of Hall Effect, photoluminescence, Cg-Vg, gate current (Ig-V_g), and DLTS.

The Si_3N_4 passivation layer thicknesses used in this work are 0, 20, 50, and 120 nm deposited on bare epilayer AlGaN/AlN/GaN and GaN/AlGaN/GaN structures. These structures will be characterized before and immediately after 1.0 MeV electron irradiation at fluences of 10^{16} cm^{-2} with room temperature (RT) and temperature dependent (TD) Hall effect and low temperature PL. These measurements were chosen to give insight into the displacement damage caused by the radiation, as a function of both Si_3N_4 thickness, device structure and irradiation, as well as to show how the mechanisms involved can be related to the lifetime and reliability of comparable HEMTs.

1.3. Investigative Questions

The questions to be investigated in this dissertation research are: What is the effect of (a) the particular device structure, and (b) the Si_3N_4 passivation layer thickness

on the transport characteristics (such as mobility, carrier density, conductivity) and electrical metrics (such as Ig-Vg, Cg-Vg) of a HEMT structure before and after irradiation with 1 MeV electrons? In particular: How do the transport characteristics (such as the mobility and carrier density) both before and after irradiation with 1 MeV electrons depend on the particular device structure and the Si_3N_4 passivation thickness? How do the leakage current measurements after radiation depend on the Si_3N_4 passivation thickness and on the device structure?

1.4. Methodology

(1) Wafers of undoped AlGaN/GaN were grown using MOCVD on 6H SiC substrates.

(2) The wafers were sectioned into four AlGaN/AlN/GaN or GaN/AlGaN/GaN sections, and different thicknesses of Si_3N_4 passivation (0, 20, 50, and 120 nm) were applied per wafer quadrant. The Si_3N_4 deposition was done by PECVD.

(3) Wafers were then diced to 0.5 cm × 0.5 cm samples using a diamond saw. Samples from each wafer were pre-characterized in order to establish a baseline and to observe the variation in native defects owing to fabrication method.

(4) Samples were characterized using temperature-dependent Hall mobility, carrier density, conductivity and its corresponding resistivity. Electrical device characterization was done through temperature dependent measurements of gate voltage, Ig-Vg, and gate capacitance, Cg-Vg.

(5) Supportive measurements included DLTS and photoluminescence.

(6) Parameters affecting device performance were modeled using radiation damage models, including simulations in Casino, a defect production algorithm based on the Bethe-Bloch equation, and a mobility scattering model using Nextnano to study the effect of structure on HEMT scattering mechanisms, the conduction band structure, and the electric field.

Radiation creates damage in these structures, but the damage of concern for AlGaN/GaN is displacement damage, which occurs when the incident electron has enough energy to move an atom from its normal lattice position. Electron irradiation using energies 1.0 MeV and higher creates point defects (e.g., N interstitials) and a number of acceptor defects, including Ga vacancies. While the radiation can create donors and acceptors, these displacements can also be described as radiation induced acceptors which cause a subsequent decrease in carrier density in the 2DEG. Additional scattering centers, also created by the radiation, reduce the mobility and conductivity and thus the device performance. In the as-grown material, defects have previously been identified as intrinsic like threading dislocations and dangling bonds at the AlGaN surface. Passivation of the surface donor states has been shown to reduce current collapse but also to increase gate leakage current.

1.5. Key Results Summary

The key results of this dissertation research are determination of:

1. The effect of 1 MeV electron radiation on AlGaN/AlN/GaN and GaN/AlGaN/GaN HEMT structures passivated with various thicknesses of

Si_3N_4 using measurements of Hall mobility, carrier density, conductivity, as well as gate (Schottky) leakage current and gate capacitance;

2. An optimum passivation layer thickness for 1.0 MeV electron irradiated AlGaN/AlN/GaN and GaN/AlGaN/GaN which preserves channel current;
3. The best configuration between AlGaN/AlN/GaN and GaN/AlGaN/GaN to assure lowest post radiation leakage current;
4. The relationship between post radiation Schottky area (gate) leakage on AlGaN/AlN/GaN and GaN/AlGaN/GaN HEMT structures and traps observed via DLTS and photoluminescence; and
5. A model for post-radiation PL and its relationship to observed post-radiation charge balance due to radiation induced acceptor and donor changes.

1.6. Preview

Chapter 2 presents an overview of the physics used in understanding the results in this study. After explaining basic HEMT device physics, including polarization and 2DEG formation, this chapter will present the physics underlying Hall mobility, carrier density and conductivity; the theory behind the observed photoluminescence transitions including the energy balance involved in donor acceptor (DAP) pairs; the physics behind both near band edge and deep centers; and a short explanation of DLTS. This is followed by a short overview of trap analysis which is a common underlying factor in all device degradation metrics as well as a brief explanation of Bethe-Bloch and Schrodinger-Poisson theory used in the models.

Chapter 3 presents a brief review of some pertinent previous 1 MeV and high energy electron radiation studies of AlGaN/GaN HEMT structures along with the models used for high energy radiation damage. This is preceded by a short discussion of radiation effects physics and models, including both displacement and ionization damage.

Chapter 4 presents experimental techniques, equipment set-ups , device layouts, and preparation techniques used. In addition, design-of-experiment tables will be given along with tables listing the experimental runs.

Chapter 5 presents the results of Hall transport measurements on both AlGaN/AlN/GaN and GaN/AlGaN/GaN structures for various Si_3N_4 passivation layer thicknesses before and after 1.0 MeV electron irradiation. Results of the modeled mobility as a function of scattering mechanisms, modeled band diagrams and electron density are shown for each structure both with and without passivation. Pre- and post-irradiation PL results are presented. Calculations of the rate-of-production of defects in each layer of the device using a defect production algorithm are also given. Finally, Casino (Monte Carlo) results are given for the structures showing the spatial location of the primary and backscattered electrons in order to assess the damage regime.

Chapter 6 presents results of gate (Schottky) leakage current and capacitance measurements before and after irradiation for both structures as a function of Si_3N_4 thickness variation. Pre- and post- radiation results for DLTS are given and related to the additional post-radiation leakage and interface trapping observed.

Chapter 7 presents an analysis and discussion of the results presented in Chapters 5 and 6, and provides detailed models. An analysis of the effects of Si_3N_4 passivation, passivation layer thickness, device structure, and radiation effects are given for both

AlGaN/AlN/GaN and GaN/AlGaN/GaN. Changes in barrier heights and threshold voltages affect the changes due to passivation and radiation, and are added to the results of Chapter 6 to enhance the analysis. Models are given that explain the observed PL and DLTS results of Chapters 5 and 6 in terms of charge balance and energy balance, as well as offering a qualitative and quantitative trap analysis that leads to the observed post-radiation changes.

Chapter 8 presents the final conclusions of the research, its potential value and suggestions for future work related to this research.

Chapter II. AlGaN/GaN Characterization Physics

High Electron Mobility Transistors (HEMTs) rely on a complex synergy of multiple materials that enable transport mechanisms on the quantum level and are explained with electrodynamics on the device level. This chapter will summarize the physics underlying both the measurements and characterization methods needed to understand the results of this research for AlGaN/GaN "always on" HEMTs.

2.1. AlGaN/GaN HEMT Physics

In Chapters 5 and 6 of this dissertation, the characterization results on the device structures will be reported. To understand these results, the basics of the device physics, the characterization techniques used, and the results obtained will be presented in this chapter. The basic structures will be discussed first, followed by the overall charge balance, the 2DEG, polarization basics, device control, as well as the purpose and effects of passivation. The chapter will conclude with a discussion of the characterization methods used.

2.1.1. Device Structure

The basic device structures used in this study are shown in Figure 2.1. It should be noted that these devices do not have a gate finger or a field plate, as is normal for a HEMT device, so the Schottky (gate area) measurements carried out in Chapter 6 must be interpreted with this understanding. For the structure on the right, the AlN layer adds to the polarization, which then raises the energy bands and, if charge in the Si_3N_4 produces

polarization in the same direction, then those bands will be raised further resulting in a greater transfer of charge and electrons into the 2DEG layer or the channel (which will be the discussed in Section 2.1.3). For the structure on the left, the GaN cap layer serves as a surface charge control layer, reducing the effect of polarization charge; the cap layer screens the 2DEG from surface traps that lead to current collapse. It therefore has a lower carrier density than a similar structure without a GaN cap. These structural parameters effect the 2DEG and hence the entire device behavior.

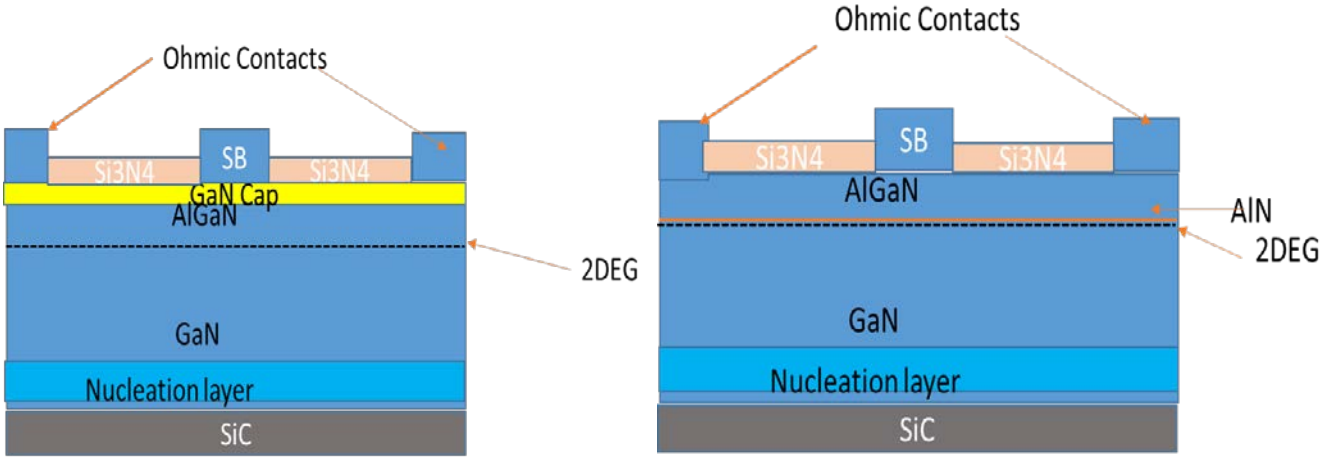

Figure 2.1. The AlGaN/AlN/GaN (left) and the GaN/AlGaN/GaN (right) device structures used in this research.

2.1.2. Charge Balance

Improved device performance and control can be obtained by understanding the source of the 2DEG electrons. The source of the 2DEG electrons in a HEMT is different for AlGaN/GaN than AlGaAs/GaAs, the latter obtaining its channel electrons from the

bulk or buffer layer. Figure 2.2 shows the general conduction band diagram for AlGaN/GaN. The balance equation for the charges (Ibbetson et al, 2000) is given below.

$$\sigma_{pz} + {}^{-}\sigma_{pz} + {}^{+}\sigma_{AlGaN} + \sigma_{Buffer} + \sigma_{surface} + {}^{-}\sigma_{AlGaN} = q\, n_s \qquad (2.1)$$

The first two terms on the right, σ_{pz} and $-\sigma_{pz}$, are the piezoelectrically polarization induced

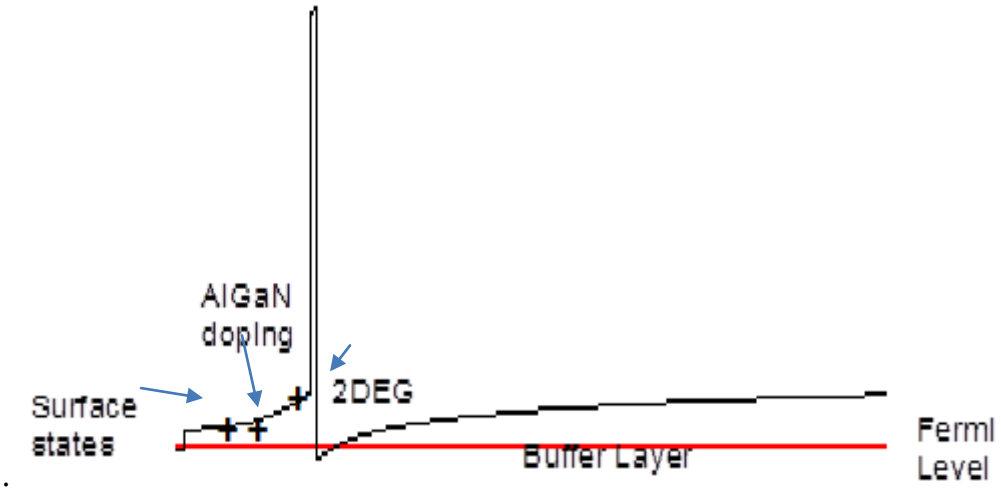

Figure 2.2. A conduction band diagram for AlGaN/AlN/GaN with an abrupt interface.

charge densities at the AlGaN/GaN interface. The polarization charges at this interface are responsible for the formation of the 2DEG quantum well in which electrons are confined. However, these charges sum approximately to a net zero dipole. There is the integrated sheet charge contributions ${}^{+}\sigma_{AlGaN}$ and ${}^{-}\sigma_{AlGaN}$ from ionized donors in the AlGaN, and thus have both positive and negative components. The fourth term is the buffer charge, which is negative if the 2DEG is to be confined to the AlGaN/GaN interface. The magnitude of this charge is ideally very small and can be assumed zero. There is also a surface charge due to ionized surface states. On the right hand side of the

equation, these sum to the negative charge in the 2 DEG, qn_s. It should be noted that these charges all sum to zero in an unbiased device since the device must be charge neutral in the absence of an external field.

We now have the charge balance Equation 2.1 reducing to the following, giving the source of the 2DEG electrons. Hence the number of electrons in the 2DEG is equal to the

$$\sigma_{surface} \pm \sigma_{AlGaN} = qn_s \tag{2.2}$$

number of ionized donors in the AlGaN $\pm$ the number of ionized donor- (or acceptor-) like states on the surface. If the AlGaN barrier is undoped, then the number of 2DEG electrons is due to the donor-like surface states; however, the AlGaN is unintentionally doped.

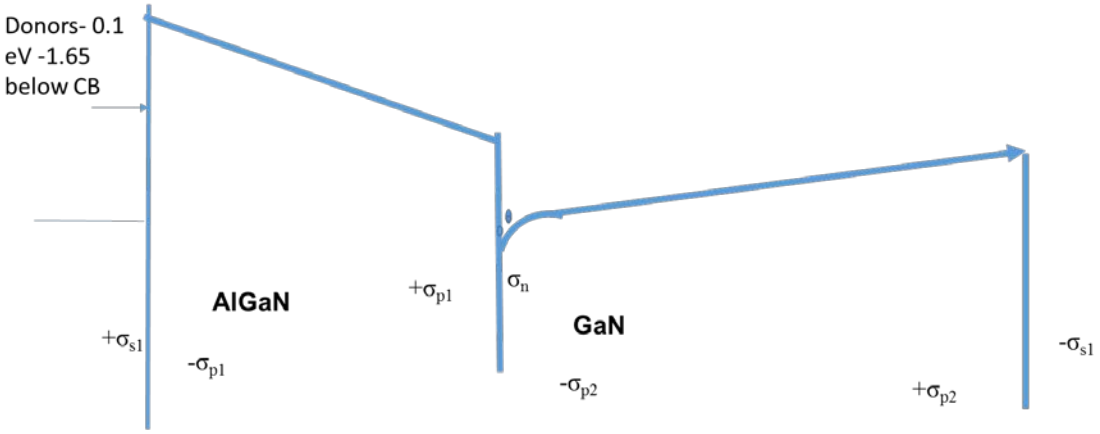

Figure 2.3. AlGaN/GaN band diagram showing polarization charges.

The band diagram in Figure 2.3 shows where the surface donors can reside and where the energy levels are relative to the conduction band. Note the surface is typically defined as having a depth of up to 1.2 eV below the conduction band, but its location is not at a fixed level. For the charge balance equation and the above band diagram, the

negative charges must equal the positive charges. Donors possess electrons which can drop to acceptor levels which are at lower energy just above the valence band (not shown). Normally, the transition to the acceptor levels will not be complete because there are more donors than acceptors in n-type GaN (also called n-GaN). The neutral area is where the band of constant slope (straight line). As a result, σ_{Buffer} is going to have a few more donors since this material is n type, but the contribution is considered negligible. The 2DEG charge is negative, due to the acceptors in the buffer. Balancing this negative charge is the positive charge from the surface (the AlGaN surface, as well as any AlGaN bulk that is charged). The polarization charges cancel out and are not mobile, but they do provide a field.

If there is a surface charge, the bands will bend and then the derivative of the band at the surface will be defined by Gauss's law. If there is a volume charge, then there is no band bending, and the depiction will be a straight line in a band diagram. If there is no charge at either the surface or in the volume, the conduction band line will be flat. If there is charge in the bulk portion, then the conduction band will be an angled straight line. When the band is curved, there is an implicit assumption that there is charge in at the surface, as the derivative of Gausses law would be non-zero.

The surface states here could be due to dangling bonds, impurities, etc., but are localized. In the band diagram above, they are the interface to the gate area. These states have to be high (the higher they are, the easier they are to transfer charge) so that efficient transfer of electrons occurs to the lowest energy state in the vicinity (i.e., the 2DEG). Also, the higher the AlGaN band edge (with increased Al content), the more likely the electrons are to transfer because the potential difference is much larger. The surface

donor states are thought to have a density of approximately 2 x 10^{13} cm^{-2}. For an electron density of ~1 x 10^{13} cm^{-2} in the 2DEG, since there are more electrons than that at the surface and all will not transfer to the 2DEG, a number of 2 x 10^{13} cm^{-2} is a reasonable approximation.

2.1.3. Two dimensional electron gas (2DEG)

The above discussion addressed how the 2DEG (as shown in Figure 2.2 and 2.3) between the AlGaN and GaN is polarization-induced and addressed the source of the carriers in the 2DEG (Eq. 2.2). The 2DEG formation is a two-part process including both that of the quantum well formation and then its subsequent population with carriers. The 2DEG for AlGaN/GaN is a triangular quantum well that can be described by a 1 x 1 Hamiltonian which will be further described in section 2.6.1 under Schrodinger-Poisson's equation (Jogai, 2003).

In the preceding sections, the 2DEG charge was shown as due to the sum of positive charges in the device. It will also be shown to be a function of the surface potential in section 2.2.3. Here the 2DEG charge is related to the surface donor states by appending the surface and interface charges to a very common integral as defined in (Ambacher et al, 2000):

$$\sigma_{2DEG} = \int_{Ed}^{Ec} Nd\,(E)[1 - f(E)]dE - \int_{Ev}^{Ea} Na(E)\,f(E)dE - \sigma_{surf} + \sigma_{in} \qquad (2.3)$$

where σ_{surf} and σ_{in} are the polarization induced bound charge at the surface and the charge at the interface. N_d is the donor trap site density and N_a is the acceptor trap site density. E_c and E_v are the energy boundaries defined by the conduction and valence band edges,

and E_d and E_a are the donor and acceptor boundaries. From here, a bare surface barrier height of ~ 1.0 -1.8 eV was calculated with a surface density for donors of ~1.6 x 10^{13} cm^{-2} eV^{-1}, which supports the model for surface donors as the source of 2DEG electrons (Prunty et al, 2000). So, again it can be assumed that surface donors are the source of electrons. At equilibrium, the Fermi level at the surface is below some of the donor states, and those ionized states contribute the electrons that give rise to the 2DEG at the interface. As the thickness of the barrier layer increases, the surface Fermi level is lowered more and more with respect to the conduction band, increasing the surface barrier causing more and more donor states to be emptied, and thus increasing the 2DEG density.

2.1.4. Polarization: AlGaN/GaN Surface and 2DEG

Significant spontaneous polarization occurs in both GaN and AlGaN. This polarization charge is due to the fact that the fixed charge accumulating at the hetero-interfaces is intrinsic and exists in the unstrained crystal. This produces polarization induced fields, and also can produce a high carrier density 2DEG at the interface between the two layers. The presence of the field can also be explained as due to a lack of inversion symmetry in the crystal; the bond between the two atoms is not purely covalent. Thus, there is a displacement of the electron cloud toward one bond direction of an atom. The result is a net negative charge on one face of the crystal and a net positive charge on the other, if the face is not neutral. Polar surfaces are a common phenomenon in many crystals.

The two components to the polarization induced field in AlGaN/GaN are (i) spontaneous and (ii) piezoelectric, which is due to mechanical strain at the interfaces from distortion of the crystal lattice. The distortion of the crystal lattice is due to a difference of lattice constants for GaN and $Al_xGa_{l-x}N$. Figure 2.4 shows the [0001] gallium face. A charge sheet is then produced at the interface as a result of this strain. The two polarizations yield a net polarization P(x), described as

$$P(x) = P_{pz} + P_{SP} = -[(3*2\,x - 9\,1\,x^2) \times 10^{--6} - 2*5 \times 10^{-6}\, C\,x \cdot cm^2] \qquad (2.4)$$

where P_{pz} = piezoelectric polarization, and P_{SP} = spontaneous polarization. As shown in Figure 2.3, charge balance requires that the polarization charges cancel out overall, i.e., the charges are not mobile, but just provide a field. The polarization is the cause of a very large 2DEG. The polarization along the [0001] axis of (Al) GaN is responsible for the band structure and charge distribution in these HEMT's, as shown in Figure 2.4. The AlGaN surface with the adjacent Si_3N_4 layer creates an interface that will be considered in this work for how it changes the device. With the built-in electric field due to polarization induced charges in AlGaN/GaN, the charge at the interface allows for an electron density of approximately 1-2 x 10^{13} cm^{-2}. The structures studied in this research are AlGaN on wurzite GaN. Heterostructures in the wurzite nitride family have (0001) interfaces which bear a surface charge σ_0 that results from the polarizations of the two alloys at the interface.

Piezoelectric polarization arises from mechanical stress and is negative if tensile, and positive if compressive. For tensile strain, the piezoelectric and spontaneous vectors are aligned parallel, and aligned anti-parallel if strain is compressive. The AlGaN total

polarization is larger than that of the GaN buffer. AlGaN and GaN layers both have negative spontaneous polarizations; the GaN buffer charge σ_{p2} (in Figure 2.3) arises entirely from spontaneous polarization (Ambacher et al, 2000).

The AlGaN crystal unit cell is slightly smaller than the GaN unit cell (AlGaN has a smaller lattice constant). The AlGaN crystal stretches to match bonds with the GaN, which then changes the charge distribution in the AlGaN and gives rise to a piezoelectric polarization which points in the same direction as the spontaneous polarization. This negative piezoelectric polarization vector points from the nitrogen atom towards the nearest neighbor Ga atom along the [0001] axis and is shown in Figure 2.4. The polarization is directed towards the bulk for Ga-faced crystals and towards the surface if N-faced. The change in polarization at the AlGaN/GaN interface results in a net positive charge layer. This positive charge draws electrons from the GaN and the gate contact.

Studies have shown that the 2DEG electron density is a strong function of the Al content of the AlGaN barrier, as well as its thickness (Kocan, 2003; Lenka and Panda, 2011). In my dissertation, the surface states will play a very important role in the charge balance and source of 2DEG electrons. For this research, I have adopted the charge balance model, referenced throughout the field of device physics (Ibbetson et al, 2000).

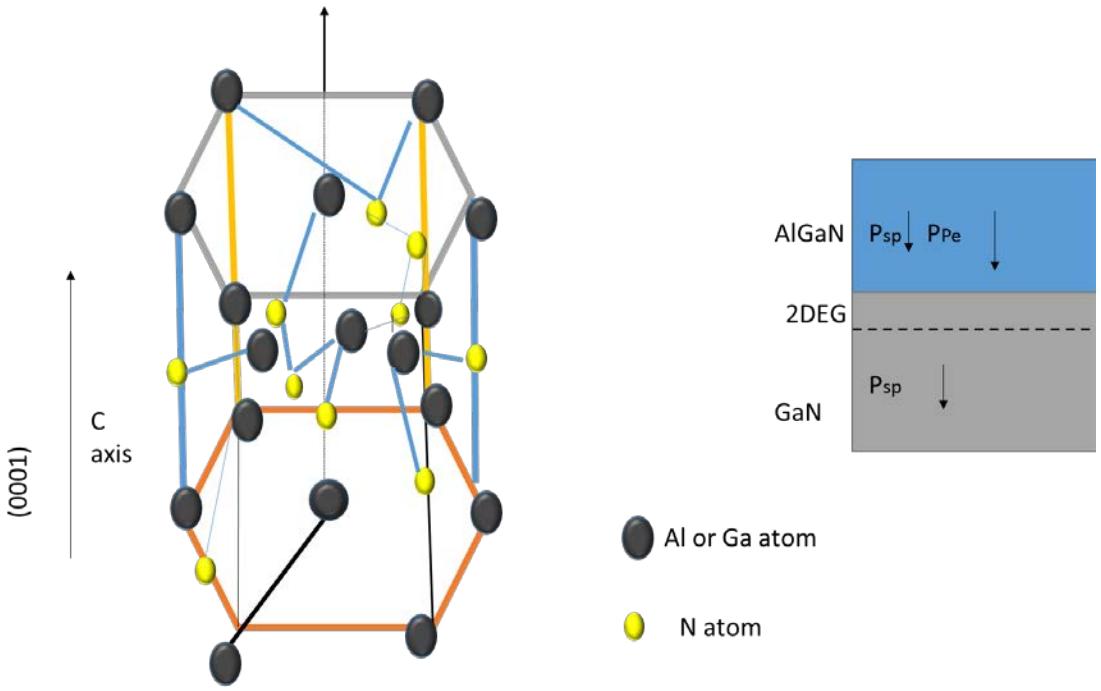

Figure 2.4. Crystal structure of GaN and AlN. Crystal structure (left), and polarization induced bound sheet charge, piezoelectric and spontaneous polarization (right), of pseudomorphic AlN/GaN heterostructures. In Ga-face heterostructures, the 2DEG is located close to the lower AlGaN/GaN interface; in N-face heterostructures, it will lie close to the upper GaN/AlGaN interface.

If there is an AlN layer, the spontaneous polarization at the AlGaN/GaN interface is given by

$$P_{SP} = P_{SP.AIN} + P_{SP.GaN}(1\text{-}x), \tag{2.5}$$

where x is the aluminum content of the $Al_xGa_{(1-x)}N$ barrier. The piezoelectric polarization is given by

$$P_{PZ} = 2^* (a - a_0/a)(e_{31} - e_{33})^*(C_{13}/C_{33})) \tag{2.6}$$

Since the spontaneous charge in the AlGaN shown in Figure 2.4 is larger than that in the GaN, as well as the fact that it aligns in parallel with the piezoelectric component, σ_{p1} is

much larger than $\sigma_{p2,}$ and as a consequence there is a net positive interface charge (σ_{p1} - σ_{p2}) that induces the 2DEG (σ_n) (Ambacher et al, 2000).

Ambacher (Ambacher et al, 2000) defined a fixed polarization charge density due to the abrupt interface in a top/bottom AlGaN/GAN heterostructure layer as follows.

$$\sigma(P_{PZ} + P_{SP}) = P(\text{bottom}) - P(\text{top})$$

$$= \{P_{PZ}(\text{bottom}) + P_{SP}(\text{bottom})\} - \{P_{PZ}(\text{top}) + P_{SP}(\text{top})\}$$

$$= \{Ps_P(\text{bottom}) - P_{SP}(\text{top})\} + \{P_{PZ}(\text{bottom}) \pm P_{PZ}(\text{top})\}$$

$$= \sigma(P_{PZ}) + \sigma(P_{SP}) \qquad (2.7)$$

If the polarization induced charge density is positive (+σ) in Figure 2.6, a 2DEG forms with a carrier concentration n_s as a result of the electrons compensating for the polarization induced charge. These charges (shown in Figure 2.3) can be related to their associated fields by applying Gauss' law

$$\nabla \bullet E = \rho / \varepsilon_0 \qquad (2.8)$$

to the hetero-interface region.

$$\varepsilon_2 E_2 - \varepsilon_1 E_1 = \sigma_{p1} - \sigma_{p2} - \sigma_n \qquad (2.9)$$

Here, ρ is the charge density, ε_1 is the permittivity of the AlGaN barrier, ε_2 is the permittivity of the buffer and E_2 and E_1 are the corresponding electric fields. The surface charge σ_{s1} is positive, and the field outside the device is zero, so the surface charge is then given by:

$$\sigma_{s1} = \varepsilon_1 E_1 + \sigma_{p1} \qquad (2.10)$$

2.1.5. Device Behavior

A simplified typical AlGaN/GaN HEMT device is shown in Figure 2.5. First, the expected behavior of a depletion mode or "always on" AlGaN/GaN HEMT, before passivation and without radiation damage is given. If it is" always on", there is always a current in the 2DEG unless a negative bias is applied to the gate, which then depletes the space charge region under the gate until pinch-off occurs. The sequence is shown in Figure 2.6 (a) and (b). GaN HEMT's are not intentionally doped as are MESFETS, and the channel gets its electrons from the unintentional doping. There is less Coulomb scattering in the channel than in non-HEMT devices, due to the lack of ionized donors which can serve as scattering centers. With less scattering, a higher mobility is achieved.

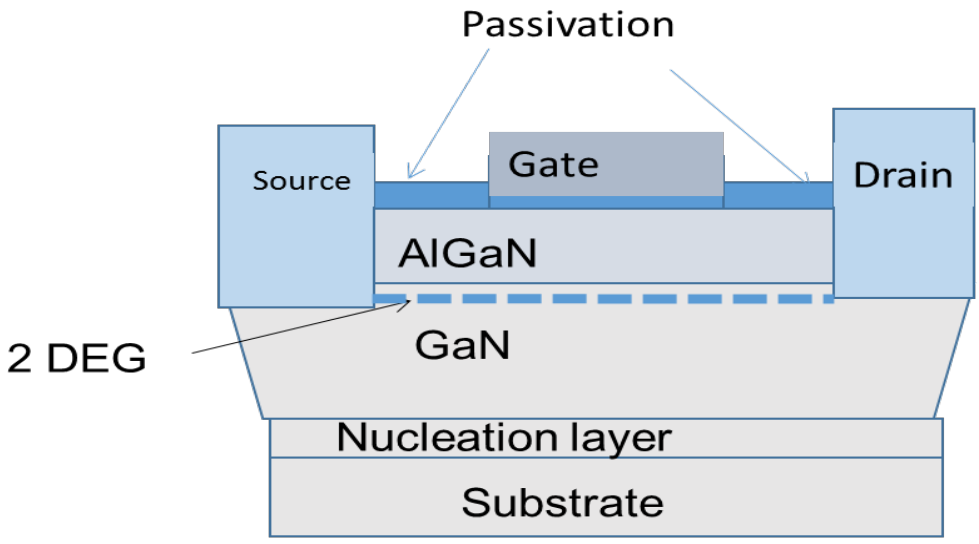

Figure 2.5 A simplified HEMT structure containing an AlGaN Schottky or donor contact layer, which serves as a source of electrons and a spacer layer.

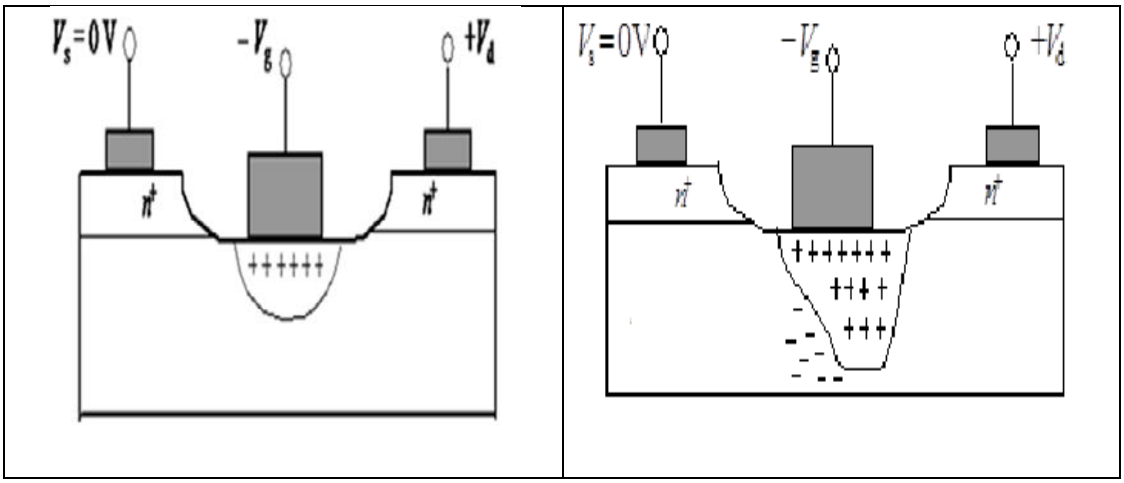

Figure 2.6. Channel depletion (left). With more negative bias, space charge increases. Channel nears pinch off (right).

Under operation, when a negative gate bias is applied, the Schottky layer becomes depleted as in Figure 2.6 (left). In Figure 2.6 (right), with further gate biasing the 2DEG becomes depleted resulting in channel modulation and modulation of the carrier concentration. Gain and amplification occur until the channel is fully depleted (pinched off).

2.1.6. The Purpose and Effect of Passivation

As discussed in Chapter 1, the benefits of the use of Si_3N_4 as a passivation layer have been proven since 2000. It has been shown to greatly improve power performance. Since passivation reduces dc to rf dispersion, and it is well know that the cause of this is due to surface traps, one can conclude that the layer passivates surface donor traps. Passivation has even been credited with doubling output power density (Kalavagunta et al, 2008). The present research effort looks at the effect of varying the Si_3N_4 passivation for 1-MeV electron irradiations.

According to Kordos *et al.* (Kordos et al, 2006) and Jeon and Lee (Jeon and Lee, 2005), there is an increase in sheet-charge density with increased tensile stress imposed by Si_3N_4 and a slight decrease in mobility resulting in an increase of the channel conductivity. There is a reduction in the surface states. Why the Si_3N_4 layer causes the mobility to decrease can be understood from both the positive field the layer causes and the additional scattering centers created from additional electrons and defect centers. Between the AlGaN and GaN layers is the 2DEG channel. One can ask how varying the Si_3N_4 layer affects the Hall measurement when Hall measurements are made through the 2DEG and not across the surface. However, there is a strong consensus that the source of the 2DEG electrons is from the surface donors as shown in Equations 2.1and 2.2, and as discussed throughout this dissertation.

Positive charges (creating a positive field) create surface carriers because the electrons are drawn towards them. So, on the surface, the number of carriers would increase and as a result there can be a new conduction channel there. Consequently, the mobility in the AlGaN, a dielectric, would go down. The Hall resistance has strong a dependence on mobility, so if mobility goes down, there must be additional scattering causing an increase in resistance.

In addition to causing surface-state reduction, induced stress is another effect of passivation (Shealy et al, 2007). There are built in electric fields due to the polarization charges described in section 1.2.4 for nitride structures grown in the [0001] orientation (Kuang, 2008). Depending on the direction of the polarization vectors, there can be an increase or decrease in carriers. In section 2.2.3, the differences in the band diagram show a surface potential difference when there is a GaN cap as opposed to not having one. The

effect of passivation that then affects the 2DEG carrier density of a device structure depends on the surface it is passivating. While a discussion of the effect of the Al content is very important and many studies have shown that the electron density is strongly correlated to the Al content of the barrier as well as to a lesser degree the barrier thickness (Palmer, 2011) , these effects not be discussed in this dissertation.

Along with the scattering mechanisms added by the passivation to explain the observed changes in Hall mobility, a defect commonly referred to as a K-center is invoked to explain how it passivates (Warren et al, 1991). The typical defect population of Si_3N_4 layers is in the range of between 0.8 – 1 x 10^{18}/cm^3. Warren *et al.* observed a K-center, described as a Si dangling bond back-bonded to three nitrogen atoms. The Si dangling bond could exhibit a charge state of neutral, positive or negative. The fixed charge could be positive or negative. It can be postulated that, due to the high percentage of hydrogen used in the PECVD process, the Si_3N_4:H layer is passivating the dangling bonds at the interface. Figure 2.7 is a diagram of the K-center dangling bond. It is hypothesized that a K-center dangling bond brings a positive field which passivates the surface donors. The defect's fixed charge state could be either positive or negative.

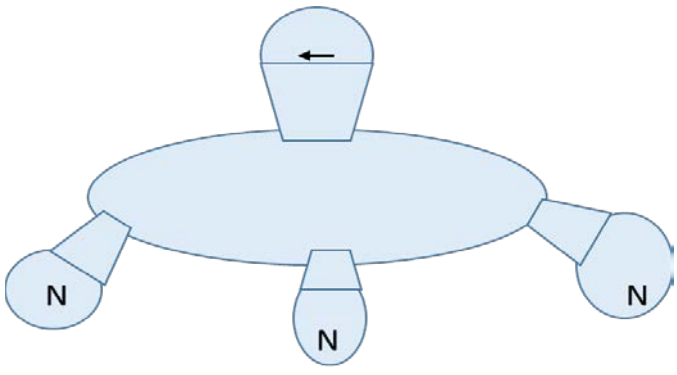

Figure 2.7. Depiction of Si_3N_4 K-center.

Passivation of nitrogen dangling bonds with hydrogen could lead to a net increase in fixed positive charge, due to the reduction of nitrogen dangling bond charge which can only exist in a negative or neutral state. This results in an increase in fixed positive charge**.** According to Wright (Wright, 2008) in studies using Si_3N_4 as a passivant for silicon solar cells, only surface recombination through defect levels in the band gap can be altered by passivation. In those studies, it was shown that Si_3N_4 greatly decreases N_{st}, which is the concentration of defects at the Si surface by reducing S_{eff} , the effective surface recombination velocity and thus could be an excellent passivant. The effective surface recombination is defined as occurring for cases where

$$S_{eff} < d/2W \tag{2.11}$$

is satisfied. The parameter d is the diffusion constant of the AlGaN/GaN, and W is its thickness**.** As will be shown in Chapter 5, with increasing Si_3N_4 thickness, the sheet concentration goes up and the mobility goes down. So perhaps the Si_3N_4 produces or enhances the surface donors (higher n_s) but adds surface scattering centers (lower mobility μ). This study will examine the effect of radiation and Si_3N_4 passivation concurrently. Some initial reported observations of the effects of Si_3N_4 are: 1) Si_3N_4 passivation reduces the density of surface traps (Vertiachikh et al, 2002); 2) Positive charges located in the Si_3N_4 neutralize the effects of filled surface states (Prunty et al, 2000); and, 3) Si_3N_4 stiffens the surface, reducing piezoelectric charge resulting from the gate bias-induced non-uniform strain in the AlGaN barrier layer (Hu et al, 2001).

2.2. Characterization Overview

First, the transport mechanisms will be discussed as characterized by the Hall system. Then the physics that is involved in the photoluminescence spectra that provide information on the spatial localization of defects will be given. DLTS will be explained, as it further aides in trap analysis done in this research. A general analysis of defects and traps follow; they are a critical limiting factor in device behavior. The basic physics and algorithms that are used in the modeling and simulation in this research are given in the last section.

2.2.1 . The Hall System

In this research, van der Pauw Hall measurements were used to measure mobility, carrier density and resistivity before and after electron irradiations. Room temperature data as well as temperature-dependent Hall measurements show pre- and post-electron irradiation variation with temperature as well as with Si_3N_4 passivation thickness. The resistivity and Hall coefficient is usually obtained by using the van der Pauw method. The sample needs to be flat, homogeneous, and isotropic, have no holes, and have line electrodes on the periphery projecting to point contacts on the surface. Two possible electrode arrangements are shown in Figure 2.8.

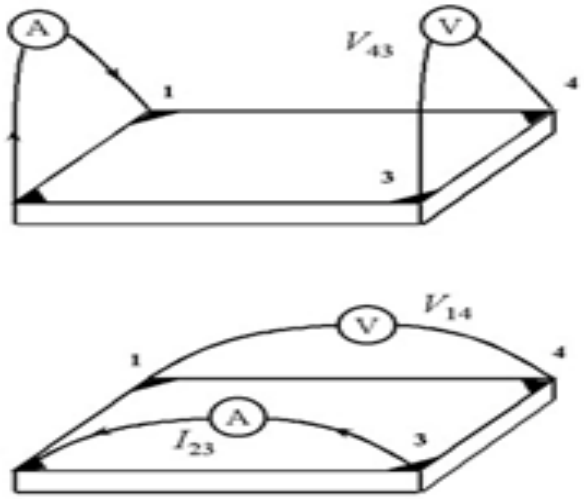

Figure 2.8. Set up for Hall measurement showing van der Pauw arrangement (from NIST website).

The four corner contacts of the sample need to be ohmic; the voltage drop across the contacts must be negligible compared with the voltage drop across the sample, so that they do not affect the I_g-V_g characteristics. The contacts need a metal work function less than the work function of an n-type semiconductor or greater than the work function of a p-type semiconductor (although few metal-semiconductor combinations satisfy this requirement). In practice, they can be composed of carriers yet have a negligible internal resistance R_c compared to that of the semiconductor, or a non-negligible R_c but obey Ohm's law for current densities of interest (Borchi et al, 1999).

From the measurement of the Hall coefficient R_H, the Hall carrier concentration n, can be obtained via:

$$R_H = E_y/j_x\, B = -\, 1/q\, n \qquad (2.12)$$

where E_y/j_x is the y-component of force which the electrons experience upon application of a magnetic field in the z direction. q is the charge on the electron and n is the electron density. From the conductivity measurement, the mobility can also be deduced. This mobility is the Hall mobility μ_H (when electrons have the same magnitude of x-axis mobility, then $\mu_H = \mu$). The conductivity is given as:

$$\sigma = n\, q\, \mu_n + p\, q\, \mu_p \tag{2.13}$$

and

$$\mu_H = R_H\, \sigma \tag{2.14}$$

Donor/acceptor energies and concentrations can typically be deduced from Hall-effect models. Low-temperature Hall-effect measurements have been used to arrive at the surface region donor concentration by way of the surface conductivity. The surface donors must then be further identified by correlating with some other analytical technique such as secondary ion mass spectroscopy (SIMS), positron emission spectroscopy, photoluminescence or DLTS. From the value obtained for μ_H and then n in equation 2.14, a charge-balance equation can be employed to determine donor and acceptor levels (Look, 1998):

$$n + N_A = N_D/(n/\Phi_D) \tag{2.15}$$

N_A and N_D are the acceptor and donor concentrations and Φ_D is the donor density of states. It will be shown that radiation changes the carrier concentration by creating acceptors or donors.

2.2.2. Mobility and Scattering Mechanisms

As an electron moves through an electric field, its momentum balance can be defined by

$$-q\,\varepsilon\,\tau_c = m_n\,\upsilon_n \tag{2.16}$$

where the subsequent electron drift velocity is

$$\upsilon_n = -(-q\,\tau_c/\,m_n\,)\,\varepsilon = \mu_n\,\varepsilon \tag{2.17}$$

In these equations, ε is the electric field, τ_c is the carrier relaxation time or lifetime, m_n is the electron mass, and μ_n is the electron velocity. The mobility (μ_n) measurements obtained in this research from Hall system measurements are strongly scattering dependent. In the observations from the Hall measurements, the electron mobility will go down after irradiation because the 1-MeV electron irradiation, along with the addition of Si_3N_4 passivation, will create scattering centers. For the momentum relaxation lifetime associated with scattering τ_m, there is a power dependence on energy which must be considered for most scattering mechanisms (Wolfe et al, 1989):

$$\boldsymbol{\tau}_m = \boldsymbol{\tau}_0 x^r \tag{2.18}$$

where x is the kinetic energy normalized to units of the thermal energy kT,

$$x = \frac{\varepsilon - \varepsilon_c}{kT} \tag{2.19}$$

The momentum relaxation time is used in defining transport parameters in the presence of an electric field. Conductivity mobility, obtained from $\sigma = q\,\mu_c\,n$, is defined by scattering:

$$\mu_c = e\langle\tau_m\rangle/m^*, \text{ and } \tau^{-1} = \tau^{-1}_{ac} + \tau^{-1}_{pe} + \tau^{-1}_{po} + \tau^{-1}_{ii} + \tau^{-1}_{dis} \tag{2.20}$$

The scattering components of the mobility μ_c from left to right are acoustic (ac), piezoelectric (pe), polar optical (po), ionized impurities (ii), and dislocation (dis). Additional scattering mechanisms that specifically contribute to the mobility of the structures in this study will be added and discussed as mobility is further defined. From here, the Hall carrier density, which is approximately equal to the sheet carrier density, can be calculated as:

$$\mu_c \sim \mu_H = e\langle\tau^2\rangle/m^*\langle\tau\rangle, \text{ and } \mu_H = R_H \sigma \quad \dashrightarrow n_H = n/r = -1/e\, R_H \sim n \tag{2.21}$$

The above scattering mechanisms in equation 2.20 can be defined as some function of the scattering potential $\Delta U(r)$, which is a perturbation that the defect produces. $\Delta U(r)$ has units of energy.

For scattering due to ionized impurities, τ_{ii}, the interaction is electrical and can be described by the Coulomb energy (Wolfe et al, 1989):

$$\Delta U(r) = Zq^2 / 4\pi\epsilon(0)r \tag{2.22}$$

which is treated as being approximately equal to a scattering potential:

$$\Delta U(r) = \frac{\boldsymbol{h^2}}{\mathbf{m}*} \left(r_B / r^5 \right)^{1/2} \tag{2.23}$$

In eq. 2.22, Z is the charge state of an impurity or defect, q is the charge of the electron, $\epsilon(0)$ is the static permittivity of the material and r is the distance between the neutral impurity and the free carrier. In equation 2.23, r_B is the ground state Bohr radius, and m* is the effective mass.

Ionized impurities can be within or outside the quantum well (2DEG). Residual impurities in AlGaN/GaN, found on the GaN, have a density usually around 10^{15} cm $^{-3}$.

With impurity scattering, due to the increase in screening effects with increasing carrier density, these affects become negligible compared to intrinsic scattering. The mobility μ_{ii} due to ionized impurity scattering usually dominates at lower temperature in semiconductors because it is proportional to $T^{3/2}$ (Look, 1998):

$$\mu_{ii} = 128 \frac{\sqrt{2}\,\pi^{1/2}\,\epsilon^2 (kT)^{3/2}}{N_I Z^2\, e^3\, m^{*1/2}\, [\ln(1+y) - \frac{y}{1+y}]} \quad , \quad y = 24\epsilon m^* (kT)^2 / \hbar^2 e^2 n \qquad (2.24)$$

In Eq. 2.24, N_I is the ionized impurity concentration. A screened Coulomb potential is used to treat the scattering caused by ionized impurities:

$$\Delta V = \frac{Ze^2}{4\pi\epsilon r} e^{\frac{-r}{\lambda_D}} \qquad (2.25)$$

where Ze is the effective ionic charge, and λ_D is the Debye length (Wolfe et al, 1989).

For acoustic and polar-optical phonons, τ_{ac}, τ_{pe} and τ_{po} can be described using scattering by deformation potentials or the piezoelectric effect. Displacements of a chain of atoms from their Bravais lattice sites can be Longitudinal (LA) or transverse (TA). For the longitudinal component, the LA scattering potential is defined as (Wolfe et al, 1989);

$$\Delta U(r,t) = \varepsilon_A \Delta \bullet u(r,t) \qquad (2.26)$$

where u(r,t) is the displacement caused by an acoustic phonon in direction and time and ε_A is the deformation potential. For piezoelectric scattering, the strain caused by LA phonons polarizes the ions in the crystal lattice and cause time- and space-varying electric fields according to

$$\Delta U(r,t) = - q\, \Psi(r,t) \text{ and} \qquad (2.27)$$

$$\Psi(r,t) = - \int E(r,t) \bullet dr \qquad (2.28)$$

where $\Psi(r,t)$ is the time- and space-varying wave function.

For optical phonons, a wave depiction is shown in Figure 2.9 below. The polar mode of scattering is due to the electric field resulting from the polarization of ions in their unit cell. Their occurrence is in crystals that have more than one atom in the unit cell. They are called "optical" because in ionic crystals they are excited easily by light (Look, 1998). The polar-mode potential is usually described as:

$$\Delta U(r,t) = - iqe^*/ \Omega\varepsilon(\infty)q_s\int\delta\, u(r,t) \bullet dr \qquad (2.29)$$

where e* is the Born effective charge and ε is the materials permittivity. Note that acceptor-type

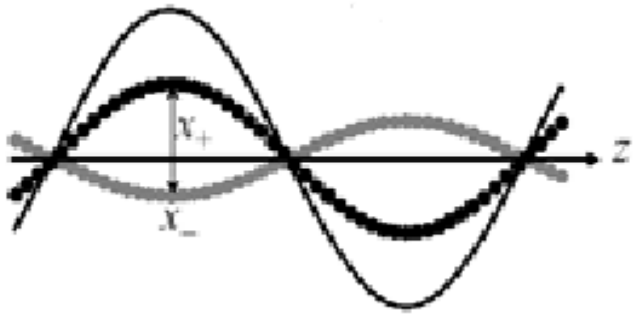

Figure 2.9. Polar modes for optical phonons.

charged defects are created by radiation damage, which scatter more than donor type (which are neutral). This damage can be considered by the term τ_{dis} in the mobility equation 2.20.

For acoustic phonon scattering, it is sufficient to consider the 2D electrons as interacting with a 3D phonon field. Acoustic, as well as optical phonons, interact with the

carriers through potentials of the following form, which connects the electron and phonon systems (Farvacque et al, 2002):

$$V_{ph,k} = A(\kappa,\omega)\,(a_{\kappa}\, e^{-i\,\kappa r} + a^{+}_{\kappa}\, e^{+i\,\kappa r}) \qquad (2.30)$$

κ is the 3D phonon momentum and a and a^{+} are annihilation and creation operators. The various functions A(κ,ω) depend on the phonon-electron coupling mechanisms. From this equation and other functions (Farvacque et al, 2002), one finds that the more confined the electronic density is, then the larger the phonon scattering effect will be.

Carrier-carrier scattering, which is most significant at low temperature, is a two-particle process interacting through the Coulomb potential. Starting with the scattering formula:

$$1/\tau^{+-} = 2\pi/\hbar^{+-} \sum|\langle n,k \mid V_{tot}(r^{+-}\omega)|\dot{n}\kappa\rangle|\hat{}2(1-\cos(k,\kappa))\delta[\varepsilon\,\dot{n}(\kappa)-\varepsilon\, n(\kappa)^{+-}\hbar\,\omega] \qquad (2.31)$$

and restricting the scattering process to quasi-elastic collisions (ω->0), there is now a term that coincides with the Episov Levinson formula (Norton, 2009) which, after an approximation, leads to larger and more realistic mobility values approximately equal to:

$$\sim (1-\exp(-\pi\, n\, \dot{n})) \qquad (2.32)$$

When carrier-carrier scattering is defect related, these defects, in addition to bringing the extra scattering, produce dangling bonds with energy levels that are different than those of the native material. They are localized states for which the Schrodinger-Poisson equation must be separately solved for. The break in the periodicity of the lattice results in a decrease in mobility and conductivity.

2.2.3. Hall Mobility and Carrier Density as a Function of Device Structure

In this research, two structures are studied; AlGaN/AlN/GaN and GaN/AlGaN/GaN. Since it will be shown that the strongest model for the source of the 2DEG electrons is the one indicating the AlGaN surface states, then whatever interfaces with that surface will affect the carrier concentration and the mobility of the carriers. So that would be either Si_3N_4 for the first structure or GaN for the second structure.

Structural parameters affect the 2DEG, and hence all other device metrics. An AlN layer reduces the alloy scattering by acting as a barrier between the 2DEG wave function and the AlGaN. This will be shown in the 2DEG wave function models in Chapter 5. The AlN layer adds to polarization, which then raises energy bands up relative to the Fermi level. If charges from Si_3N_4 act in the same direction, then the conduction band will be raised and there will be more transfer of charge and electrons into the localized 2DEG. A discussion on how an AlN interlayer affects AlGaN/GaN HEMT structures follows.

Figure 2.10 below shows the difference a thin AlN layer will cause in changing the effective ΔE_c (Meneghinni, 2008).

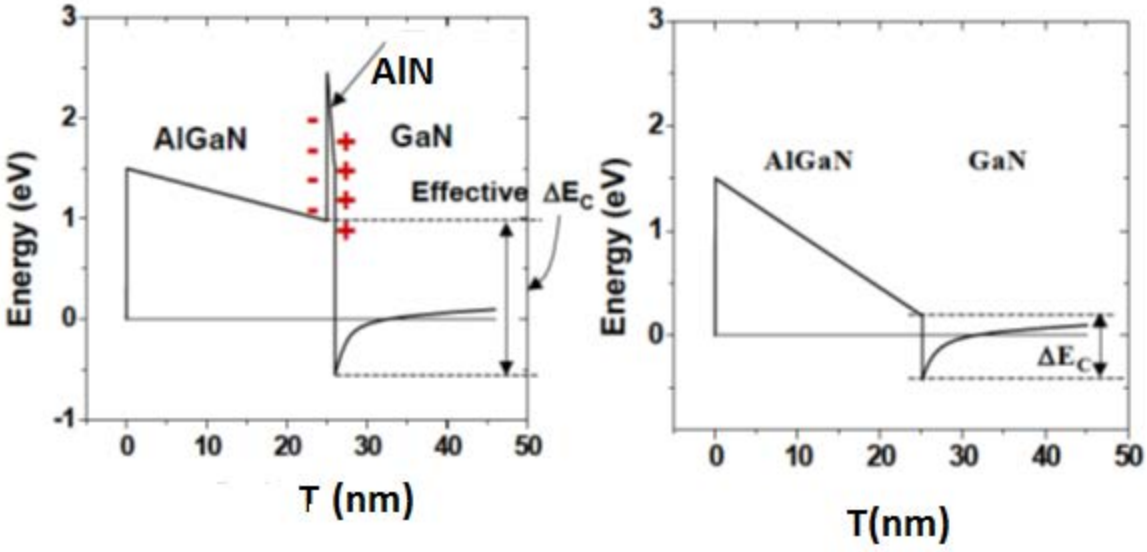

Figure 2.10: Band diagram comparisons for structure with an AlN interlayer on the left and without the interlayer on the right. The horizontal axis is thickness. Note the change in ΔE_c (from Shen, 2004).

The samples in this study have a 1-nm AlN layer, and so the conduction band offset ΔE_c or potential drop will be about 0.9 eV (Meneghinni, 2008), which then gives

$$\Delta E_{c,eff} = \Delta E_{c,AlGaN} + \frac{q^2 \quad (\sigma_{AlN} \quad - n_s)}{\varepsilon * \varepsilon_0} * t_{AlN} \quad = 1.4 \text{ eV} \tag{2.33}$$

This value is about double the offset of a typical HEMT. For the structure on the right in Figure 2.10, just AlGaN/GaN without an interlayer or cap, the 2DEG density can be written as:

$$n_s = \frac{\sigma_{AlGaN} * t_{AlGaN} - \frac{\varepsilon \varepsilon_0 \ \varphi_B}{q} + \frac{\varepsilon_0 \varepsilon (\ \Delta E_{c,AlGaN} \ )}{q^2}}{t_{AlGaN} + d_0} \tag{2.34}$$

For the structure on the left, with an AlN interlayer, the increase in 2DEG density can be written as:

$$n_{s,AlGaN/AlN} = \frac{\sigma_{AlGaN} * t_{AlGaN} + \sigma_{AlN} * t_{AlN} \quad - \frac{\varepsilon \varepsilon_0 \varphi_B}{q} + \frac{\varepsilon_0 \varepsilon (\Delta E_{c,AlGaN})}{q^2}}{t_{AlGaN} + t_{AlN} + d_0}$$

$$= \frac{\sigma_{AlGaN} * t_{AlGaN} - \frac{\varepsilon \varepsilon_0 \varphi_B}{q} + \frac{\varepsilon_0 \varepsilon (\Delta E'_{c,eff})}{q^2}}{t_{AlGaN} + t_{AlN} + d_0} \tag{2.35}$$

The net polarization charges and thickness of the AlGaN and AlN layers are σ_{AlGaN}, σ_{AlN} , t_{AlGaN} , t_{AlN} ; and $\Delta E_{c,AlGaN}$ is the conduction band discontinuity. There is a change in the energy band slope as compared to a sample without an interlayer (as on the right). Adding the effective conduction band discontinuity term to n_s gives a structure with AlN having a higher n_s.

For structures with GaN caps, there is reduced dispersion without additional passivation. With a cap, the distance is increased between the channel and the surface, and there is less surface potential fluctuation. Also, a GaN cap serves as a surface charge control layer, reducing the effect of polarization charge. It also screens the 2DEG from surface traps that lead to current collapse. Later, it will be shown that the GaN/AlGaN and AlGaN/GaN interfaces have anti-parallel polarization vectors. Figure 2.11 is a band diagram of a GaN cap structure.

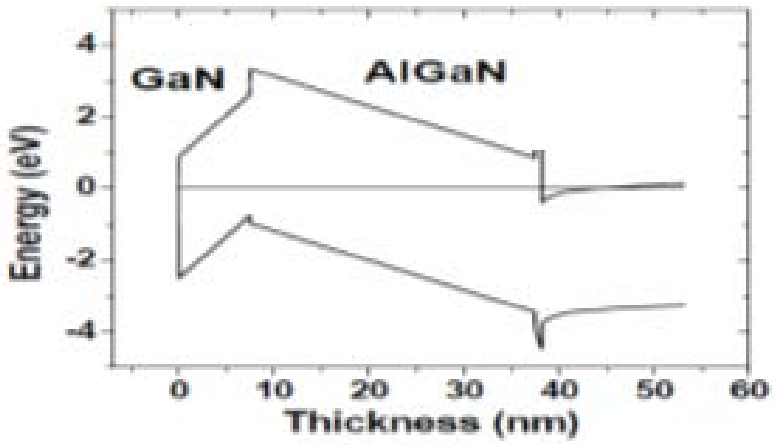

Figure 2.11. Band diagram of a GaN/AlGaN/GaN structure with a 7 nm GaN cap (from Shen, 2004).

For the GaN cap structure, the 2DEG sheet charge density in the channel goes down as compared to a structure with no GaN cap. The reason is that the polarization charges at the two interfaces, GaN/AlGaN and AlGaN/GaN, cancel each other out. The effect of the cap turns out to be similar to applying a negative bias, particularly with thicker caps. The cap field points to the GaN/AlGaN interface. This decrease in carrier density can be described in terms of the surface potential, φ_S:

$$n_s = \frac{\sigma_{AlGaN} * t_2 + t_1 - \frac{\varepsilon \varepsilon_0 \ \varphi_{Bs}}{q}}{t_1 + t_2 \ d_0} \tag{2.36}$$

where t_1 is the GaN cap thickness and t_2 is the AlGaN thickness. The distance between the center of the 2DEG wave function and the AlGaN/GaN interface is d_0. This explains the decrease in carrier density in terms of the cap thickness and the higher surface potential. I will show in subsequent chapters that a high mobility results for structures with the GaN cap. This cannot be directly compared with the AlGaN/AlN/GaN structure, since the structures had little in common. However, general comparisons between

AlGaN/AlN/GaN and GaN/AlGaN/AlN/GaN by others have shown there is still a decrease in carrier density with the addition of a GaN layer and an increase in mobility, due to perhaps less carrier-carrier scattering.

2.2.4. Carrier Density

Sheet carrier density, often used synonymously with the term 2DEG, is a fundamental device metric. In the previous subsection, it was defined in terms of the surface potential for a structure with an AlN interlayer and then GaN cap, clearly indicating that the concentration of carriers in the 2DEG is device-structure dependent. It can alternatively be defined as the sum over all states or N_i concentrations in each sub-band in the quantum well:

$$N_s = \sum N_i \frac{m^* k_B T}{\pi \hbar^2} \ln(1+ \exp([E_f - E_i]/k_B T)) \quad (2.37)$$

where m* is the effective mass of the electron, E_f is the Fermi energy, E_i is the energy band level, and T is temperature. The term in parenthesis is the Fermi-Dirac distribution function, or F(E). For a semiconductor, the density of electrons is related to the density of available states and the probability that each of these states is occupied. The distribution term, for electrons with localized levels like those for impurities or defects can be written as a generalized distribution function (Sze and Ng, 2007):

$$F(E) = \frac{1}{1+ K \exp([Ef - Ei]/kBT)} \quad (2.38)$$

with K being the factor that accounts for degeneracy. K= 1 is for band electrons, while K= ½ is for donor electrons and K = 4 is for acceptor electrons assuming two degenerate

upper valence bands, common for most direct gap III-V materials. The slight splitting which occurs in GaN is ignored.

The relationship between the previously discussed carrier mobility and carrier density in AlGaN/GaN quantum wells is that the former strongly decreases with increased carrier density. This is because with increased carriers, the combination of phonon, carrier –carrier and interface defect scattering bring down the mobility. This is shown in Figure 2.12.

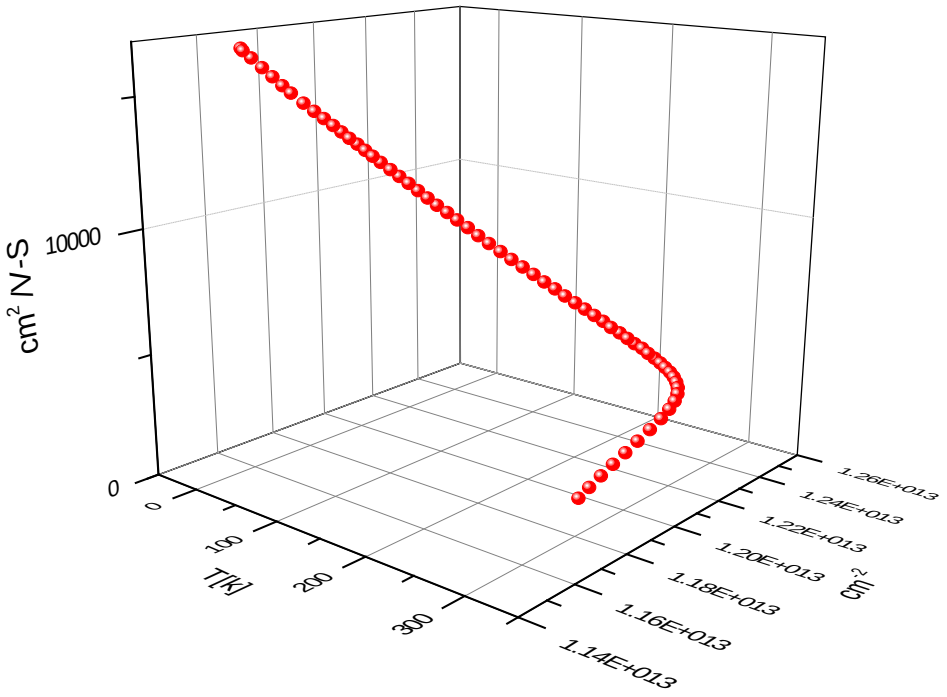

Figure 2.12: Temperature-dependent Hall data from an unpassivated sample showing that as carrier density (x-axis) increases, mobility decreases (y-axis).

2.2.5. Conductivity

Hall conductivity is an important metric for device performance. It is the product of the mobility and carrier density discussed above:

$$\sigma = q \mu n_s \quad (2.39)$$

It is taken from the Hall resistivity measurements, for which it is generally the mathematical inverse. For the samples in this study, it is mobility dominated. However, when the conductivity degrades, it can be concluded that either carriers are lost or mobility is going down due to scattering, or both, as in the case with 1-MeV electron irradiation.

2.3. Photoluminescence Physics

With photoluminescence (PL), one can determine certain impurities in semiconductors. It is well suited for shallow level impurities, but can also be applied to deep-levels. It can provide simultaneous information on many types of impurities in a sample. Low-temperature measurements are desirable to obtain the fullest spectroscopic information by minimizing thermally activated non-radiative recombination processes and thermal line broadening. The thermal distribution of carriers excited into a band contributes a width of ~ kT/2 to an emission line originating in that band, so it is necessary to cool the sample to reduce the width. Thermal energy kT/2 is 0.8 meV at T= 4.2 K. Room temperature measurements are often used to provide spatial PL maps of doping and trap densities. Laser excitation (quasi-monochromatic) is typically used in PL experiments, but broad-band light sources, such as lamps can also be used.

2.3.1. The Photoluminescence Peak

Samples are excited with a laser as the energy source:

$$h\gamma > E_G \quad (2.40)$$

where $h\gamma$ is the photon energy and E_G is the band gap energy, thereby generating electron-hole pairs by one of several mechanisms. Photons are emitted in the case of radiative recombination, but not in the case of bulk or surface non- radiative recombinations. Some of the photons may be reabsorbed in the sample, of reflected at the exit surface provided they are directed at the surface within the critical angle. When a photon generates an e-h pair, Coulombic attraction can lead to the formation of excitons (electrons and holes remain bound to each other in a hydrogen–like state). This excited state is called a free exciton (FE). Its energy is slightly less than the band gap energy required to create a separated e-h pair. An exciton can move through the crystal, but because it is a bound e-h pair, photoconductivity changes do not occur. When the FE is bound (localized) to an existing defect, the corresponding energy state is referred to as a bound exciton (BE) prior to the recombination (annihilation) of the exciton and is slightly lower than the FE recombination energy. For example, the hole in the FE can be attracted to a neutral donor (has an "extra" electron). There is a similar scenario for BEs recombining in the vicinity of neutral acceptors. The observation of PL emission attributed to FE recombination is indicative of having material that is sufficiently pure and free of non-radiative centers. In many cases, not all of the collapsed exciton energy is re-emitted as light. Phonon can be emitted and often PL spectra show many orders of phonon replicas.

Bound exciton recombination dominates over FE recombination in less pure material. Another recombination channel is referred to as an electron-acceptor transition. A free electron can recombine with a hole on a neutral acceptor. Also, a free hole can recombine with the electron in a neutral donor. A final common recombination involving

impurities is when an electron on a neutral donor recombines with a hole on a neutral acceptor (referred to as D-A recombination). Its emission line has an energy modified by Columbic interaction between the donors and acceptors.

In the case of band-to-band recombination (exciton binding energy not included), the role of phonons can be understood through energy conservation:

$$h\gamma = E_c - E_v \pm \hbar\Omega \tag{2.41}$$

where $\hbar\Omega$ is the energy of the phonon. Because the 3rd term, the phonon energy, is energetically more costly when positive (+) and requires having a population of phonons, it is more likely to have phonon emission (- term), rather than phonon absorption (+ term). For conservation of momentum, we have:

$$k_v + q = k_c \tag{2.42}$$

where q is the phonon momentum and k_v and k_c are the electron momenta in the valence and conduction bands.

2.3.1.1. DX Centers

A classical DX center (donor next to an "X" unknown) is sometimes called a shallow- deep transition. For the materials studied here, the normal DX is a shallow level that has become deep due to alloying (for example, with Al). Doping does not cause this effect. "DX –like" means it can just be a common donor (impurity defect, etc.), but in this work, these centers can also transfer over their electrons to the 2DEG region to give 10^{13} electrons. If there are not sufficient numbers of donors or DX centers, then the electrons have to come from somewhere else; the surface being that other possibility.

Nitride semiconductors are easy to dope n-type; in fact, they often exhibit unintentional n-type conductivity. In the past, it was believed that nitrogen vacancies were the source of unintended doping. However, it is now a consensus that unintentional impurities, such as oxygen or silicon, are most likely the explanation for the observed n-type conductivity. Oxygen exhibits a very interesting behavior in nitrides. In GaN, it behaves as a shallow acceptor, but when the band gap is increased (either under hydrostatic pressure, or by alloying with Al), the oxygen undergoes a transition to a deep center (DX center). Oxygen also can behave as a deep acceptor, i.e., it becomes a compensating center.

Oxygen becomes a deep level in AlGaN when the Al concentration exceeds about 30% (Kuang, 2008). Silicon does not undergo the DX transition. Silicon should therefore act as a shallow donor in AlGaN up to very high Al concentrations. Note, however, that oxygen tends to be unintentionally incorporated in compound semiconductors with high Al content; and any oxygen that is present in AlGaN with more than 30% Al will act as a compensating center for electrons.

2.3.1.2 Excitons

This section describes exciton quasi-energy states and extends the discussion in Section 2.3.1. When a photon is absorbed by an electron in a solid, and the energy of the photon is equal to the amount of energy between the state in which the electron is currently located and some other unoccupied state, a transition between states can occur. This is known as the Bohr condition. With electrons in semiconductors, the electrons absorbing photons with energies larger than the band-gap energy are easily promoted

from the valence band into the conduction band, because of the near-continuum of empty states available. When an electron is excited into a vacant space in the conducting band, the electron leaves behind a hole. This hole behaves very much like an electron of positive charge. Once such an excitation occurs, the first possibility is that the two particles drift apart, the electron in one direction and the hole in another. The other thing that can happen is the formation of an exciton. This metastable dual-particle system is known as a FE. Because you essentially have a negatively charged particle in close proximity to a positively charged particle, the two can trap each other and form something that looks very much like a hydrogen atom, with a binding energy of a few meV, which reduces the excited state energy. The exciton is a then a hydrogenically bound electron-hole pair. It has bound energy levels just like those in the hydrogen atom.

This exciton can itself migrate or, after some amount of time, the electron will spontaneously recombine with the hole, emitting light in the process. The energy of the luminescence will generally be less than the material's band-gap energy, and because most semiconductors have band-gaps in the visible region of the electromagnetic spectrum, some of the light is usually occurring in the visible region as well. Figure 2.13 is a diagram illustrating these possibilities.

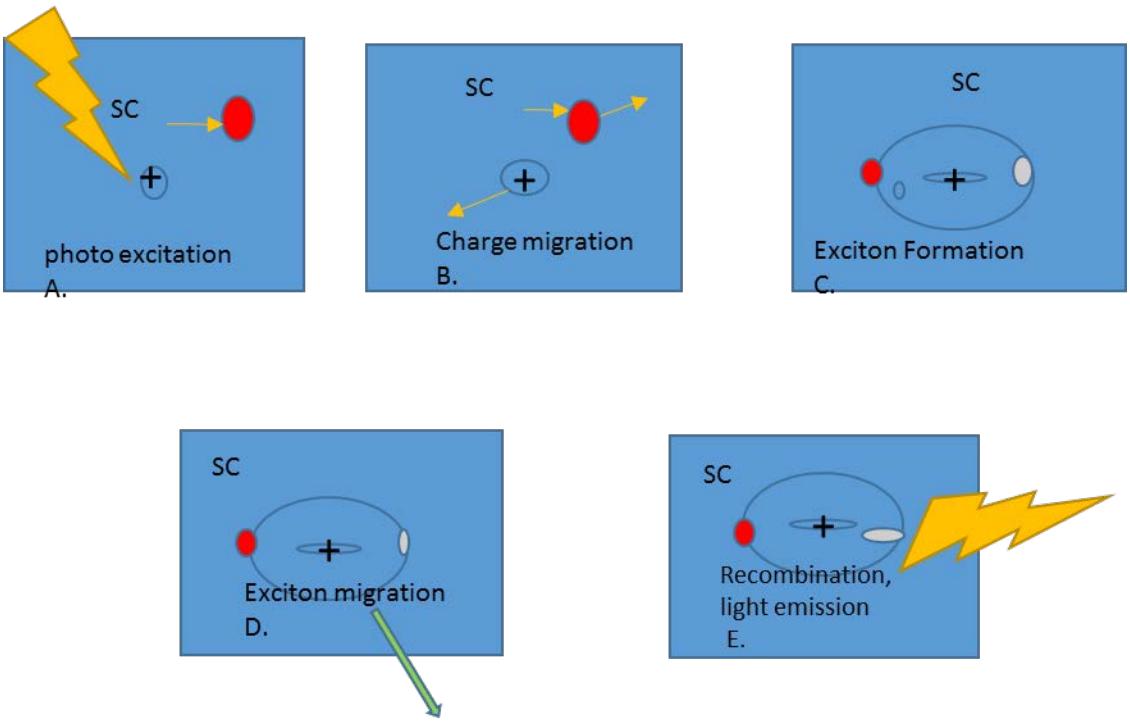

Figure 2.13. Depictions of some of the light-driven processes in a semiconductor. (A) Photons from an ambient light source are absorbed by an electron. The electron (red) is excited into the conducting band, leaving behind a hole (blue). (B) The electron and hole can move independently of each other (charge migration). If many excitations happen and electrons can be made to flow in one direction, and holes in another, the material can be the basis of a solar cell. (C) Alternatively, the electron and hole can entrap each other, forming a hydrogenic bound state known as an exciton. (D) The exciton may itself migrate through the material, or (E) the electron and hole can recombine, in many cases emitting a photon. Photons emitted by excitons in an ideal material are nearly monochromatic.

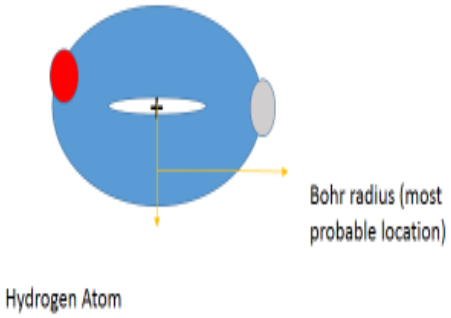

Figure 2.14. Hydrogen atom showing its Bohr radius.

In Figure 2.14, when in its lowest energy state, the electron orbiting the hydrogen nucleus (a proton) has a roughly spherically symmetric probability distribution. That is, for a given distance from the nucleus, the electron has an equal probability of being found in any direction from the nucleus. The most likely distance at which the electron can be found is known as the Bohr radius, which is equal to about 0.05 nm.

An exciton radius, shown in Figure 2.15, is like a metastable hydrogen atom. It has orbitals and states just like a hydrogen atom, and it also has a Bohr radius (known here as the exciton-Bohr radius, alpha) which is the most likely distance the electron will be away from the hole. This distance is usually quite a bit larger than that of a hydrogen atom, because the exciton is not formed over "free space". That is, there are other electrons in the background that change the electrostatic forces which determine what the "optimal distance".

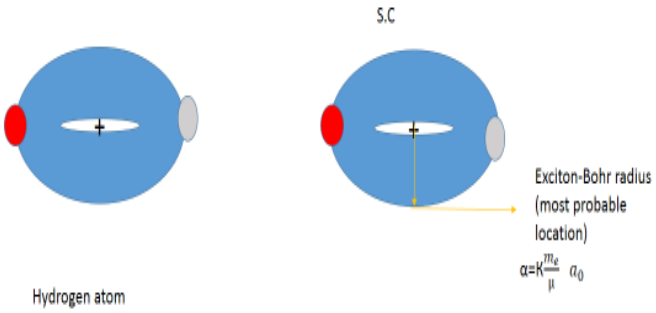

Figure 2.15. The exciton–Bohr radius is depicted.

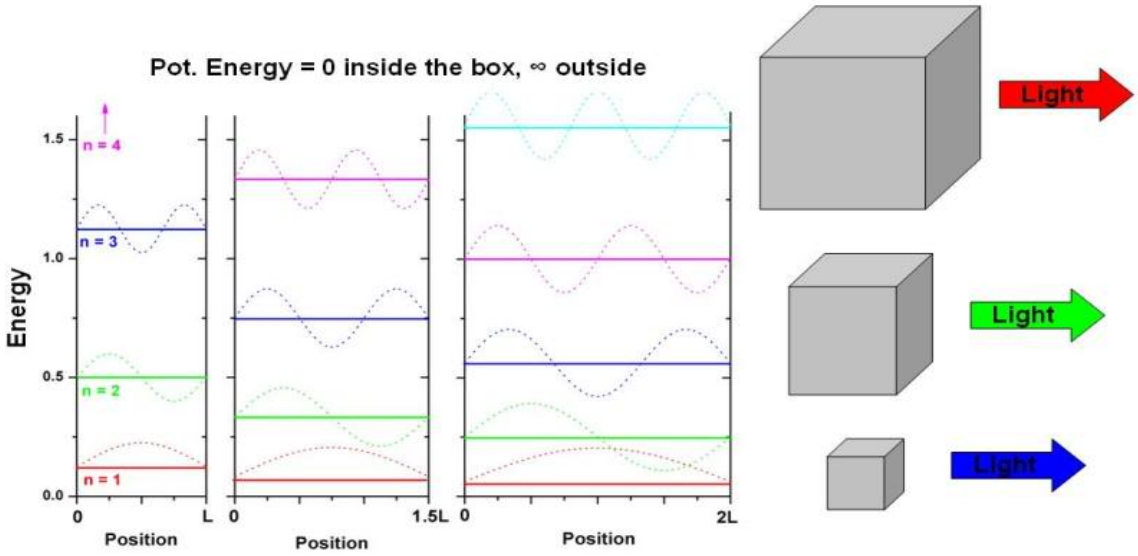

Figure 2.16. Allowed energy states vs. box size for confined system.

Basically, the exciton-Bohr radius is scaled by a constant known as the dielectric scaling factor kappa, which is the ratio of the material's dielectric response to that of free space. The value of kappa depends on the material and typically ranges from 3-12 for common semiconductors. In the case of atoms/molecules, we find that the electron/particle is only allowed to have certain energy values, and its probabilistic position is defined by orbitals, described by wave-functions in the quantum mechanical sense. As illustrated in Figure 2.16, as energy levels get closer together as the box size increases, this means that light emitted from an excited electron in a big box is lower energy – or more red colored (longer wavelengths) – than an excited electron in a small box. So, it is for the larger exciton radius as opposed to hydrogen.

2.3.2. The Yellow Line Emission

As previously mentioned, unintentional doping in AlGaN/GaN is due to shallow donors, and PL results on the samples in this study imply that these donors are oxygen or silicon (Neugebauer and Van de Walle, 1996; Mattila and Nieminen, 1997; Lee et al, 1997; Kwon et al, 2000). There are many models invoking defect complexes and substitutional sites, but Colton (Colton, 2000) believes unintentional silicon is replacing nitrogen (Si_N) or oxygen replaces nitrogen (O_N). Based on the effective mass of GaN, the hydrogenic donor binding energy was calculated to be E_d = 33 meV, comparable to the ionization energies of for Si_{Ga} = 30.8 meV and O_N = 32.4 meV. The exciton Bohr radius α was calculated to be 0.529 Å $(m_0/m^*)\varepsilon$ = 23 Å . There is a large amount of evidence (Colton, 2000) that supports a donor-acceptor pair (DAP) transition. The resulting emitted photon from the recombination changes equation 2.41 to:

$$\hbar\omega = E_g - E_A - E_D + e^2 / (\varepsilon R) \qquad (2.43)$$

Here E_g is the band gap energy of ~3.47, and E_A and E_D are the acceptor and donor binding energies, respectively. In the last term, R is the distance between the donor and acceptor which defines the Coulombic attraction between the donor and acceptor charge states. To be noted is that the V_{GA}, an acceptor defect, involved in emission in the yellow spectral region (thus Yellow Line, or YL transition), has the lowest formation energy of any native defects in n-GaN. A donor acceptor pair transition occurring with PL defined by equation 2.43 is represented below.

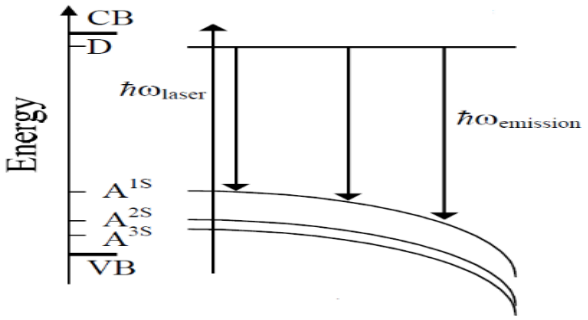

Figure 2.17. Donor-acceptor pair transition occurring in PL.

2.3.3. The Blue Line

Emision in the blue region of the visible spectrum is believed to be due to a transition involving a complex with Mg. The Mg acceptor on a gallium site (Mg_{GA}) is believed to have a hydrogenic binding energy of about 200 meV, with some reports indicating a value up to 250 meV (Kwon et al, 2000). Calculating again as done for the donor site above, but instead for a hole and using the effective hole mass, the acceptor Bohr radius is estimated to be 4 Å. As for the YL, there are a number of models that define the BL transition occurring. The one that best fits the PL spectra in this research is the $Mg_{GA} - V_N$ transition (Reshchikov and Markoc, 2005).

2.4. Deep Level Transient Spectroscopy

Deep Level Transient Spectroscopy (DLTS) can be used to determine carrier concentration, activation energy and capture cross section (Look, 2006). DLTS is a measure of capacitance transients, defined as:

$$\Delta C = C(t_1) - C(t_2). \tag{2.44}$$

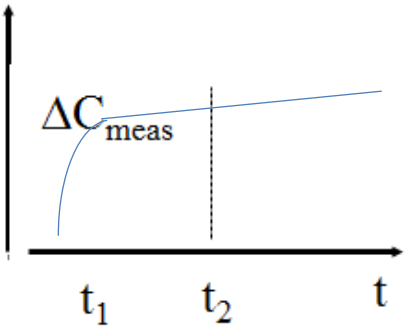

Figure 2.18. Change in capacitance ΔC with time, t.

With a reference frequency, obtained from voltage-pulse repeating rates, this then is multiplied by a constant to get a "rate window". As the temperature is swept from t_1 to t as in Figure 2.18, once the emission rate of carriers from a defect in the sample equals the rate window at T_{peak}, a peak is obtained from the spectrum as shown in Figure 2.19.

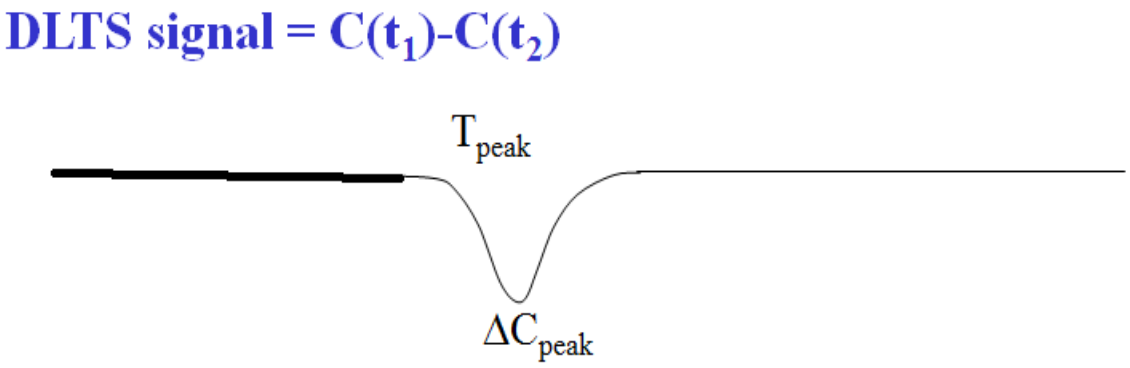

Figure 2.19. Formation of DLTS peak.

The emission rate constant e_n can be expressed as:

$$e_n\,(T_{peak}) = \frac{\ln\,(t2/t1)}{t2-t1} \qquad (2.45)$$

The measurement is performed on semiconductor devices that possess a voltage-modulatable space-charge layer. Note that Schottky diodes reveal only majority carrier traps. Given this, a reverse-biased Schottky barrier on the sample is subjected to a forward-bias pulse in order to flood the depletion region of the device with electrons, temporarily filling the traps in the region. Once the original reverse bias is reestablished, the temporary filled electrons (or holes) will be re-emitted.

From a set of the emission rate and the corresponding temperature pairs, one can make an Arrhenius plot, which provides a defect activation energy for the thermal emission process. The Arrhenius plot is the $\ln(e_n/T^2)$ as a function of 1000/T. Usually this energy (sometimes called the defect energy level) together with the plot intercept value are defect parameters used for its identification or analysis. On samples with low free carrier density, conductance transients have also been used for a DLTS analysis (Look, 2001).

2.5. Defects, Donors, and Traps

Impurities can be shallow or deep. Shallow impurities are impurities which require little energy to become ionized - typically around kT/2 or less. Deep impurities require energies larger than the thermal energy to ionize so that only a fraction of the impurities present in the semiconductor contribute to free carriers. If a deep impurity is greater than five times the thermal energy away from either band edge, it is very unlikely

to ionize. These impurities are traps because they can be act as recombination centers in which electrons and holes fall and annihilate each other.

In addition to impurities, bulk traps can be due to lattice mismatches (interface states), dangling bonds (surface), or various types of damage by radiation. Traps are studied because they affect and limit the performance of devices. A main objective of this research is to examine radiation-induced displacement which leads to damage-induced degradation in AlGaN/GaN HEMTs. It has been shown previously (Kalavagunta et al, 2008), that carrier removal due to traps in the unintentionally doped AlGaN layers change the space charge in these structures with a subsequent decrease in the 2DEG density, which in turn reduces the drain current in the device. Bulk traps in the GaN channel region and other regions of the device degrade the 2DEG density (by removing carriers) as well as the mobility in the device. This, in turn, degrades the performance of the device. While not addressed in this study, mobility degradation is closely coupled with the self-heating in the device. The donor-like surface traps, that will be described throughout this study, and which reside in the gate-drain and source-gate access regions, cause the majority of the gate-lag in the device. These traps at the AlGaN/Si_3N_4 surface are decreased away from the surface. Gate-lag increases with increased bulk traps (Kalavagunta et al, 2008), and contribute to the reduction of the 2DEG density.

Many studies have attempted to identify the traps in AlGaN/GaN bulk as well as surfaces and interfaces (Binari et al, 2002; Khan et al, 1994; Vetury et al, 2001). One method of studying and characterizing traps is through capacitance measurements. DLTS, which is a transient capacitance measurement, can identify deep level defects. Look (Look, 2001) has identified fitting parameters to be used in conjunction with Hall carrier

density data, starting with the donor-acceptor charge balance equation given in equation 2.5. For an n-type, donor-dominant sample:

$$n + N_A = \frac{N_D}{1+\frac{n}{\emptyset_D}} \tag{2.46}$$

where $\emptyset_D = (g_0/g_1)\, N_c' \exp(\alpha_D/k) T^{3/2} \exp(-E_{D0}/kT)$. The ratio g_0/g_1 is a degeneracy factor (=1/2 for an s state), $N_c' = 2(2\pi m_n^* k)^{3/2}/h^3$, h = Planck's constant, E_D is the donor energy, k = Boltzmann constant, and E_{D0} and α_D are defined by : $E_D = E_{D0} - \alpha_D T$ (showing a linear temperature dependence of E_D). These, along with N_D for donors and N_A for acceptors, would also be the fitting parameters. If more than one donor state exists within a few kT of the Fermi energy, then equivalent terms are added on the right hand side. More information on the fitting steps is given by Look (Look, 1998). The fitted donor and acceptor concentrations were 6.7 $x10^{15}$ and 1.7 x 10^{15} cm^{-3}, respectively. V_{GA} is often the dominant acceptor in undoped GaN. After 1.0-MeV irradiation, both the number of acceptors and donors increase by an amount that is ~ 1 cm^{-3} by each bombarding electron per cm^2 , which gives a production rate of ~1 cm^{-1}. The vacancy is thought to be a N vacancy V_N , and the acceptor is thought to be a N interstitial N_I. The donor activation energy E_D is .06 eV, making V_N a shallow donor (Look, 2001).

Theory suggests that the V_N defect has a level in the conduction band (CB) which when occupied, autoionizes into a hydrogenic configuration, i.e., with an energy about 30-40 meV below the conduction band. The donor and acceptor created in 1-MeV irradiations are strongly believed to be donor and acceptor components of the nitrogen Frenkel pair, that is, the N vacancy and the N interstitial. The model given by Look confirms the expected donor nature of V_N and demonstrates the rare appearance of an

(N_I) as an acceptor. Both N and Ga atoms are displaced by 1 MeV irradiation, as will be addressed in Chapters 3, 5 and 7.

2.6. The Physics and Numerical Methods Behind Simulations

Both analytical models were done in Mathcad and self-consistent models were done in Nextnano. The analytical models in Mathcad did calculations of the depth of the 1 MeV electrons based on the Bethe Bloche algorithm and the production rate of damage done in AlGaN/GaN by 1 MeV electrons. Additionally, Casino Monte Carlo simulations were done to see where the locus of damage was.

2.6.1. Schrodinger Poisson: Self-consistent Solution of Schrodinger's equation

An electron characterized by its wave function Ψ(r), and spin orientation s, must satisfy the time-independent Schrodinger equation. The electron can be considered as a plane wave with wave vector K and de Broglie wavelength, $\lambda = \frac{2\pi}{K}$. A method for incorporating impurities and radiation effects into the Schrodinger Poisson models is given here. If the electron is traveling in a force free area where it does not interact with other electrons, the Hamiltonian contains only a kinetic energy term, with the momentum operator, $P = -\hbar^2/2m$, and Schrödinger's equation is:

$$-\hbar^2/2m\,\Psi(r) + V(r)\,\Psi(r) = E\,\Psi(r) \tag{2.47}$$

In a solid, the effective mass form of Schrodinger's equation is:

$$\frac{\hbar^2}{2}\frac{\delta}{\delta z}\left(\frac{1}{m^*}\frac{\delta\psi}{\delta z}\right) + \frac{\hbar^2}{2m^*}(k_x^2 + k_y^2)\psi i + \Delta E_c + e\Phi - e\Phi_{xc}) + a_c\,(\gamma_{xx} + \gamma_{yy} + \gamma_{zz})\psi i = E_i(k)\,\psi \tag{2.48}$$

where k_x and k_y are the electron wave numbers, and m^* is the effective mass. Herein a set of eigenenergies E_i and their corresponding wavefunctions $(\gamma_{xx} + \gamma_{yy} + \gamma_{zz})\psi i$ can be modeled. With knowledge of the allowable eigenenergies and their spatial distributions within that eigenstate ($|\psi_i(x)|^2$), then the electron density n_i cm^{-2} can be calculated from:

$$n_i = \frac{m^* k_B T}{\pi \hbar^2} \ln(1+ \exp([E_f - E_i]/k_B T)) \quad (2.49)$$

The above Schrodinger equations represent the unperturbed lattice. The Hamiltonian is simply:

$$H = \hbar^2/2m + V(r). \quad (2.50)$$

For a lattice perturbed by an impurity, ϕ:

$$H = \hbar^2/2m + V(r) - \phi \quad (2.51)$$

So then for a lattice perturbed by irradiation, a term for the potential for displacement (acceptor or defect) is included. The potential is Coulomb-type. Assuming there is a fixed voltage across the device and starting with:

$$V = IR, I = V/R. \quad (2.52)$$

Ohm's law can now be adjusted to account for the passivation thickness and the electron irradiation.

$$V= V(x,h) + V_e(x,h) \quad (2.53)$$

where h= Si_3N_4 thickness, and the V_e in the second term is the electron irradiated potential. We know that V changes with h(x,h) or the radiation perturbation. With irradiation, the lattice is perturbed and its distribution is changed because of

displacements. So for a lattice perturbed by an impurity, the Hamiltonian can be now written as:

$$H = h^2/2m\,\nabla^2 + V(x) - \frac{Zq^2}{4\pi\epsilon r} = H - \frac{Zq^2}{4\pi\epsilon r} \quad (2.54)$$

with Poisson's equation being: $d^2\varphi(x)/dx^2 = \rho/\epsilon_0$.

Since the systems being modeled contain more than one electron, the potential energy of each electron is both a function of the conduction band edges and the electron-electron interactions, and the right hand side of Possion's equation can be written as:

$$q/\epsilon_0\,[p(x) - n(x) + N_D(x) - N_A(x) + N_T(x)]. \quad (2.55)$$

Here, the terms $N_D(x)$ and $N_A(x)$ account for the donor and acceptor doping concentrations and $N_T(x)$ is the radiation-induced trap concentration. Poisson-Schrödinger solvers are implemented in the Nextnano software. With Nextnano, the quantum well energy states were numerically determined, as well as the mobility scattering mechanisms**.** The electron density n_i in Equations 2.51 and 2.52 are nonlinearly coupled until both n_i and E_c satisfy Schrodinger's equation.

Figure 2.20 is a flow chart which summarizes the processes used in the Nextnano program. By solving Schrodinger's and Poisson's equations simultaneously, the electron wave function and density is obtained along with electric field, band diagram position information, and surface and electrostatic potentials. By varying the input parameters of structure and doping density, then the trap density, changes in scattering mechanisms, changes in the quantum mechanical description of the structure, as well as the mobility and carrier density can all be fitted and compared with experimental results.

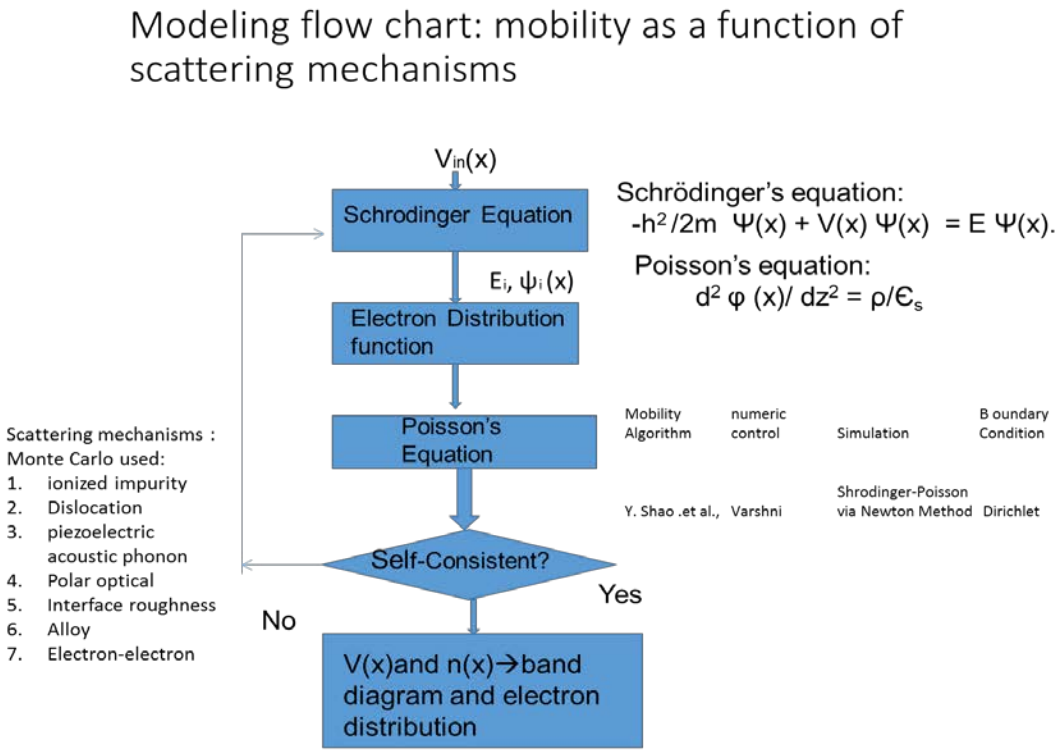

Figure 2.20. Nextnano simulations used to compare mobility and sheet carrier densities with the observed experimental results from the HEMT epi-stack structures follow this flow chart.

2.6.2. CASINO

CASINO is a Monte Carlo-based modeling tool that can simulate the electron radiation trajectory, depth and energy distributions, as well as radiation intensity. Casino models will be shown in later chapters to aide in analyzing the damage due to electron radiation. The models for the paths of the electrons assume both elastic and inelastic scattering. The inelastic interactions include secondary electrons, backscattered electrons, and continuum x-ray radiation (bremsstrahlung) results. Figure 2.12 is a screen shot of the electron distribution with 50 nm of passivation on an AlGaN/AlN/GaN sample. Figure 2.22 is an x-ray intensity plot as a function of depth for nitrogen for the same

sample. The continuum radiation intensity I emitted by the decelerating particle (acceleration a, decelerating force is F, and tparticle mass m) is (Warren et al, 1991):

$$I \sim a^2 \sim (F/m)^2 \tag{2.56}$$

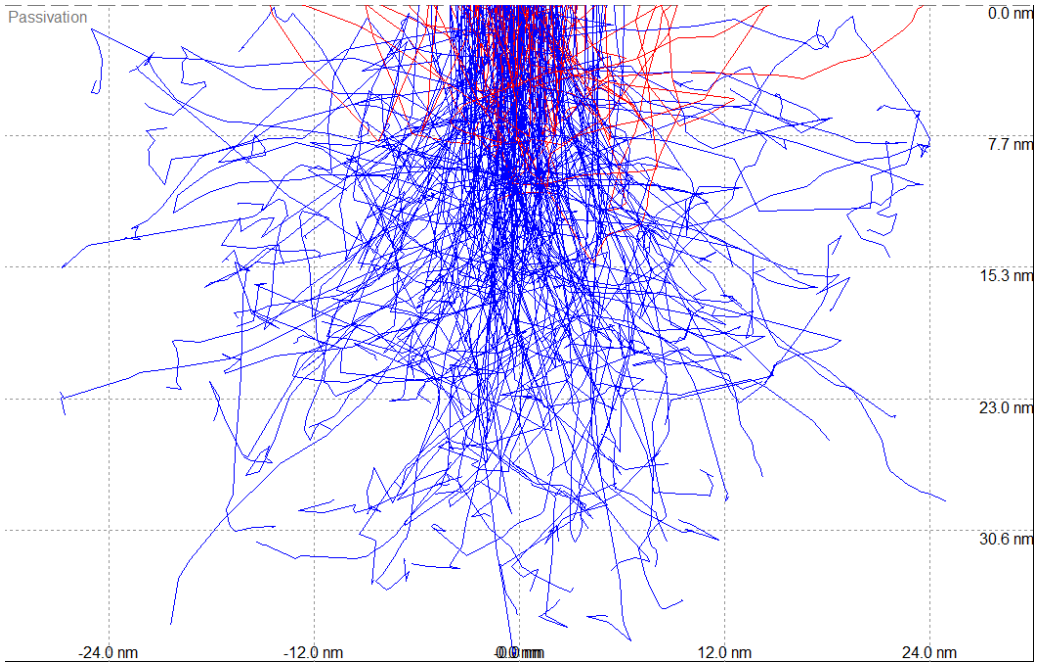

Figure 2.21. Casino's Monte-Carlo simulation of electron paths through a HEMT sample going through the Si_3N_4 passivation. The backscattered electrons are in red, while the absorbed electrons are in blue. The incident electrons were 1 keV and there were 200 electron trajectories.

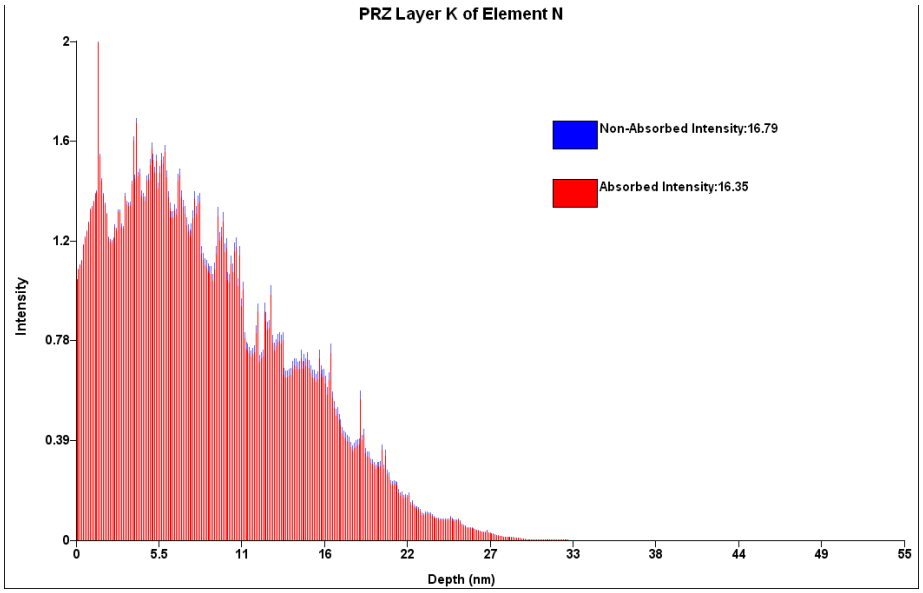

Figure 2.22. X-ray intensity for Nitrogen in a HEMT sample with 1-keV electrons and 200 electrons trajectories.

III. Overview of 1-MeV Electron Irradiation Effects

3.1. Introduction

Chapter 2 covered the basic physics needed to understand the results and conclusions in this dissertation. When electron radiation interacts with matter, in particular semiconductors, there is an additional set of physics that must be understood. In this chapter, I address 1 MeV electron irradiation, as radiation effects are specific to the source of the radiation as well as the energy and dose, for any given material and structure. Silicon nitride passivation is used on HEMTs, but not much is understood of how various thicknesses will perform once deployed in space-borne high radiation environments. Devices need to be not just shielded from radiation damage but they need to remain operational in these environments. The studies in this research were undertaken to determine the effect of the variation of Si_3N_4 buffer layers combined with electron radiation on AlGaN/GaN heterostructures. Experimentally, the irradiation was applied in order to increase the electron trapping at the interface, thus providing an enhanced interface quality to examine the defects. In this chapter, models useful in understanding radiation of 1-MeV electrons will be examined. Electron irradiation is known to cause radiation-induced device degradation, and it has been shown previously that 1-MeV irradiation produces point defects and creates acceptors (Look et al, 1997; Look, 2001). Two studies will be presented along with their findings with high energy radiation.

It has also been proven (Polenta et al, 2000) that the dominant 1-MeV radiation induced vacancy defect in GaN is the nitrogen vacancy (V_N). Theory suggests that the V_N defect has a level in the conduction band (CB) which when occupied, auto ionizes into a

hydrogenic configuration with an energy about 30-40 meV below the conduction band. The donors and acceptors created in 1 MeV-irradiation are believed to be donor and acceptor components of the N-Frenkel pair, that is, the N vacancy and the N interstitial. The model given by Look confirms the expected donor nature of V_N and demonstrates the rare appearance of an (N_I) as an acceptor (Jackson, 1999).

This chapter will briefly give an overview of previous 1-MeV radiation research. Then the physics of high energy radiation effects will be discussed, along with models for displacement (NIEL) and ionization damage. A quick synopsis of the other forms of radiation will be given, followed by a short discussion on some of the well-known previous work that studied the effects of 1 MeV irradiation.

3.2. MeV Electron Radiation Effects

When electron radiation impacts AlGaN and GaN, what happens depends on the stopping power and thickness of the sample (Jackson, 1999). This research will focus on Non Ionizing Energy Loss (NIEL), which describes the energy loss from incident particles as a result of displacement of an atomic species. Ionization is thought to occur also with 1-MeV irradiation, but it is difficult to decouple from displacement damage loss and it is believed to not be persistent in AlGaN/GaN HEMT structures. The rate at which these particles lose energy anywhere along their tracks, or the electron stopping power, has two components (Jackson, 1999; Agullo-Lopez, 1988; Polenta et al, 2000). Agullo-Lopez and Jackson detail both collisional and radiative stopping power. What Jackson calls collisional is more appropriately called ionization loss. Collisional loss typically means that an entire atom is displaced.

Both collision and radiative stopping powers are average values over the distribution of atoms in a material. The radiative component generated as energy loss per unit path length, is characterized by the emission of Bremsstrahlung radiation in the electric field of the atomic nucleus or of the atomic electrons (McKelvey, 1962). This is indicated by a characteristic length X_0 which is the mean distance though which the electron loses all but 1/e of its energy by Bremsstrahlung. According to Tsai (Tsai et al, 1966), it is:

$$1/X^0 = 4\alpha r^2 \, N_{a\,/}A\{Z^2 [L_{rad} - f(Z)] + ZL'_{rad}\} \qquad (3.1)$$

Prior to being absorbed, the energy from Bremsstrahlung radiation travels far from the particle track (McKelvey, 1962). With high energy electrons, the predominant energy loss in matter is by Bremsstrahlung. At lower energies, the primary loss is through ionization as well as other processes. Scattering is considered ionization when the energy loss per collision is below 0.255 MeV (Agullo-Lopez el al, 1988). Note that in the case of Bremsstrahlung, one must also consider the possibility of further ionization or displacement by the emitted radiation. It is usually small, but it is necessary to check to see if this has occurred.

In general, a fast charged particle incident on matter makes collisions with atomic electrons and nuclei through the Coulomb force (Agullo-Lopez et al, 1988). When entering the GaN/AlGaN crystal lattice, fast incident electrons collide with lattice atoms, if they do not pass completely through the material as described above. Collision stopping power's energy loss can be through an elastic or inelastic interaction. The inelastic interactions are Coulombic, and are characterized by a coupling of the motions of the affected targets to the vibrational structure of the material. These collisions can

result in ionization, excitation or atomic displacements. The latter elastic collisions result in defects due to displacement damage by knocking the Ga, N, or Al atoms out of their lattice positions. According to Polenta (Polenta et al, 2000), 1-MeV electrons create V_N related centers that have a thermal activation energy of 0.06 eV (Goodman et al, 2000). Both shallow donors and acceptors can be produced at an equal rate with 0.42 MeV electrons (Look et al, 1997). It has been shown that for AlGaN and GaN, electron stopping power models indicate ionization and excitation dominate, as the majority of the energy deposited in the material remains close to the incident electron tracks.

Collisional energy transfer varies with the atom's atomic mass. Massive nuclei absorb very little energy but because of their greater charge, may cause deflection of the incident particle. Gallium atoms have a lower binding energy than nitrogen in GaN. Atomic electrons take up appreciable amounts of energy from the incident electron beam without causing significant deflection (Agullo-Lopez et al, 1988). More energy is transferred to the less massive N atom resulting in displacements. These are also characterized as point defects such as vacancies and interstitials. High-energy electrons have a propensity for producing point defects (Agullo-Lopez et al, 1988; Look et al, 1997). DLTS studies of electron irradiation show at least three defect levels (Fang et al, 2011). These defects create scattering centers and thus decrease the net mobility if these scattered electrons contribute to electron-electron scattering in the 2DEG. Apart from this, the scattering is Coulombic and occurs outside the 2DEG region.

Studies (Hu et al, 2007) show for GaN lattice atoms, high energy electrons (~1 MeV) should be able to produce displacement damage resulting in line defects. Line defects are not expected from primary knock-on atoms, for such cascades require ~290

eV for N and 41 eV for Gallium (Look et al, 2005). Gate leakage was also observed, which increases due to trap-assisted tunneling through the AlGaN layer as a result of radiation induced trap creation. The increase in drain current either resulted from the increase in carrier concentration in the 2DEG, or the carrier concentration remained constant and the electron mean velocity increased within the 2DEG.

It is important to know how far the radiation will travel in the material, and this can be determined by the stopping power of the material. The Bethe-Bloch equation is used to determine the stopping power and, from it, the displacements per volume for GaN (McKelvey, 1962):

$$-dE/dx = 2\pi N_a r^2 m_e c^2 \rho Z z^2 /A \ \beta^2 [In(2m_e \gamma^2 v^2 W_{max} /I^2) \ -2\beta^2 - \sigma - 2C/Z] \quad (3.2)$$

where

β = v / c;
v velocity of the particle
E energy of the particle
x distance travelled by the particle
c speed of light
ze particle charge
e charge of the electron
m_e rest mass of the electron
n electron density of the target
I mean excitation potential of the target
ε_0 permittivity of free space

For the high energy limit, after some manipulation and using $\beta \sim 1$, the above equation can be reduced to:

$$-dE/dx \approx [2 \ In \ (\frac{2m_e c^2}{I_e}) + 3 \ In \ \Upsilon - 1.95] \quad (3.3)$$

where m_e is the electron mass, c is the speed of light and I_e is Mc^2, where M is the ion mass. By integrating Equation 3.3, the maximum energy transferred from the electron to the atom is given by:

$$E_m = \frac{2E(E+2m_e c^2)}{Mc^2} \quad (3.4)$$

The above equation is equal to the energy needed for an atomic displacement, so $E_m = E_d$. The values of E to produce Frenkel pairs are 0.18 MeV for nitrogen (for a V_N -N_I Frenkel pair) and E= 0. 51 MeV for gallium (for a V_{GA}- Ga_I Frenkel pair) (Van Vechten, 1988). Look has predicted (Look et al, 1997) a shallow donor and trap production rate of 1 cm^{-1} of thickness. In Chapter 5, the production rate for the above Frenkel pairs as calculated by a defect production algorithm based on the Bethe Bloch equation (equations 3.2 and 3.3).

The damage from high energy electrons has been generalized in theory (Jackson, 1999) and Agullo-Lopez (Agullo-Lopez et al, 1988). The damage can be summarized to be: dislocation damage creating acceptors and donors, positive (or negative) threshold voltage shifts, and gate leakage. When traps are introduced, there is a reduction in conductivity, mobility and minority carrier lifetime. So when electron radiation passes through an AlGaN/GaN structure, the fast electron damage can be summarized by the type of defects produced and why.

A fast charged particle incident on matter makes collisions with atomic electrons and nuclei. When entering the crystal lattice, it collides with lattice electrons. The loss of energy by the incident particle occurs almost entirely in collisions with electrons. For incident electrons, both energy loss and scattering occur in collisions with atomic electrons, so the path is much less straight .After a short distance, electrons tend to

diffuse into the material, rather than go up in a rectilinear path. Defects are created, and can be acceptorlike. These defects create scattering centers and thus decrease the net mobility. The scattering is Coulombic. There can be a positive threshold voltage shift due to the trapping effects in the gate area. The defects are thought to be deep acceptor like, and the mobility degradation caused by Coulomb scattering in defects mostly outside of the 2DEG region. There is irradiation gate leakage, and both donors and acceptors are created by the radiation. At 0.45 MeV, a N vacancy (V_N) is created, but at 1 MeV a Frenkel pair consisting of a nitrogen vacancy and interstitial can be created, as well as a gallium vacancy.

For energy transfer in a Coulomb collision between an incident particle and a stationary free electron, any of the following can occur: (a) for energetic collisions, the binding of the electron in the atom can be neglected; the electron can be considered free and initially at rest in the laboratory. (b) The collision is elastic and Coulomb scattering is in the rest frame of incident particle. This scattering can be in the AlGaN and measured with Hall mobility measurements. (c) Gate leakage occurs if the collision results in damage that creates hopping sites. This will be examined with I_g-V_g measurements in Chapter 6. The elastic as well as inelastic scattering is modeled in CASINO, and the individual scattering mechanisms are modeled in Nextnano. The number of defects created by primary electrons is modeled using a defect production algorithm along with the electron trajectory.

Incident 1-MeV electrons create damage, both displacement and ionization. For this dissertation, the damage of interest is displacement damage. However ionization could be occurring but it is difficult to decouple from displacement damage and it

typically does not persist in AlGaN/GaN HEMTs. Starting with the concept that high energy electrons hit an AlGaN\GaN target, I have modeled energy vs. depth for both the atomic constituents of AlGaN and GaN and Si_3N_4. Based upon both experimental observations and theoretical calculations, some hypothetical assumptions can be made: a) the incident electron energy is high enough to cause displacements in the lattice of nitrogen, aluminum or gallium (if passivated, then also in silicon): this energy of the incident electron E_e needs to be such $E_e > E_{interaction} + E_B > E_{thres}$ where $E_{interaction}$ is the energy of interaction and E_B is the binding energy of the electron in the target atom, which, when combined, needs to be able to cause a displacement and be greater than E_{thres}. b) The maximum energy transferred occurs at normal incidence. Also, because this is 1-MeV electrons, the effects are relativistic.

From here, the underlying principles or basic physics involved are: the conservation of kinetic energy, the conservation or momentum, and the equations of energy momentum balance. There is a minimum energy E_D that will displace the atom from the quantum well (the well here is defined by the place where the atom sits in the lattice with an upper bound given by up the point where it is out of that spot and in an inter-lattice position), but the displacement is temporary because the energy imparted to the atom from the bombarding electron causes instability such as vibration so that the atoms tends to fall back into the well (Figure 3.1). The actual energy needed to produce a displacement is much larger. The calculated value for displacement energy E_D is now known to be a lower limit. This data does not fit the experimentally obtained values, so there are missing assumptions or physics not incorporated into the model. The adequacy

of the model is determined by the accuracy with which the hypothetical assumption (or the hypothesis) accounts for the observed data. Solving for displacement energy:

$$E_d = 2\,(m_e/M)\,E_{thres}\,/m_e\,c^2\,(E_{thres} + 2m_e\,c^2) = E_d\,(eV) = E_t(E_t + 1.022x10^6)/470 \times 10^6\ A \quad (3.5)$$

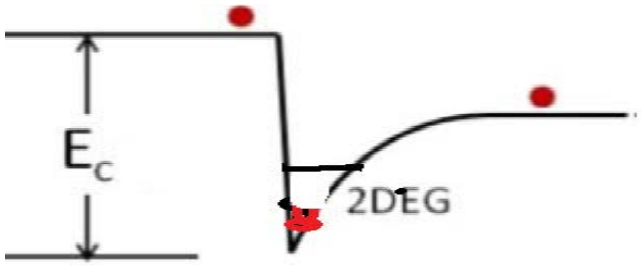

Figure 3.1. Particles scattered out of the quantum well to nearby layers of AlGaN or GaN.

The threshold energy E_{thres} necessary to produce an atomic displacement is then just given by the condition T max=E_m = E_d, where E_d is the displacement. For nitrogen, E_d = 32.5 eV and for gallium E_d = 24.3 eV are predicted. The corresponding values obtained experimentally are much greater: E_d = 66 eV for nitrogen and E_d = 38 eV for gallium. The higher observed energies than the predicted E_D are explained by the fact that displacement of an atom needs additional energy in order for the displacement to not be pulled back into the quantum well by the very strong polarization induced field at the AlGaN/GaN interface, thus higher energies are needed.

The displacement energy values can also be determined using a computer model as follows: using a production rate = σ_D x F= σ_D x n^{14} and from there $\sigma_{d\,=}$ (π b'^{2} /4)[((T_{max}/ E_d)-1)) – β^2 In(T_{max}/ E_d) + $\pi\alpha\beta$\{2[(T_{max}/ E_d -1)$^{1/2}$ -1]- In(T_{max}/ E_d), where α =

$Z/137$, $\beta = v/c$, $b = 2Ze^2/m_e v^2$ and $b' = b(1- \beta^2)^{1/2}$. The results of this model will be shown in Chapter 5 in the discussion of the defect algorithm results. This can now be used to calculate the number of displacements for non-uniform damage. By integrating

$$dn/dt = N_o \sigma_d n_e v_e \quad , \tag{3.6}$$

n can be obtained to yield the amount of atomic displacements. N_o is the number of atoms per unit volume, n_e is the number of electrons crossing the unit area in 1 sec in the beam, and v_e is the incident electron velocity.

Another method used for under 1-MeV electron irradiation is based on values for GaN and adapted from the Mott-McKelvey-Feshback algorithm) (Lu et al, 2012) :

$n_{GA}/cm^3 = (N_o(\text{ molecules/mole}) * \rho(gm/cm^3) * 1/A(gm/mole) = N_o \rho/A =$

molecules/mole = $6.02204 \times 10^{23} \times 5.6/81.36 = 4.14 \times 10^{22}$

is the number of Ga and N per cm^3. A production rate of defects is obtained using $\sigma_D(cm^2) \times n(cm^{-3}) = (4.36 \times 10^{-24}) \times (4.14 \times 10^{22}) = 0.18$ /cm for nitrogen. Again, we are starting with the concept that high energy electrons hit an AlGaN/GaN crystal lattice target. Assumptions are then made that: ionizing radiation deposits a small amount of radiation via the incident electrons. The particle is Rutherford scattered due to the Coulomb repulsion between the incident electron and the atomic conduction band electron. This energy is absorbed and then deflected which results in the ejection of a valence band electron to the conduction band (an e-h pair is created). If ionizing energy $E_i > E_B$, the radiation can remove an electron from the atom (referred to as atomic ionization). The incident electron then travels through the material and can continue to cause ionization. The atom from which the electron was removed may recoil with sufficient E_D to become displaced from the lattice, also resulting in ionization.

The number of e-h pairs generated in a semiconductor via radiation absorption is material dependent (band gap), and dependent upon the thickness of the material and the type of radiation. When ionization occurs, there must be conservation of momentum. In the ionization process, if fully absorbed, incident electrons lose an amount of energy equal to the kinetic energy of the electrons plus the binding energy E_B used to free the electron from the atom. Ionization is generally characterized as inelastic; there can be excitation and displacement also. Energy momentum balance for electrons is first described:

$$\begin{aligned} Q_{\max} &= \tfrac{1}{2}MV^2 - \tfrac{1}{2}MV_f^2 \\ &= \frac{4mM}{(M+m)^2}(\tfrac{1}{2}MV^2) \cong \frac{4mE}{M} \end{aligned} \tag{3.7}$$

Q_{max} is the maximum imparted momentum by the incident electron and M is the mass of the target atom or particle and V is their velocity. E is the incident energy and m is the mass of the electron. Once ionization occurs, the e–h generation is defined by:

e-h generation:

$$\begin{aligned} g_0 &= \frac{\text{energy per rad} \cdot \text{density}}{\text{pair generation energy}} \\ &= \frac{\frac{100 ergs}{g-rad} 2.37 \frac{g}{cm^3}}{10^7 \frac{erg}{J}(1.6\times10^{-19}\frac{J}{eV})3.6\frac{eV}{pair}} \end{aligned} \tag{3.8}$$

Ionization due to 1-MeV electrons can be summarized as: (1) incident electrons interacting with a lattice atom scatters an electron. For nitrogen the energy is 14.8 eV needed to ionize. Once ionization occurs, an energy greater than 3 times the energy gap of the interaction atom is needed for the ionization to persist and form e-h pairs. For atomic ionization to occur, the energy of the ionizing electron needs to be greater than the

binding E_B of the atom. This process repeats as the electrons continue to move through the material until recombination occurs.

The amount of energy deposited into ionization can be determined from the stopping power dE/dX in equation 3.2. To determine the number of atoms experiencing ionization per second, the range R of the particle in the material needs to be determined. From there, the IP = number of ion pairs/cm^3–sec: (electron energy/e-h generation energy for material)* J* 1/R. One then finds the number density for the material: N_{Ga} or N_N . The fraction of ions experiencing ionization per second is IP/N. N_e is the number of electrons generated and can also be obtained from ionization tables and added to original number N_0 to get the total number of ions after radiation:

$$N_{tot,e} = N_e + N_0 \tag{3.9}$$

The reality is that it has proven to be difficult to decouple effects of ionization and displacement in AlGaN\GaN HEMTs.

3.3. Previous 1-MeV Electron Irradiation Studies on AlGaN/GaN HEMTs

Since space-borne electronics are subject to various species of radiation damage, I will briefly mention some previous studies. First, studies of radiation damage from neutrons, protons, electrons, or gamma rays are summarized. Then, prior studies on 1-MeV electron or higher irradiations will be given.

Cobalt-60 gamma radiation effects (Atkas, 2004) showed gamma radiation did not degrade the large signal transient response for the device. Neutron radiation interactions can trigger nuclear transformations and be very radioactive. Protons are heavy and carry charge, so therefore are not easily deflected and can travel far compared

to other particles. Other reports (White et al, 2003,Karmarkar et al, 2005, Kalavagunta, 2009, Hwang et al, 2014) have focused on radiation effects on electronics. In his dissertation (Kalavagunta, 2009), Kalavagunta studied the role of traps in RF and DC device degradation. Neutron irradiation studies have been published (McClory, 2008; Lu et al, 2012; Petrosky et al, 2009; Polyakov et al, 2008; Govarkov et al, 2006). Lower energy electron irradiation studies have also been done (McClory, 2008; Jarzen, 2005; Sattler, 2004; Moran, 2009; Green, 2003). Lower energy electrons have a greater probability of interacting with their target because of their slower speed. Among those making significant contributions to understanding 1-MeV and higher energy electron irradiation are Fang (Fang et al, 2010), Polenta (Polenta et al, 2000) and D. C. Look (Look et al, 1997), who are referenced throughout this dissertation. The following is a summary of Fang and Look's study (Fang et al, 2009) on the effect of 1-MeV electron irradiation on AlGaN/GaN HEMT Schottky barriers, which has many parallels to the research in this dissertation.

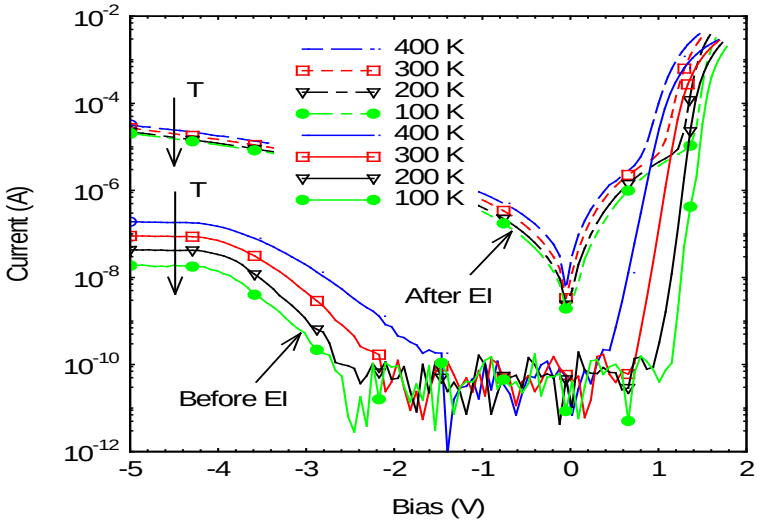

Figure 3.2. Effect of 1-MeV electrons on I-V-T characteristics (1-MeV electrons with dose of $5x10^{15}$ cm^{-2} at room temperature (from Fang et al., 2009)

Before electron irradiation, Figure 3.2 shows that the current in forward bias I_F can be described by thermionic emission. However, the reverse bias current I_R shows less T-dependence, indicating there is tunneling conduction. After electron irradiation, there is a significant increase of both forward I_F and reverse I_R. The increase is more than two orders at the reverse bias current of V_R= -5 V. Since there is not a strong temperature dependence, but the post radiation I_F and I_R show strong electric-field dependence, this also is an indicator of the dominancy of tunneling conduction.

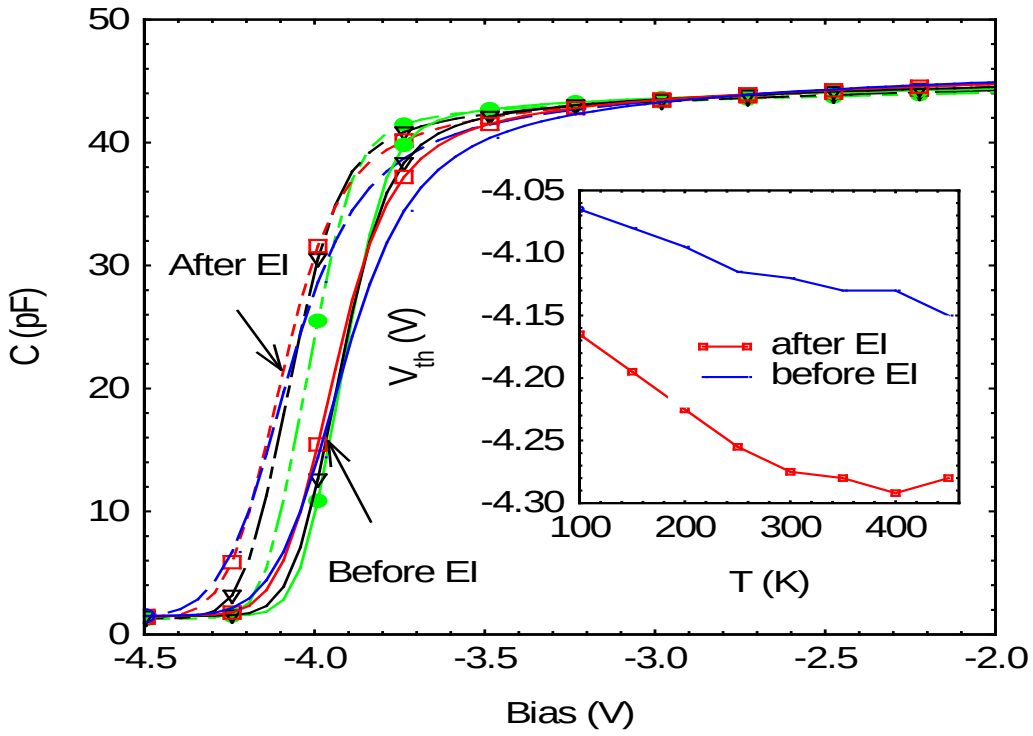

Figure 3.3. Effect of 1-MeV electrons on C-V-T characteristics (from Fang et al., 2009).

In their examination of capacitance voltage, the threshold voltage (V_{th}), in the insert in Figure 3.3 shows the structure going more positive after electron irradiation, as

well as with decreasing temperature. At T<300 K, the rate of change of V_{th} is lower before irradiation (ΔV_{th}= -0.28 mV/^{o}C), than after (ΔV_{th}= -0.55 mV/^{o}C). The electron irradiation causes a negative shift of the V_{th}'s, with a shift of -0.16 V at 300 K. Similar threshold voltage shifts will be shown in the studies in this research. In their research, the electron irradiation did not change the 2DEG carrier concentration, which is 7.5 x 10^{19} cm^{-3} at 300 K (determined from C-V).

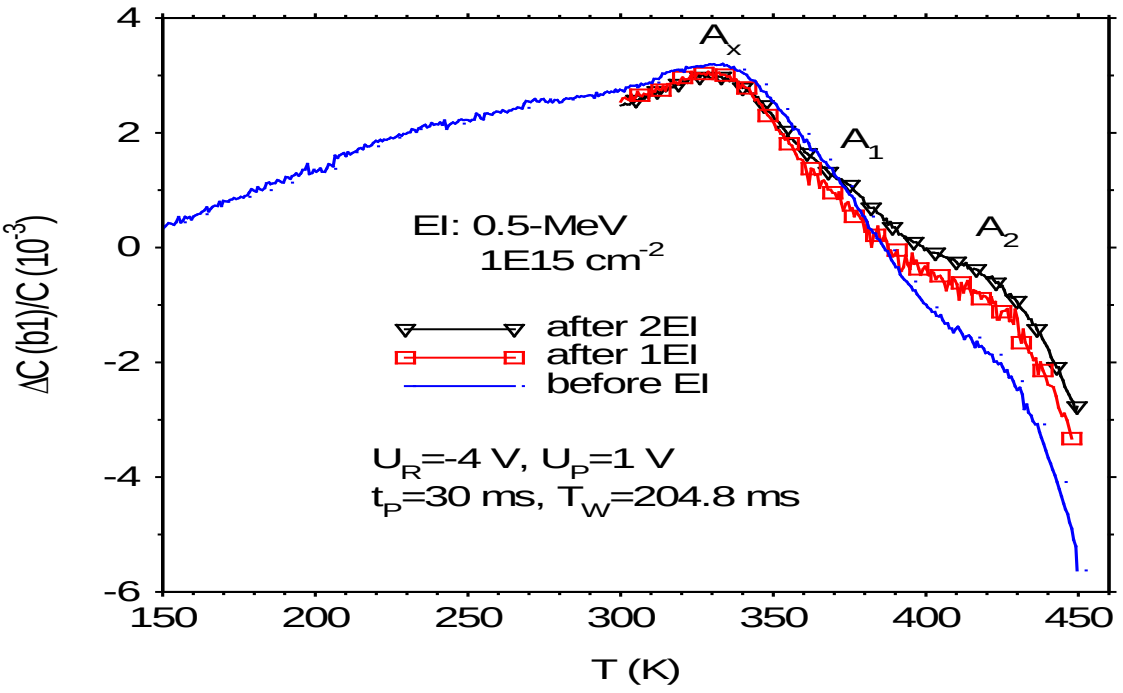

Figure 3.4: Effect of 0.5-MeV electrons on deep traps in a SBD with a large Schottky contact (ϕ=200 μm; from Fang et al., 2009).

In the DLTS measurements of Figure 3.4, three traps were found pre-irradiation (A_x, A_1, and A_2). The trap A_2 persisted after consecutive 0.5-MeV irradiations, shown on the shoulder of negatively-going spectra, and exhibits a continuing increase. The

negatively going DLTS signal is related to a hole-like trap at high temperatures by these same authors (Fang et al, 2009).

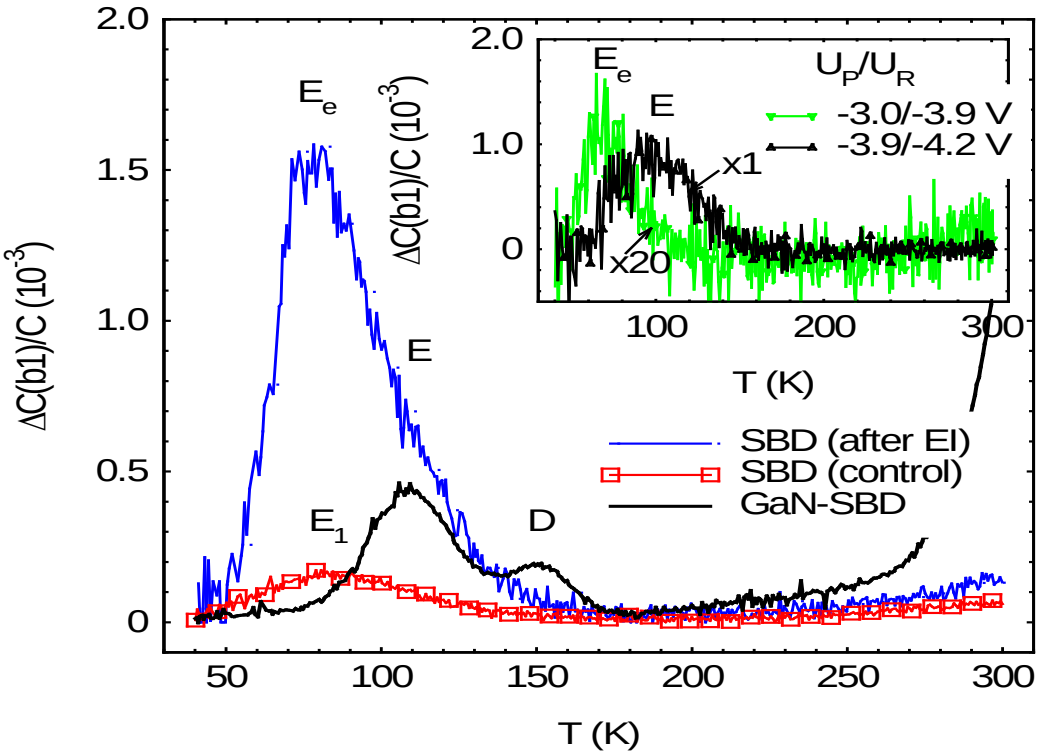

Figure 3.5. Three Schottky barrier diodes were compared: irradiated and non-irradiated AlGaN/GaN Schottky barrier diodes, along with an irradiated GaN-Schottky barrier diode (Fang et al, 2009).

Finally, the effect of 1-MeV electron irradiation on shallow traps E and E_e (which will be looked at more in Chapter 6) are observed in different regions in Figure 3.5. Three Schottky barrier diodes (SBDs) were compared: irradiated and non-irradiated AlGaN/GaN SBDs, and an irradiated GaN-SBD. A weak E_1 trap peak was found in the control AlGaN/GaN SBD (an as-grown trap in GaN buffer layer). The E_e trap (0.09 eV) was induced in the irradiated AlGaN/GaN SBD. The pre-existing D (0.25 eV) and E

(0.13 eV) traps are also induced in the irradiated GaN-SBD. For the irradiated AlGaN/GaN SBD, E is in the buffer region and E_e is in the 2DEG region.

The conclusion of this prior study (Fang et al, 2010) is that irradiation causes a significant increase in leakage current, which is dominated by tunneling. A negative shift of threshold voltage (V_{th}) in the pinch-off region is observed. The radiation creates deep traps A_e (~1.1 eV) and A_2 (1.2 eV) and E_e (0.09 eV). In turn, these irradiation-induced traps can account for the increase of leakage currents and shift of V_{th}. As compared to traps A_2 and E in irradiated GaN, traps A_e and E_e in irradiated AlGaN/GaN show differences in activation energy and electron-capture behavior.

The next study is based on a technical report (Georgievich, 2008) and on the research and papers by A.Y. Polyakov *et al.* (Polyakov et al, 2008). Results concluded that the radiation hardness of the AlN/GaN HEMTs is about an order of magnitude higher than for AlGaN/GaN HEMTs for high energy electron irradiation. The reason for such difference in radiation hardness most likely comes from the lower thickness of the AlN barrier and correspondingly the lower density of radiation defects in the region near the barrier GaN interface.

After irradiation with a dose of 5×10^{15} cm^{-2}, the capacitance in the depletion region was decreased to the values close to parasitic capacitance for both structures indicating that the buffer was rendered insulating. That means that the electron removal rate was close to 0.4-0.6 cm^{-1}. A similar removal rate was observed for electron irradiated n-GaN films grown by MOCVD. The carrier removal rate is similar in MOCVD and MBE material. Measurements of the buffer resistivity on the AlGaN/GaN sample with the barrier removed by etching showed that the sheet resistivity was about 10^{10} ohms per

square after irradiation with a dose of 10^{16} cm^{-2} electrons. The resistivity showed an activation energy of 0.6 eV; i.e., the activation energy was that of the main compensating center in GaN. That means that all shallow donors that were undercompensated in the initial samples were compensated by irradiation. They also showed that the main compensating agent in electron irradiated n-GaN films is the E_c-1 eV acceptor related to nitrogen interstitials N_i. Optical DLTS (or ODLTS) spectra measured before and after irradiation on an AlN/GaN HEMT structure (Figure 3.6) showed a negative broad hole traps band due to dislocations which are modulated by positive peaks from electron traps E1, E2, and E3. Their corresponding respective activation energies are 0.2 eV, 0.25 eV, and 0.6 eV. These are the electron traps dominant in the GaN buffer before irradiation. After irradiation they saw additionally an electron trap E4 with the activation energy 1 eV and the Arrhenius signature very similar to the N_i deep acceptors produced in n-GaN (Georgievich, 2008). They claimed that electron irradiation of AlGaN/GaN HEMTs can be used to "correct" the technology when it fails to produce semi-insulating buffers, but only in cases when the concentration of residual donors is not much higher than 10^{15} cm^{-3}. For higher concentrations, the buffer compensation can still be achieved as they confirmed in measurements on a second HEMT structure, but it required doses in excess of 9×10^{16} cm^{-2} and the amount of increase in the channel conductivity accompanying this buffer compensation was unacceptable.

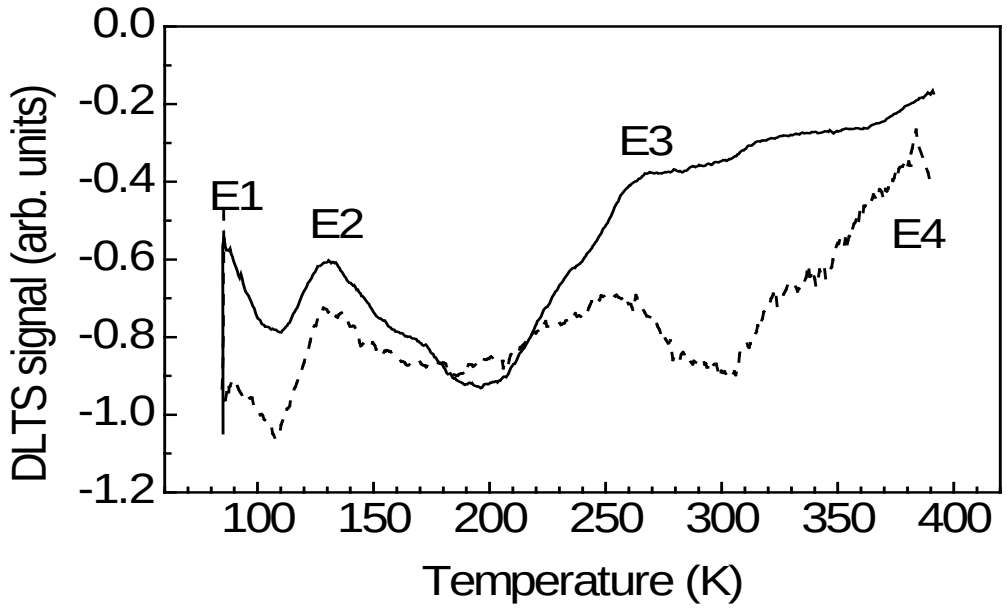

Figure. 3.6. ODLTS spectra measured in the AlN/GaN sample before (solid line) and after (dashed line) irradiation with 10^{16} cm^{-2} 10-MeV electrons (from Georgievich, 2008).

The result of electron irradiation on C-V characteristics of the MOCVD HEMT is shown in Figure 3.7. The capacitance value in depletion was initially high, about 400 pF, and then gradually decreased with dose until, at 9×10^{16} cm^{-2}, it became close to 10 pF. This indicates full compensation of the buffer. Since the residual donor concentration in this structure was estimated as $(3\text{-}5) \times 10^{16}$ cm^{-3}, these data suggest a carrier removal rate of 0.3-0.6 cm^{-1}. It was concluded that the average electron removal rate was about 0.5 cm^{-1}, irrespective of the growth method, and for a concentration range $(1\text{-}50) \times 10^{15}$ cm^{-3} for various dopings. This group studied 2DEG characteristics of variously grown AlGaN/GaN HEMT structures, and demonstrated a strong increase in 2DEG concentration when switching from AlGaN to AlN barriers. Analysis of C-V data from MOCVD grown and MBE grown AlGaN/GaN HEMT structures allowed them to

determine which had insulating and which had conducting buffers. This analysis was corroborated by conductivity and C-V measurements on respective buffer structures exposed by the barrier removal technique involving etching in hot phosphoric acid.

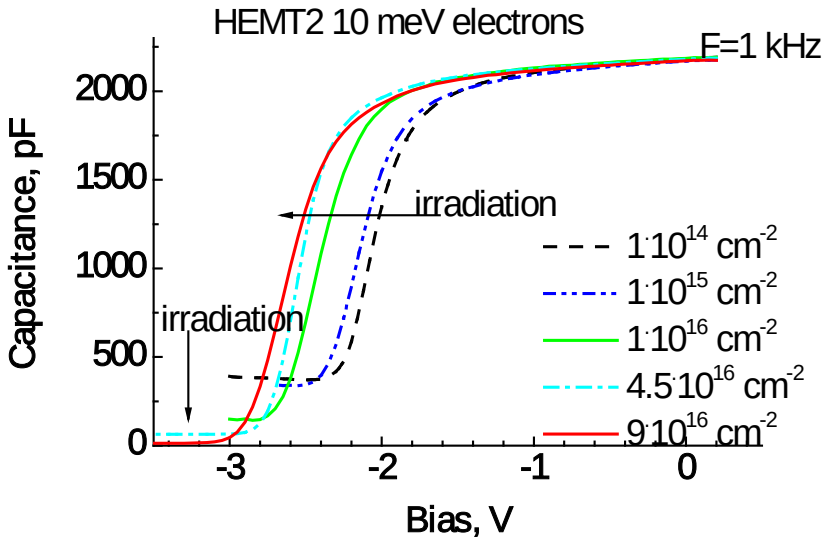

Figure. 3.7. C_g-V_g characteristics measured on the AlGaN/GaN MOCVD sample HEMT before and after irradiation with electron doses of 10^{14}, 10^{15}, 1.5×10^{16}, 4.5×10^{16}, 9×10^{16} cm^{-2} (from Georgievich, 2008).

In this same study, admittance spectra measurements and DLTS/ODLTS measurements performed on AlGaN/GaN HEMT structures showed an important role of electron traps with activation energy 0.2, 0.25, 0.6, 0.9 eV in these structures. In particular these traps were at least partly responsible for the low temperature shift of C-V characteristics to lower negative bias upon cooling at large reverse bias. This was clearly demonstrated by application of the specially developed “reverse DLTS” technique which is similar to ordinary DLTS, but involves pulsing of the structure from lower to higher

reverse bias. The general idea of the method is that the hysteresis occurs due to tunneling of electrons from the Schottky contact into the barrier or the buffer. The charge captured on these traps needs to be removed by an activation process. Thus, temperature scans in a "reverse DLTS" technique allow one to determine the energy and capture cross section of the traps involved. Their detailed studies strongly suggest that in MBE-grown structures, the traps in question are located in the GaN buffer.

The previous report showed irradiation also caused increases in the GaN buffer resistivity. Like other studies in this area previously discussed, with the electron irradiated structures, the effect is explained by introduction of point defects. The defects are predominantly the nitrogen-interstitial-related E_c-1 eV acceptor centers. With this study, the electron irradiation caused a shift in the threshold voltage in both directions, first towards more negative values, then towards more positive values. They did not gain complete understanding of the first process, but attributed it to the increase of the positive space charge in the AlGaN barrier. The positive threshold voltage shift was explained as due to increased compensation of conductivity in AlGaN barriers.

Irradiation of n-AlGaN/GaN heterostructures with electrons had little effect on the density of electrons in the accumulation region of the structure, but decreased the electron concentration in the n-AlGaN film with a rate much lower than for n-GaN. It was found in p-AlGaN that the main effect of the electron irradiation was the creation of deep electron traps near 1.2-1.3 eV as measured from the conduction band edge. These traps are most likely located in the AlGaN/GaN interface region (2DEG). There is a bias dependence of DLTS peak amplitude and a similarity of this trap energy and signature in electron irradiated n-GaN, n-$Al_xGa_{1-x}N$/GaN (for x=0.10 and 0.25).

In the next chapter, I will describe the experimental techniques used in this research. Then, chapters with the results of the commonly identified radiation induced defects and traps will be given. Results are always structure and material dependent, so very small nanoscale differences can lead to easily detected macroscopic changes.

IV. Experimental Equipment and Procedures

4.1. Introduction

This chapter describes the experimental setups and equipment used to do the research for this dissertation. Chapter 2 gave the underpinning to understand what the experiments and equipment described in this chapter will produce the results and analysis in Chapters 5 through 7. The underlying physics behind all the measurements mimicking radiation effects was given in Chapter 3.

4.2. Device Preparation

For the HEMT epi-stack structures, wafers of undoped AlGaN/AlN/GaN and GaN/AlGaN/GaN were grown using MOCVD on 4H-SiC substrates with the dimensions shown in Table 4.1. Wafer IQ13 had a GaN cap and a 19.7 nm AlGaN layer. Wafers IQ15 and IQ16 had no cap layers, but an AlN interlayer and an 18-nm AlGaN layer. Samples were diced to 0.5 × 0.5 cm using a diamond saw. To examine the impact of silicon nitride passivation on AlGaN/GaN heterojunction devices, the effects of the passivation layer thickness was investigated at various thicknesses (0, 20, 50, and 120 nm) on bare epilayer AlGaN/GaN structures. The electron energy of the beam was 1.0 MeV and the fluence was 10^{16} cm^{-2} for the electron irradiations, which were done at Wright State University. The Wright State radiation lab was easily accessible to do the electron irradiations. Previous studies have been done with electron irradiation on RF GaN HEMTs to characterize their degradation. However, the unique aspects of my

approach over these others is: None of these previous studies exclusively included the role of the Si_3N_4 thickness in the formation of the surface states, either intrinsically or following irradiation.

Table 4.1. Dimensions of AlGaN/GaN device layers. * is for wafer IQ13.

Barrier	AlGaN	18 nm / 19.7 nm*
Passivation cap	GaN*	2 nm*
Interlayer	AlN	1 nm
Buffer	GaN	1700 nm

Three mask levels were used to fabricate various planar metallic structures, including Ohmic and Schottky contacts, on the top (AlGaN) layer in order to facilitate Hall-effect, C-V, and DLTS measurements, as shown in Figure 4.1. The top-level structure labeled "layout" has 3 layers: 11 is ohmic; 12 is Schottky; 30 is nitride protect. The Ohmic stack consisted of Ti/Al/Ni/Au, and the Schottky stack, Ni/Au. The Schottky was 300 μm in diameter. The sample surfaces were cleaned using standard isopropyl-acetone solutions. To create good Ohmic contacts, the wafer was subjected to a rapid thermal anneal at 850 ^{o}C in a nitrogen ambient. The silicon nitride layer was deposited by PECVD. When this process was complete, the wafer was diced into 5-mm x 5-mm pieces (Fig. 4.2) using a diamond saw for Hall-effect and DLTS measurements. Figure 4.3 shows the structure of the device used in this research.

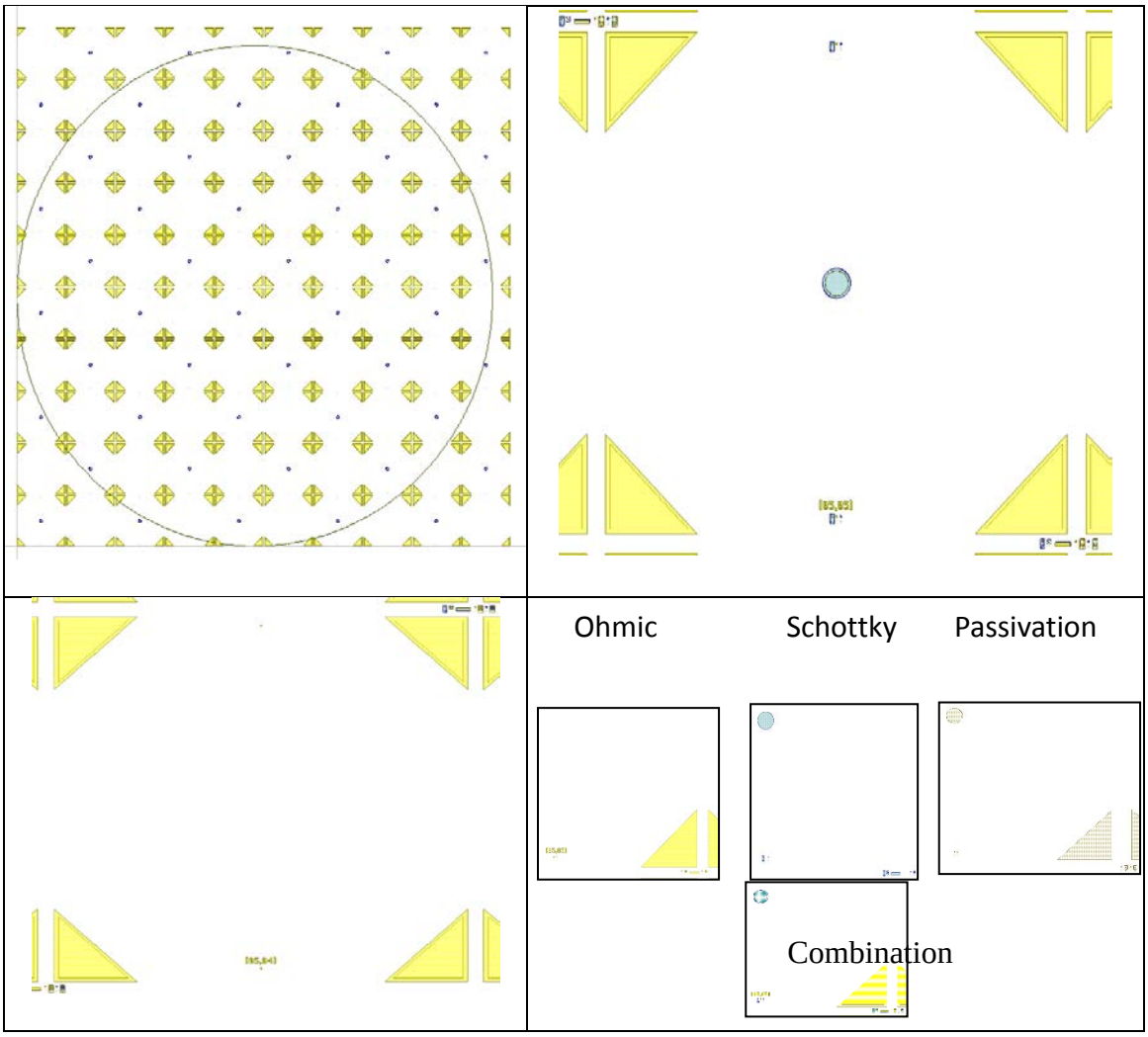

Figure 4.1. Three stage mask design. Pane 1 in the upper left is the 2” wafer overview. The upper right is the Schottky cell layer, the lower left is the ohmic cell layer, and the bottom right is the combination of the individual layers.

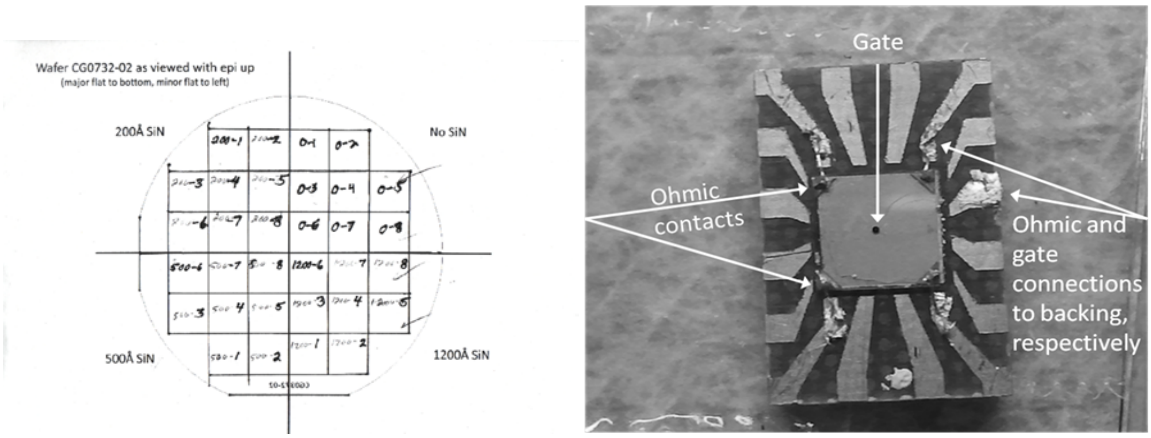

Figure 4.2. The layout of the Si_3N_4 deposition per wafer quadrant and a sample mounted for irradiation on the right.

Table 4.2. Hall and PL Experimental Overview.

Surface Fabrication	B:3 stage mask designed- metal stack for ohmic contacts = Ti-Ni-AL-Au
Anneal	RTA 850 ^{o}C nitrogen
PL laser	HeCd laser (325 nm) covered 3550 angstroms to 7450 angstroms; Post radiation- 266 nm laser
Hall system characterization	Pre-radiation- Post radiation Mobility, carrier concentration, resistivity
Si_3N_4 Thickness	0, 20, 50, or 120 nm

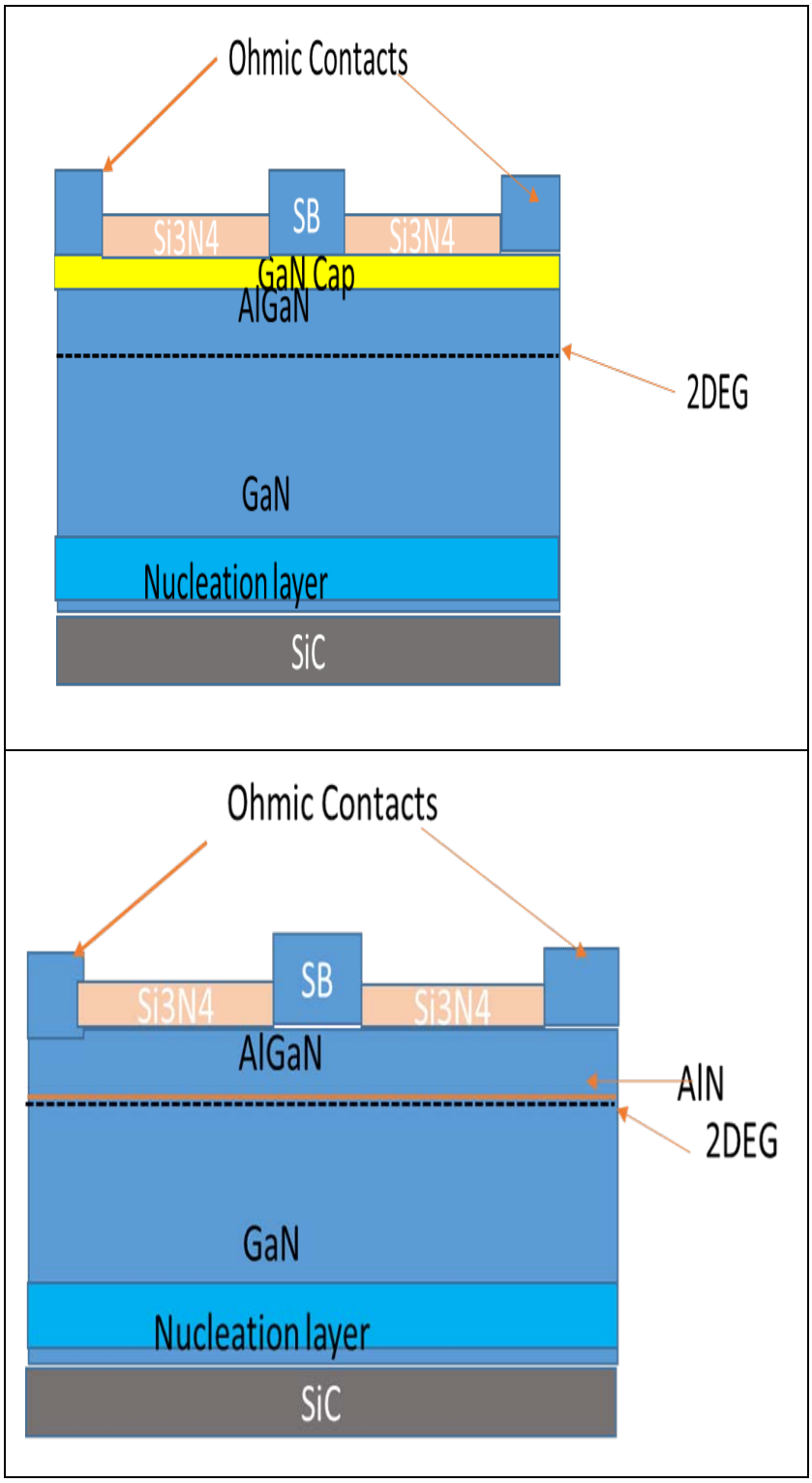

Figure 4.3. Device structures for GaN/AlGaN/GaN and AlGaN/AlN/GaN.

4.3. Design of Experiment

For the Hall system study of transport mechanisms, a 2 factor of design of experiment was conducted wherein:

- The radiation energy and fluence were held constant for all irradiations;
- The Si_3N_4 thickness and temperature were varied per device structure.

Tables for the setups for the Hall characterization experiments are in the Appendix. Other tables will be given throughout the dissertation that summarize experimental results. For the Hall characterization of AlGaN/AlN/GaN, eight sample sets were run.

4.4. Electron Irradiation Experiments

The 1.0-MeV electron irradiations summarized in this chapter were done to mimic the environment in which AlGaN/GaN HEMTs are subject to in space applications. I studied the displacement damage as well as leakage current changes. Figure 4.4 is a picture of the Van der Graff at Wright State University used in the experiments. The electron irradiations per structure are summarized in the tables in the Appendix. The energy is held stable to less than 1%. Samples were affixed mechanically to a water-cooled end-station. Pre-irradiation characterization indicated that the fluence varied no more than 5% over the sample. The beam current was ~2.0 μA and dosimetry was performed using a calibrated Brookhaven Instruments 1000c current integrator. The irradiations were made with the sample under a vacuum of ~ 1 x 10^{-6} Torr.

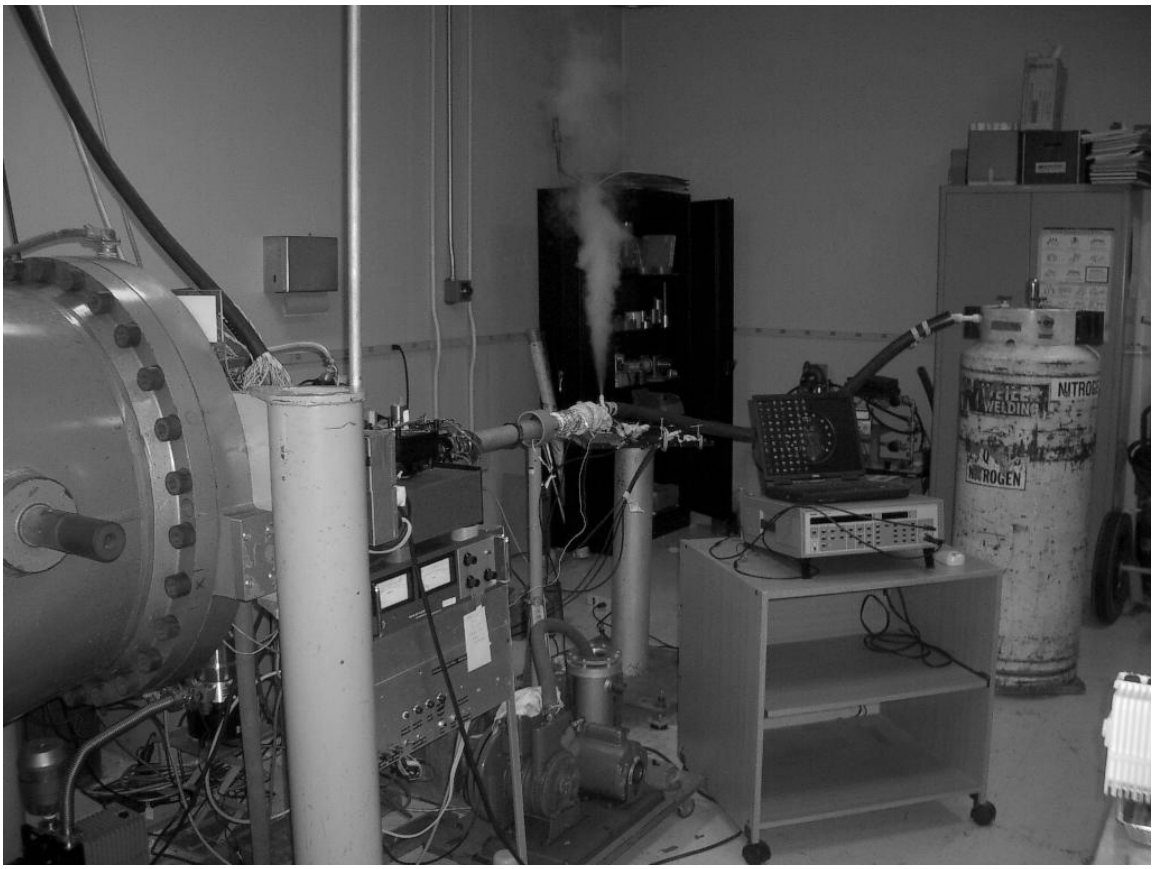

Figure 4.4. High Voltage Engineering Van de Graff accelerator at Wright State University (Dayton, OH).

4.5. Characterization Experiments

The methodology for characterization was divided into three main areas: (1) Hall system electron transport characterization, (2) gate (Schottky) electrical measurements for leakage current studies, capacitance and DLTS, and (3) optical characterization using PL for spatial localization of defects. Other experiments such as FTIR and AFM were performed but are not included in this dissertation. Readers are encouraged to contact the author for further information on the additional work.

4.5.1. Hall Characterization

As mentioned above, wafers of undoped AlGaN/GaN were grown using MOCVD on 4H-SiC substrates. The surface fabrication consisted of a Si_3N_4 layer deposited on AlGaN with a metal stack configuration for the Ohmic contacts consisting of Ti-Ni-Al-Au. The surface fabrication was applied using a 3-stage mask shown in Figures 4.1 and 4.2. These contacts were required for Hall system characterization, as well as for gate (Schottky) measurements. To establish repeatability and sample consistency, 24 device structures were electron irradiated (eighteen passivated and six unpassivated) using a Dynamitron electron accelerator at Wright State University.

The layer structure of the device prior to Si_3N_4 layer deposition is given above. The temperature-dependent Hall measurements were accomplished using a Lakeshore 7507 automated system having a temperature range 12 - 800 K; a resistance range 10^{-3} to $10^{13}\,\Omega$; and, a magnetic-field range 0 - 10 kG. An Accent HL5500 automated system with probes for on-wafer device measurements was used for room temperature measurements.

4.5.2. Electrical Characterization for Gate (Schottky) Leakage Current and Capacitance.

The same wafer preparation described above for Hall system measurements was used for Schottky measurements, but extra grounding and mounting was done for samples being tested on the systems shown in Figures 4.5 and 4.6. Since these structures are not transistors that have a gate, electrical measurements were done by making Ohmic contact assignments as a “source” or “drain”. Then, a reverse bias was applied to the Schottky metal stack to deplete the space charge area for the n type depletion mode

Figure 4.5. Setup used in for I_g-V_g, C_g-V_g and DLTS studies.

structures used. Capacitance voltage (C_g-V_g) and current-voltage (I_g-V_g) measurements were done at 1 MHz for a temperatures between 100 and 400 K. All other experimental factors were held constant.

4.5.3. Deep Level Transient Spectroscopy

In order to perform DLTS measurements on a sample, it was first measured before hand to see if there was enough rectification to get DLTS trap information both before and after irradiation. Immediately after each pulse with the DLTS measurement, the rf capacitance changes by ΔC, whereby ΔC is negative for majority carrier traps and

positive for minority carrier traps. If a Schottky diode is used, or if in a pn junction the reverse bias is only reduced by a pulse bias $V_{imp} \sim V_r$, othen nly majority carrier traps are recharged. The degree of trap filling depends on the filling pulse time width t_{imp} and on the capture coefficient of the traps $c_{n;p}$, which is often formally expressed as the product of the thermal velocity times the capture cross section of the trap for the corresponding carrier type. If the pulse width is large enough (on the order of the pulse repetition period), one speaks of "saturation pulses", hence all deep levels in the space charge region should be filled after the pulse. For sufficiently small pulses, only a portion of all levels are filled, hence the signal gets smaller. Figure 4.7 shows an example of a DLTS measurement with the hole-like traps revealed. The DLTS complements the leakage current measurents and can identify some of the intrinsic as-grown defects as well as radiation-induced defects that lead to device degradation.

Figure 4.6. Accent DL8000 digital DLTS system (with both LN_2 and LHe cryostats).

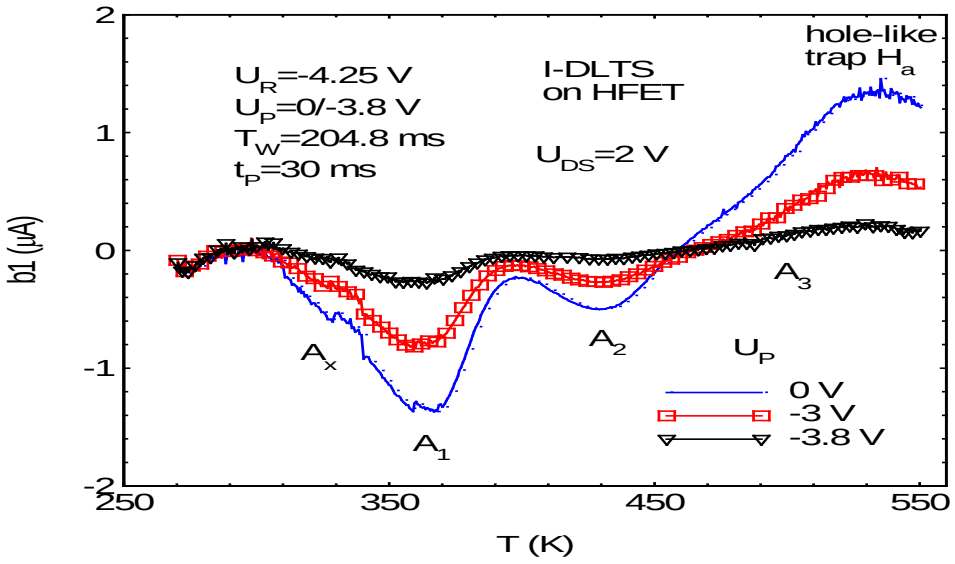

Figure 4.7. Hole-like traps in AlGaN/GaN from DLTS. Trap A_1 is associated with threading dislocations. This figure shows the DLTS capacitance transient with varying applying voltage but constant T_W (time width) and constant τ_p (filling pulse).

4.5.4. Optical Characterization: Photoluminescence

Photoluminescence (PL) was accomplished using a HeCd laser (325 nm) as excitation source and with an emission detection range varying from 3550 to 7450 Å. The laser beam path is shown in Figure 4.8 as the incoming red arrow. The PL spectra were measured using a Spex 1250M spectrometer with a 2400 grove/mm grating blazed at 3000 Å, typical for wide-band-gap applications. Samples from each wafer were pre-characterized in order to establish a baseline and to observe the variation in radiative native defect centers owing to fabrication method. Post-radiation PL were taken using a 266-nm laser. Figure 4.9 provides the orientation and beam depth for the PL experiments. Penetration depths were assumed to vary as $1/e^{\alpha d}$ where $\alpha = 2.25 \times 10^6$ cm^{-1} for Si_3N_4 and is about 10^5 cm^{-1} for GaN. Photoluminescence can give information of the impurity as well as other donor and acceptor energies. The post-irradiation PL peaks give a good

indication of how the irradiation has changed the donor-acceptor population and can help to explain post-radiation Hall measurement results, as well as the radiation induced defects that lead to decreased conductivity and increased leakage current.

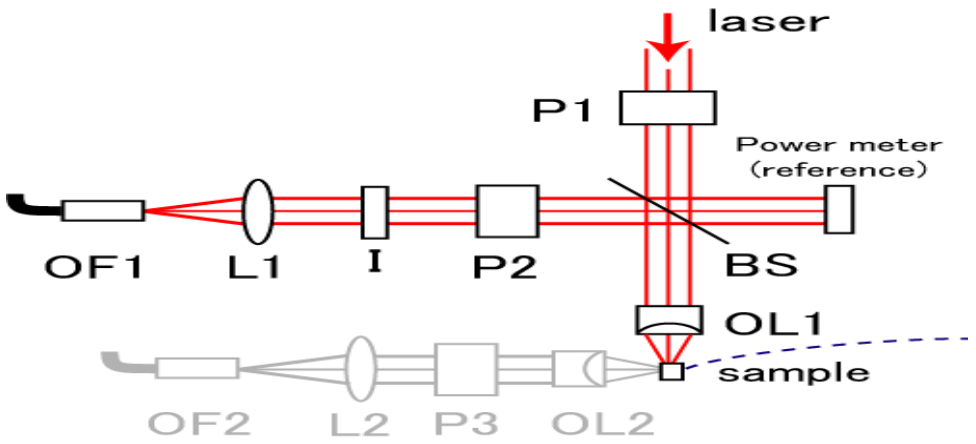

Figure 4.8. PL setup for AlGaAs.

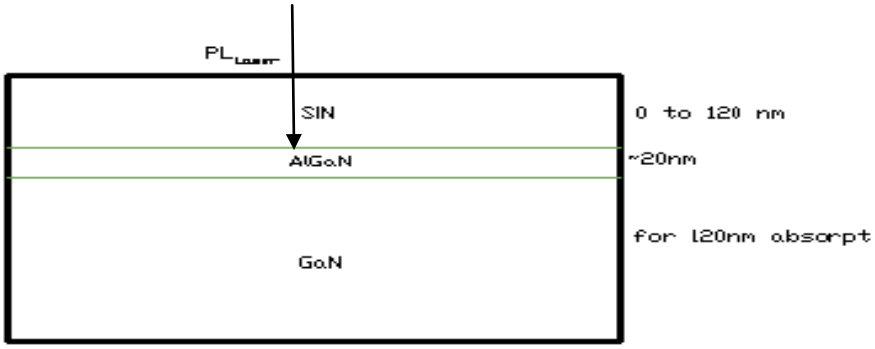

Figure 4.9. Orientation of the beam for PL measurements. For all thicknesses of Si_3N_4, the beam penetrated to the GaN layer.

V. Experimental and Analytical Results for Electron Transport Characterization

In Chapter 2, the physics needed to understand the devices researched in this study was given. This chapter discusses the effects of Si_3N_4 and radiation on the transport properties obtained by Hall system measurements, both with and without passivation and before and after electron irradiation. Also two different AlGaN/GaN HEMT structures were used. Both experimental and modeling results are shown. The focus first is on the Hall metrics of mobility, carrier density, and conductivity and then on the qualitative analysis of the traps and impurities that affect these metrics using PL data. Quantitative results are given by employing analytical models which show the depth of interaction as well as production rate of defects for Ga, Al, and N atoms. These models for the electron damage use a defect production algorithms based on Bethe Bloche (ICRU, 1984), previously described in Chapter 3. For the spatial distribution effects of the radiation, CASINO simulation results show where most of the damage occurs.

The mobility as a function of scattering mechanisms was modeled self-consistently to show the sum of the mechanisms contributing to the total mobility, and how they vary with structure and temperature dependence. The results are fitted and tied to experimental data in Chapter 7 for further analysis. The Hall carrier density and conductivity are also investigated as function of structure, silicon nitride passivation layer thickness and electron irradiation. Preliminary defect analysis is given by PL, which resolves the spatial localization of defects and can be correlated to a donor-acceptor defect pair through conservation of energy calculations. This chapter will answer the first set of investigative questions presented in Chapter 1, which are: What is the effect of

(a)The particular device structure and (b) the Si_3N_4 passivation layer thickness on the transport characteristics (such as the mobility, carrier density, conductivity).

5.1. Effect of Structure and Silicon Nitride Passivation Layer Thickness on Electron Transport Properties in Electron Irradiated AlGaN/GaN

In this study, the effects of the passivation layer thickness were investigated at various thicknesses (0, 20, 50 and 120 nm) on a structure with an epi-stack as shown in Chapter 4, and then measured before and immediately after 1.0-MeV electron irradiation using a fluence of 10^{16} cm^{-2}. It has been shown previously that radiation of this energy produces point defects and creates acceptors (Goodman et al, 2000). Hall measurements were used pre- and post-irradiation to observe changes in carrier density and mobility as a function of silicon nitride thickness and temperature. These measurements indicated the degree of preservation of mobility and conductivity as a function of Si_3N_4 thickness after irradiation. Additionally, Hall system measurements were used to observe changes in carrier concentration as a function Si_3N_4 thickness. These measurements were carried out to give information about the surface donor states and the Si_3N_4 charge at the interface. Hall carrier density data implies that the surface states are donors.

First, mobility as a function of scattering mechanisms will be looked at, then their modeled scattering mechanisms as they vary with structure. Experimental data will show the effect of structure, as well as variation of silicon nitride passivation thickness on transport properties for electron irradiated devices. Experimental results from PL will be used to support the Hall measurements, which are pointing to a number of trapping mechanisms seen in the donor-acceptor pair transitions.

Since mobility in HEMTs is a function of the scattering mechanisms the carriers encounter, the scattering will be looked at along with models that compare the structures and the effects of silicon nitride passivation both before and after irradiation.

5.2. Room Temperature Mobility Results.

Throughout this study, the effects of varying the passivation layer thicknesses are investigated on HEMT structures. Post radiation results show the degree of preservation of mobility and conductivity is a function of Si_3N_4 thickness. The following results are from 300-K Hall system measurements for mobility on AlGaN/AlN/GaN and GaN/AlGaN/GaN structures.

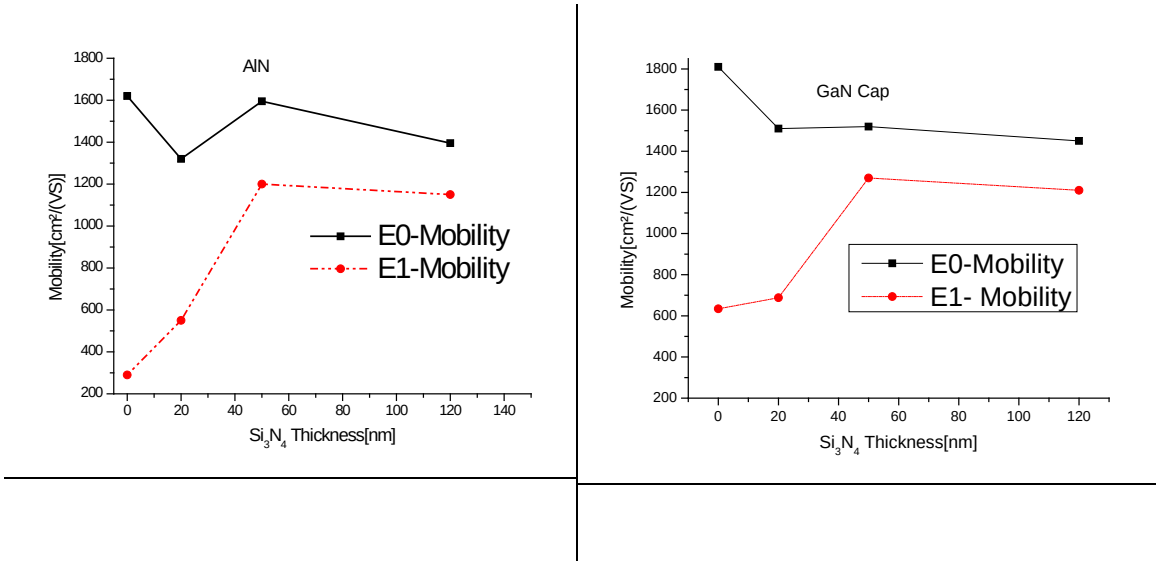

Figure 5.1. Comparison of 300 K mobility pre- (E0) and post- (E1) the 1-MeV irradiation for AlN (left) and GaN (right) cap structures.

The room temperature change in mobility between pre- (E0) and post- (E1) mobility is shown in Figure 5.1 for the two structures. The presence of the GaN cap

reduces the scattering and therefore increases the mobility in the unpassivated sample; but its effect, as compared to the AlN structure, shows the difference in measured results diminishes comparatively with increased passivation layer thickness. Post radiation, with 50-nm passivation, the effects begin to merge. Noticeably, there is a big improvement in the post-irradiation mobility over the unpassivated structure starting with 50 nm passivation, even relative to its higher starting mobility for the GaN cap. Once 50 nm is reached, there is little change in the range between 50 and 120 nm passivation layer thickness. For the structure with an AlN interlayer, with a 300% improvement in mobility for the 120 nm sample and a 314% improvement for the 50 nm sample over the unpassivated sample, a *claim* can be made for substantial improvement and preservation of the device 2DEG mobility after irradiation with 1 MeV electrons. The GaN cap samples average improvement in mobility with passivation trailed the AlN structure, but started at significantly higher mobilities.

5.2.1. Mobility as a Function of Scattering Mechanisms and Centers

The temperature dependent as well as room temperature mobility measurements obtained for the structures in this research as a function of scattering mechanisms is described in this section. By incorporating the additional mechanism of alloy scattering found in HEMT structures, as well as interface roughness, over what was given in Equation 2.20, the mobility can be described as**:**

$$\mu_c = e\langle\tau_m\rangle/m^*, \text{ and } \tau^{-1} = \tau^{-1}_{ac} + \tau^{-1}_{pe} + \tau^{-1}_{po} + \tau^{-1}_{ii} + \tau^{-1}_{dis} + \tau^{-1}_{alloy} + \tau^{-1}_{IR} \quad (5.1)$$

The alloy scattering is decreased by the use of an AlN interlayer, in the AlN structure, and the interface roughness is increased with a use of a GaN cap, due to its effect of the

2DEG sub band levels (Ng et al, 1998). From Equation 5.1 , the Hall mobility, which is the averaged sum of these scattering mechanisms, can be calculated as:

$$\mu_c \approx \mu_H = e\langle\tau^2\rangle/m^*\langle\tau\rangle \text{ , and } \mu_H = R_H \sigma \text{ ---} \rightarrow n_H = n/r = -1/e\ R_H \quad (5.2)$$

Scattering can be intrinsic or extrinsic, and I will briefly review each of the scattering mechanisms of concern that were described in more detail in Chapter 2 and the role they play in the structures in this study. Ionized impurities in AlGaN/GaN HEMTs are the source of unintentional doping. The HEMTs are unintentionally polarization doped and this is confirmed by the positively charged donor surface states in the AlGaN. If the thickness of the AlGaN barrier is high enough, ionized impurity scattering is not strong or dominant. These impurities contribute electrons to the 2DEG and account for the PL transitions that will be shown later.

Dislocations in the lattice occur when the GaN is not grown on a GaN substrate, which results in lattice mismatch. Threading dislocations have been the subject of many studies (Marino et al, 2010). Threading dislocations (the Coulomb potential is associated with the charge and the scattering potential is associated with the dislocation strain field) act as scattering centers and have a large core potential and deformation potential. Charged dislocations can cause scattering of electrons in the 2DEG. Like ionized impurity scattering defects, they only have an effect at low carrier densities. When threading dislocations reach a value of 10^{10} cm^{-2}, they can have an effect and are believed to be a cause of leakage current (Ng et al, 1998; Weimann et al, 1998), showing up as hole-like traps in AlGaN/GaN DLTS (will be discussed in Chapter 6) and will be briefly addressed in section 5.3. Figure 5.2 below is a microscopic depiction of a distorted crystal showing an edge dislocation. The yellow emission occurring at 2.2 eV in the

AlGaN/GaN PL on the right is believed to occur due to an acceptor trap formed at the end of an edge dislocation (Look, 1989). The associated PL spectra at 2.2 eV shown is for samples with 0, 20, 50 and 120 nm of Si_3N_4 thickness, so these deep intrinsic traps persist with surface passivation, although there is some degradation of peak due to the attenuation of the PL beam going through the passivation layers. More PL examples will be given in section 5.3.

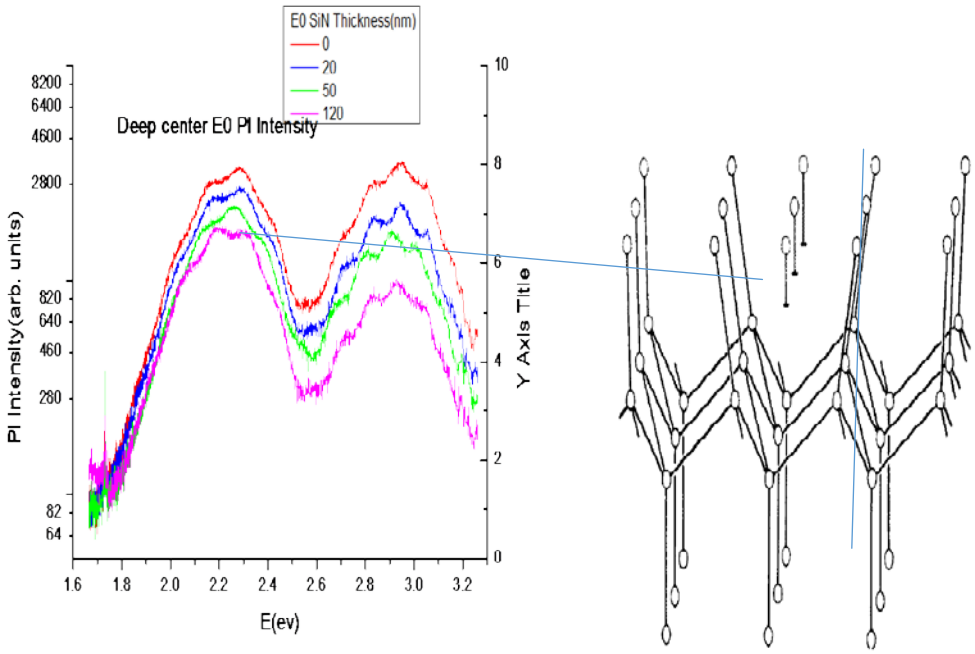

Figure 5.2. Microscopic view of distorted crystal threading dislocations (right picture taken from Look, 1989).

Acoustic phonons interact with electrons through the deformation potential and piezoelectric coupling. Atomic displacements are produced by acoustic mode vibrations. A secondary effect is the piezoelectric potential which occurs in compound semiconductors lacking a center of symmetry and interacting atoms are partially ionized. There is a difference in polarization charges between the AlN or AlGaN and GaN, which

leads to dipole dislocations and scattering of electrons in the 2DEG. Scattering due to phonons is the largest scattering contribution that limits mobility at higher temperature. The acoustic and optical phonon scattering drops the mobility with increasing carrier density. Acoustic mode lattice vibrations induce changes in the lattice spacing, which changes the band gap from point to point (Meyers, 2008). This results in the crystal being deformed at these points so the potential is called a deformation potential. The relaxation time (Norton, 2009) parameter is due to the averaged sound velocity.

The optical phonons have high energy and interact with electrons through the polar optical potential. Increasing the carrier density leads to a rise in the Fermi level. This occurs upon reaching values (over the first sub-band ground state energy). This is larger than the optical phonon energy and occurs as soon as the carrier density reaches ~$8x10^{12}$ cm^{-2}. Thus, the more optical phonon emission processes, the more the contributions to the free carrier mobility decreases.

Evidence for increased carrier-carrier scattering is shown in Figure 5.3. The relationship between Si_3N_4 thickness, mobility and carrier density is not always linear, but there is an explainable relationship. Mobility correlates to carrier density in AlGaN/AlN/GaN usually inversely, until saturation. With the GaN cap structure, once 2DEG carrier density saturation occurs, there are other processes occurring, depending on the thickness at which saturation is reached. If the saturation is reached at 20 nm in the GaN cap structure, then a significant lowering of mobility does not occur and it is not correspondingly the lowest mobility. When saturation occurs at 50 nm or 120 nm, then the mobility drop has is affected by the strain due to the thickness of the layers. Figure 5.4 shows a plot of carrier density and mobility at 300 K as a function of Si_3N_4

passivation. The carrier density and mobility are inversely proportional; that is when one goes up, the other goes down, as implied by equation 2.13. The interface roughness scattering potential amplitude V_0 in the square quantum well is approximately determined by assuming that local fluctuations of the interface position and of the roughness amplitude shrinks with well width. As the 2DEG waveform moves closer to the barrier (due possibly to things like increases in carrier density), there is scattering from interface roughness. Structures wherein the higher waveform sub-bands fill quicker, like those with a GaN cap, will have less interface roughness scattering and thus higher mobility because the higher sub-bands are further removed from the AlGaN interface.

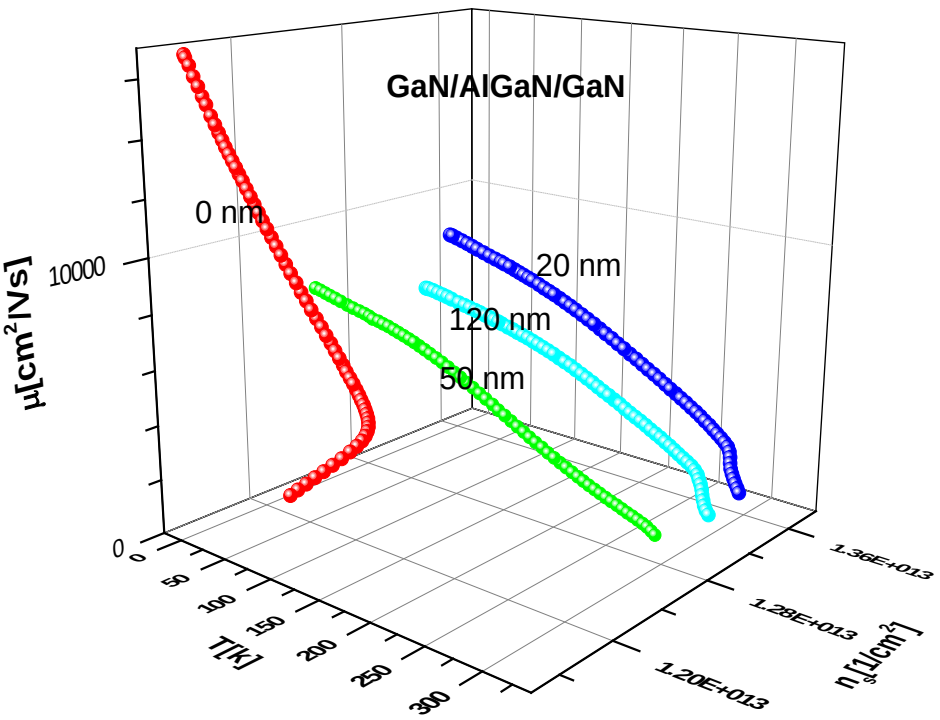

Figure 5.3. Mobility as a function of carrier density and Si_3N_4 thickness in a GaN cap sample with its carrier density saturating at 20 nm. The higher the carrier density, the lower the mobility. The carrier density to Si_3N_4 thickness relationship is not the same for the AlGaN/AlN/GaN structures.

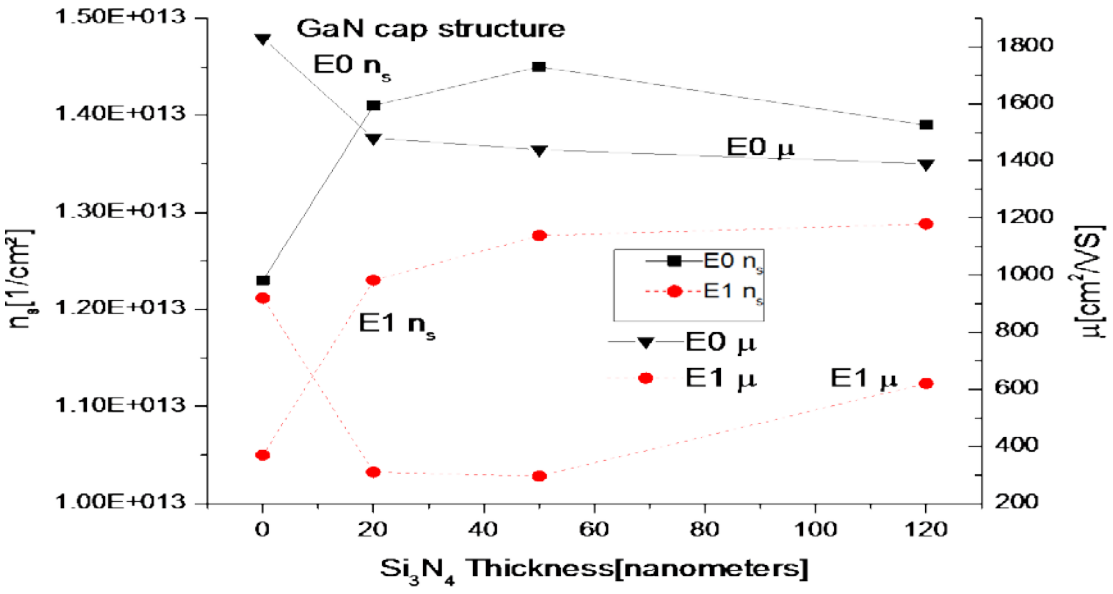

Figure 5.4. The approximately inversely proportional relationship between mobility and carrier density is shown. At 300 K, as carrier density goes up, mobility goes down due to carrier-carrier scattering.

Alloy disorder scattering comes from the tail of the 2DEG waveform in the binary GaN penetrating the ternary AlGaN barrier. The alloy potential in the barrier randomly varies. As carrier density increases, the waveform penetration increases. This will shift the waveform closer to the barrier interface, and thus increase scattering and decrease mobility. The tail of the 2DEG waveform is decreased with the use of an AlN interlayer, because alloy scattering is reduced (Norton, 2009), thus allowing for higher mobility relative to an AlGaN/GaN structure with no interlayer.

5.2.2 Modeled Scattering Mechanisms for the Two Different Structures

The scattering mechanisms in equation 5.1 were modeled using a program called Nextnano and shown in this section for both AlGaN/AlN/GaN and GaN/AlGaN/GaN. Modeled differences in scattering are based on no passivation or 50 nm of silicon nitride passivation layer thickness. The results give information about how Si_3N_4 may be affecting the mobility as a function of scattering mechanisms for each device structure.

In modeling the mobility using Nextnano, Schrodinger and Poisson equations were solved self consistently to obtain values for the energies of the individual quantized levels, the occupancy of the sub-bands, the electron densities in the 2DEG, energy band diagrams, and the total mobility as a function of scattering mechanisms. An explanation of Schrodinger and Poisson equations was given in Chapter 2.

The electrostatic potential needed in this model was obtained from Poisson's equation. Also built into the model is the image and exchange correlation potentials using Numerov's numerical method (Norton, 2009). Table 5.1 is a summary of the values of the scattering mechanisms taken directly from the modeling results shown in Figures 5.5 to 5.10. Table 5.2 summarizes the main material parameters used in the models. In Figure 5.6, the ionized donors at the surface are the largest scattering mechanisms. Residual scattering is from the GaN. Residual impurity concentrations are usually around 10^{15} cm^{-3}. In Figure 5.7, with the addition of 50 nm of Si_3N_4, the sheet carrier density has increased and the total mobility has decreased.

Table 5.1. Scattering mechanisms used in Nextnano models. For Figure 5.6, the temperature range T [K] is given as 1 through 41, and for Figures 5.5 and 5.7 through 5.9, 1< T <351 K.

Temperature	μ_total (m^2/V-s)	μ_ionized (m^2/V-s)	μ_ionized Bg(m^2/V-s)	μ_acoustic (m^2/V-s)	μ_polar (m^2/V-s)	μ_alloy (m^2/V-s)	N_s (cm^{-2})
1	9.8208	11.5039	425.8777	532.8409	1.0E15	93.5970	2.24E15
11	8.16407	11.19416	420.3947	48.4409	1.0E15	98.6895	2.20E15
21	6.68542	10.37912	405.7079	25.3734	1.0E15	88.0628	2.09E15
31	5.66326	9.68972	392.8802	17. 1884	2.8E12	79.0469	1.99E15
41	4.91125	9.0779	381.1501	12.9961	5.6E08	72.0139	1.90E15

Table 5.2 Material Parameters used in mobility scattering models.

	Symbol/unit	GaN(wurzite)/Reference	AlGaN/reference
Electron effective mass	(m^*/m_o)	0.228 [A]	0.228 [A]
Mass Density	(g/cm^3)	6.1 [B]	
Conduction Band offset	ΔE_c / eV	0.333 [C]	
Band gap	E_g / eV	3.45	3.47
Donor level	E_D/ eV		$V_c - 0.2$
Default donor concentration	cm^{-3}	$5x10^{16}$ [B]	$4x10^{16}$ [C]
Acceptor level	E_A/eV		$V_c - 3.0$
Default acceptor level	cm^{-3}	2.5 $x10^{16}$ [B]	
Interface roughness parameter	nm	1.5 [A]	1.5 [A]
Static dielectric constant	ε_0	9.6 [A]	9.5
Piezoelectric constant	V/cm		$-0.58\ x - 0.22(1- x)$
LO phonon energy	meV	90.5 [B]	
	[A] Asgari et al, 2004; Asgari et al, 2005; Asgari et al, 2011. [B] Hsu and Walukiewicz, 1997. [C] Hu et al, 2001; Hu et al, 2007		

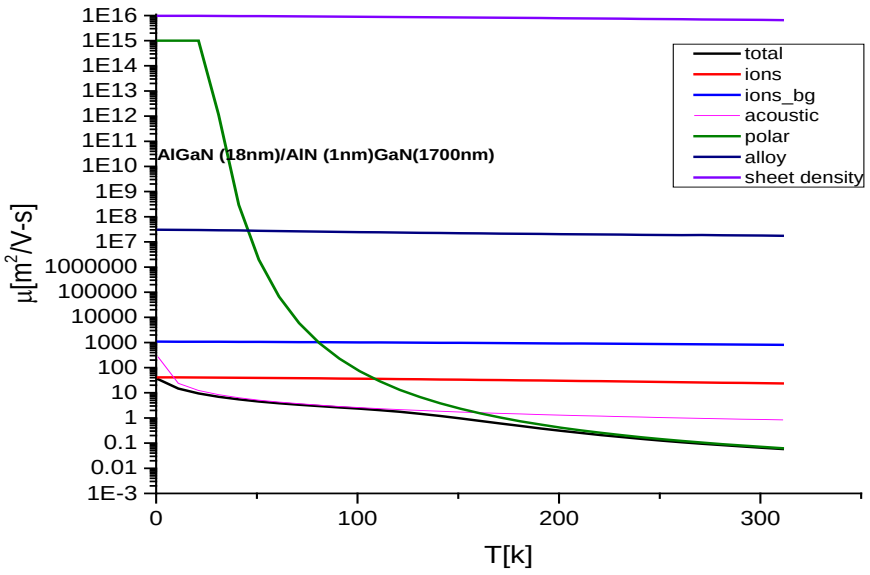

Figure 5.5. AlGaN/AlN/GaN modeled scattering mechanisms 0 to 320 K. The most dominant scattering mechanism is acoustic phonon, while at lower temperatures the least dominant is polar optical.

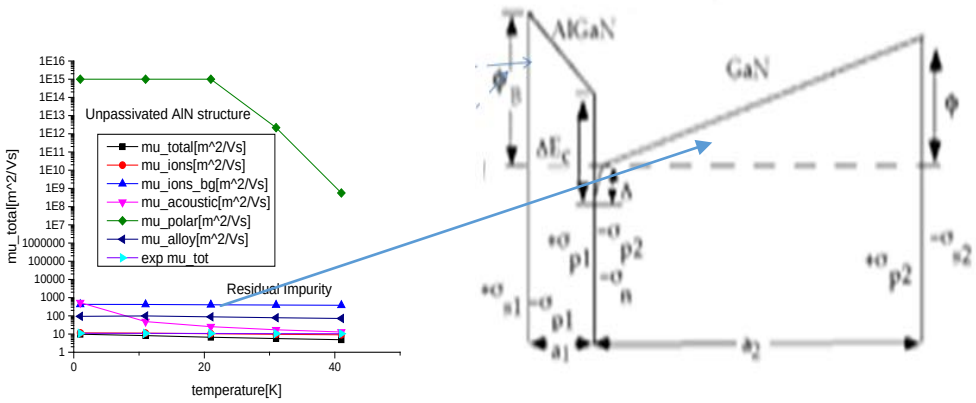

Figure 5.6. Model of AlGaN/GaN with AlN spacer layer, showing the ionized background scattering which is due to residual impurity scattering. This model shows the scattering for temperatures from 0 to 40 K. The scattering is in units of m^2/V-s. The polar optical scattering is not a significant contributor to the total mobility for this temperature range.

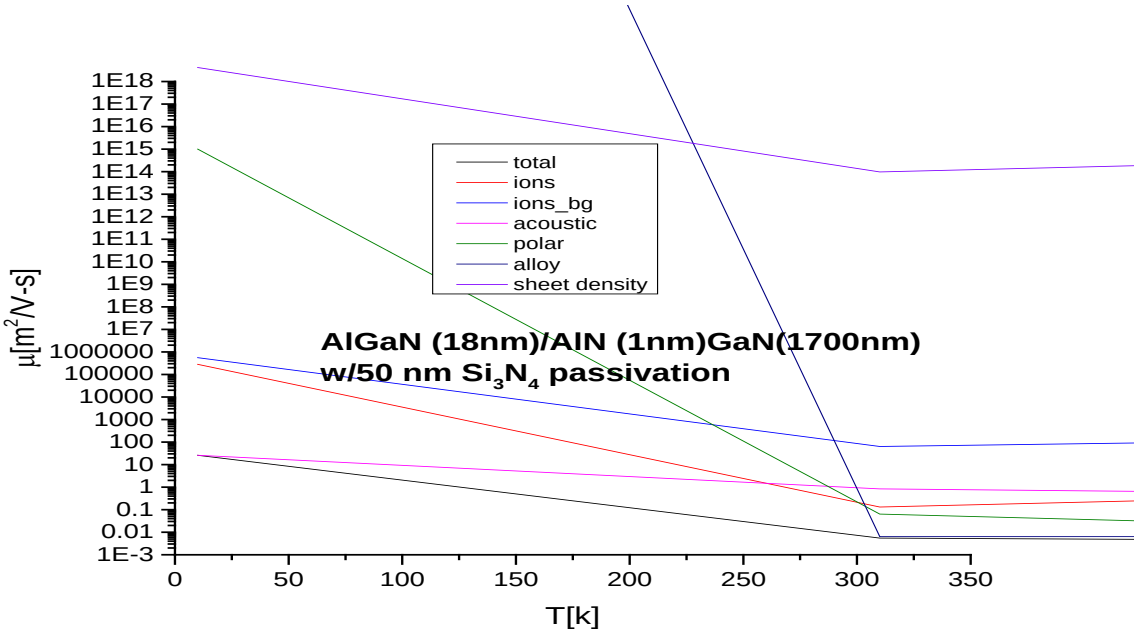

Figure 5.7. AlN structure with 50 nm Si_3N_4 scattering mechanisms 0 to 320 K.

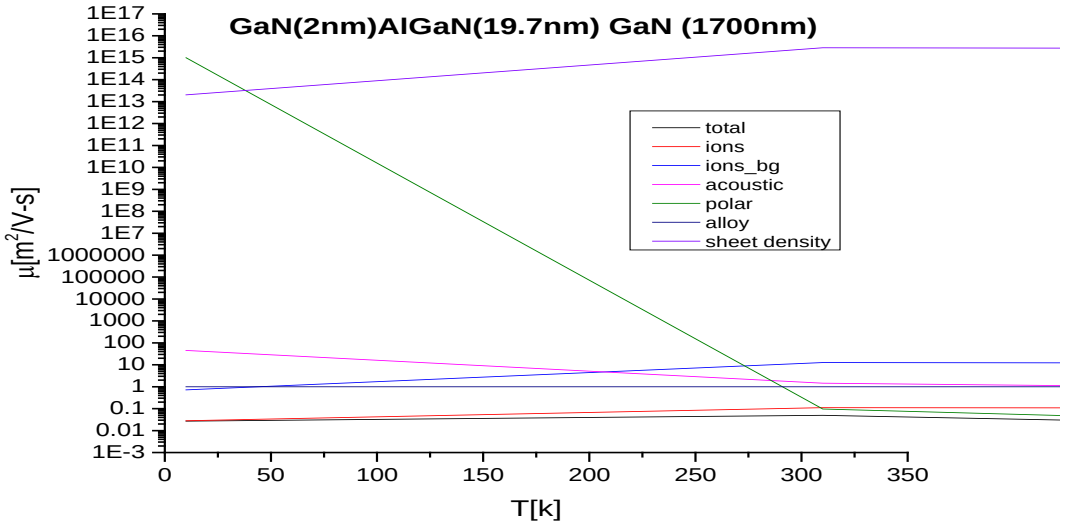

Figure 5.8. GaN cap structure scattering mechanisms from 0 to 350 K. The units are given in Table 5.1. To see how each scattering mechanism affects total mobility, see equation 5.1.

The sheet carrier density is ~ 2E13 m^{-2} in Figure 5.8 for the GaN cap structure as opposed to ~ 1E16 m^{-2} for the structure with the AlN interlayer in Figure 5.5. Alloy and ionized impurity scattering now contribute more to the total mobility, shown also below in Figure 5.9. The GaN cap, which serves also as a passivation layer, changes the temperature dependent behavior of the polar optical scattering.

The sheet carrier density has increased with the addition of the 50 nm of passivation in Figures 5.7 and 5.9, but the alloy scattering now plays a bigger role has reverse effects as shown in Figure 5.10. For the passivated AlN structure, **t**he alloy scattering decreases more rapidly than in the unpassivated sample. With the GaN cap sample, passivation gives a lower alloy scattering for the same range in the unpassivated sample. All samples maintain a flat alloy disorder potential, regardless of the structure or Si_3N_4 passivation.

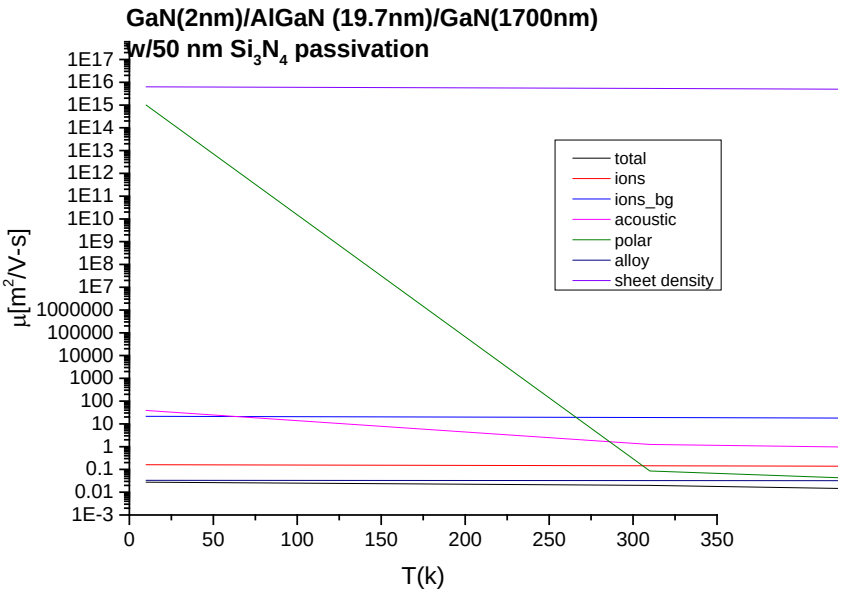

Figure 5.9. GaN cap structure with 50 nm Si_3N_4 scattering mechanisms from 0 to 320 K. The top curve, sheet carrier density, has units of cm^{-2}.

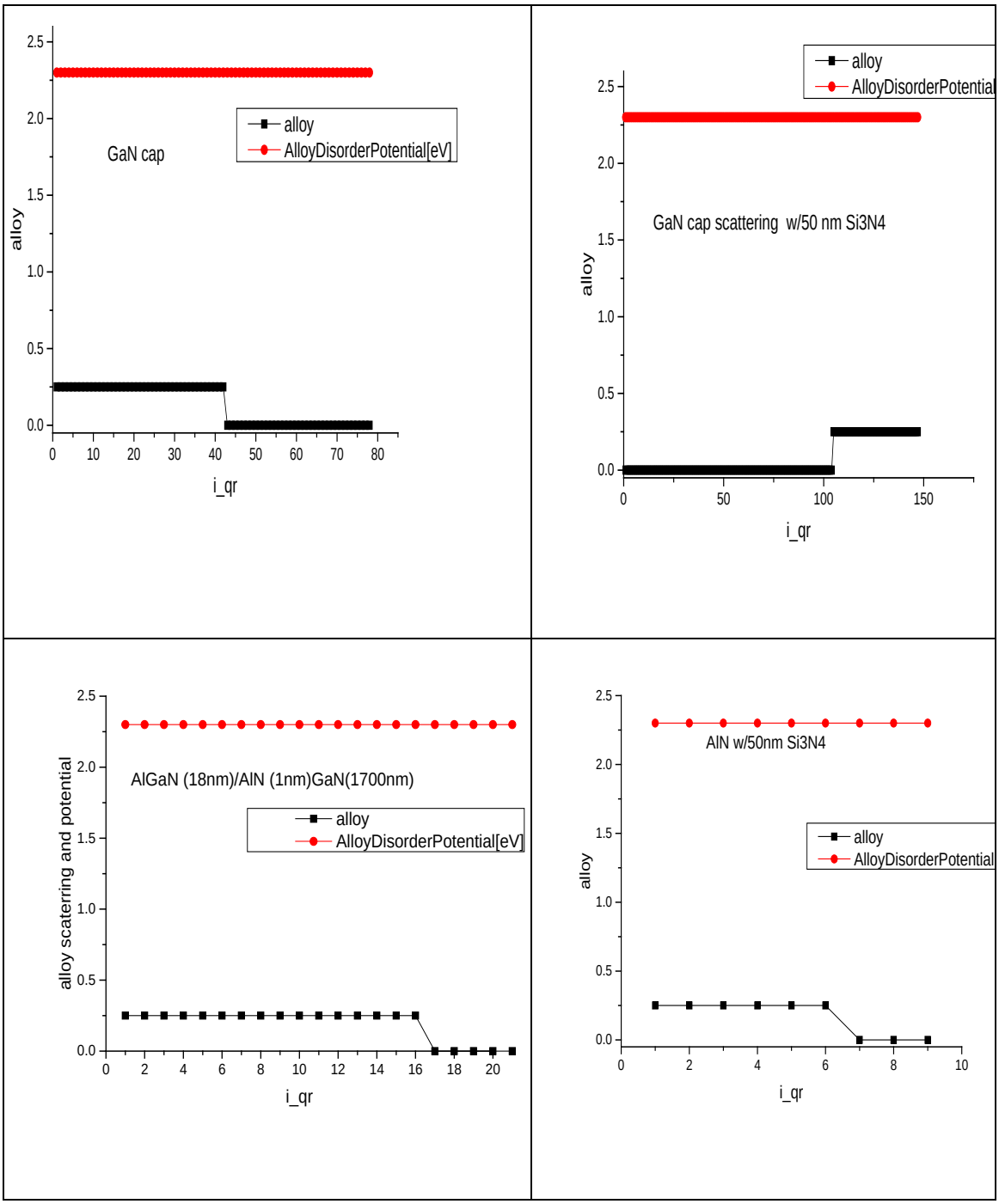

Figure 5.10. The modeled alloy potential and scattering as a function of region. Upper right and left: There is a slight drop in alloy scattering in the AlN interlayer region with Si_3N_4. Lower Right: the results are for the GaN cap structure with 50 nm of Si_3N_4 passivation.

The mobility due to alloy scattering only is described by (Asgari et al, 2011):

$$\mu_{\text{alloy}} = \frac{2^{3/2}}{3}\pi^{1/2}\ \frac{e\hbar^4}{V_c\alpha(1-\alpha)E_{AB}^2\, m^{*5/2}\ kT^{1/2}} \tag{5.3}$$

It can be seen that there is some temperature dependence with this mobility, and it would effectively decrease the mobility as the temperature increases. Since the y axis is a log scale and the higher the values are less of a contribution, it shows alloy scattering contributes less to the decrease in total mobility in AlGaN/AlN/GaN, regardless of passivation until room temperature. With the GaN capped structures, the alloy scattering contributes more to the total mobility, but does not show the temperature dependence, so one of the other terms contributing to the alloy scattering may be countering the effect, like the potential term $V_c\alpha(1-\alpha)E_{AB}^2$. Perhaps it is nondegenerate for the GaN cap structure over a wider temperature range. The cap structure has a higher total mobility, due in part to the fact the GaN cap structure is showing less phonon scattering, as well as a lower sheet density, which would mean less carrier-carrier scattering. The residual scattering, to be found in the GaN bulk is lower but the acoustic and polar optical scattering is slightly higher.

5.2.3 Experimental Carrier Densities

In HEMTs, the electric field is very high, so mobility is not necessarily the most important metric. Saturation velocity must be evaluated, and thus the carrier density. So in addition to looking at channel conductivity, which is mobility dominated, it is also important to consider how the carrier density connects to Schottky (gate)current

measurements. The Schottky (gate) current results to be presented in Chapter 6 relate to a corresponding carrier density.

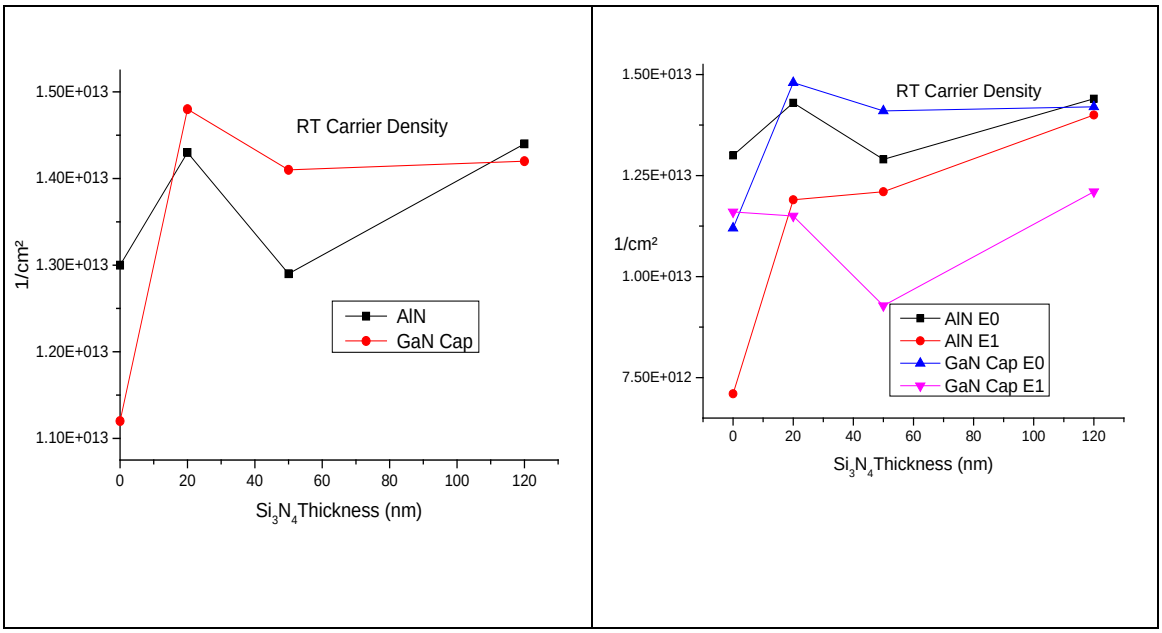

Figure 5.11. Pre-irradiation (E0) comparison of (left) AIN vs. GaN cap carrier density and the pre- and post-irradiation (E1) carrier density comparison of both structures.

The left side of Figure 5.11 shows the room temperature comparison of carrier density prior to irradiation. There is some sample-to-sample variation for all Hall parameters due to processing irregularities, so averaged values are presented. The post-irradiation results (on the right) show the passivated GaN cap structure loses a larger percentage of carriers as compared to the unpassivated GaN cap. The unpassivated cap structure gains carriers, but the unpassivated AlN structure loses carriers. The radiation may be creating more donors in the former, but more acceptors in the latter.

With passivation, post-irradiation carrier density loss is minimal in the AlN structure with 50 or 120-nm passivation layer thicknesses, whereas 20 nm is less effective

(right side, Figure 5.11). From section 5.2.1, increases in carrier density lead to a raising of the Fermi level upon reaching values (over the first sub-band ground state energy) larger than the optical phonon energy. When the carrier density reaches values as large as $1.3x10^{13}$ cm^{-2}, the mobility reaches a constant value of 1100 cm^2 $V^{-1}s^{-1}$. This, in principle, should be the maximum mobility in quantum wells at large carrier densities. However, the combined phonon and carrier–carrier scattering mechanisms do not explain the saturation of mobility at lower carrier densities or the sharp mobility decay that starts at carrier concentrations of ~1.4 x 10^{13} cm^{-2} (Wolfe et al, 1989) and is shown in Figure 5.13.

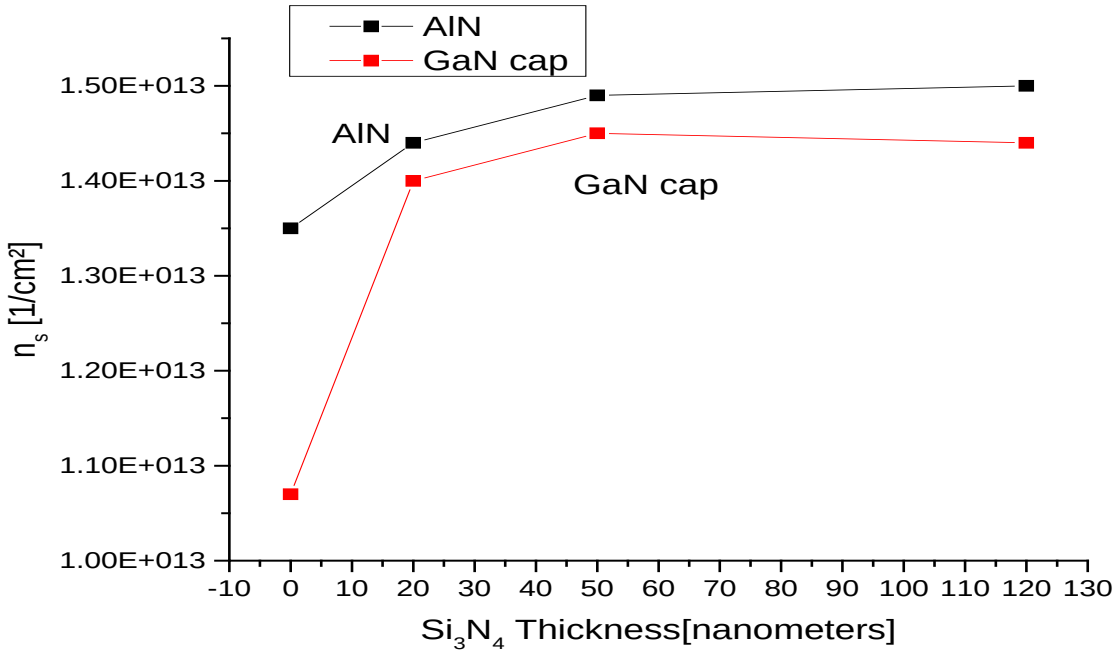

Figure 5.12. Averaged 300-K results over the sample sets show that the AlGaN/AlN/GaN structure has a higher carrier density prior to irradiation than a structure without an interlayer.

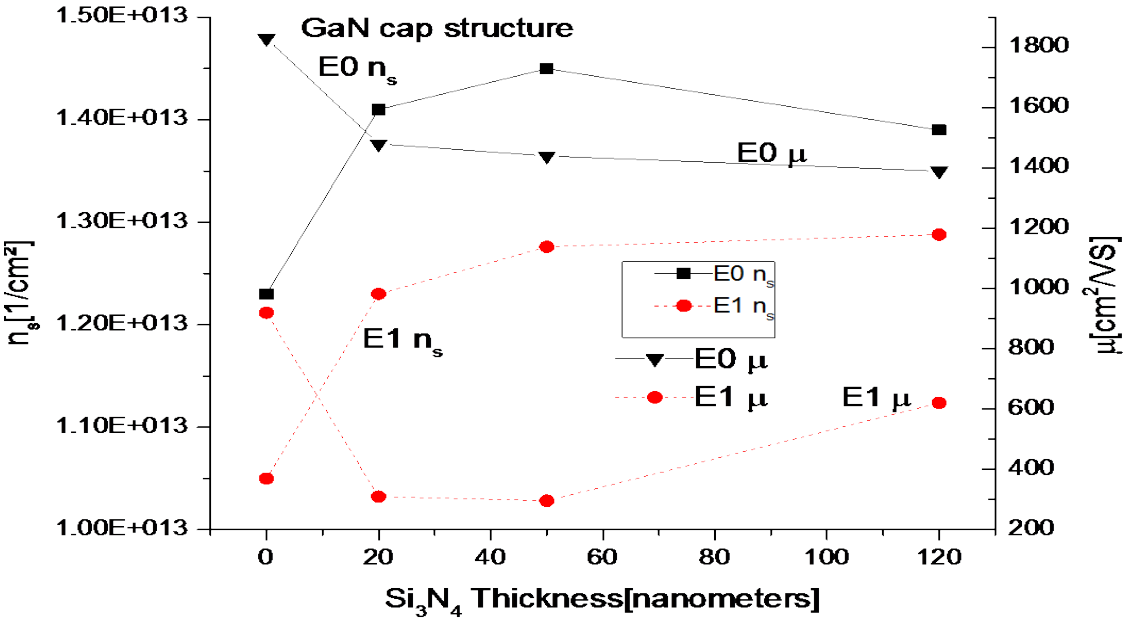

Figures 5.13. The pre- (E0) and post- (E1) irradiation 300-K carrier density and mobility for the GaN cap structure.

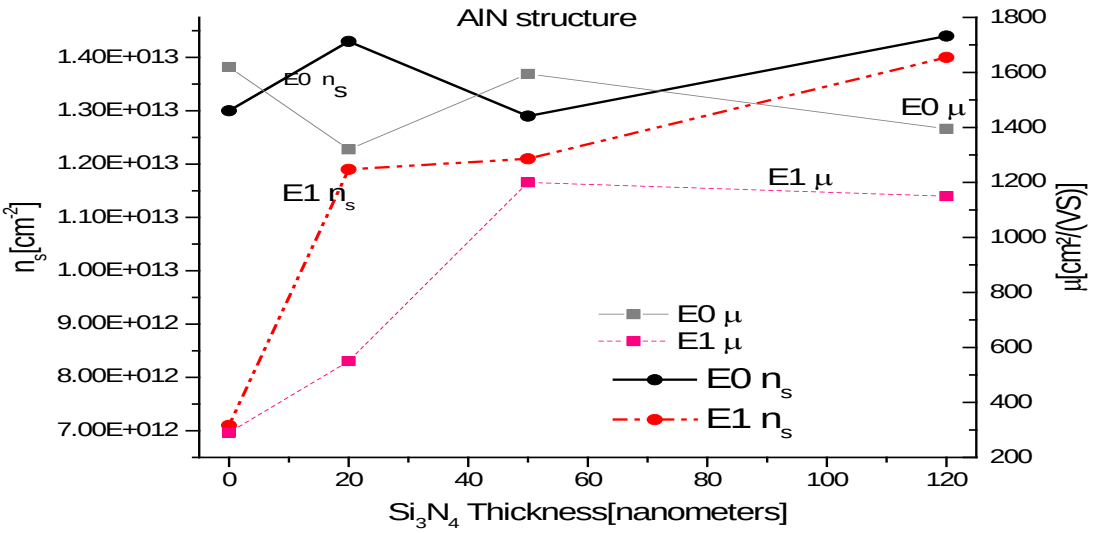

Figure 5.14. The pre- (E0) and post- (E1) irradiation 300-K carrier density for the structure with an AlN interlayer.

The room temperature and temperature-dependent carrier density results in Figures 5.12 through 5.14 show the effects of structure, passivation layer thickness, and 1.0-MeV electron radiation on the Hall carrier density for the samples in this study. The AlN structures show a consistently higher carrier density but lower mobility (Figures 5.12 and 5.14) with passivation layer thickness, both before and after irradiation. For increasing temperature, in accordance with Fermi Dirac statistics, there is a greater probability that higher sub-bands will be occupied.

$$n_i = (e^{(\epsilon-\mu)\,kT} + 1)^{-1} \tag{5.4}$$

For the corresponding mobility, it is shown according to Asgari (Asgari et al, 2004) in Figure 5.15 in the next section, that the higher two sub-bands have a greater mobility at low temperatures. For the most part, mobility μ and carrier density n_s are inversely proportional. As room temperature is approached, the higher sub-bands quickly decrease in mobility.

5.2.4. Modeled Conduction Bands as a Function of Structure and 2DEG Electron Densities

A more detailed discussion is outside the scope of this research, but models of the conduction band profiles and first subband electron densities for the two structures were attempted and are shown in Figures 5.16 through 5.22. Wavefunction models of the 2DEG carrier density for both the AlGaN/AlN/GaN structure and the GaN/AlGaN/GaN structure are shown. Such information is useful in analyzing the change in current conduction and tunneling mechanisms, as well as being able to identify the relative

locations of traps and impurities in one structure versus another and with the addition of varying passivation layer thicknesses as the surface potential varies.

It should be noted in Figure 5.15 that the second sub-band wave function ψ^2 is significantly farther from the interface than the first sub-band. As a result, electrons in the higher sub-bands are not confined and situated as closely to the AlGaN interface. The low-temperature dominant scattering mechanisms will not affect electrons in the higher bands. These include impurity, interface roughness and alloy scattering. So the higher sub-band electrons will have a weaker piezoelectric scattering than those in the first sub-band. As discussed previously and shown in the modeled temperature-dependent plots, acoustic phonon scattering is a dominant scattering at room temperature.

Relative to the effect of variation of structure as done in this study, it is known that structures with GaN caps have a quicker rate of fill for the upper sub-bands than do structures without a GaN cap. Therefore, low-temperature mobility should be higher than for a structure without this cap. This is shown by comparing Figure 5.24 with Figure 5.25. Without an AlN interlayer, which appears as a spike in the conduction band at 18 nm, there would be an increase in alloy scattering. The electron density is difficult to represent in Figure 5.17 because of the change in scaling necessary with the addition of 50 nm silicon nitride, which has an $E_g \sim 5.4$ eV. An enhanced "zoom in" of a portion of the figures is included. Note there is an additional electron density occurring outside of the 2DEG area with the addition of 50-nm passivation. Figure 5.18 shows the electron density when 50 nm of Si_3N_4 is added to an AlN structure.

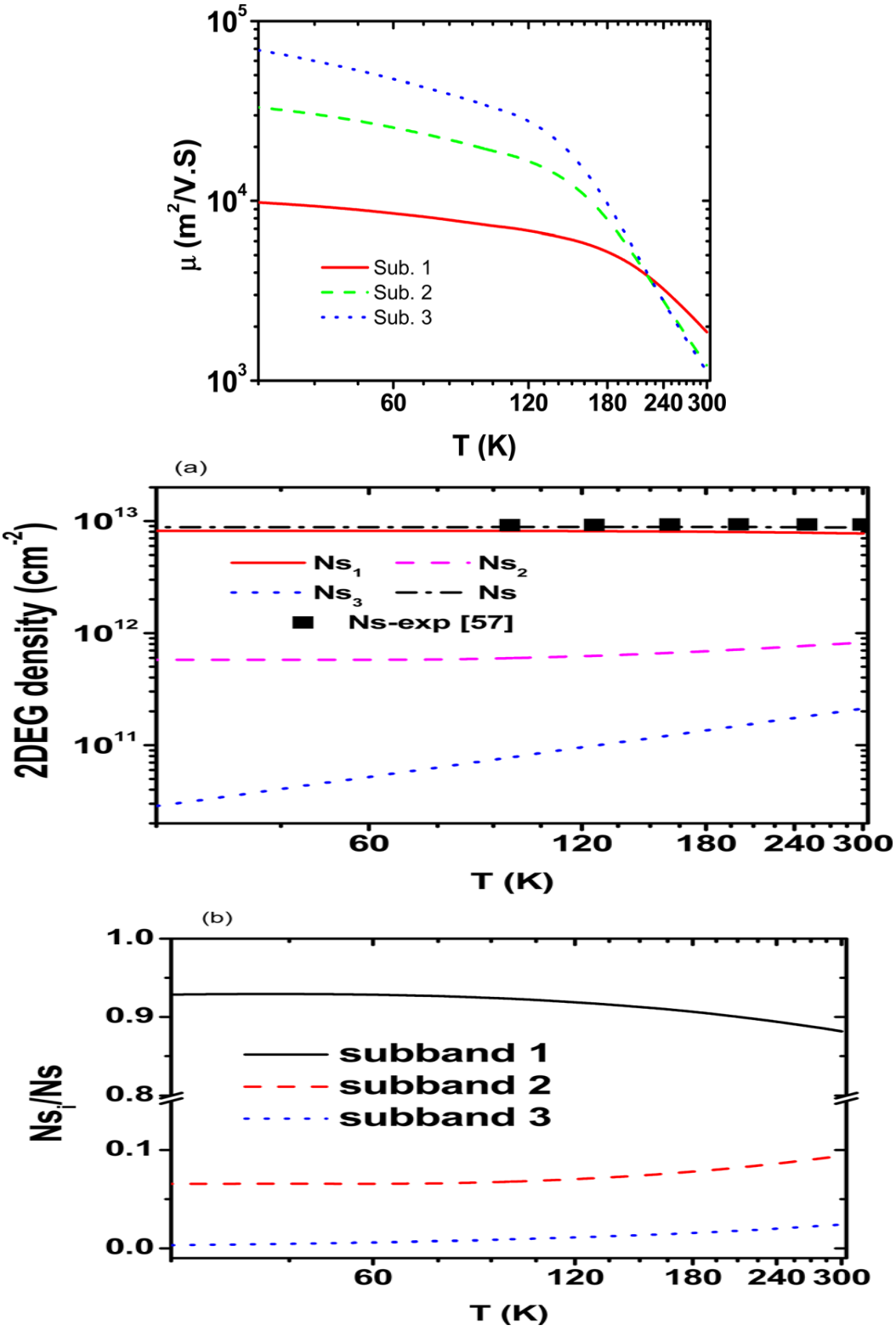

Figure. 5.15. The 2 DEG sub-band mobility and carrier density (Ng et al, 1998).

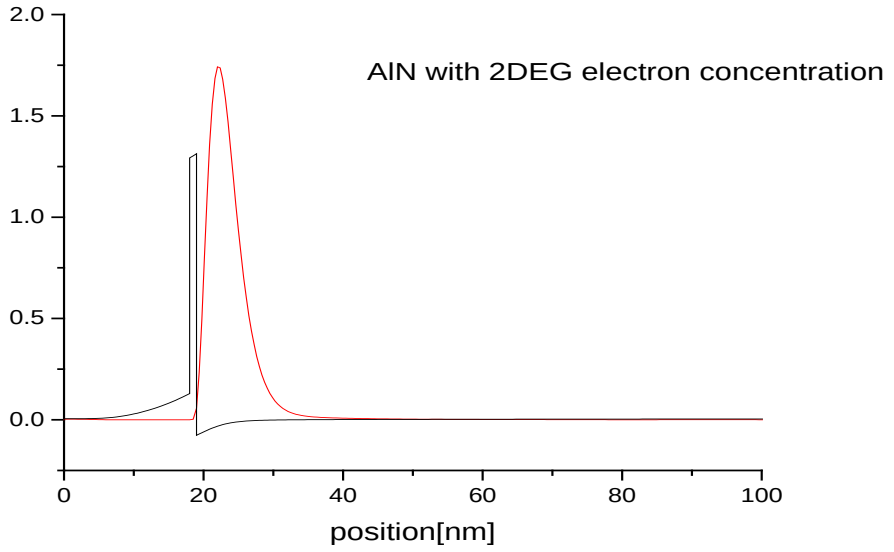

Figure 5.16**.** Modeled first sub-band energy and conduction band for AlN (1 nm) in $Al_{0.25}Ga_{0.75}N/GaN$.

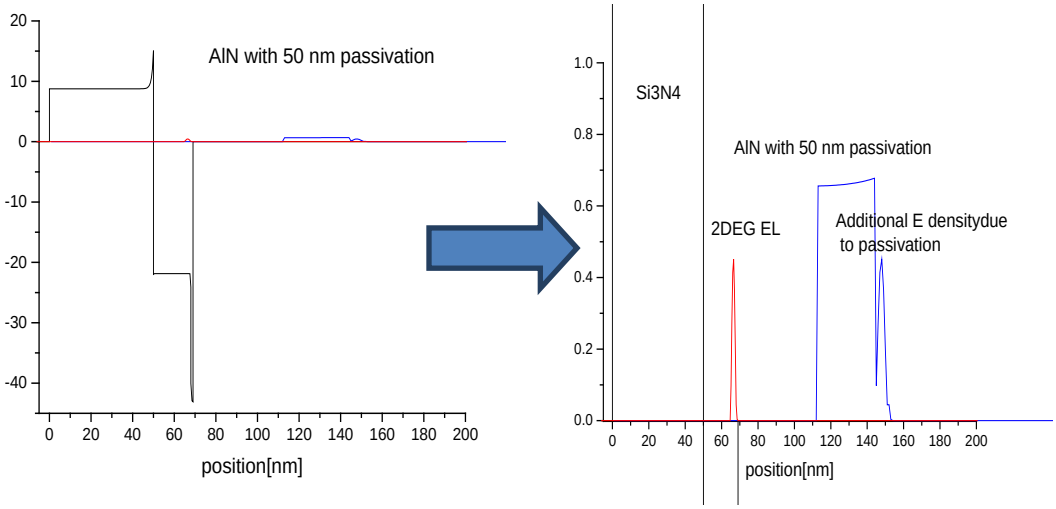

Figure 5.17. Modeled first sub-band energy and conduction band for Si_3N_4 (50 nm) and AlN (1 nm) $Al_{0.25}Ga_{0.75}N/GaN$(left) along with zoom of the area showing the electron density.

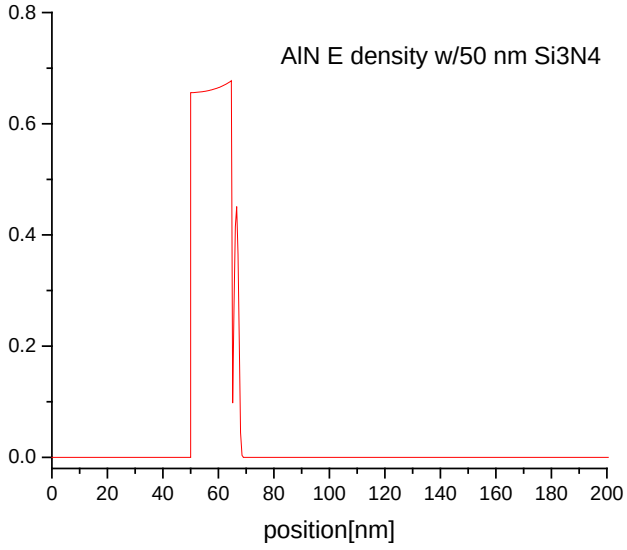

Figure 5.18. The electron density for the AlGaN/GaN/GaN structure with 50 nm of Si_3N_4.

Figures 5.19 through 5.22 model the GaN gap structure without and with 50 nm passivation, and their electron densities. Figure 5.22 shows how far the waveform extends into the GaN as opposed to the model in Figure 5.16 where there is an AlN spacer layer keeping the tail of the wavefunction from spreading into the GaN.

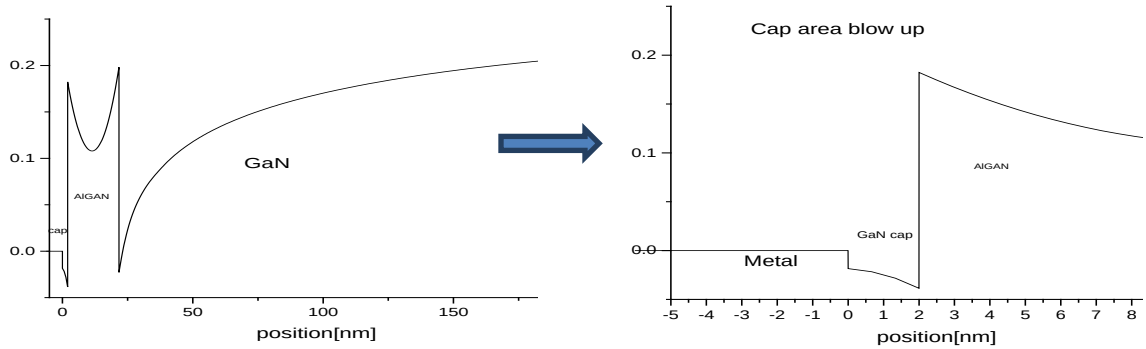

Figure 5.19. Modeled conduction band for GaN (2 nm)/AlGaN/GaN (left) with enlarged view of the cap area.

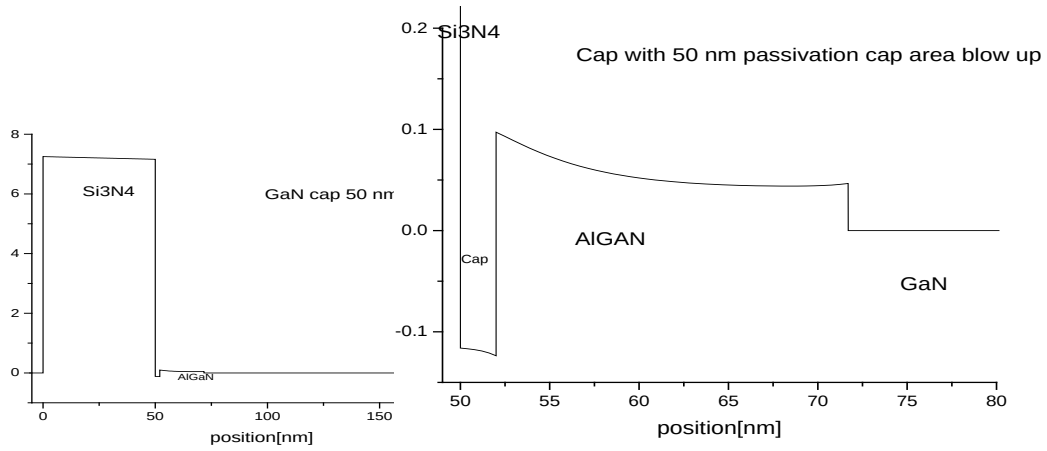

Figure 5.20. Modeled conduction band for Si_3N_4 (50 nm)/GaN (2 nm) $Al_{0.25}Ga_{0.75}N$/GaN (left) and enlarged view of cap area (right).

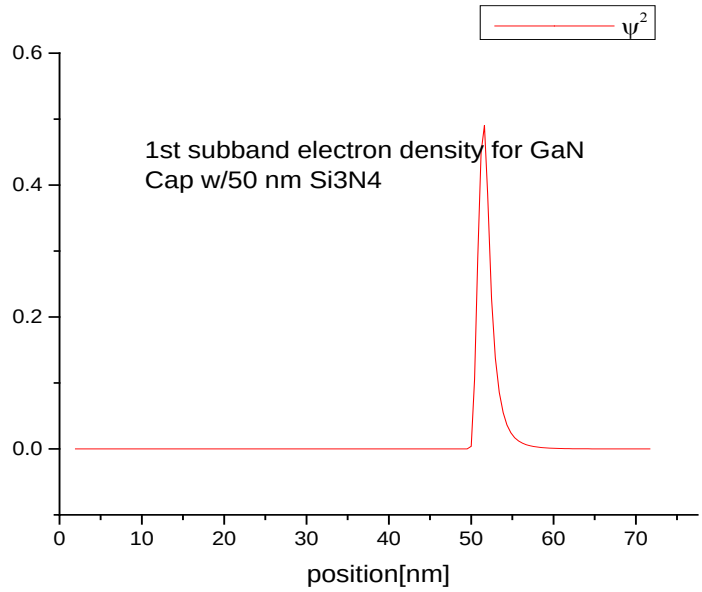

Figure 5.21. Modeled electron density for Si_3N_4 (50 nm)/GaN (2 nm) $Al_{0.25}Ga_{0.75}N$/GaN between the edge of the Si_3N_4 and the front boundary of the GaN.

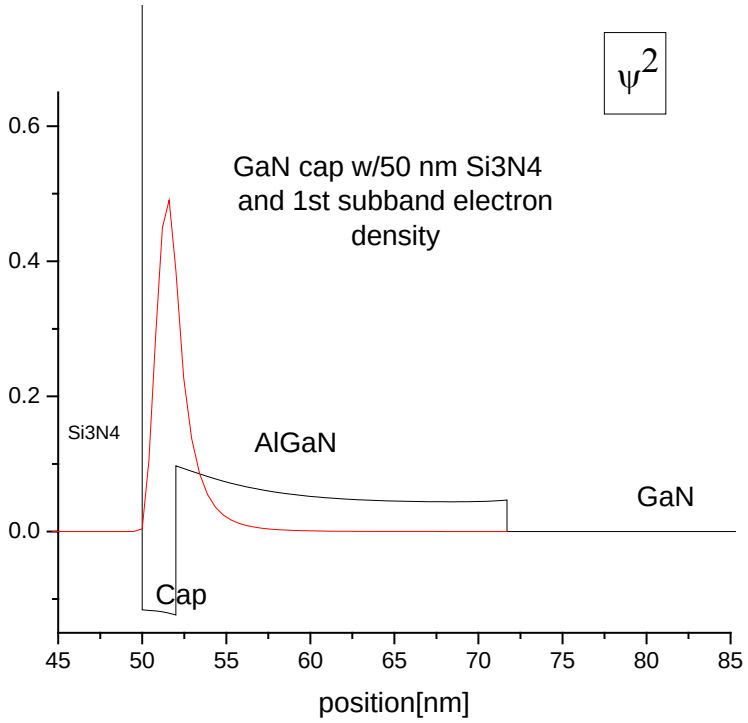

Figure 5.22. The first electron wave function in the 2DEG area of the GaN cap structure.

5.2.5. Experimental Conductivity Results

Figure 5.23 gives the conductivity comparisons between pre- and post-irradiation for both structures, for which the use of an unpassivated GaN cap will be later shown as more robust to leakage currents. The improvement for the AlGaN/AlN/GaN structure after irradiation with 120 nm Si_3N_4 thickness was about a factor of 8 over the unpassivated, and for the GaN cap was about a factor of 5.5 over the unpassivated. A silicon nitride thickness of at least 50 nm is needed for improvement in post-radiation conductivity for both structures. The conductivity given in equation 2.13, which is a product of the mobility μ and the carrier density n_s, is restated below.

$$\sigma = q\,\mu n_s \tag{5.5}$$

In Figure 5.23, the conductivity is changing either due to mobility or carrier density.

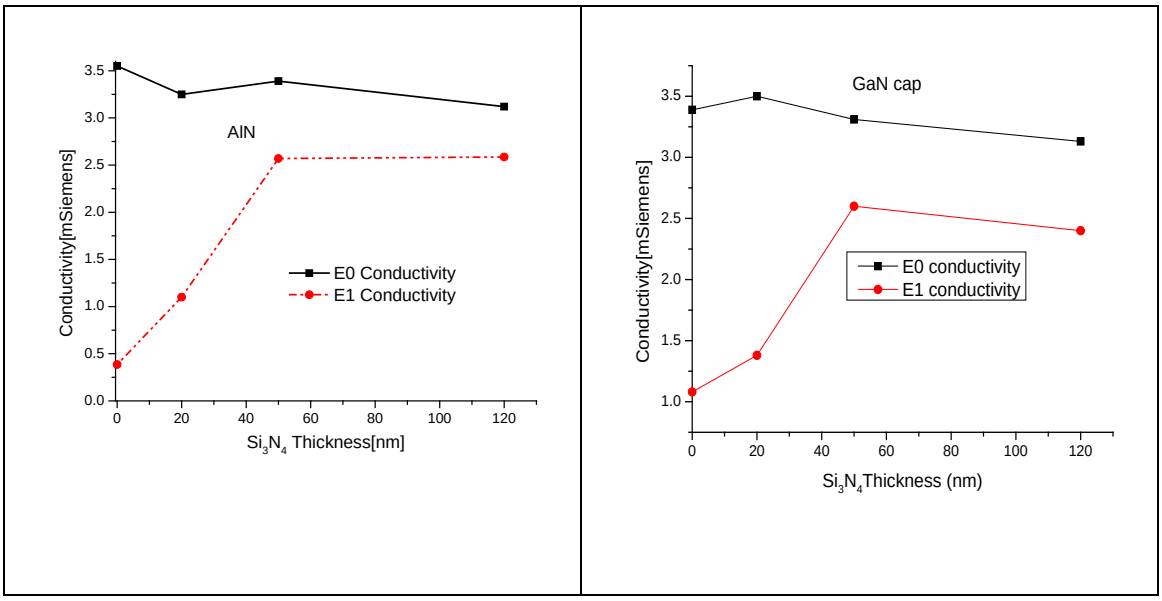

Figure 5.23. Comparison of 300-K conductivity pre- (E0) and post- (E1) 1-MeV irradiation on AlN (left) and GaN (right) cap structures.

If the mobility is being affected, then induced acceptors (and subsequent scattering centers) are scattering the electrons and reducing the mobility contribution to the conductivity. High mobility always dominates, until phonons (at higher temperature) kick in, and mobility goes down. As it can be concluded with the corresponding mobility in Figure 5.1, the irradiation is producing scattering centers. These centers would result in the capture a hole and electron, indicating Si_3N_4 is non-radiative. The interface is the same regardless of the thickness of the silicon nitride, and will still have dangling bonds. The thicker the Si_3N_4, the more strained are the underlying layers (Hu et al, 2007). This strain translates into a difference in the induced field responsible for the 2DEG density.

5.2.6. Additional Effects of Silicon Nitride Passivation

For both structures in Figures 5.1 and 5.23, Si_3N_4 is not a significant effect pre-irradiation, but after irradiation, there is a significant improvement in mobility once there

is 50 nm or more of the passivation layer. There is a saturation point for benefits of additional thickness of passivation, as there is little improvement between 50 and 120 nm of passivation thickness. If Si_3N_4 is the source of a more positive field, then charge balance as shown in equations 5.6 through 5.12 assures more electrons will transfer through to the 2DEG. Also, with increased thickness of a passivation layer comes increased tensile stress and carrier density. A positive surface charge at the Si_3N_4/AlGaN interface would have a field effect, resulting in more transfer of electrons from donor-like surface states into the empty states that are lower in energy. When surface traps are passivated by Si_3N_4, it appears that more electrons are able to transfer to 2DEG.

The mobility is determined by scattering mechanisms as shown in section 5.2.2. Thus, it can be deduced that adding Si_3N_4 will bring additional electrons and scattering centers, thereby reducing the mobility. The charge at the AlGaN/GaN interface is due to polarization charges, either positive or negative, as is the charge at the Si_3N_4/AlGaN interface. With the resulting polarized atoms, there is higher charge on one side, and electrons are drawn because of polarized charge. So the changing measurement resulting from the varying thickness of Si_3N_4 could be attributed to either increasing or decreasing the electrons because of its presence. If Si_3N_4 is positively charged as indicated by Meyer (Meyer, 2008), then increasing amounts of Si_3N_4 when the layer is made thicker, should result in a higher net positive charge. With the changed charge balance ratios, the effect on the device would be to attract more electrons into the 2DEG. This then results in the Hall carrier density increase. Equation 2.1 (Ch. 2) can be written as:

$$\sigma_{pz,AlGaN} + -\sigma_{pz,\,AlGaN} + {}^{+}\sigma_{AlGaN} + \sigma_{Buffer} + \sigma_{\,surface} + -\sigma_{\,AlGaN} + {}^{+}\sigma_{AlN} + \sigma_{pz,\,AlN} + -\sigma_{pz,AlN} = q\, n_{s,AlN} \quad (5.6)$$

The polarization charge vectors act in the same direction for the AlGaN and AlN, so there will be an increase in the 2DEG sheet charge density. For the GaN cap, we have:

$$\sigma_{pz,AlGaN} + -\sigma_{pz,\ AlGaN} + {}^{+}\sigma_{AlGaN} + \sigma_{Buffer} + \sigma_{\ surface} + -\sigma_{\ AlGaN} + {}^{-}\sigma_{Cap} + \sigma_{pz,\ Cap} + -\sigma_{pz,Cap} = q\ n_{s,Cap} \quad (5.7)$$

The polarization charge vectors at the GaN/AlGaN interface, ${}^{-}\sigma_{Cap}$, are anti-parallel or in opposite directions. The last two terms on the left hand side of the equation are zero, so that net charge for the 2DEG density is reduced.

To account for the addition of Si_3N_4 in the AlN structure, let the left hand side of Equation 5.6 for the AlN structure be called "X", so it can be written:

$$X + \sigma_{pz,Si3N4} + -\sigma_{pz,\ Si3N4} + {}^{+}\sigma_{Si3N4} = q\ n_{s,AlN,P} \quad (5.8)$$

Since silicon nitride is amorphous and has no polarization charges, the equation will reduce to:

$$X + {}^{+}\sigma_{Si3N4} = q\ n_{s,AlN,P} \quad (5.9)$$

Assigning a value of "Y" to the left hand side of equation 5.7 and now accounting for the extra layer of Si_3N_4 passivation, equation 5.7 becomes:

$$Y + {}^{+}\sigma_{Si3N4} = q\ n_{s,Cap,P} \quad (5.10)$$

The results throughout this chapter will show that the sheet-carrier density increases with Si_3N_4 passivation layer thickness, as in equations 5.9 and 5.10. AlN adds to polarization charge, and changes the band structure (Figure 2.10a versus Figure 2.10b). Since it is the net charge at the AlGaN/GaN or AlN/GaN interface that attracts the electrons into the 2DEG, increased positive charge from Si_3N_4 allows increased transfer of electrons into 2DEG and thus higher Hall carrier densities for structures with this interlayer are observed in the results throughout this section. The benefit of the GaN cap structure is it

serves as a surface charge control layer, reducing the effect of polarization charge; it screens the 2DEG from surface traps that lead to current collapse.

5.2.7. Temperature-Dependent Mobility and Carrier Density

Temperature-dependent studies provide useful information to indicate whether scattering potentials that have a 1/T dependence are present (see sections 5.2.1 and 5.2.2). From ~0 to 350 K, Figures 5.24 and 5.25 show that the relationship is very similar for both structures for the unpassivated change in mobility with 1-MeV electron irradiation. The mobility for both structures can be correlated to their respective carrier densities, to be shown next. The greater the carrier density the more scattering and a lower mobility results. For both structures, the 50 to 120 nm passivation proves most beneficial post radiation in preserving mobility over the temperature range studied.

The structure with the AlN interlayer (see Figure 5.26) shows a higher carrier density pre-irradiation than the structure with the GaN cap (Figure 5.27). The explanation was given in section 5.2.3. There is an alignment of the AlN and AlGaN polarization vectors, resulting in increased σ_0 at the 2DEG interface such that the carrier density is increased (Klein et al, 1986). This leads to the radiation-induced changes in carrier density verified also in the charge balance relationships.

For the post-radiation charge balance for both structures, the radiation affected both the sheet carrier density and mobility. The specific charges contributing to the2DEG that are affected by radiation from equations 5.6 and 5.7 are:

$$^{+}\sigma_{AlGaN} + \sigma_{Buffer} + \sigma_{surface} + -\sigma_{AlGaN} \qquad (5.11)$$

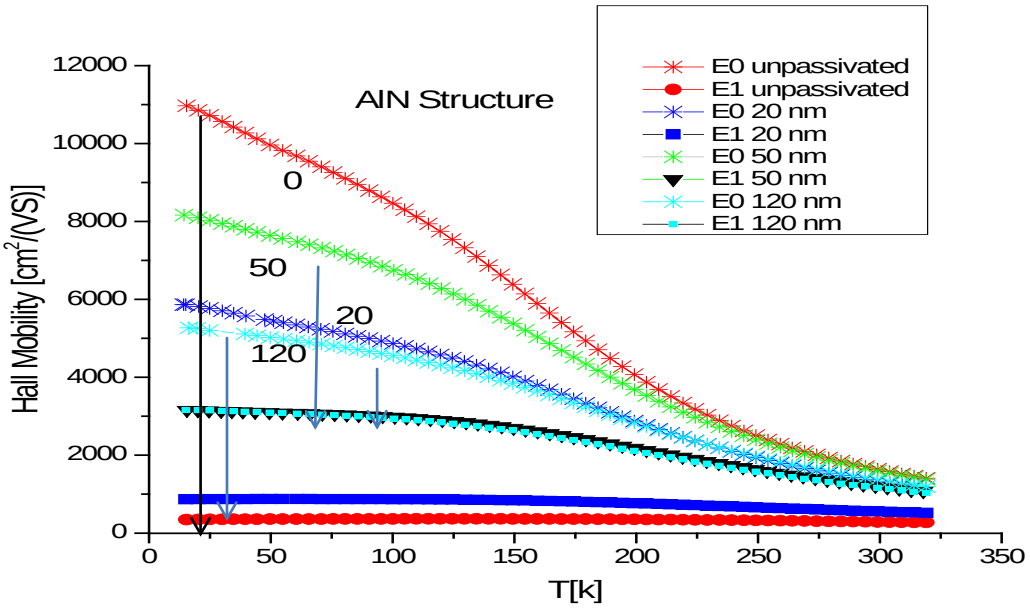

Figure 5.24. Temperature-dependent mobility as a function of Si_3N_4 thickness for AlGaN/AlN/GaN structure before (E0) and after (E1) 1-MeV electron irradiation.

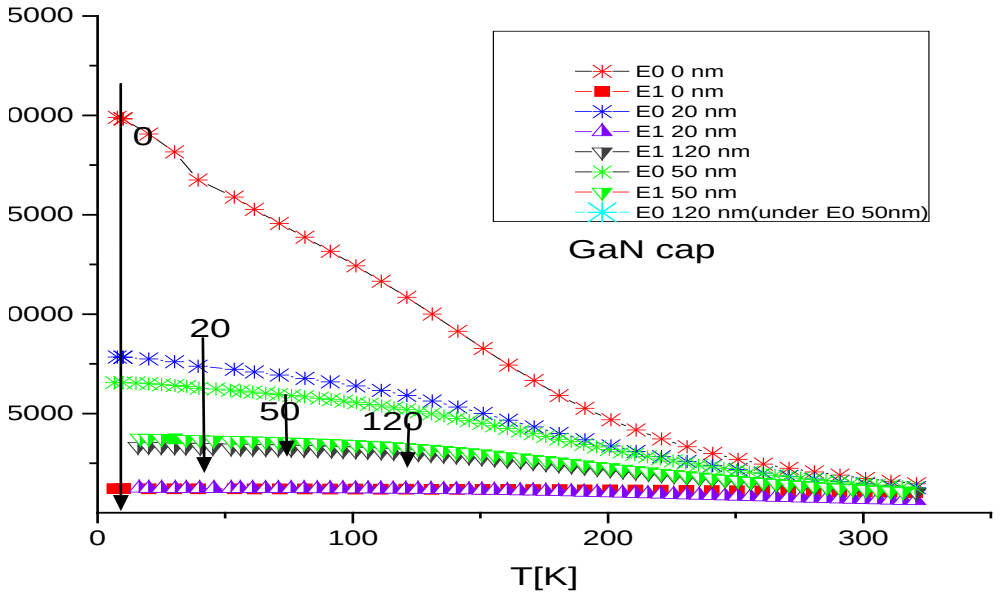

Figure 5.25. Temperature-dependent mobility as a function of Si_3N_4 thickness for GaN/AlGaN/GaN before (E0) and after (E1) 1-MeV electron irradiation.

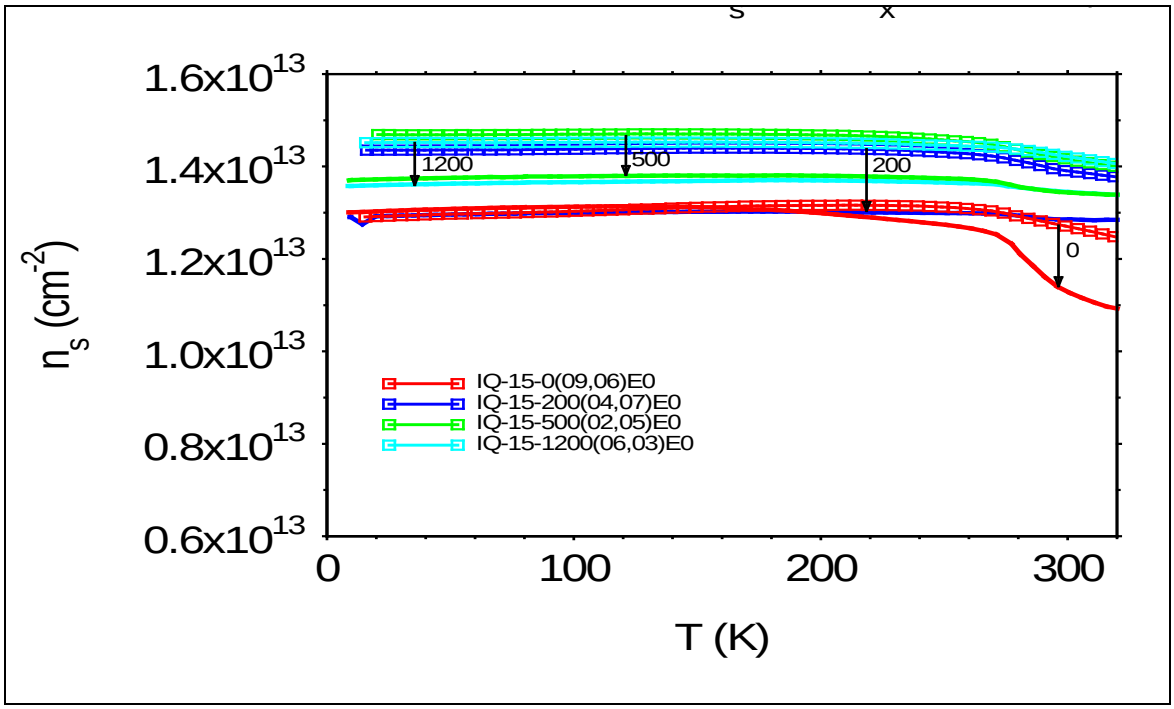

Figure 5.26. Temperature-dependent carrier density for AlGaN/AlN/GaN shows a higher carrier density than the GaN cap structure; there is little change in the pre- and post-radiation unpassivated carrier density (red), until room temperature.

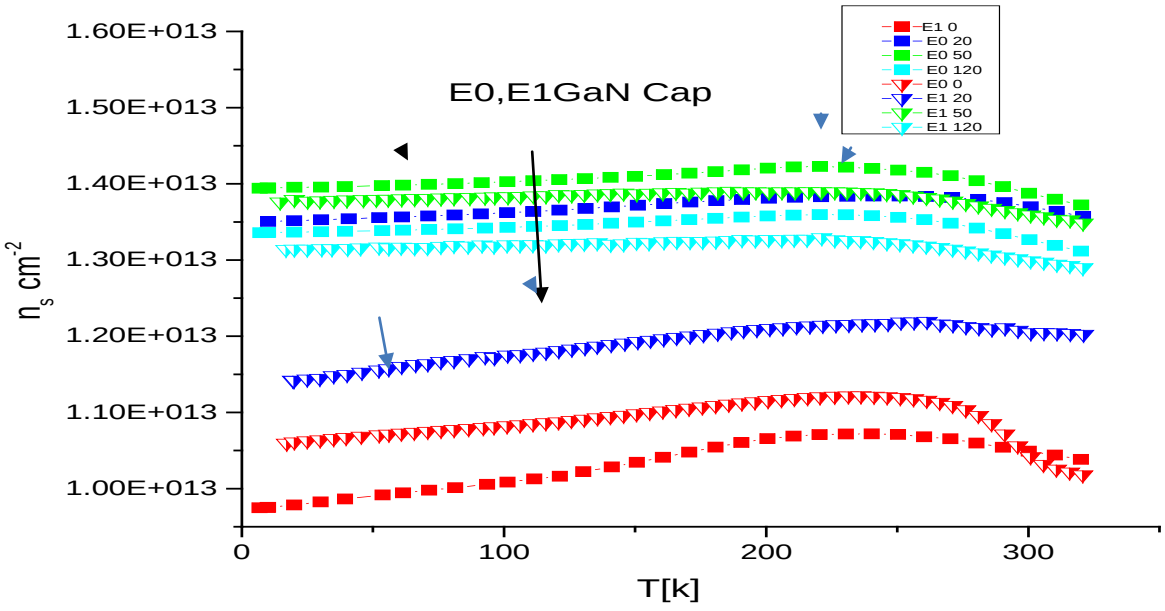

Figure 5.27. Temperature-dependent carrier densities for GaN/AlGaN/GaN show the unpassivated carrier density does change pre- and post-radiation, but is opposite the passivated samples with an increase in carriers post irradiation, until room temperature when the effect is slightly reversed.

Since the 1-MeV electron irradiation creates acceptor-type charges in the AlGaN, then the $-\sigma_{AlGaN}$ changes will be more dominate and contribute to the charge balance by reducing the net total charge. Additionally, although the GaN buffer does not significantly contribute, it is also changed by the radiation. If there is some ionization of the surface charges, then the above term for post radiation can be written as

$$^{+}\sigma_{AlGaN,E1} + \sigma_{Buffer,E1} + \sigma_{surface,E1} + -\sigma_{AlGaN,E1} = \Delta\sigma_{AlN,E1} \quad (5.12)$$

The post irradiation irradiated charge balance equation for a passivated AlN structure given in equation 5.9 can then be written as:

$$q\, n_{s,AlN} - \Delta\sigma_{AlN,E1} = q\, n_{s,AlN,P,E1} \quad (5.13)$$

Using equation 5.10 for the GaN cap structure, the post-radiation passivated sheet carrier density can be expressed as:

$$q\, n_{s,Cap} - \Delta\sigma_{Cap,E1} = q\, n_{s,Cap,P,E1} \quad (5.14)$$

The addition of the passivation layer is observed to reduce the mobility. Referring back to equation 5.1, the the addition of Si_3N_4 will introduce more carrier-carrier scattering, and the equation will change as follows:

$$\mu_c = e\langle\tau_m\rangle/m^*, \text{ and } \tau^{-1} = \tau^{-1}_{ac} + \tau^{-1}_{pe} + \tau^{-1}_{po} + \tau^{-1}_{ii} + \tau^{-1}_{dis} + \boldsymbol{\tau^{-1}_{c\text{-}c,\,P}} \quad (5.15)$$

For the carrier mobility given in equation 5.1, the 1-MeV electrons cause ionization and displacement damage. The mobility as a function of scattering relaxation after irradiation can be written with the addition of three extra terms, shown in bold face type in the following equation.

$$\mu_c = e\langle\tau_m\rangle/m^*, \text{ and } \tau^{-1} = \tau^{-1}_{ac} + \tau^{-1}_{pe} + \tau^{-1}_{po} + \tau^{-1}_{ii} + \boldsymbol{\tau^{-1}_{ii,E1}} + \tau^{-1}_{dis} + \boldsymbol{\tau^{-1}_{dis,E1}} + \boldsymbol{\tau^{-1}_{c\text{-}c,E1}} \quad (5.16)$$

Thereby, the post irradiation mobility is reduced. The last term adds the additional Si_3N_4 carrier–carrier scattering and radiation-induced acceptor scattering. More analysis along with a model will be presented in Chapter 7.

5.3. Photoluminescence Measurements for Spatial Localization of Defects

Chapter 2 gave the details of how a PL emission created as a result of incident light from a laser can qualitatively identify traps and impurities in semiconductors by its energy position. Traps in AlGaN/GaN lead to degradation in device performance, such as DC to RF dispersion (Kalavagunta, 2009; Hu et al, 2007), gate leakage, and current collapse. Traps change transport properties which include degraded mobility, carrier density and conductivity. Traps and defects can be in the bulk, surface or interfaces. They can be intrinsic or extrinsic. If they are shallow donors, they can be compensated for impurities such as oxygen or silicon impurities (Kalavagunta, 2009).

Intrinsic traps can be due to lattice mismatching or threading dislocations created in the growth process. Figure 5.28 shows lattice dislocations (left side) and point defects (right side). Additionally, there are positively charged surface donor traps that result from dangling bonds. Table 5.3 summarizes the traps in AlGaN/GaN along with their respective energies (Klein et al, 1986). A discussion follows on the Yellow line (YL) trap and Blue line (BL) below, and is shown in Figure 5.29, using the pre and post radiation deep center PL spectra of the samples in this study. This is followed by showing the GaN PL signatures seen in samples in this research. How the PL varies with Si_3N_4 variation prior to irradiation will be shown and then the post-radiation changes to the PL spectra will be reported.

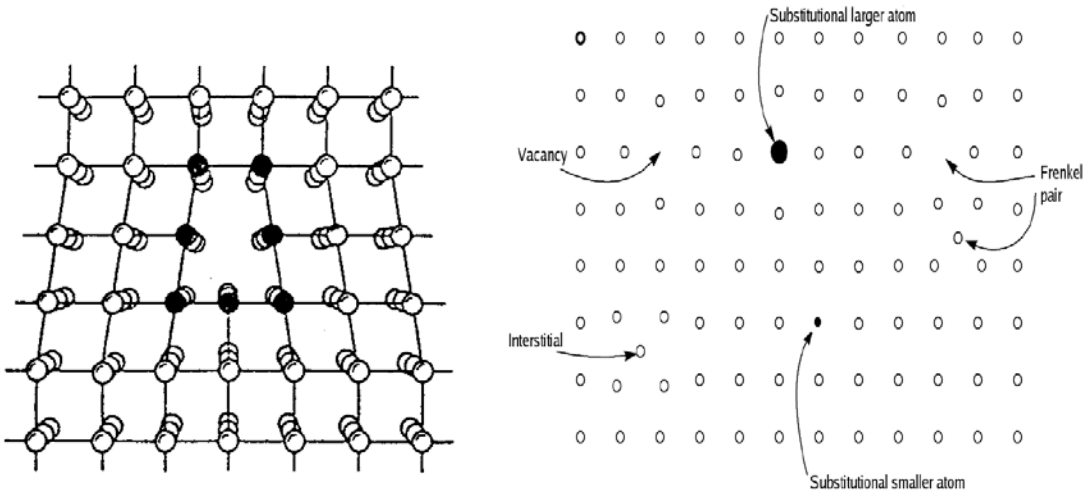

Figure 5.28. Volumetric dislocation on the left and a point defect on the right

Table 5.3. Trap location summary (CB = conduction band).

General description	Distance from CB	Reference
Deep level	1.8 eV and 2.85 eV	Klein et al, 1986
Lattice dislocation	0.5-0.6 eV	Polyakov et al, 2008
Nitrogen interstitials/Gallium vacancies	1.0 eV	Polyakov et al, 2008
Nitrogen vacancy	0.18-0.27 eV	Cho et.al, 2001; Fang et al, 2009; Polenta et al, 2009; Look et al, 2005
Nitrogen antisite	0.5 -0.6 eV	Cho et.al, 2001; Polenta et al, 2009;
YL/acceptor defect/Ga vacancy	2.2 eV	Reshchikov and Markoc, 2005; Calleja et al, 1997
BL	2.8 eV	Look, 2006
(Via DLTS)	0.58 and 1.1 eV	Ogino and Aoki, 1980
AlGaN/Nitrogen vacancy	0.85 eV	Fang et al, 2009
AlGaN (irradiation induced)	0.33 eV, 0.38 eV	Hogsed et al, 2005

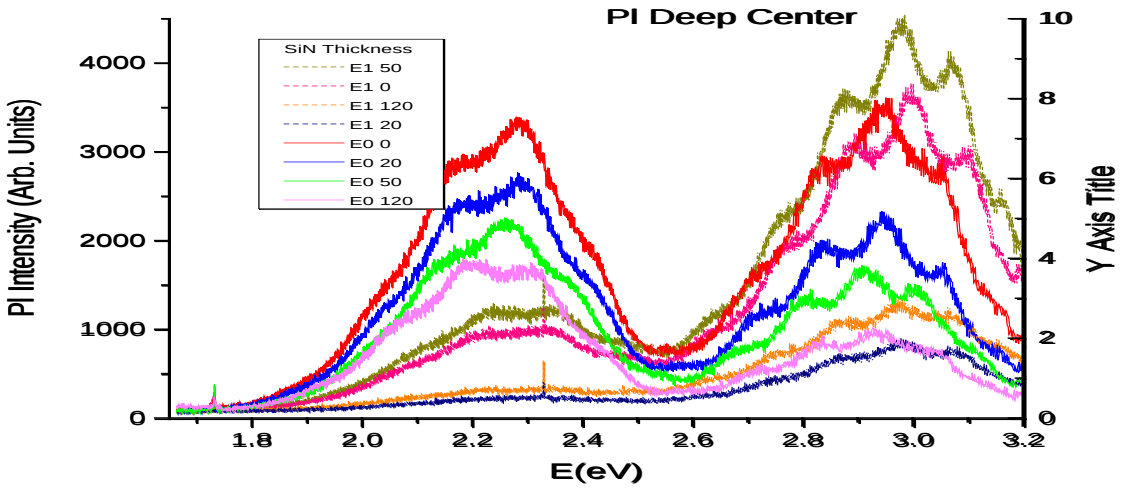

Figure 5.29. Radiation producing centers change the PL peak intensities indicating change in acceptor defect population leading to the 2.2 eV deep center PL.

5.3.1. Initial Look at Effect of Si_3N_4 Thickness on PL from Deep Centers

The yellow line (YL), as shown in Figure 5.29 in the deep center PL peaks near 2.2 eV and is due to a transition with a shallow acceptor level (Colton, 2000) believed to be V_{GA}. The acceptor trap level may lie along an edge dislocation line at the end of an atomic plane (Meyer, 2008). Cathodoluminescent studies (Polenta et al, 2000) further describe these centers as edge dislocation lines. The yellow emission can also be defined as occurring when the electron wavefunctions of adjacent trap sites overlap (Meyer, 2008). For the effect of the Si_3N_4 layer thickness, there is simply a linear attenuation of the PL light with the passivation layer thickness before irradiation. Post irradiation, the thicker or more dense the layer, more non-radiative centers are created that can result in the capture of an electron or hole at 3.0 eV.

5.3.2. GaN PL Signatures and Defect Trap Locations

In the PL spectrum shown in Figure 5.30, the classic peaks associated with GaN are seen. The main peak at 3.463 eV is the result of the collapse of an exciton bound to a DX center. As described previously in Chapter 2, the exciton is an electron- hole pair, bound by the Coulomb interaction. They seek out and orbit around a neutral donor located below the conduction band at E_d. Because it is metastable, it collapses and thus we have a radiative recombination peak. This peak is from the GaN buffer and is representative of the bulk material. The collapsed exciton releases its energy as a radiative emission. Two additional side bands, separated from the main PL peak by the multiples of the LO phonon energy of ~ 90 meV are also seen in Figure 5.30 due to momentum-conserving recombinations.

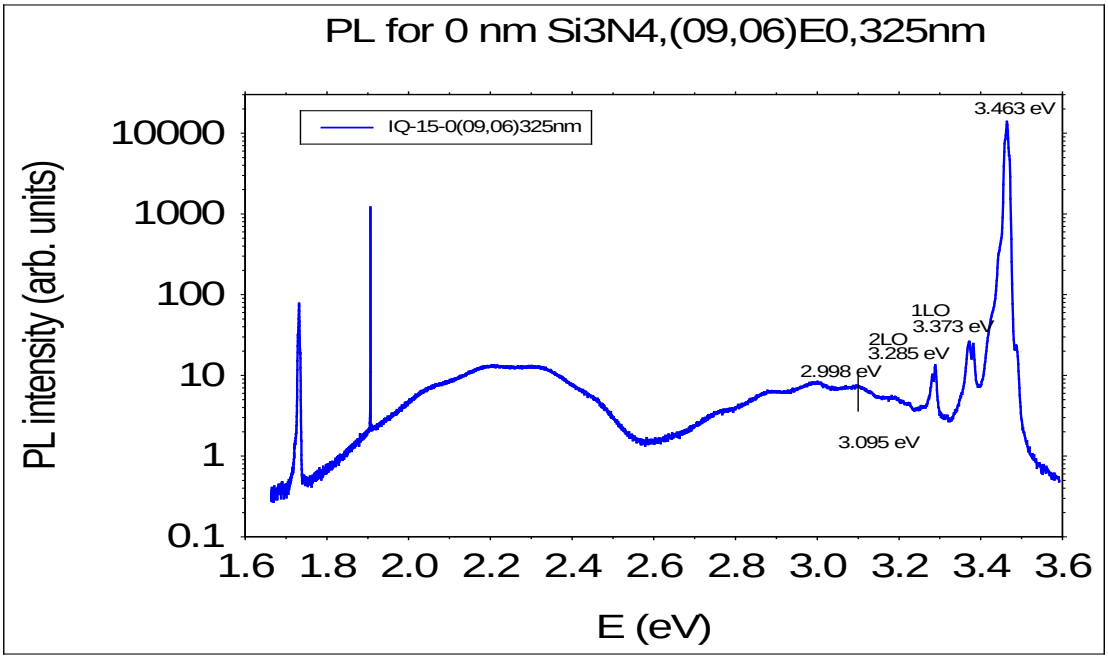

Figure 5.30. The unpassivated, pre–irradiation spectrum excited using a HeCd laser. There is a 2nd order transition occurring at 1.7 eV and is due to the use of a diffraction grating, $n*\lambda = 2\ d \sin\theta$. The 2nd order of the laser line appears at 1.9 eV.

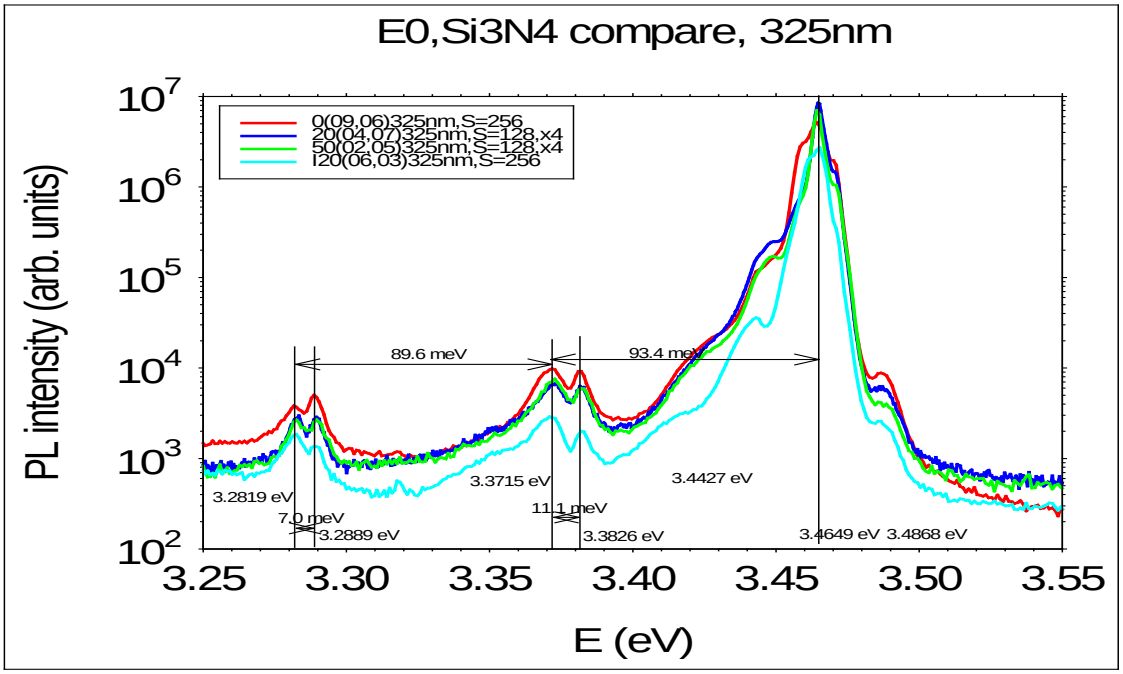

Figure 5.31. PL spectra from 3.25 to 3.50 eV, showing the dominant D^oX peak and the non-radiatively produced phonon replica peaks. Note vertical log scale.

Figure 5.31 shows the PL observed in the range from 3.25 to 3.55 eV, in the near band edge vicinity. These spectra are for all the thicknesses of Si_3N_4 and are shown on a vertical log scale. Subsequent figures will zoom in closer to show the variation of peak height with Si_3N_4 passivation thickness. A free exciton can be observed at 3.478 eV. Its binding energy is 0.025 eV. When this binding energy is added to 3.478 eV, one obtains 3.503 eV, the result is what the band gap would be.

For the observed dominant peak above, the light emitted would need to be 3.465-0.093=3.372 eV, which is where the first phonon replica line is. The phonon replica here is part of a doublet, so it is related to a small shoulder the same distance away. The second set of phonon peaks are about 0.093 eV away from the first set. All these peaks show that conservation of energy is maintained when the exciton annihilates.

Two main neutral donor bound exciton (D^0 X) peaks were observed: Oxygen donors give rise to PL at 3.46 eV and Si donors give rise to PL at 3.466 eV. Again, it can be assumed we are looking at GaN with the PL light, because AlGaN so thin (~18 nm). The oxygen-related BE are likely a result of processing, from oxygen in the growth and annealing environment.

5.3.3. Effect of Variation of Si_3N_4 Passivation on Deep Center and Near Band Edge

Figure 5.32 shows that the PL light passing through the samples is attenuated linearly. A model for the transitions that cause the YL and BL emission is shown further below. There is a yellow band (YL) at 2.2 eV for n-type GaN from a shallow donor to a deep acceptor. The YL is associated with oxygen and appears at 2.2 eV. The blue band at 3.0 eV seen in semi-insulating material such as silicon carbide, which is the substrate for these samples, is most likely the source of Magnesium (Mg). The Mg (acceptor) on Gallium site is 200 meV. Mg can be complexed with Nitrogen vacancies.

Figure 5.33 presents the results of the pre-irradiation NBE PL measurements. The D^0 X from Oxygen in Figure 5.33 involves the collapse of an exciton attached to an isolated O_N. There is observed a shift in the main D^0 X peak occurring at 3.46539 eV due to the GaN being grown on a SiC substrate, as opposed to what is observed in unstrained GaN (Calleja et al, 1997).

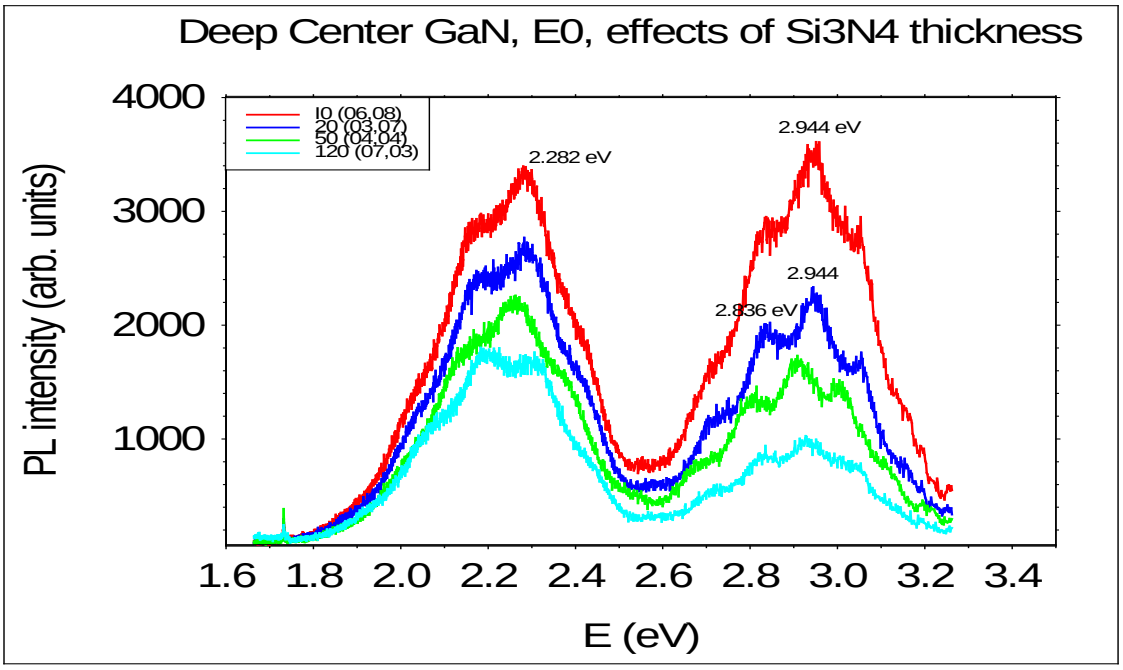

Figure 5.32. E0 Deep center PL with variation of Si_3N_4 thickness, showing the YL peak at 2.3 eV and the BL peak at 3.0 eV.

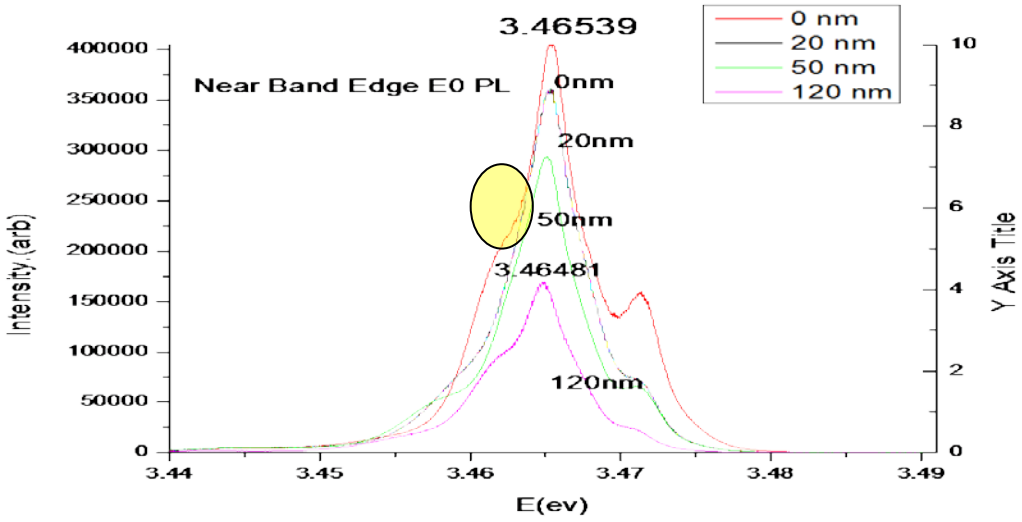

Figure 5.33. Near band edge showing a mono-atomic attenuation of the PL light with Si_3N_4 thickness.

The reason for the peak shift is GaN is wurtzite and the silicon carbide (SiC) substrate is hexagonal. The higher tensile strain when grown on SiC can be explained by the differences in lattice constants. The main peak in unstrained GaN is at 3.471 eV. GaN has lattice parameters of a=3.189 Å and c= 5.185 Å. SiC has lattice of a=3.07335 Å and c=10.053 Å, causing a strain shift and thus peak at 3.46539 eV for the unpassivated sample, and 3.46481 eV at 1200 Å Si_3N_4 thickness, due to compressive tensile strain. The peaks at 3.46 eV is substantially reduced by the 120 nm of Si_3N_4, but one observes the emergence of a peak at ~3.479 eV. Si_3N_4 has a lattice parameters a=7.596 Å and c=2.711 Å. While not studied extensively in this research, this strain plays a role in device performance (Reshchikov and Markoc, 2005).

Below is a plot of how the Si_3N_4 attenuates the pre-irradiation PL.

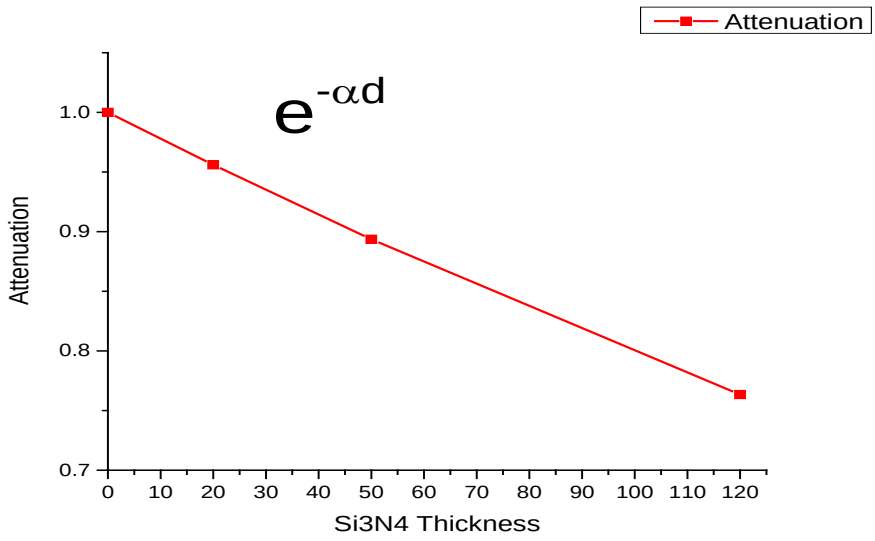

Figure 5.34. Linear attenuation of the PL light with increase in Si_3N_4 thickness.

The variation with Si_3N_4 thickness-absorption depths were calculated, Figure 5.34, showing absorption falls with (Si_3N_4 thickness) off as $1/e^{\alpha d}$. So for 120 nm, depth penetration is approximately the Si_3N_4 thickness. Using $I/I_0 = 1/e^{\alpha d}$, at a thickness of 120nm, 76% of the light is getting through. There are other explanations for the decrease in intensity of the main PL peak due to Si_3N_4. As shown, based on the calculation for attenuation, as the 325-nm laser passes through thicker material, there is less light reaching the GaN and subsequently a lower PL intensity. Some of the light is also reflected at interfaces. The observed intensity differences are not just due to the attenuation of the light. PL is based on radiative recombination, so non-radiative centers could also cause non-radiative recombination. For Si_3N_4 and AlGaN, typical surface states are non-radiative centers.

Additionally, since the PL data show the Si_3N_4 passivated samples have lower energy peaks, this possibly means there is tensile strain. It looks like with increasing Si_3N_4 thickness, red shifts in energies are occurring. The thicker the Si_3N_4, the more tensile strain on the GaN (Colton, 2000). Some attribute the increase in strain to an increase in sheet charge density (Colton, 2000), in agreement with this study which is showing higher electron sheet charge density with increasing Si_3N_4 passivation thickness.

Important in trap analysis and assessing device degradation are identifying donors and acceptor density changes. In AlGaN/GaN, there are DX centers and other donors that give rise to levels 0.2 to 0.3 eV below the conduction band. This is not so deep that it can't transfer over to the GaN. It doesn't have to be a classical DX center, as described in Chapter 2. As the source of un-intentional doping that makes the GaN n-type, if there are

not enough of those electrons to transfer over to the 2DEG to give 10^{13} cm^{-2}, then they have to come from somewhere else, the surface being that other possibility.

5.3.4. Effect of 1-MeV Electron Irradiation and Si_3N_4 Passivation

The previously described peak at 3.4649 is shown in Figures 5.35 and 5.36 and is the result of a different process than those in the deep center for the YL and BL. The YL is associated with gallium vacancies, and the BL is associated with nitrogen vacancies. The near band edge peak results from an exciton bound to a D^0X collapse. Below is shown the post radiation (E1) comparison of all the Si_3N_4 thicknesses for NBE and deep center PL.

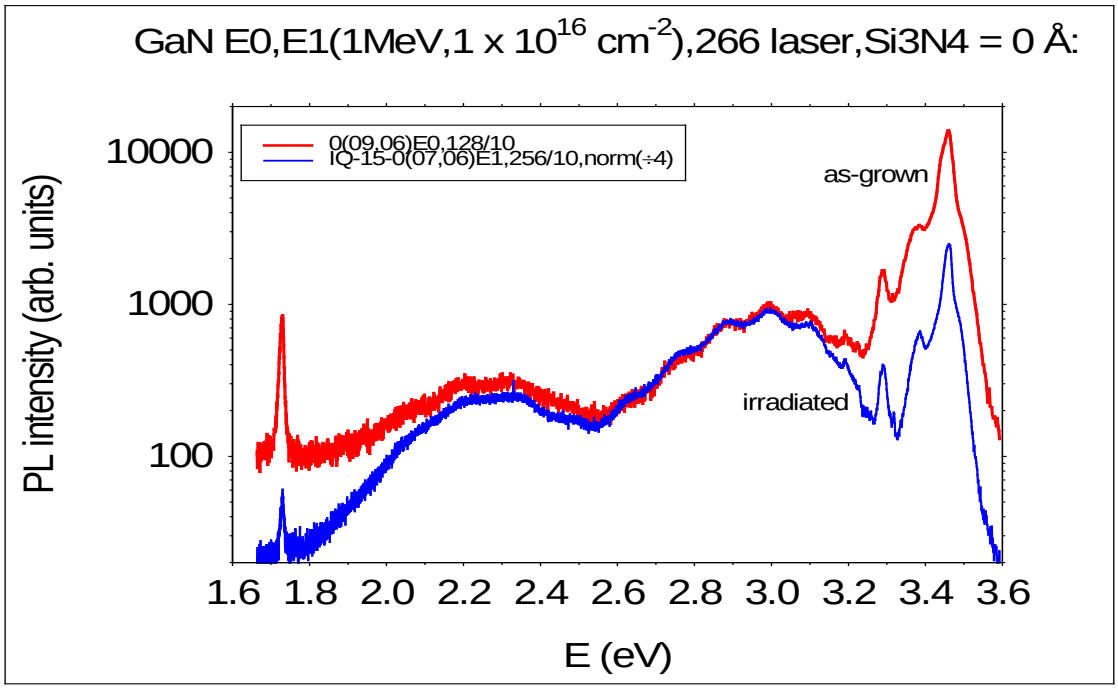

Figure 5.35. PL from unpassivated samples after 1-MeV irradiation. Deep centers are not affected as much as shallow centers by irradiation.

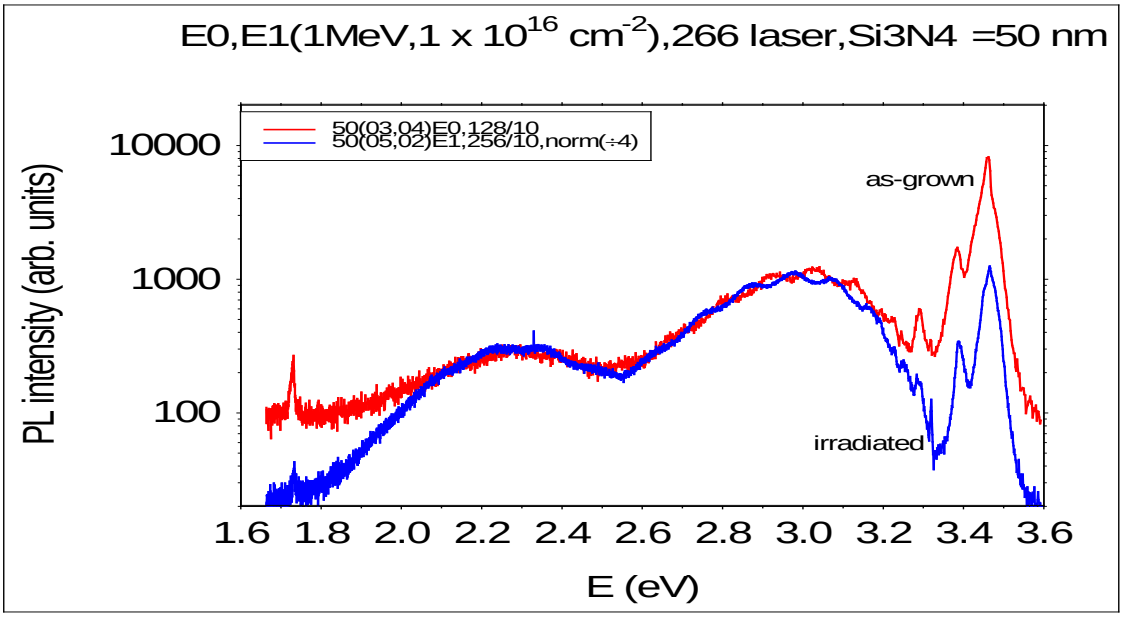

Figure 5.36. PL from sample with 50-nm passivation layer after 1-MeV irradiation. Deep centers are not affected as much as shallow centers by irradiation.

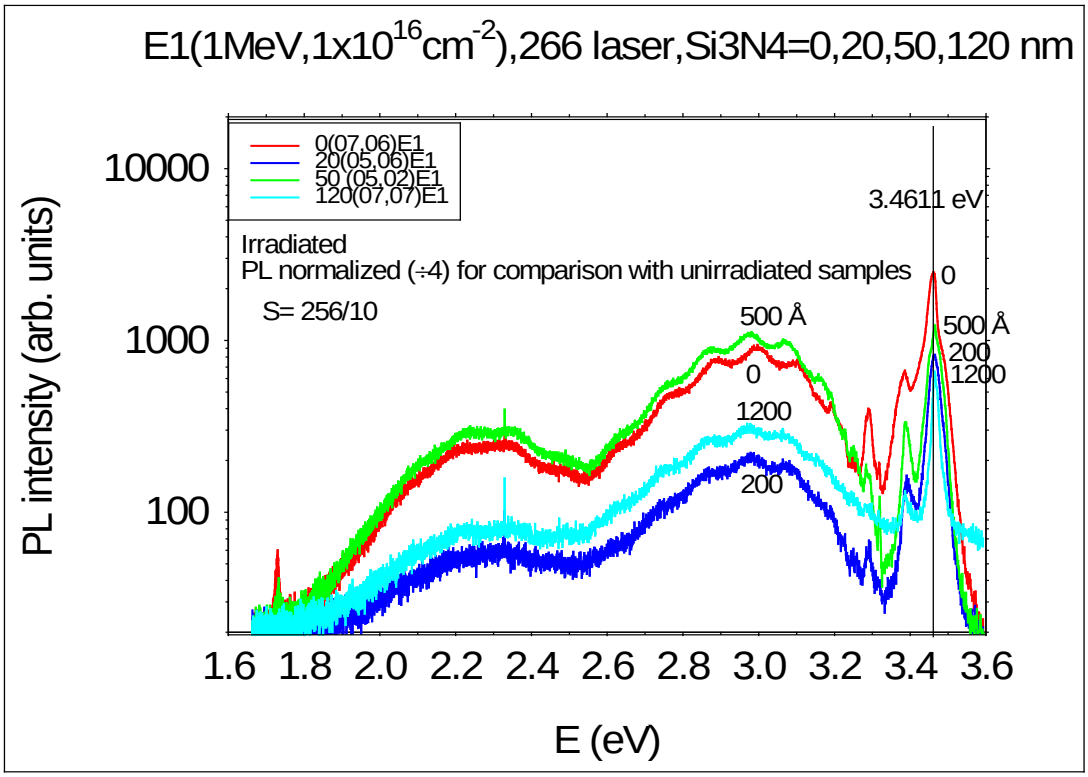

Figure 5.37. PL taken after 1-MeV irradiation showing deep center to NBE region.

Figures 5.35 and 5.36 compared the normalized pre- and post-irradiation (E0, E1) PL data for AlGaN/AlN/GaN for an unpassivated and 50-nm passivated structure. In Figure 5.37, the normalized irradiated samples for 0,20, 50 and 120 nm are compared. By comparison with the data shown in Figure 5.31, it is clear that the order of intensities of the peaks have changed. Before the irradiation, the peak intensities of both the YL (2.2 eV) and BL (3.0 eV) changed monotonically with Si_3N4 thickness. The irradiation has changed the shallow donor and defect concentrations that produce the YL and BL transitions. This tells us what the radiation produced defects are. The change in Hall carrier densities, the defect production algorithms, and the DLTS in Chapter 6 should concur as to what the radiation has done. The post 1-MeV electron irradiated PL that includes the NBE region is shown in Figure 5.38. Notice that in addition to being degraded, the near band edge peaks are broadened by the irradiation, indicating possibly lattice displacement damage. The NBE degradation relative to the un-irradiated for the NBE is evident in Figures 5.34 and 5.35 for no passivation and 50-nm passivation. In Figure 5.38, there is a greater degree of peak degradation in the near band edge.

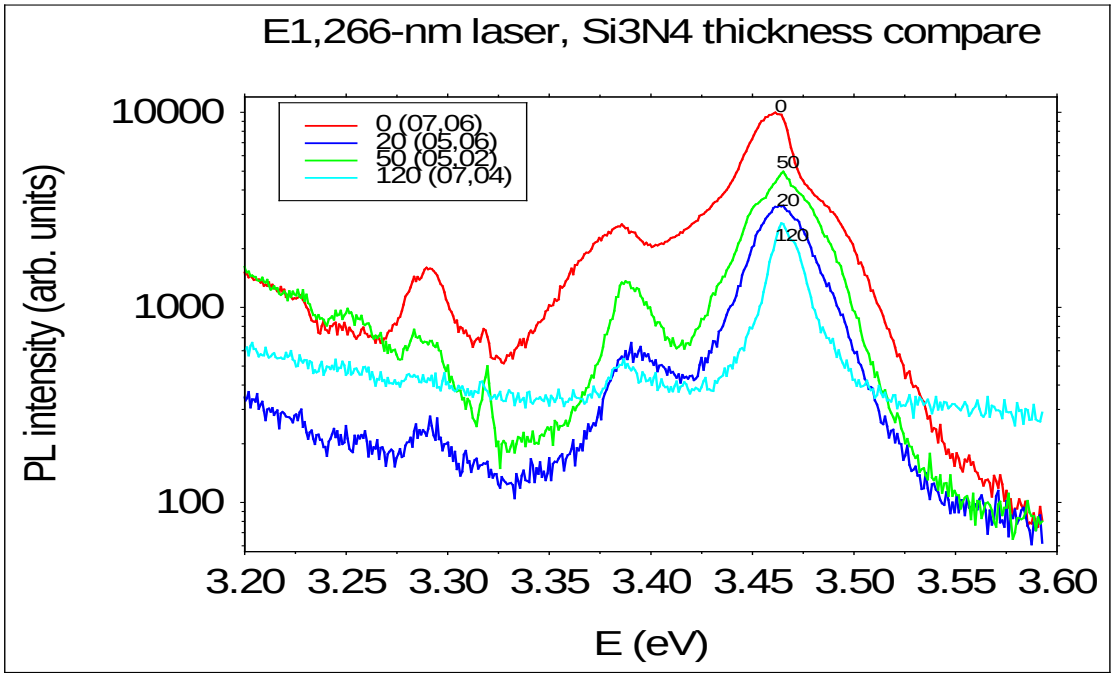

Figure 5.38. PL taken after 1-MeV irradiation for the emission region from 3.20 to 3.60 eV, which includes the near band edge.

Clearly in Figure 5.38, the electron irradiation is destroying the components of PL peak formation at the DX center peak, perhaps by ionizing the neutral donors that the excitons attach to. However, in the deep center, shown in Fig 5.39 below, the YL is degraded post-irradiation. The E_A for the 2.2 eV YL is attributed to V_{GA} .But the peak intensity for the 3.0 eV BL increases . Analytical data that will be shown in section 5.4 from defect production algorithms show V_N as the dominate defect produced throughout the structure. In Chapter 3, V_N was reported to be the main radiation induced defect. Radiation increases the V_{GA} production also, but perhaps the ratio of either O or Si that can cause the peak has been altered due to the radiation. The peaks are related to the energy of the donors or acceptors in the transitions. V_N is below the Fermi level and is

neutral. A model will be given in Chapter 7 that explains the observed PL changes and what that says about the traps, donors, acceptors and impurities in these samples.

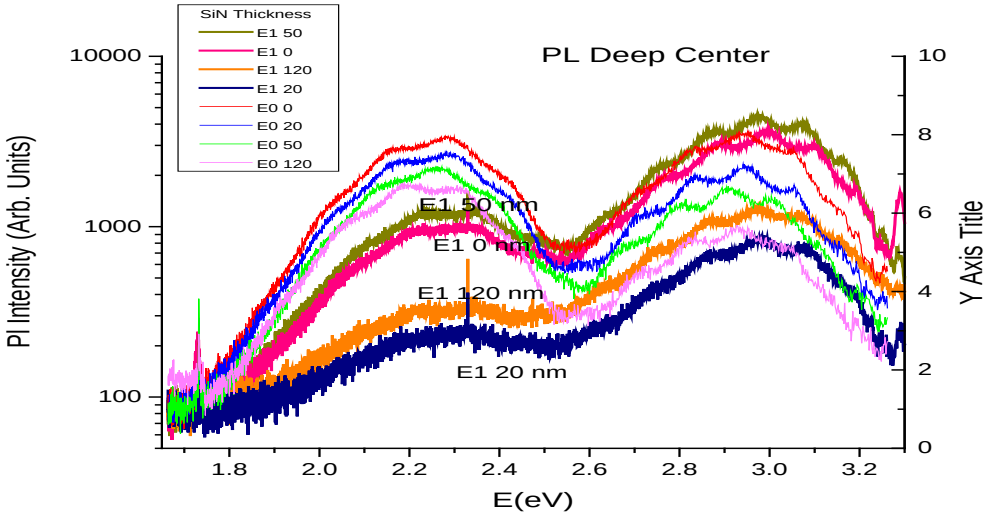

Figure 5.39. The pre- and post-1-MeV radiation deep center PL for the sample variation range. The top 4 curves for the YL at 2.2 eV are the pre-irradiation spectra and the bottom 4 curves are post irradiation (E1). For the BL~3.0eV, the order of the curves is changed, believed to be due to both more V_n being created and no reduction in the available Mg involved in the transition that forms the peak.

5.4. Radiation Effects: Analytical and Monte Carlo Models of Radiation Damage and Defect Production

Chapter 3 addressed basic radiation effects. Now some of the modelled radiation effects done on the structures in this research will be described and interrelated with the presented results. Analytical models using defect production algorithms modeled the rate of defect production and the distance travelled by the incident 1-MeV electrons as a function of distance. Bethe Bloche was used as the algorithm, with some modifications. However, these models did not incorporate stress, heating, or polarization effects.

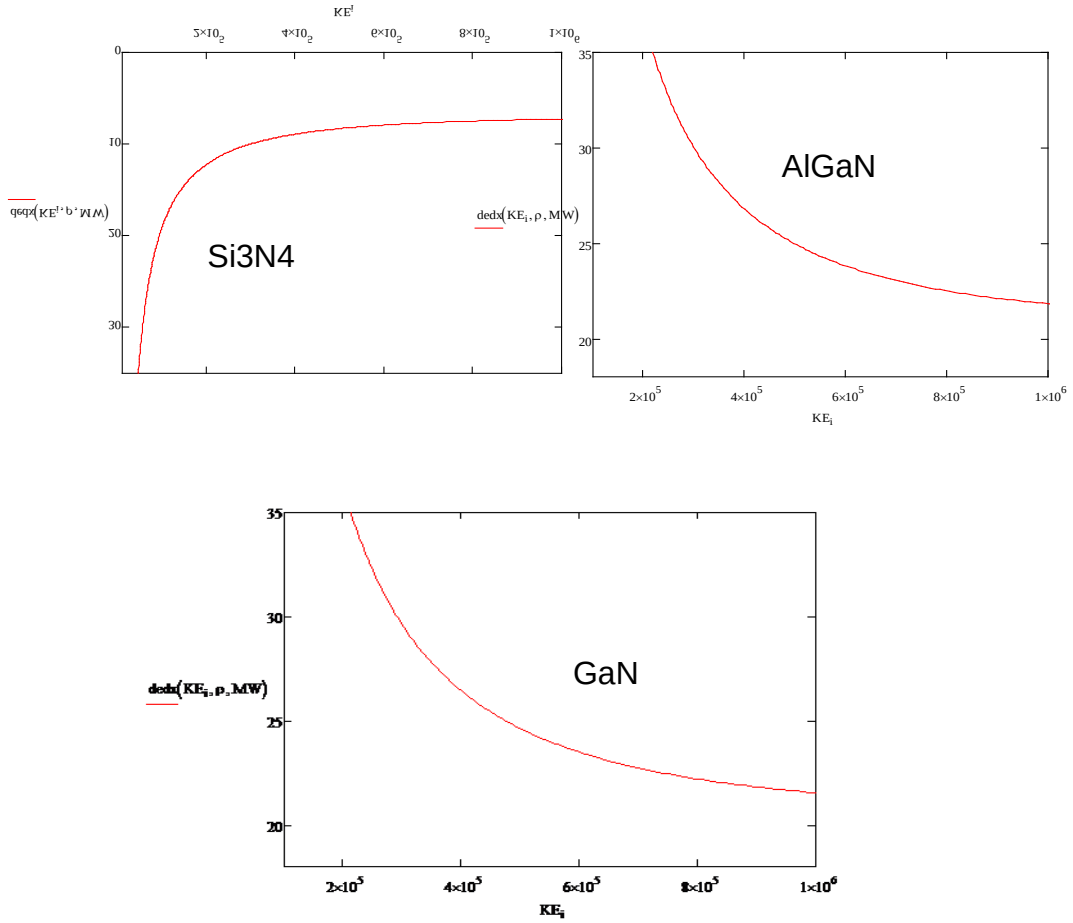

Figure 5.40. Modeled mean free path depth of 1-MeV electron through Si_3N_4 (left), through AlGaN (right), and through GaN (bottom) as a function of kinetic energy.

5.4.1. Modeled Defect Production Algorithm Results

The algorithm used for the results shown in the Figure 5.40, as well for the other results shown in this section, is adapted from the Mott-MecKelvey-Feshback algorithm,

which is based on the Bethe Bloche formula given in Chapter 3. It calculates the number of defects per layer produced by 1-MeV electron irradiation. The steps are given here to obtain the production rate of defects, which are shown in Table 3, and were evaluated as follows:

1. For each atom in each layer of AlGaN/GaN, the cross section σ (see equation 3.2 of Chapter 3) was computed by the kinetic energies (KE), displacement energies (E_d), atomic number (Z), and densities (Mc) per atom in interaction. The displacement energies were also discussed in Chapter 3 (section 3.1.3).

$$\sigma(KE, Ed, Z, Mc2) := \begin{cases} \gamma \leftarrow \dfrac{KE}{mc2} + 1 \\ \beta \leftarrow \sqrt{1 - \dfrac{1}{\gamma^2}} \\ \alpha \leftarrow \dfrac{Z}{137} \\ Em \leftarrow \dfrac{2 \cdot KE \cdot (KE + 2 \cdot mc2)}{Mc2} \\ b \leftarrow \dfrac{2 \cdot Z}{\beta^2} \cdot \dfrac{1.44}{5.11 \cdot 10^5} \\ X \leftarrow \dfrac{Em}{Ed} \\ \left[\dfrac{\pi \cdot b^2}{4} \cdot \left(1 - \beta^2\right) \cdot \left[X - 1 - \beta^2 \cdot \ln(X) + \pi \cdot \alpha \cdot \beta \cdot \left[2 \cdot \left(\sqrt{X} - 1\right) - \ln(X)\right]\right]\right] \text{ if } X \geq 1 \\ 0 \text{ otherwise} \end{cases}$$

To obtain, for example, for AlGaN;

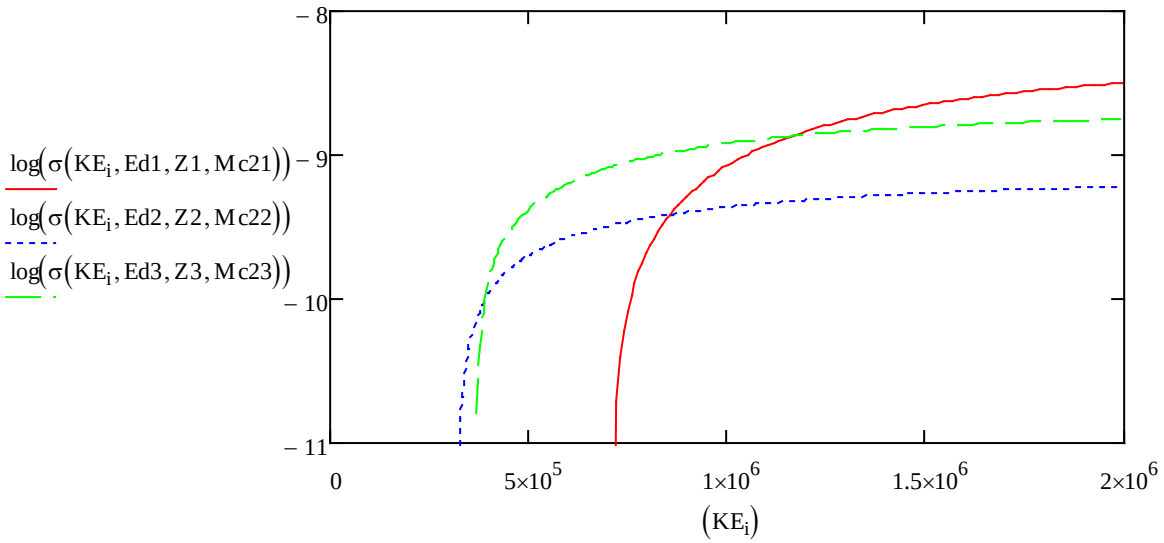

To obtain the stopping power, a modification of equation 3.3 was used, dE/dx:

$$\begin{aligned}
\text{dedx}(KE,\rho,MW) := \;& \gamma \leftarrow \frac{KE}{mc2} + 1 \\
& \beta \leftarrow \sqrt{1 - \frac{1}{\gamma^2}} \\
& \tau \leftarrow \frac{KE}{mc2} \\
& F2 \leftarrow -\ln\left(2\cdot\beta^2\right) + \frac{1}{2}\cdot\left[\ln\left[\tau^2\cdot(\tau+2)\right] - \left[1 + \left[\frac{2\cdot\tau+1}{(\tau+1)^2}\right]\right]\cdot\ln\left[2 + \frac{1}{(\tau+1)^2} + \frac{1}{8}\cdot\left(\frac{\tau}{1+\tau}\right)^2\right]\right] \\
& B01 \leftarrow Z1\cdot\left(\ln\left(\frac{2\cdot mc2\cdot 10^6\cdot\beta}{I0(Z1)}\right) + F2\right) \\
& B02 \leftarrow Z2\cdot\left(\ln\left(\frac{2\cdot mc2\cdot 10^6\cdot\beta}{I0(Z2)}\right) + F2\right) \\
& sdedx \leftarrow \frac{.307174}{\beta^2\cdot\frac{MW}{2}}\cdot\left(\frac{B01}{2} + \frac{B02}{2}\right) \quad \text{if} \quad KE \geq 0 \\
& 0 \quad \text{otherwise} \\
& \rho\cdot sdedx
\end{aligned}$$

And again for Nitrogen in AlGaN, the result was:

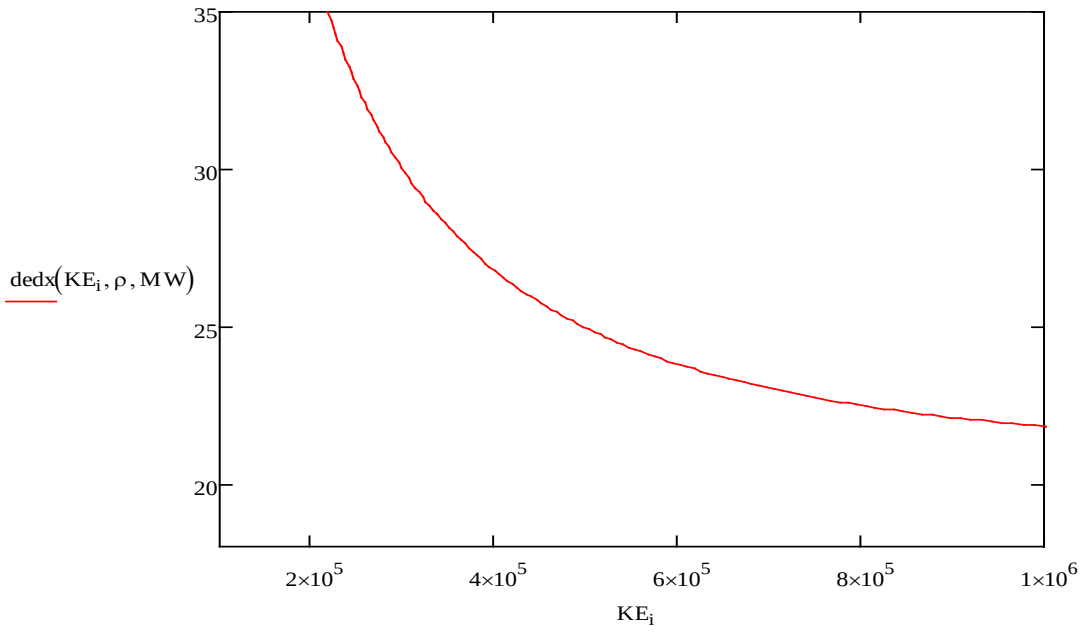

To obtain the kinetic energy as a function of depth and the log of the cross section as a function of depth, the mean free path λ was calculated resulting in:

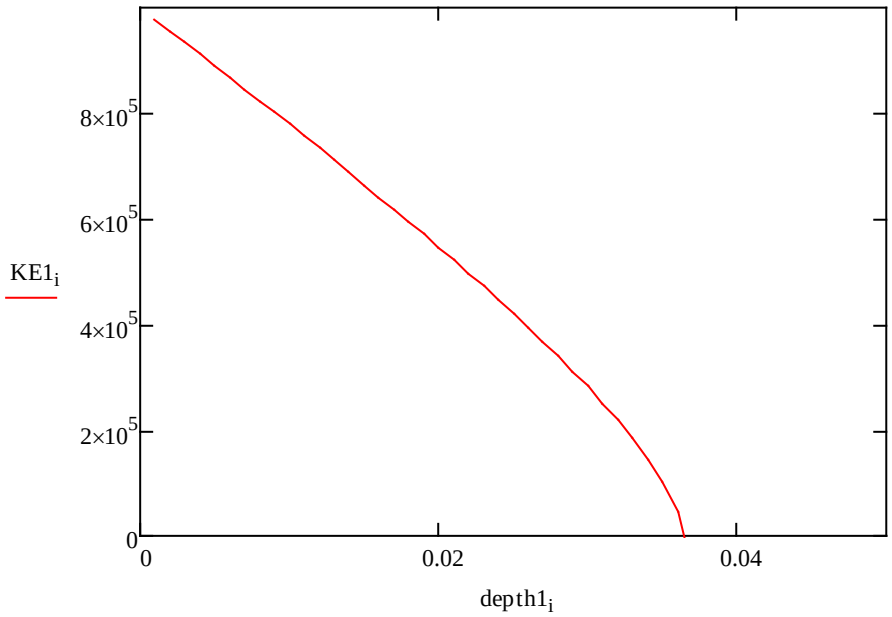

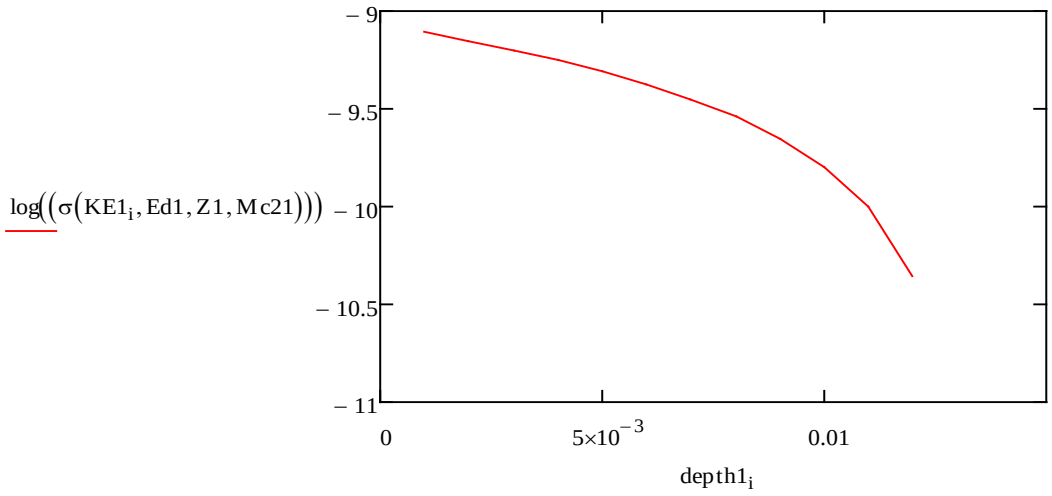

The final production rate of defects were calculated and tabulated below, using:

$$production1 := dosenm \cdot n1 \cdot \sigma\left(10^6, Ed1, Z1, Mc21\right)$$

Where dosenm is the radiation dose used for my samples and was 10^{16} cm^{-2} ,which was then converted to nm^{-2}; n1 is a programmatically obtained value and Ed1 is the displacement energy of the particular atom (for AlGaN there will be Ed1, Ed2 and Ed3), and Mc21 stands again for the density.

Table 5.4. Table is based on defect production algorithm model, showing that the highest production rate for damage is for lattice atoms gallium, nitrogen, aluminum and silicon.

						Effect of Si_3N_4		
	GaN/1700nm	GaN cap/2nm	AlGaN/18nm	AlGaN (W cap)/ 19.7nm	AlN/ 1 nm	Si_3N_4/20nm	Si_3N_4/50nm	Si_3N_4 / 120nm
Ga/nm^3	$15.77x10^8$	$18.55x10^5$	$2.15x10^7$	$2.36x10^7$	-	-	-	-
N/nm^3	$8.134x10^8$	$9.57x10^5$	$1.483x10^7$	$1.623x10^7$	-	$43.6\ x10^6$	$1090.13x10^6$	$2616.3x10^6$
Al/nm^3			$1.483x10^7$	$1.623x10^7$	-			
Si/nm^3	-	-	-	-	-	$46.12x10^7$	$1115.63x10^7$	$2766.3x10^7$

Table 5.4 summarizes the results for the number of defects produced by each atom in each layer that is affected by incident 1-MeV irradiation. The initial layer to encounter the incident electron from the beam will be AlGaN or Si_3N_4 (if passivated) and if it is the structure with the AlN interlayer. The initial layer will be the GaN cap or the Si_3N_4 layer above it (if passivated) for the GaN cap structure. The number of radiation induced defects, for example if we consider Nitrogen, can be correlated to the $N_I - V_n$ pair (the Frenkel pair). The evidence of radiation induced defects was shown in the previous PL data, the fitted Hall carrier density and mobility data, and will be further verified in the DLTS, C_g-V_g and I_g-V_g data. The next section will give a snapshot of the CASINO results, which show the damage based on the simulated interactions for primary, secondary and backscattered electrons. More analysis will be given and correlated to the defect analysis in this research in Chapter 7.

5.4.2 Location and Distribution of Damage: from CASINO

CASINO shows the majority of the damage for an unpassivated structure is in the AlGaN, the first layer encountered, and the incident electron loses energy with depth as shown in the defect product algorithm plot of de/dx in section 5.4.1. The unpassivated sample has a greater range for the hits as a function of depth. The 50-nm passivated sample has the smallest range for hits as a function of depth.

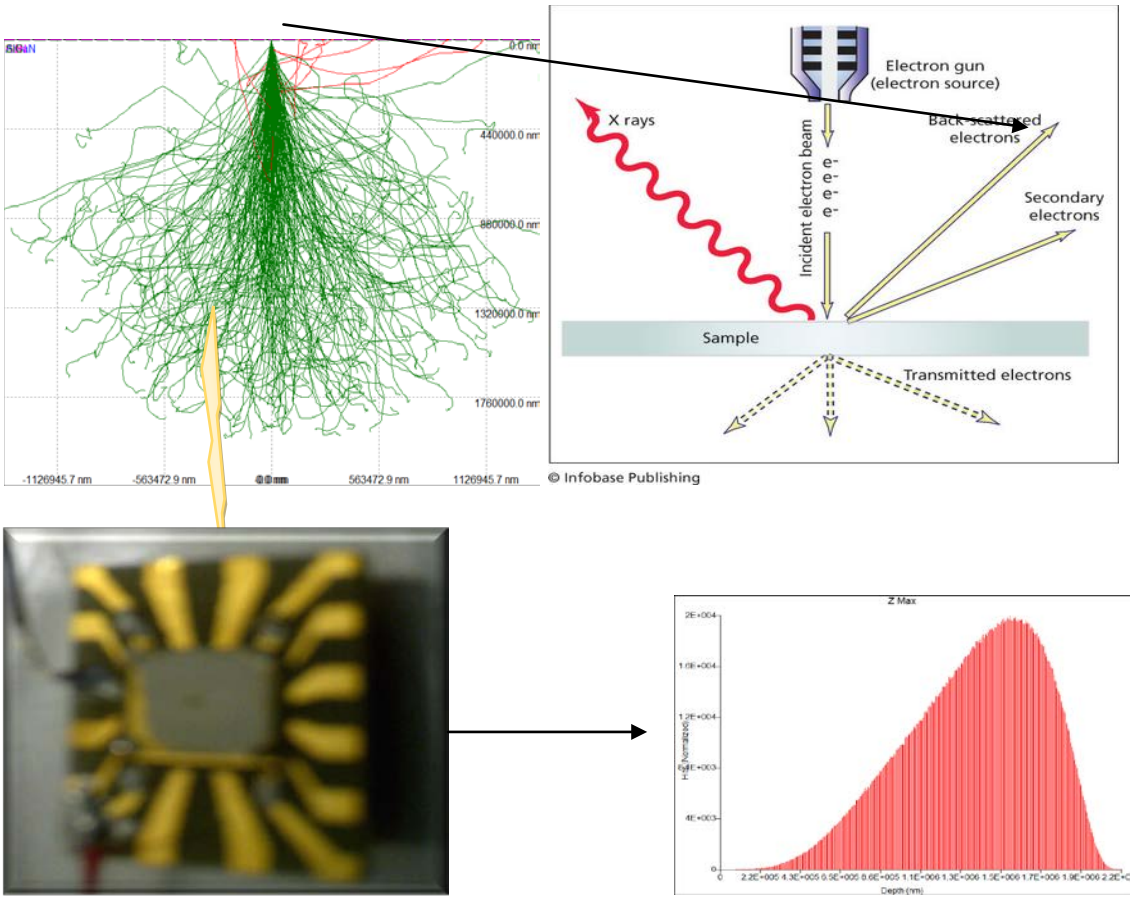

Figure 5.41. A cartoon scenario of the results from CASINO; the red lines on the upper right plot are the backscattered electrons. The left figure represents the distribution hits in the device being simulated.

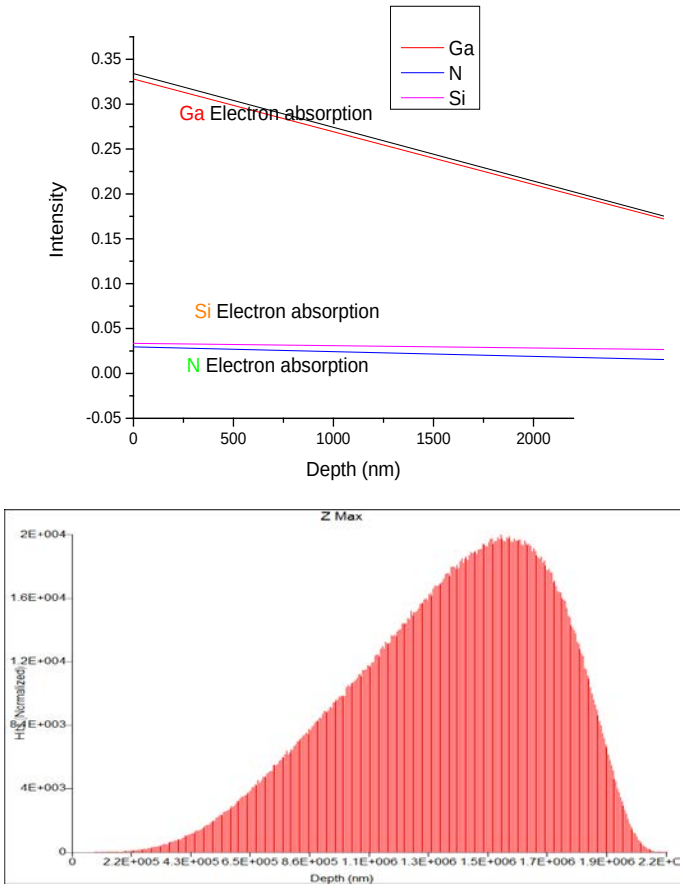

Figure 5.42. CASINO Monte Carlo simuations of 1-MeV electron irradiation in an AlGaN/AlN/GaN sample with 50 nm of Si_3N_4 passivation. The upper plot gives electron absorption as function of depth and intensity. The lower plot gives the normalized hits as a function of depth.

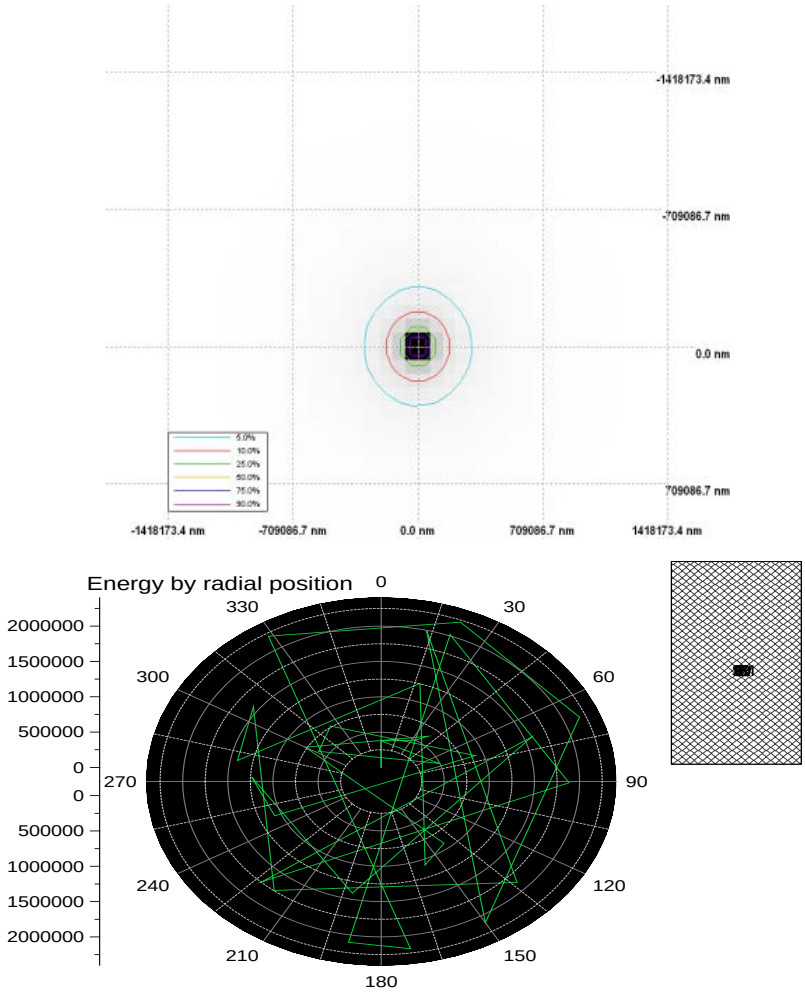

Figure 5.43. XY radial energy as a function of position, showing the locus of energy distribution.

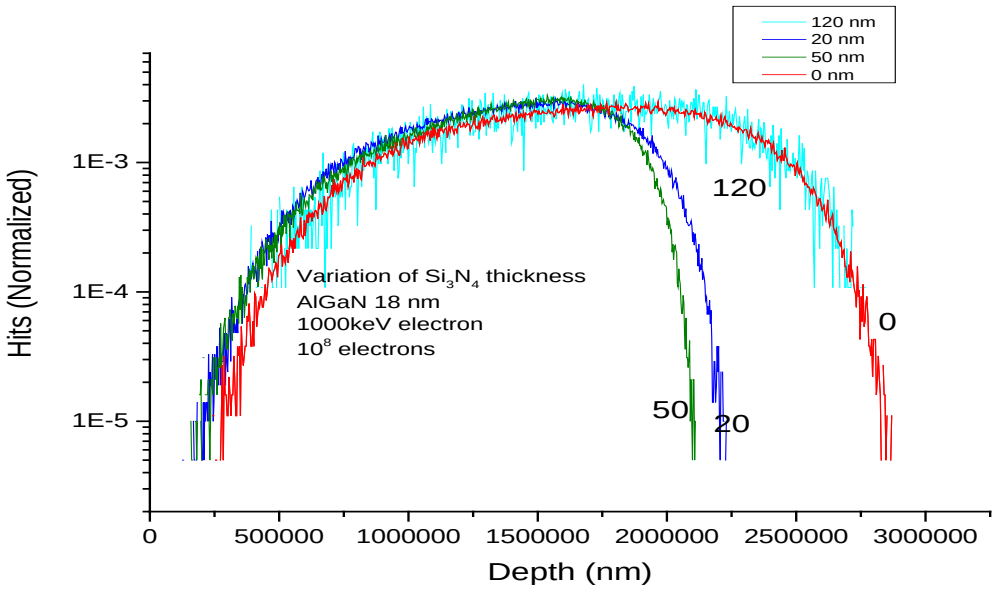

Figure 5.44 Normalized hits by 1 MeV electrons at a fluence of 10^8 nm^{-3} as a function of Si_3N_4 thickness on AlGaN (18nm)/AlN (1nm)/GaN (1700 nm).

5.5. Preliminary Conclusions and Investigative Questions Answered

This chapter addressed the characterization and analysis of the electron transport in 1-MeV electron-irradiated AlGaN/GaN HEMT structures, which varying thicknesses of Si_3N_4 passivation layer. It has been shown that the radiation response from 1 MeV electron irradiation is Si_3N_4 dependent and device structure dependent for AlGaN/GaN HEMT's with respect to the electron transport characteristics such as Hall mobility, carrier density and conductivity. Mobility models show the breakdown in the change in scattering mechanisms with respect to structure. Damage production algorithms enumerate the amount of the damage per atom per layer per structure. CASINO models show the distribution of hits based on Monte Carlo scattering, and where the damage is most probably clustered as well as how the variation of silicon nitride passivation is responding to the radiation.

VI. Characterization of Variation of Silicon Nitride Passivation Thickness on Electron Irradiated AlGaN/AlN/GaN and GaN/AlGaN/GaN Electrical Properties

6.1 Introduction

HEMT degradation and failure is often manifested by a drop in current at constant bias conditions. For this reason, it is important to analyze the factors involved in current degradation. In Chapter 2, the structure and general device physics was discussed. Most importantly in this was the device control for which the defects, especially the traps, negatively impact. The impact of defect concentration on the sample current was shown in Chapter 5 to correlate with changes in the Schottky barrier measurements. In this chapter the effects of passivation thickness and radiation on the I_g-V_g, C_g-V_g, and DLTS results for each structure will be looked at. Additionally, the transport property results from Chapter 5 (mobility, carrier density and conductivity) can be related to sample electrical performance via $J = \sigma E = ne\mu E = nev$, where μE is the carrier velocity. Low fields exist in the region of the Ohmic contacts, i.e., source and drain regions. High fields exist in the region under the gate. The saturation velocity is very important to device performance, hence it is important to study carrier density as was addressed in Chapter 5 and the corresponding saturation velocity. One has $v_{low\ field} = \mu E$ and $v_{sat,high\ field} = \mu E[1+(\varepsilon_0/\varepsilon)^2]^{-2}$.

As the results and discussion proceed, it must be remembered, as previously stated, that the structures in this study have a Schottky metal stack which are not functionally gates since they do not span the channel (which extends throughout the sample). Nor do they have a field plate. First the leakage current, I_g-V_g, will be considered, as it changes with passivation thickness and with irradiation, for both

structures. Then the same will be done with the Schottky (gate) capacitance-voltage behavior, C_g-V_g. A sampling of the calculated transconductance will show how the Schottky modulates the current under an applied gate bias. The further analysis of traps via DLTS will identify some of the intrinsic as well as the radiation induced traps responsible for the device behavior with varying Si_3N_4 layer thickness and radiation. These measurements are various forms of characterizing donor and acceptor populations; the results tie into and correspond to the Hall measurement and PL results given in Chapter 5. A unified model to explain the observed changes due to Si_3N_4 thickness and 1-MeV electron irradiation will be given in the final discussion and analysis in Chapter 7.

6.2. Effect of Structure, Passivation and 1 MeV Irradiation on Gate Leakage Current and Gate Capacitance.

Both C_g-V_g-T, I_g-V_g-T as well as room temperature I_g-V_g and C_g-V_g measurements were done to study the effect first of variation of Si_3N_4. Then with this variation of Si_3N_4 layer thickness, the effect of 1-MeV radiation at a fluence 10^{16} cm^{-2}. The measurements were performed on both structures. The impact of variation of passivation layer thickness on AlGaN/AlN/GaN and GaN/AlGaN/GaN device performance then follows (device structure and experimental details are in Chapter 4).

6.2.1. Leakage Current I_g-V_g

A perfect Schottky contact would have no leakage under reverse bias, which is the operating condition for a HEMT. If the barrier is of poor quality, carriers can bleed into the insulator/semiconductor. More typically, gate leakage is due to trap-assisted tunneling through the barrier to the channel, which is why leakage current needs to be

studied. Leakage current studies are a way to quantify damage in the structure, like trap assisted or defect assisted tunneling. Also it can indicate parasitic currents going to the gate. The effects of passivation thickness and temperature on the leakage current results are shown before and after 1-MeV electron irradiation.

The room temperature I_g-V_g for both AlGaN/AlN/GaN and GaN/AlGaN/GaN structures are compared in Figures 6.1 and 6.2. There are changes in the reverse bias leakage current that correspond to passivation thickness, but little change as the forward bias increases at 300 K. This would indicate that as the voltage sweeps from positive to negative, the trapping effects due to the thickness of the passivation, which are increasing the leakage current, are more profound in the negative bias. This should be identifiable with DLTS.

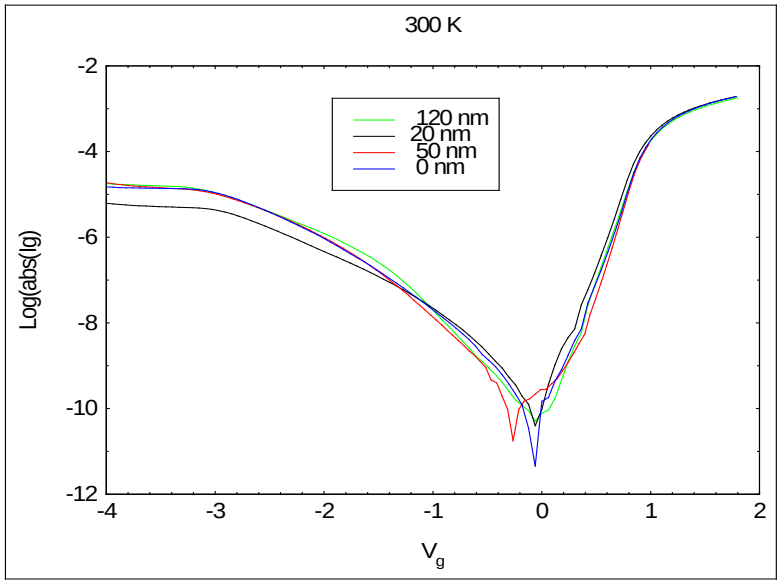

Figure 6.1. Room temperature comparison of Si_3N_4 passivation variation (0, 20, 50, 120 nm) for AlGaN/AlN/GaN.

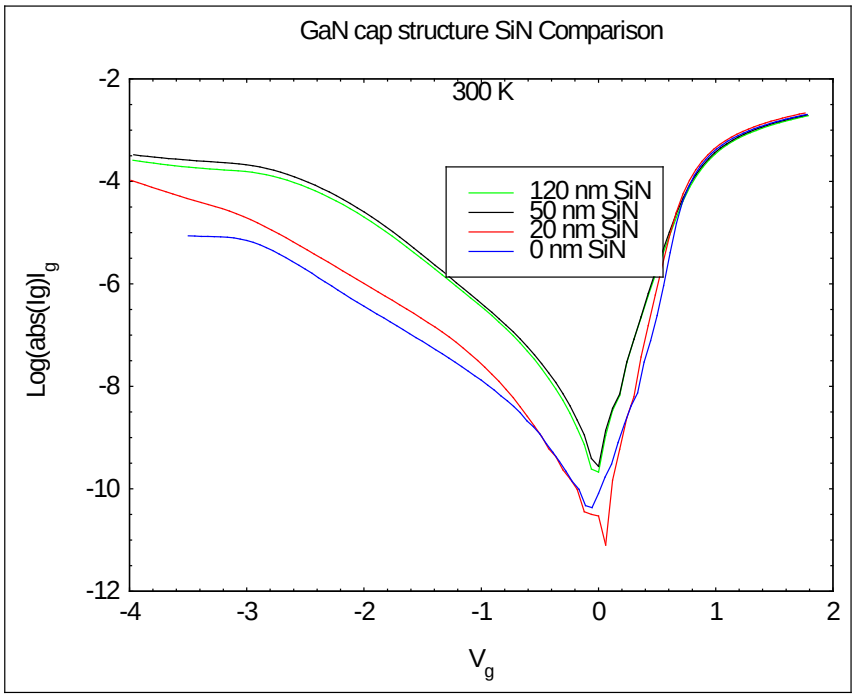

Figure 6.2 Room temperature comparison of Si_3N_4 passivation variation (0,20,50,120 nm) for GaN/AlGaN/GaN.

Figure 6.1 presents I_g-V_g for the variation of passivation for AlGaN/AlN/GaN and Figure 6.2 presents I_g-V_g for the variation for GaN/AlGaN/GaN. Data are taken at room temperature pre-irradiation. The structure with the GaN cap is more affected by Si_3N_4 for all passivation layer thicknesses in reverse bias. It exhibits a monotonic increase in leakage current with Si_3N_4 thickness that can be correlated to the carrier density for these structures. Therefore, the conclusion is drawn that for these structures, the increase in tunneling is due to the increase in carriers, which increases with the passivation layer thickness. For the GaN cap structures, the lowest leakage current occurred for the unpassivated structures. For both structures, the 50- and 120-nm reverse bias I_g-V_g are nearly equivalent, perhaps due to carrier saturation at 50 nm thicknesses (ICRU, 1984).

The carrier densities for these samples can, however, only partially explain the results for these passivation layer thicknesses. The 20-nm passivation thickness may contain pinholes, and typically shows anomalous results. The 20-nm results are not consistent likely due to a non-uniform distribution of pinholes.

The average increase of the leakage current in the reverse bias region was for the GaN cap HEMTs between the unpassivated and 120 nm passivated structure is 28%. Neither structure showed a strong change in forward bias behavior with passivation thickness. In reverse bias, the current is being drawn to the gate area, and in the interfacial area between the gate and the Si_3N_4 passivation, there is a contribution to leakage current. The N_{IT} should then be nominally similar in contribution to the leakage current for passivated samples.

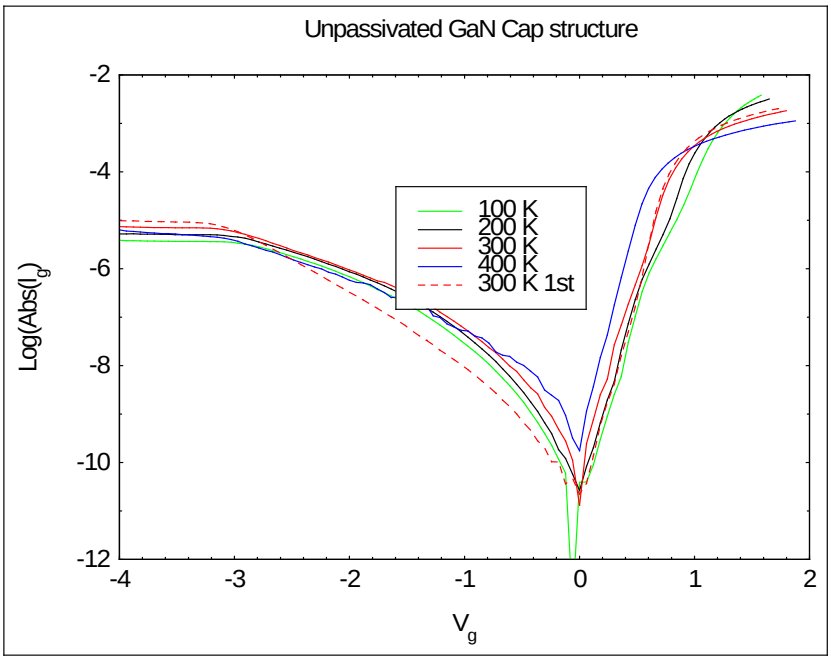

Figure 6.3. Temperature dependent I_g-V_g -T for unpassivated GaN cap sample. There is little temperature dependence in reverse bias, where I_g is nearly constant after pinch off.

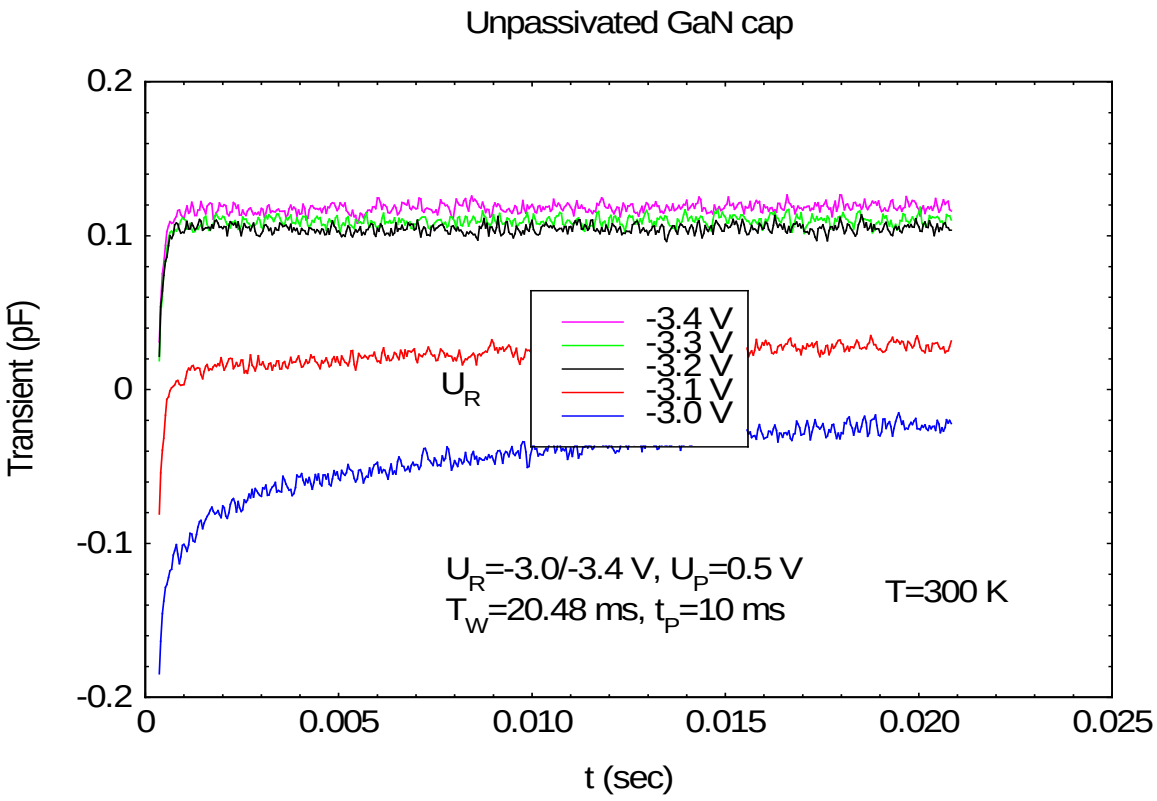

Figure 6.4. Capacitance transients for the unpassivated GaN cap sample showing its electric field dependence for voltage sweep from -3.0 to -3.4 V at 300 K.

Temperature dependent measurements (100-400 K) were done for all 8 structures, and all showed reverse bias currents that were not strongly temperature dependent, as can be seen for the unpassivated GaN cap I_g-V_g–T shown in Figure 6.3. Results obtained by Fang and Look (Look et al, 1997; Look, 2001) on AlGaN/GaN HEMTs were interpreted as indicating that this behavior resulted from tunneling conduction rather than as thermionic currents. As in that referenced study, the forward bias currents have a slight kink thought to be from a low bias tunneling current. The “kink effect” has been investigated by others (Look, 2001; Meneghesso et al, 2009). The kink is believed to be due to carrier trapping and de-trapping, leading to charge buildup and removal. Figure

6.4 shows that these samples are, however, strongly electric-field dependent in the range between -3.0 to -3.4 V. This is another indicator of the strong trap presence that persists through a range of applied fields.

The capacitance transients in Figure 6.4 are for a constant t_p of 10 ms with variation of the applied field. The higher the electric field, the greater the capacitance transient, implying there is greater accumulation as the field increases. For all samples, the leakage current is nearly independent of temperature. This is a strong indicator that the conduction mechanism is trap-assisted tunneling.

Next, the post-1-MeV irradiation effects will be shown. It is known that electron irradiation can result in increased leakage current. The pre- and post-radiation results for the two structures are compared for temperatures ranging from 100 to 400 K. These plots demonstrate the effect of passivation in increasing the relative change in the gate leakage current after irradiation.

In Figure 6.5, the lack of temperature dependence persists. Figure 6.5 presents I_g-V_g –T for the unpassivated GaN/AlGaN/GaN HEMT structure in the temperature range 100 to 400 K for pre- and post-irradiation. Figure 6.6 shows the increase of the I_s-V_g T leakage current with 50-nm passivation over the pre-irradiated for the GaN/AlGaN/GaN structure. It can be concluded that leakage current increases with temperature, due to the thermal activation of traps in the Schottky interface area. The DLTS trap E, which has a production rate of ~0.2cm^{-1}, shown later in the DLTS section, may be the cause of the radiation induced leakage and is more identifiable in the AlGaN/AlN/GaN sample.

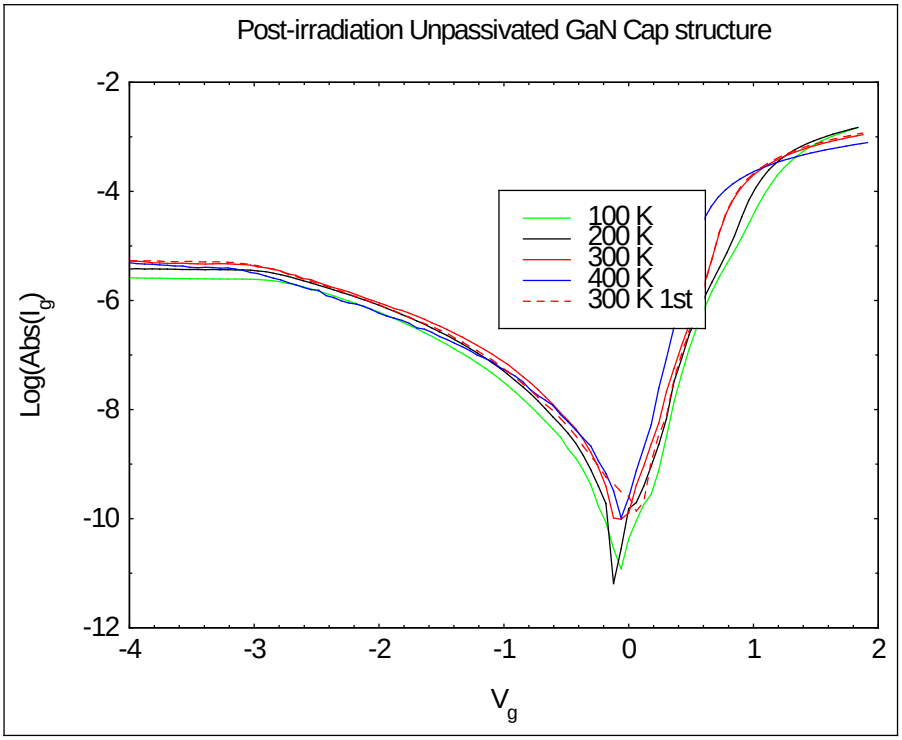

Figure 6.5. Temperature dependence of I_g-V_g after 1-MeV electron irradiation for unpassivated GaN/AlGaN/GaN.

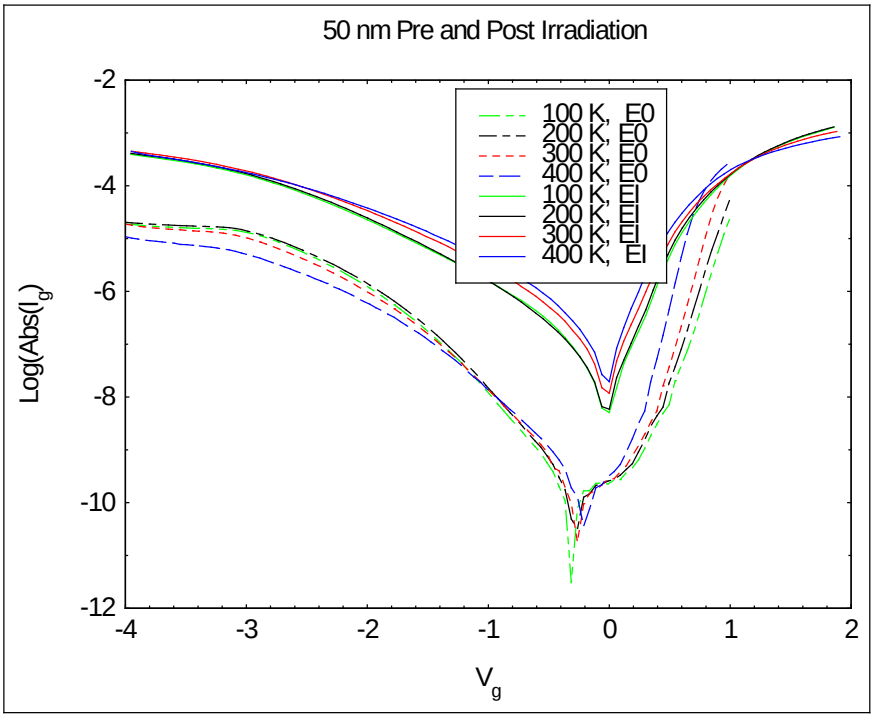

Figure 6.6. Pre(E0) and post(E1) irradiation, 50 nm Si_3N_4 passivated AlGaN/AlN/GaN, showing the increase in post radiation leakage current(solid lines).

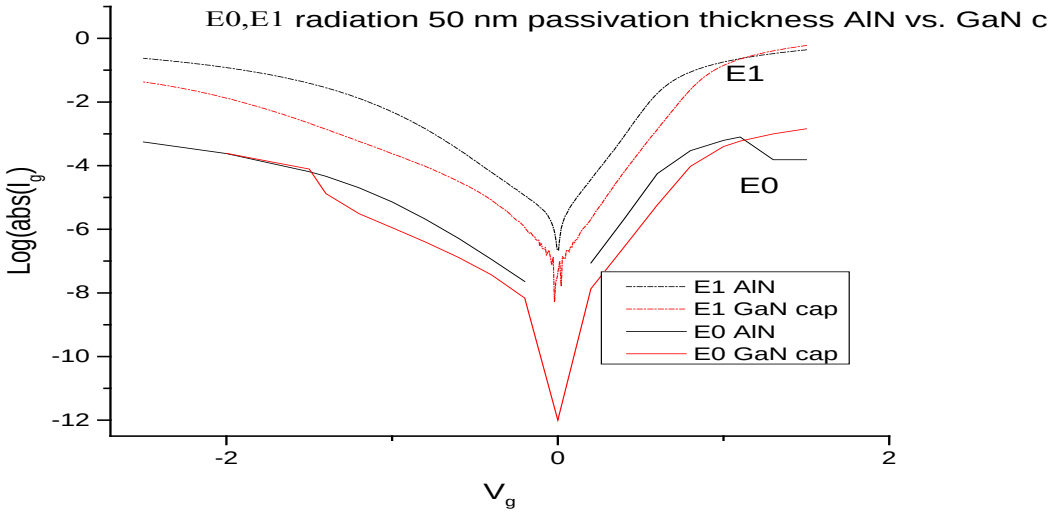

Figure 6.7 The pre (E0) and post(E1) radiation leakage current of both the AlN structure and the GaN cap structure for a 50-nm passivation layer thickness, showing that the GaN cap structure has less leakage.

Figure 6.7 presents I_g-V_g for the 50-nm Si_3N_4 passivated HEMTs for both structures at 300 K pre- and post-irradiation, showing the effect of the GaN cap in reducing the leakage under 1-MeV irradiation. Here, the GaN cap structure appears to be more radiation hard. Less leakage is observed in the GaN cap structure as it has a higher barrier and there is less tunneling. In actual transistors, the GaN cap combined with Si_3N_4 passivation has shown record output power performance and long-time stable RF operation (Meneghesso et al., 2009). The structures in this study are Schottky diodes. It is noted and important that for both structures the gate area resistance is greater than the channel resistance. The gate area(Schottky) resistance is given by:

$$R = (V_s/\mu)^* (L/V_d) \quad (6.1)$$

Some of the difference can be explained by the differences of the distance to the edge of the Si_3N_4 which is ~19 nm for samples with an AlN interlayer SBD but ~ 22 nm for

samples with a GaN cap SBD. Defects can be created near the barrier in the gate area; electrons can tunnel through the barrier and there can be leakage current due to tunneling from the hopping conduction. With the cap structure, the defects/traps introduced by Si_3N_4 are not on the AlGaN barrier, but on the top GaN cap layer. So, there should be less tunneling contribution to gate leakage current. There can be pre-irradiation leakage through threading dislocations,which can form a conduction path as shown in Chapter 5.

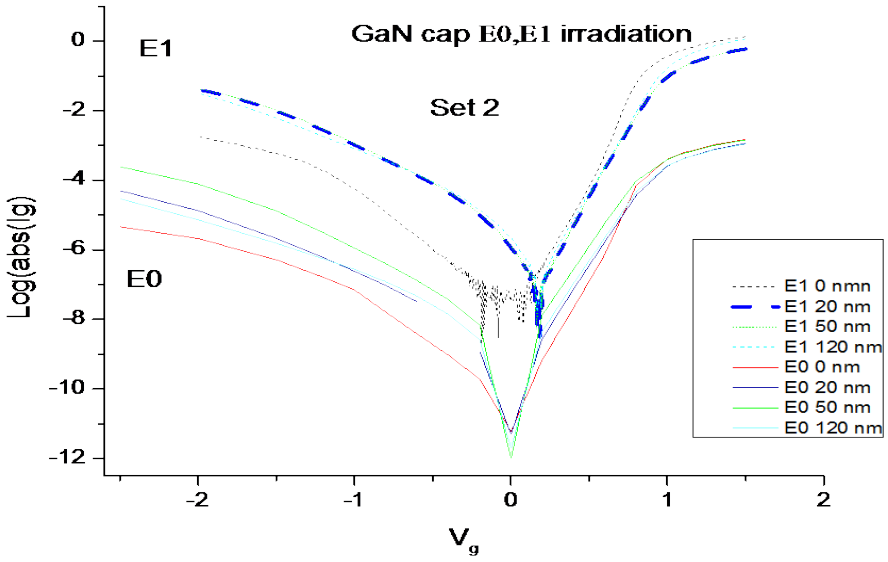

Figure 6.8. Si_3N_4 thickness variation with GaN cap pre- (E0) and post- (E1) radiation leakage current comparison showing a shift right E1 for the passivated structures.

In Figure 6.8, a comparison of the room temperature gate leakage measurements for all the Si_3N_4 thickness are presented for before and after radiation. The observed shift to the right of V_g =0 for the irradiated cases (top 4 curves) is due to the available conduction or interface states. The radiation is shifting the threshold voltage to a higher bias. This is expected because the radiation changes the available conduction or interface states. Also, the un-irradiated device does not have to be centered at the origin. In Figure

6.8, correlations can be made to the radiation induced changes for the GaN cap structure 300 K Hall carrier density result, shown in Figures 5.14 and 5.27.

Post-irradiation gate leakage can be caused by degradation of the Schottky to a smaller barrier, shown in Table 6.1 below. Irradiation can also physically damage the barrier by causing Schottky metal inter-diffusion. An example of physical damage to the Schottky metal is shown in a close examination of Figure 3.2, where in the bias range between -1 to +1 the upper irradiated (E1) curves have become ohmic, perhaps due to damage in part of the gate. As the bias increases in both directions there is recovery, since the damage was confined to a small enough area. Since defects can be created near the barrier (Meneghinni, 2008), electrons can then hop through the barrier allowing leakage from tunneling. (Petrosky et al, 2009).There can also be pre-irradiation leakage from dislocation damage that occurs during growth; the dislocation could be conductive. (Petrosky et al, 2009; Fang et al, 2009; Meneghinni, 2008).

According to Sze (Sze and Ng, 2007), the observed post-irradiation changes in the forward-bias slopes I_g-V_g curves may be an indication of a change in current mechanism, such as diffusion vs. recombination. Forward bias current is at an almost constant steep slope until the applied gate voltage becomes greater than the Schottky barrier height and then it increases rapidly. This is observed in the I_g-V_g plots in this chapter at ~1V. When changes in forward bias current occur between 0 and 1 V, this is an indication of damage that has led to a decrease in the Schottky barrier allowing charge carriers to pass through more easily. Table 6.11 shows the decrease in SBD with radiation as well as the changes with Si_3N_4 concentration. Figure 6.9 shows the additional factor of temperature in barrier height lowering.

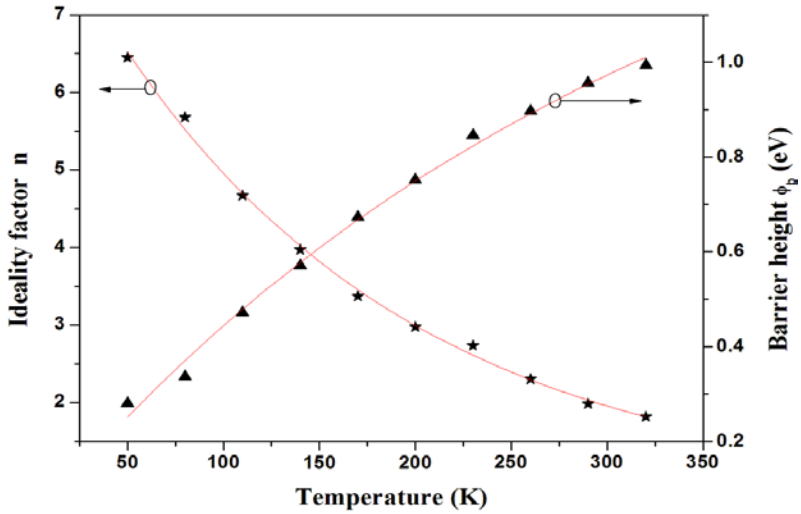

Figure 6.9. Temperature dependent Ideality factor vs. Barrier Height. The barrier height, øb, and the ideality factor, n, as a function of temperature for the (Ni/Au)/AlGaN/GaN/SiC Schottky barrier diode (Saadaoui et al, 2011).

The ideality factors and barrier heights are extracted from the pre and post radiation forward bias curves. The ideality factor goes down with passivation. Lower ideality factors indicate better performance, but they increase with radiation , except for the 50 nm passivation thickness, meaning that in this thicknesss other things are happening . Thet Hall results report this thickness is best for channel preservation, but the barrier height is a function of the gate current, and is taken from the intercept of the slope of the forward bias curve . Radiation is know to lower the Schottky barrier height by introducing traps with allow for hopping across the barrier and thereby effectively lowering it. The increase in leakage current, can be related to the additional interface states that passivation brings at the SB interface, thus lowering of the barrier height. All the samples have the same minimum gate current. The samples were exposed to the same dose. Based on the post-irradiation results, this says that the AlGaN/GaN material is

affected by the radiation as a function of the Si_3N_4 layer, because the barrier height is changing both with passivation layer thickness and radiation. A large barrier height leads to a small leakage current and high breakdown voltage, which improves the noise level and power performance of the device.

Table 6.1. Pre-irradiation (E0) and post radiation (E1) GaN cap Ideality and Barrier heights for GaN/AlGaN/GaN.

S_3iN_4 Passivation Thickness(nm)-sample #	N-factor (Slope)		Φ barrier height $\phi_b = \frac{kT}{q}\ln\left(\frac{AA^*T^2}{I_S}\right)$,	
S_3iN_4 Passivation Thickness(nm)-sample #	N-factor (Slope)		Φ barrier height $\phi_b = \frac{kT}{q}\ln\left(\frac{AA^*T^2}{I_S}\right)$,	
	E0	E1	E0	E1
0 -0707	5.80845	5.94051	10.09099	7.15112
20-0509	5.4169	5.46359	9.73236	7.18152
50 -0503	5.4603	5.41889	9.53705	7.12663
120-0604	5.45793	5.50773	9.74453	6.99962

6.2.2. Capacitance Voltage C_g-V_g.

For the samples in this study, the substrate was too insulating to do a sandwich-type capacitance measurement. The C_g-V_g was done across the top from the gate to one of the corner ohmics; the ohmics were designated as s1, s2 and s3. When a gate capacitance measurement is made, with a reverse bias applied to the gate or in this case the Schottky contact, the carriers are pushed away from the gate until the area under the Schottky depletes. The phases the device goes through were explained in Chapter 2 in HEMT device physics. The C_g-V_g measurement results in this section will show how the capacitance changes when a reverse bias applied to the Schottky changes with temperature, device structure, Si_3N_4 thickness and 1-MeV electron irradiation.

The C_g-V_g measurements can be generically profiled with Figure 6.10 above. For Figures 6.12 through 6.17, the flat or "on" capacitance is when the device is in accumulation mode and is the capacitance of the AlGaN, equivalent to C_{ox} in a MOS device. When in depletion mode the capacitance is represented by the series C_{tot} equations 6.2a and 6.2b. The value of the capacitance is due to the combined series capacitance due to the AlGaN and passivation layers. Repeating the equations from Chapter 2, for the AlN structure, the total capacitance can be defined as (Fagerlind et al, 2010):

$$C_{tot} = C_{pass}\, C_{barr} /(C_{pass} + C_{barr}) \tag{6.2a}$$

For the structure with the GaN cap it is:

$$C_{tot}=C_{pass}C_{barr}C_{GC}/[(C_{barr}C_{GC}/C_{pass})+(C_{barr}C_{pass}/C_{barr})+ (C_{pass}C_{bar}/C_{GC})] \tag{6.2b}$$

where C_{tot} it is defined as a series connection of C_{pass} ,C_{barr} and C_{GC} , which are the capacitances of the passivation layer, the AlGaN barrier and the GaN cap, respectively.

As stated by (Fagerlind et al, 2010), for the parallel plate calculation, these calculations can yield higher values than those measured because of the electron distribution relative to the measurement. The values will be given and discussed in Chapter 7.

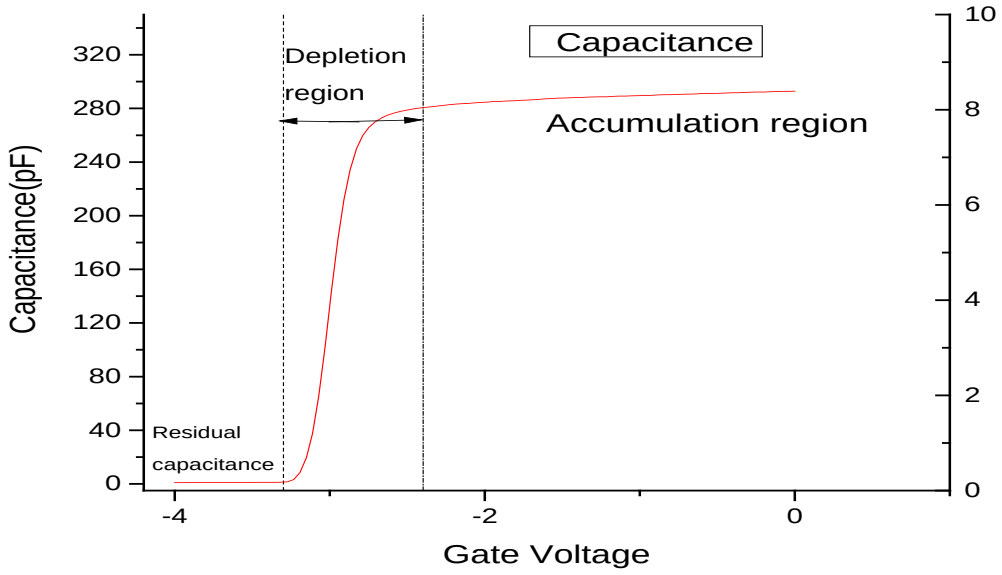

Figure 6.10. C_g-V_g from an unpassivated sample showing the accumulation and depletion and residual capacitance areas.

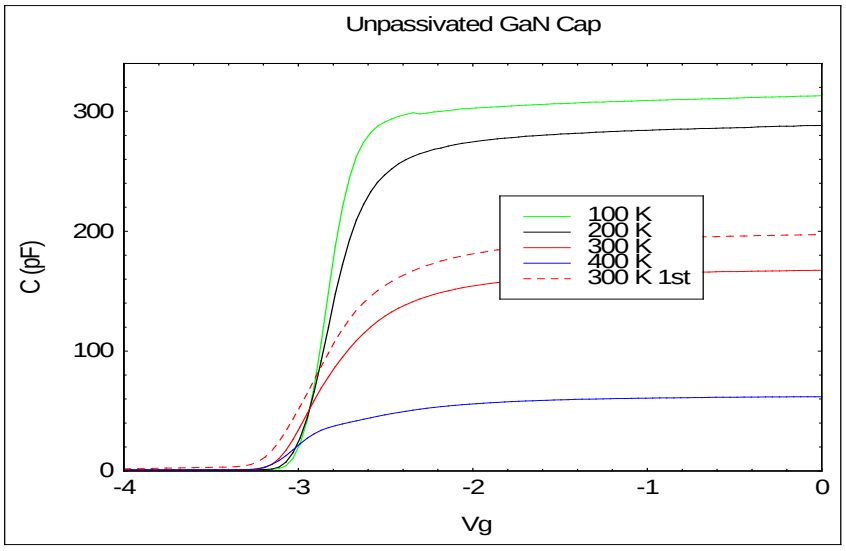

Figure 6.11. Temperature-dependent (100, 200, 300, 400 K) unpassivated C_g-V_g GaN/AlGaN/GaN with Ni/Au SBD. V_{th} shifts positive with decreasing temperature as device cuts off.

With temperatures of 300 K or above, Figure 6.11 shows that the gate capacitance decreases and "stretches out" in the depletion area. The threshold voltage (V_{th}) shifts negative relative to the 100 K and 200 K as a result of less carriers. The decrease in capacitance is due to thermal migration of arriers away from the gate area while the stretch out is due to mobile interface defects/traps N_{it} that lower the saturation capacitance.

$$\Delta N_{it} = C(\frac{\Delta V_{it}}{q}), \tag{6.3}$$

where *C*, for the structures being studied, is a series capacitance as given in equation 6.2a or 6.2b, and ΔV_{it} is the shift in voltage of the depletion region of the pre- and post-irradiation C_g-V_g curves. It can be can be used as a measure of time-dependent radiation-induced interface trap formation (McClory et al, 2007), which will be shown in Chapter 7. The interface traps cause the stretch out along the voltage axis and an interface trap capacitance, C_{Nit}, can be added to the total capacitance. This adds another term that can be added to equation 6.2a and 6.3:

$$C_{tot} = C_{pass}\, C_{barr}\, C_{Nit} /(C_{pass}\, C_{barr} + C_{barr}\, C_{Nit} + C_{Nit}\, C_{pass}) \tag{6.4a}$$

So now equation 6.4a can show a decreased capacitance for the AlN structures:

$$C_{tot}=C_{pass}C_{barr}C_{AlN}\, C_{Nit} /[(C_{barr}C_{AlN}C_{Nit})+(C_{barr}C_{pas}C_{Nits})+ (C_{pass}C_{bar}C_{AlN}) + (C_{pass}C_{bar}C_{Nit}/C_{AlN})] \tag{6.4b}$$

However, if the measurement is done such that the capacitance of the AlN layer is not involved, then equation 6.4a will be the total capacitance. For the GaN Cap structures, the total capacitance may be defined as:

$$C_{tot}=C_{pass}C_{barr}C_{GC}\,C_{Nit}\,/[(C_{barr}C_{GC}C_{pass})+(C_{barr}C_{pass}C_{Nit})+\,(C_{Nit}\,C_{bar}C_{GC})\,)+(C_{GC}C_{pass}C_{Nits})] \quad (6.4c)$$

The unpassivated AlN structure has a higher saturation capacitance, but the opposite is true for the GaN cap structure. Figure 6.12 shows that the capacitance decreases with increasing Si_3N_4 thickness for the structure with the AlN layer. In this case the Si_3N_4 could be increasing the barrier height. It can be shown with equations 6.4b, 6.4c and 6.6 that, an increasing dielectric thickness of Si_3N_4, leads to a larger depletion layer "d", so that the capacitance is reduced. The saturation capacitances for the AlN structure respectively are: 200, 192, 191 and 180 pF, for Si_3N_4 thicknesses of 0,20,50 and 120 nm, which show a 10% decrease from unpassivated with a 120-nm passivation layer. While there may be more trapping at the SBD interface area for the AlN interlayer structure, it has a greater saturation capacitance corresponding to its higher carrier density, as previously pointed out. This is shown comparatively in Figure 6.19. For the GaN cap structure, the capacitances are 172, 190, 183 and 178 pF respectively. The cap layer may mitigate some of the trapping effects at the SBD interface. Since the structure with the GaN cap already has a layer above the AlGaN before Si_3N_4 passivation, the series configuration is different in that case; that is, the effect of the total capping layers on the 2DEG is what affects the capacitance. For the structure with the GaN cap, it is a combination of the cap and the Si_3N_4 that changes the 2DEG and thus the amount of saturation capacitance measured. The carrier density for the cap structure shown in Figure 6.12 below correlates to its C_g-V_g. For the structure with the AlN, the capacitance is measured across 2 layers in series, whereas for the GaN cap structure, across 3 layers in series; i.e., the Si_3N_4 (C_{pass}) and AlGaN (C_{barr}) or the Si_3N_4 (C_{pass}), GaN cap (C_{GC}) and

AlGaN (C_{barr}), from the Schottky to the ohmic contact. Since only a portion of the channel is under the SBD, as shown here in Figure 6.13, there are parts of the channel that are not modulated by the Schottky, or they are said to be “ungated”.

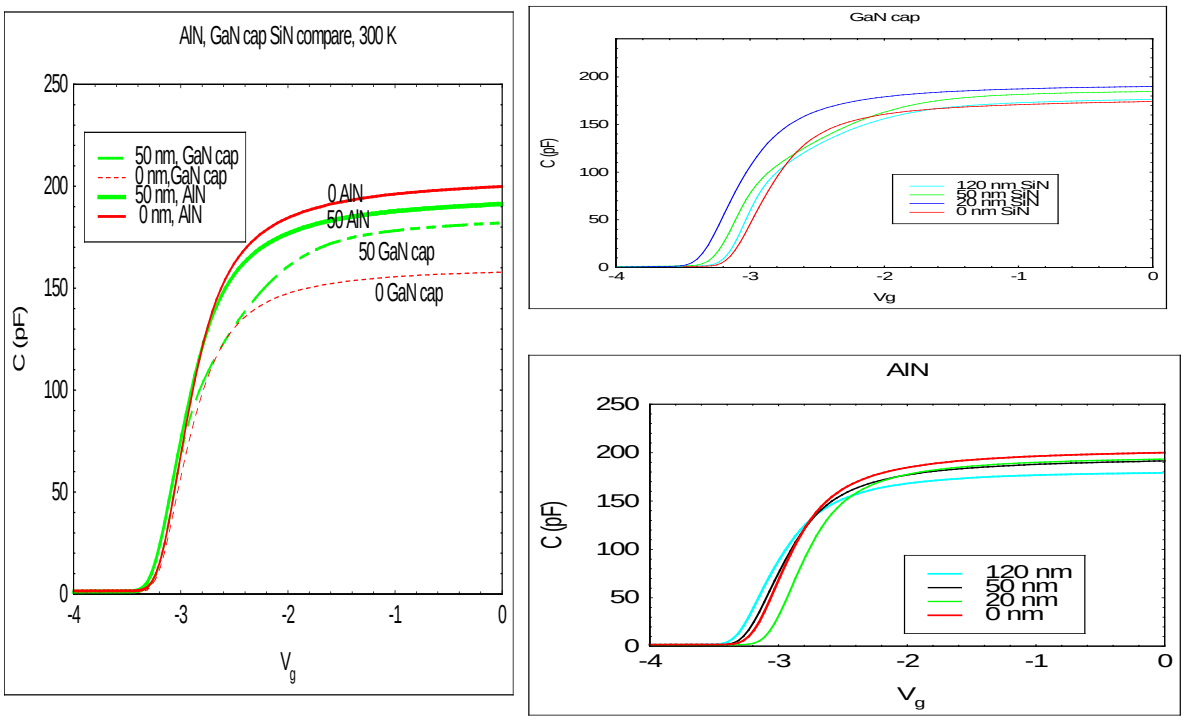

Figure 6.12**.** Comparison of Si_3N_4/AlGaN/AlN/GaN (IQ 15) with Si_3N_4/GaN/AlGaN/GaN (IQ 13) room temperature C_g-V_g (left). The unpassivated AlN structure has a higher saturation capacitance, but the opposite is true for the GaN cap structure.

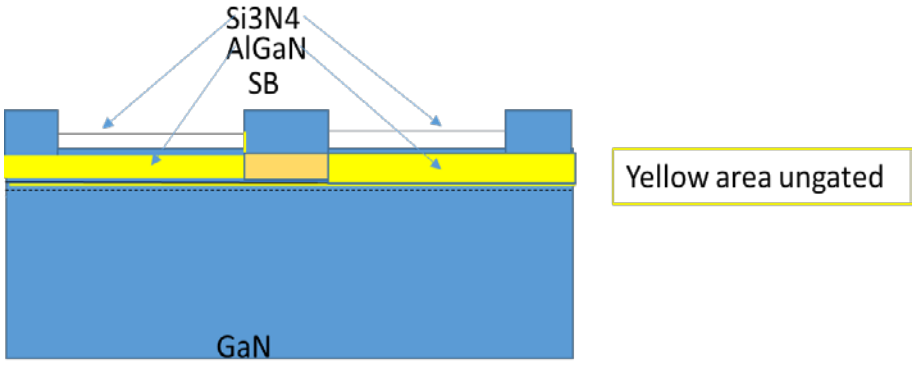

Figure 6.13. Generic AlGaN/GaN structure (not to scale) showing that some of the channel lies under the SBD and some is ungated.

While Figure 6.13 is not to scale, the Schottky (~gate) current measurements are for the area of the channel under the gate while the Hall 2DEG measurements are across the channel. With the capacitance measurements, the passivation effect is countered, as the passivation incorporates the traps it introduces and it is approximately equal to C_{pass}. By rearranging equation 6.4, it will be shown that the interface trap density due to the passivation can be calculated.

A possible explanation for the V_{th} shift of the C_g-V_g curve to the right in the depletion area, or more positive direction, for samples with 20 nm passivation (Figure 6.12, lower right), as opposed to a shift to the left, or more negative direction (as for samples with the 50 and 120 nm passivation), is the fact that it has been observed that thin layers of Si_3N_4 tend to relax, releasing electrons and going more positive in the absence of the strain seen in greater thicknesses. With no strain present, the thickness of the layer might not be conducive to creation of trap sites. On the other hand, for the GaN capped sample (Figure 6.12, upper right), which has an extra layer and thus an additional dielectric incorporated, as in equation 6.2b, a different response is measured.

For structures with the AlN layer, the C_g-V_g curve shows the device moving to a more negative threshold for passivation thicknesses greater than 20 nm, which suggests it requires more of a negative bias to reach depletion. The direct correlation of saturation or "on capacitance" with carrier concentration is also shown for the structure with the GaN cap by comparison with Figure 6.19. That is, the higher the measured Hall carrier density, the higher the saturation capacitance. Passivation evidently reduces the ability of the surface donor states to provide electrons for the 2DEG as evidenced by the decrease in saturation capacitance with increasing Si_3N_4 thickness.

6.2.2.1 Post Radiation Effects Results

For the structures with an AlN interlayer, there is a temperature dependent positive voltage shift after irradiation, along with a stretch out of the shape as compared to the pre-irradiation curve, indicating the formation of radiation-induced interface traps. (McClory et al, 2007). The "stretch" is in the slope of the C_g-V_g curve between accumulation and depletion.

Figure 6.14 shows the changes in capacitance as the bias changes before and after radiation. Under high negative bias and as the current goes to zero, the electrons move up to the gate until the electrons are depleted, at which point the capacitance goes to zero and the device pinches off if there is a gate. In negative bias, the band moves up to where electrons are, the depletion width gets wider and the bulk causes the Fermi level to shift down. This makes it more attractive for the electrons to be drawn to the gate rather than the 2DEG. In reverse bias, the depletion width, d, becomes infinitely large at around -3.2 V and the capacitance (gate source) goes to zero as equation 6.6 would imply. At low reverse bias, the capacitance is saturated and flat due to only small changes in the 2DEG peak depth (Look, 1989).

While the GaN cap structure in Figure 6.14 does not suffer from stretch out in the depletion area post irradiation, the lower carrier density and lower electric field (0.9 V) at the gate metal (Schottky) interface is less than that of AlGaN (1.5 V). The radiation creates acceptors which cause a loss of conduction band electrons. The Fermi level is lowered, which appears to raise the conduction band, as shown on Figure 6.14 on the right. This leads to a post radiation threshold voltage shift in the positive direction (McClory et al, 2007).

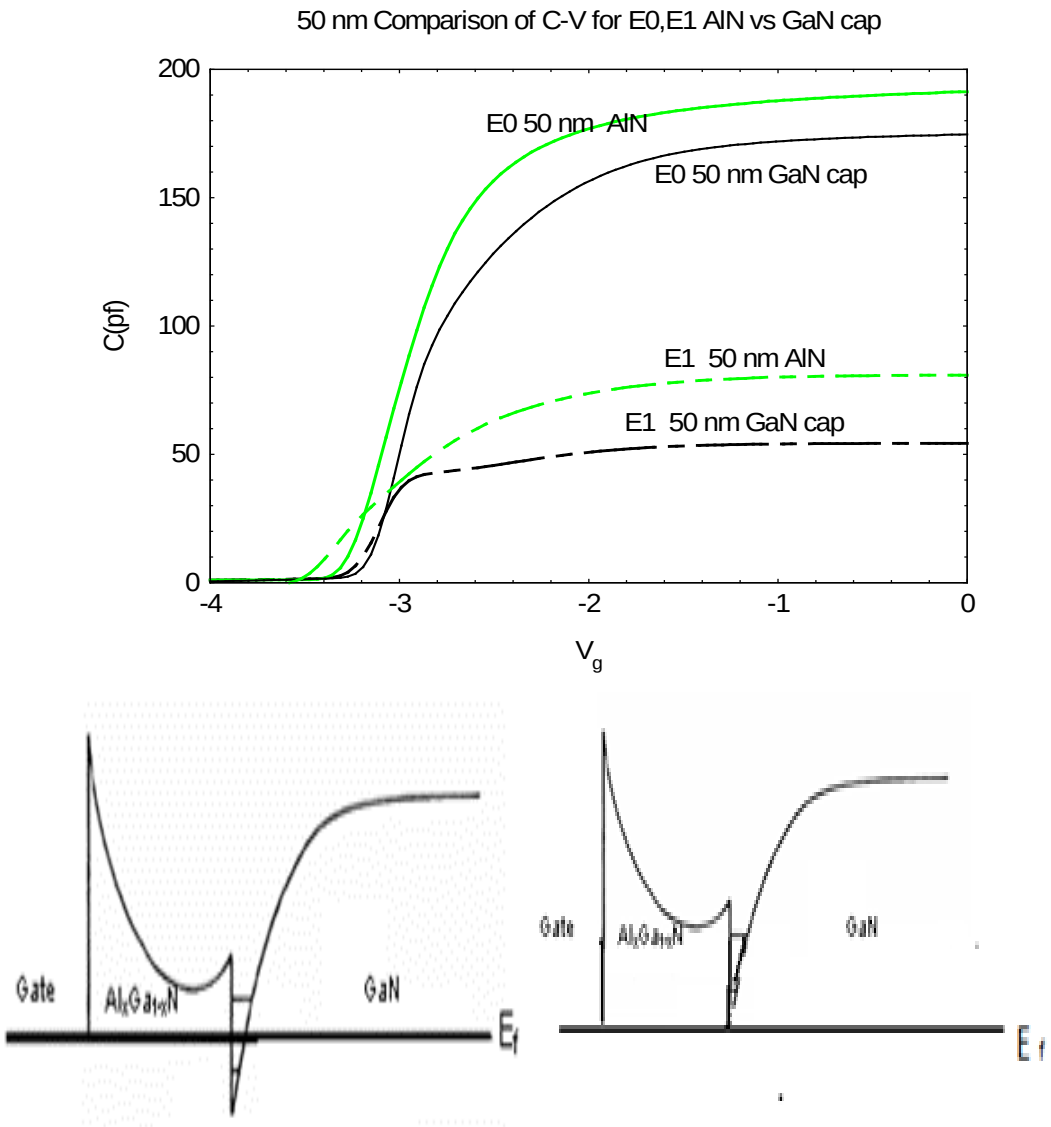

Figure 6.14 The pre- (E0) and post- (E1) irradiation C_g-V_g of 50-nm passivation layer thickness on the AlN and GaN cap structures shows a decrease in capacitance for both structures.

Figure 6.15 presents the E1 C_g-V_g –T for the unpassivated GaN cap structure. At 300 K, a slight change is observed in the forward and reverse sweeps; meaning there are traps that be detected between the forward and reverse bias sweep. Figure 6.16 presents

the post irradiation (E1) C_g-V_g –T for unpassivated E1 50 nm showing annealing effects on the AlN sample, which are minimal.

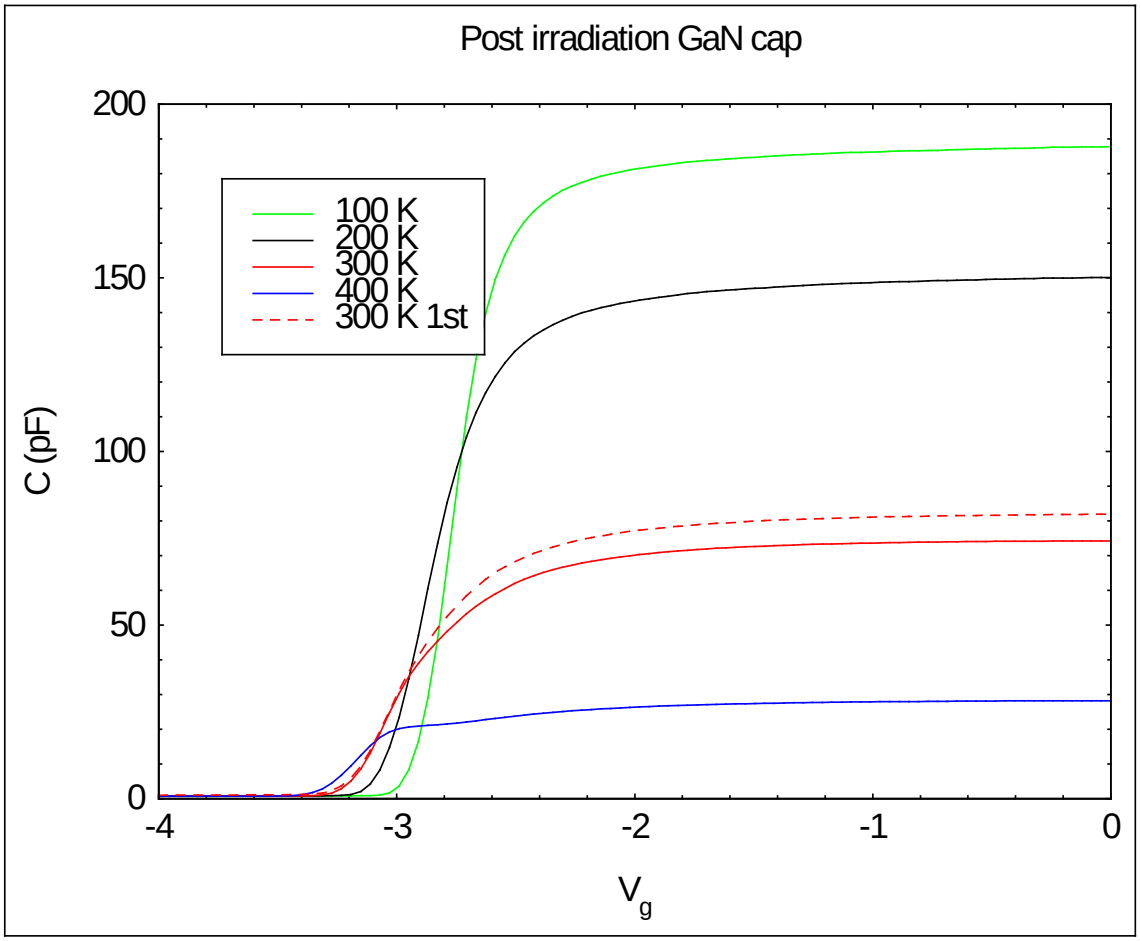

Figure 6.15 Post(E1) C_g-V_g -T for unpassivated GaN/AlGaN/GaN.

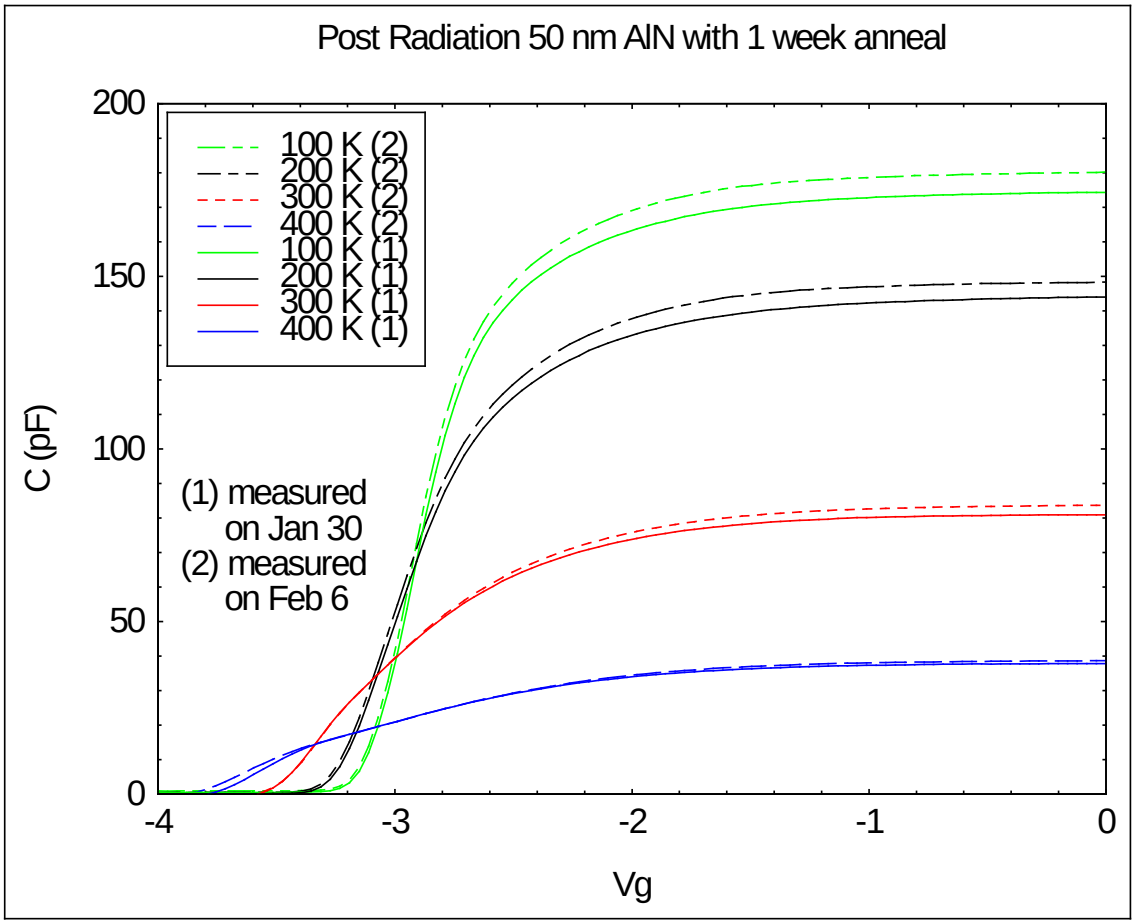

Figure 6.16. E1 C_g-V_g-T 50 nm with annealing effects, AlN sample at room temperature.

There is very little observed annealing at 1 week after irradiation. At 300 K and higher, there is a stretch out of the C-V curve in the depletion area believed to be attributed to the thermal activation of electrons in traps at the interface.

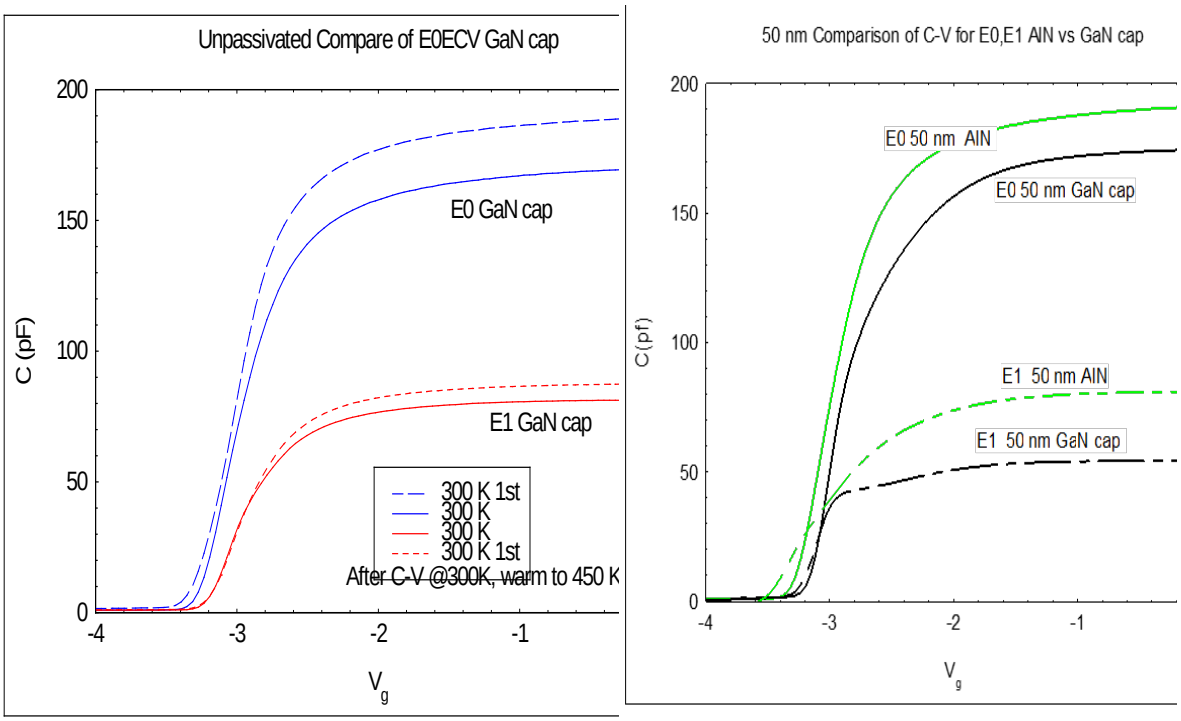

Figure 6.17. GaN cap sample at room temperature; C_g-V_g comparison of pre- and post-irradiation on unpassivated (left) and AlN vs. GaN cap pre- and post irradiation and on 50 nm SiN passivated structures (right).

Figure 6.17 (left) shows the room temperature change in C_g-V_g and shift to the right of V_{th} for the unpassivated HEMT, with a 53 % decrease in the saturation capacitance. The change post irradiation between the two 50-nm Si_3N_4 structures in the saturation capacitance differs by 57% for the AlN structure and 72% for the GaN structure, with the V_{th} stretching out for the AlN structure (right).

In Figure 6.18, the post irradiation degradation in C_g-V_g can be correlated to the average increase or degradation in Hall carrier density shown in Chapter 5. One theory about why the post irradiation C_g-V_g curves stretch out is because acceptor traps above the Fermi level in the GaN band gap are neutral. Radiation can change the acceptor trap density and location. When an applied voltage reaches depletion, the acceptor traps

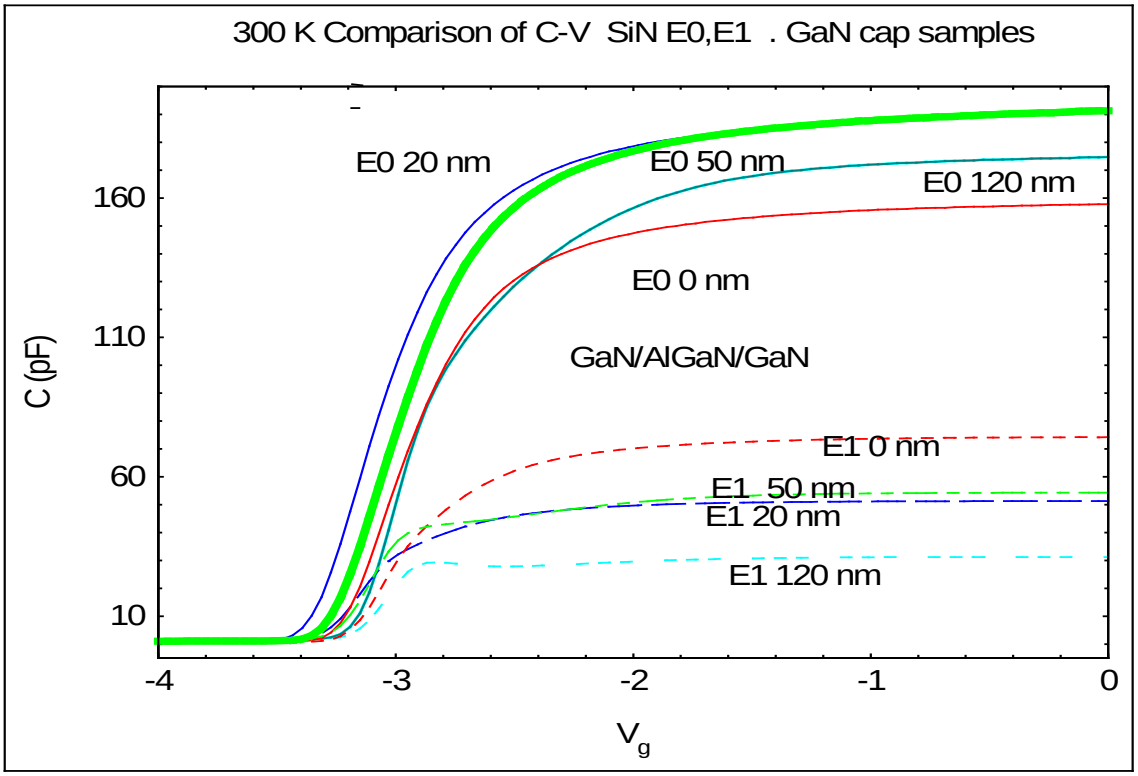

Figure 6.18 300 K comparison of C-V showing effect of variation of Si_3N_4 thickness before and after 1 MeV electron irradiation on GaN/AlGaN/GaN.

begin to move below the Fermi level, trapping electrons, requiring greater applied voltage to reach the same capacitance as without them. The conduction band height relative to the Fermi level E_f will change as in Figure 6.14b.

In his research, McClory (McClory et al, 2007) concluded that positive ΔV_{th} shifts (such as seen in Figure 6.17, left side) can be attributed to trapping of net positive charge in the interface layer. For the observed post radiation 300 K ΔV_{th} seen in the structures in this study, the shift is more positive post radiation and is not correlated with an increase in the sheet carrier density, but may be due to the increase of shallow donors, the V_N, which migrate and build up at 300 K. Radiation induces changes in the donor acceptor density and also changes the charges and the field at the Si_3N_4/AlGaN and Si_3N_4/GaN

interfaces. The radiation creates donors and acceptors; the post radiation decrease in Hall channel electrons shown in Chapter 5 is known to be caused by the radiation induced acceptor traps. The DLTS radiation induced trap labeled as E shown in Figures 6.33 through 6.35 are believed to be due to a shallow donor trap in the buffer near the 2DEG.

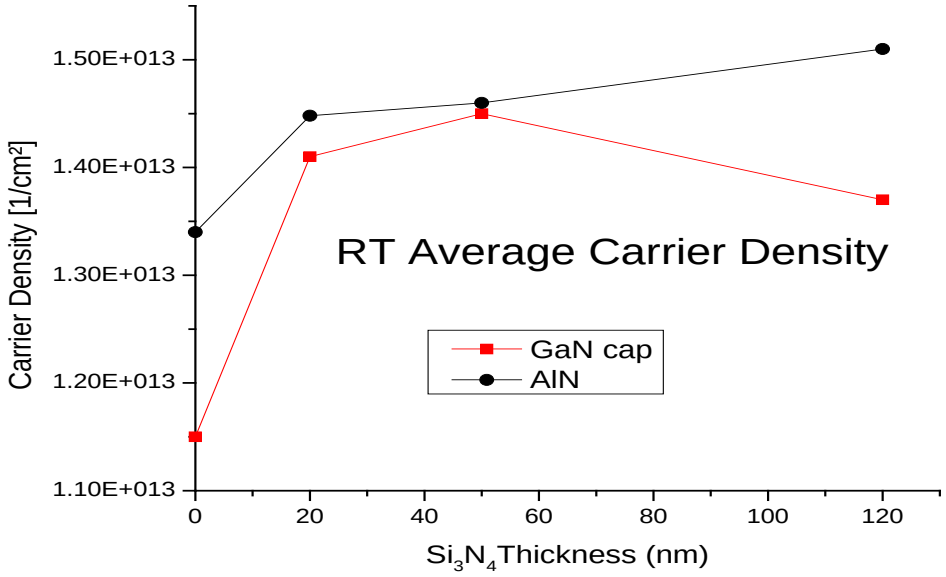

Figure 6.19. Comparison of S_3iN_4/AlGaN/AlN/GaN (AlN) with Si_3N_4/GaN/ AlGaN/GaN (GaN cap) room temperature Hall carrier density. The unpassivated GaN cap structure (red curve at 0) has a significantly smaller carrier density than the passivated structures.

The unpassivated GaN cap carrier density in Figure 6.19 is a decrease from that of the AlN structure. For the GaN cap passivated structures, the first sub-band in the 2DEG is believed to saturate quicker (Asgari et al, 2005) for reasons discussed in Chapter 5. But more importantly, the AlN has a stronger polarization contribution to the 2DEG carrier density.

It is shown in the C_g-V_g –T data of Figures 6.11 and 6.15 that the saturation (due to the finite number of electrons available) capacitance decreases with temperature. Choosing, for a HEMT to approximate the capacitance C by:

$$C = \varepsilon A/d \tag{6.6}$$

where d is the distance between the Schottky and the peak of the electron wavefunction, the change in the distance d when the structure changes can be explained.

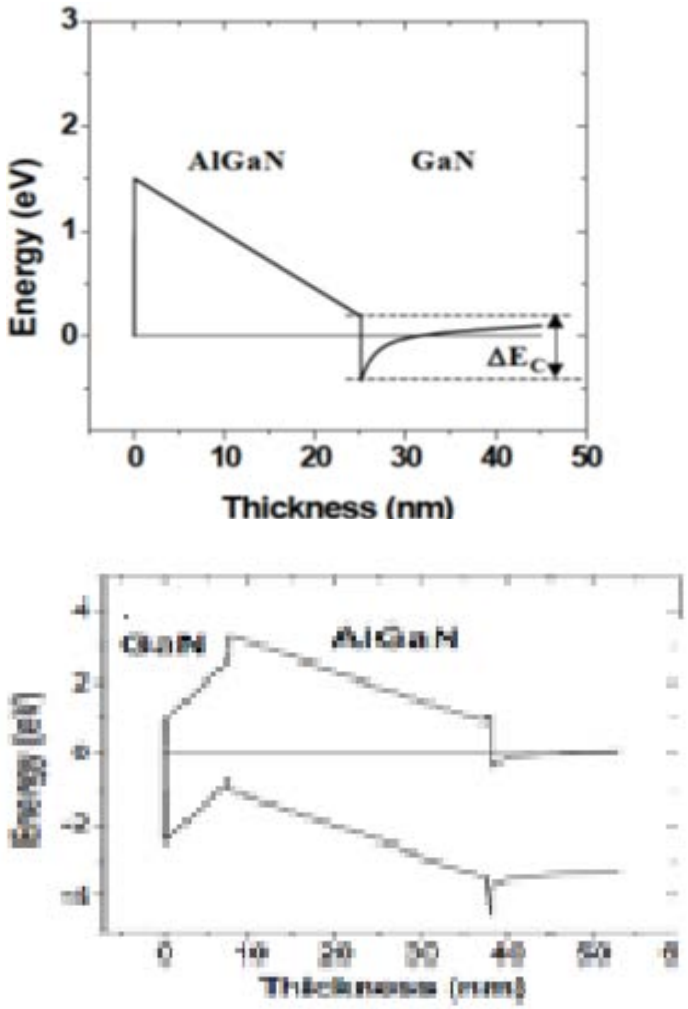

Figure 6.20**.** The figures above are referred to in the text and are used to explain why sheet carrier density and capacitance changes with a thin GaN cap (lower), as opposed to not having a cap layer (upper).

In Figure 6.20 above the "d" in equation 6.6 is increased with the addition of a GaN cap, thus lowering the capacitance for an unpassivated sample. This is shown in Figures 6.12, 6.14 and 6.17. Also, as has been explained in Chapter 2, sections 2.1.3 and 2.1.4, the contribution to the 2DEG is decreased using equations 2.4 and 2.39.

The electron wavefunction or carrier density n_s may be derived from the integration of the capacitance (Sze and Ng, 2007):

$$qn_s = \int_{-\infty}^{V_{gs}} C_g \; d\,V_{gs} \tag{6.7}$$

Here V_{gs} is the gate source voltage. To obtain donor (as well as acceptor) information, start with the 1-dim Poisson equations (Kim et al, 2006):

$$\frac{d^2\,\emptyset^2}{dz^2} = -\frac{\rho(z)}{\epsilon} \;\; , \rho(z) = e[-n(z) + p(z) - N_A(z) + N_D(z)\,] \tag{6.8}$$

and the above equation takes the form:

$$n_s = N_c \int_0^{\infty} \frac{2/\pi^{1/2}}{1+e(x+u)} x^{1/2} d\,x \tag{6.9}$$

Using equation 6.7 and 6.8 above and setting d= w_d for the depletion approximation, after some manipulation, carrier concentration profiles may be obtained through the capacitance (Look, 1989):

$$[N_D(w_d) - N_A(w_d)] \;=\; \frac{C^3}{e\epsilon A^2 \;\frac{dC}{dV}} \tag{6.10}$$

The three dimensional concentration obtained from the capacitance is often used as a rough estimate of the 3D concentration in the 2DEG. From the peak concentration in the

C_g, a rough approximations of $n= N_D – N_A$ gave 2.3 x 10^{19} cm^{-3} for the GaN cap unpassivated structures, and 2.3 - 2.68 e^{19} cm^{-3} for the AlN unpassivated structures.

6.3. Transconductance and Diode Measurements

Measurements were done to see how the structure conducts across 2 opposite ohmics. In a typical HEMT device, the gate is much larger than the size of the Schottky in this study, and it would be capable of depletion a larger amount of the I_{ds}. That is, for a gate, all of the current would be forced to go under it when the bias was applied, but since the structures have a Schottky, the current doesn't go from drain to source, only a small portion, as seen below, goes under the Schottky. So the measurements below only have relative meaning as to the ability of the Schottky to modulate the current with no gate finger. $I_d = I_{ds}$ is the current measured between the two ohmic (corner) contacts and Ig is the current measured on the center Schottky dot. A V_d of 5 V was applied to one corner and the opposite corner was grounded. A V_g on the Schottky was then swept from -3.2 to to 1.8 V.

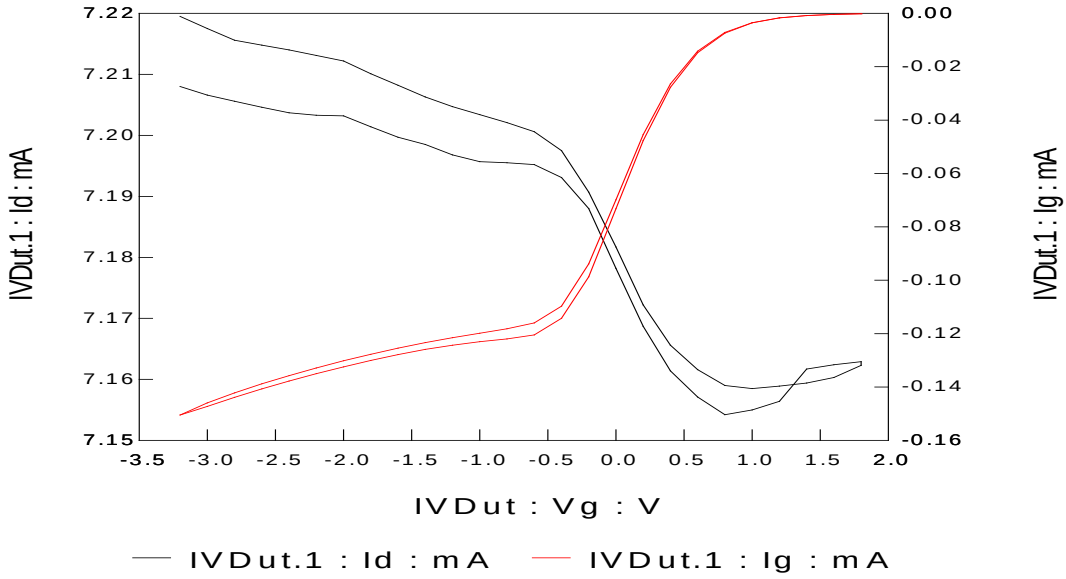

Figure 6.21. GaN/AlGaN/GaN with 120-nm passivation; Transconductance (black curve).

In Figure 6.21, the Transconductance can be calculated as the slope of I_{ds}:

$$G_m = d\, I_{ds}/dV_g = 1.45 \times 10^{-5}\ A/V. \qquad (6.11)$$

Here A is for Amps and V is for voltage. It is because the Schottky (gate area) is so small that there is very little ΔI_{gs} or change in current as the voltage applied to the gate sweeps. In the next two figures, measured on structures with an AlN interlayer, again there is little change in the current with respect to the applied gate voltage.

In the 20 nm passivated sample, the $G_m = d\, I_{gs}/dV_g = 2.36 \times 10^{-5}$ A/V, and for the 50 nm, $G_m = d\, I_{gs}/dV_g = 2.72 \times 10^{-5}$ A/V. Overall, I_{ds} did change slightly, but only by a total of about 0.1mA. The 50 nm sample shows the highest transconductance, as the 50 nm passivation throughout the metrics of characterization has performed best.

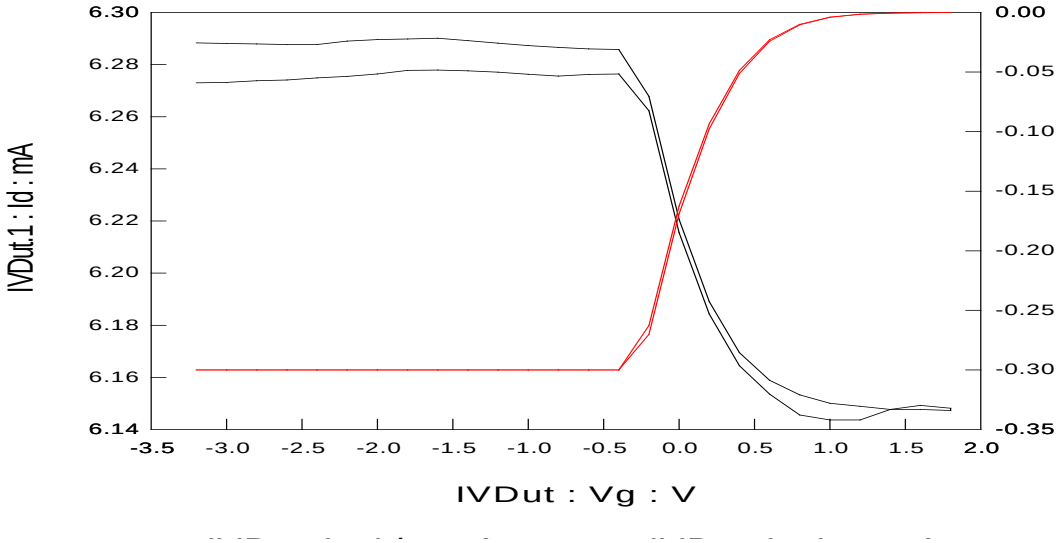

Figure 6.22a. Post irradiation for AlGaN/GaN/GaN structure with 20 nm passivation Transconductance.

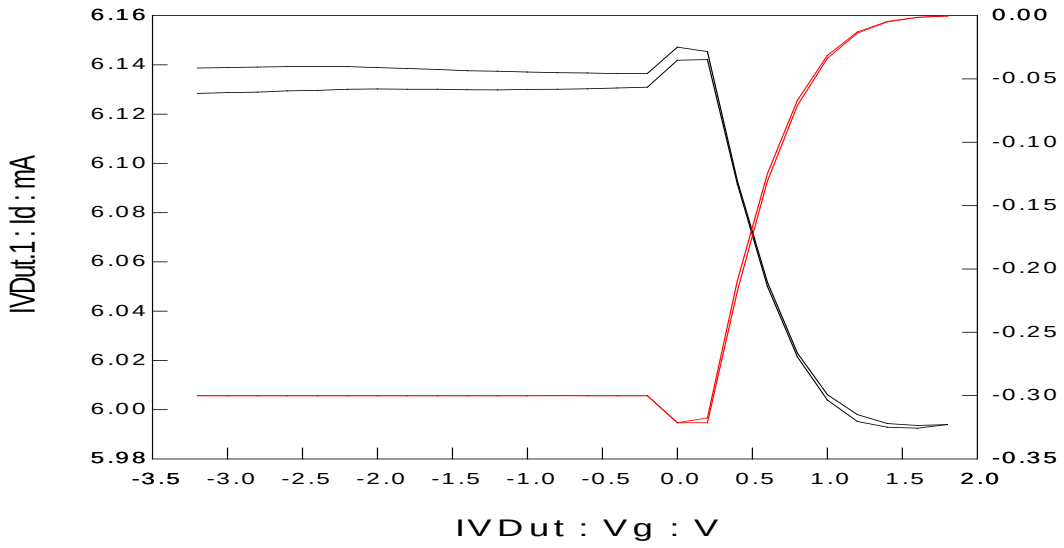

Figure 6.22b. Post radiation AlGaN/GaN/GaN structure with 50 nm Passivation Transconductance.

6.4 Deep Level Transient spectroscopy

As there are traps that can be identified with DLTS current transient analysis, a pictorial view of trapping processes DP1 and DP2 is shown in Figure 6.23. In the ON-state, the gate current injects electrons into AlGaN and the surface, and some of these electrons are trapped in this region (DP1). Some of the channel electrons are captured by the traps in the channel or in the buffer (DP2). On the other hand, in the V_{DS} = 0 state, only the first process (DP1) occurs in both the source and drain sides. To determine the traps within the AlGaN and GaN, the reverse bias and filling pulse height was varied.

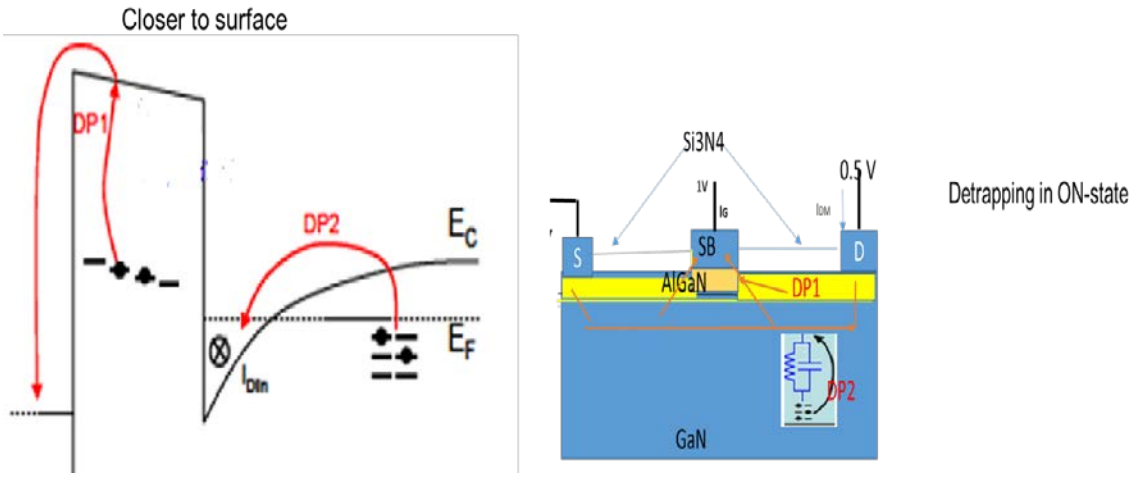

Figure 6.23**.** Process used in obtaining DLTS trap peaks (from Joh and del Alamo, 2011).

In the next set of DLTS, U_r is the reverse bias applied to the gate. Expressed differently, a reverse biased Schottky barrier on the sample is subjected to a forward bias pulse in order to flood the depletion region of the device with electrons, temporarily filling the traps in the region. Once the original reverse bias is returned to, the temporarily filled electrons (or holes) will be re-emitted.

Having a set of the emission rate and corresponding temperature pairs, one can make an Arrhenius plot, which allows for the deduction of defect activation energy for the thermal emission process. Usually this energy (sometimes called the defect energy level) together with the plot intercept value are defect parameters used for its identification or analysis. The donor-like surface traps, that will described throughout this study, and which reside in the gate-drain and source-gate access regions, cause the majority of the gate-lag in the device.

The relationship between passivation layer thicknesses vs. tunneling has been established previously. The traps identified in the DLTS that are believed to be causes for the leakage current, such as trap E, will be the trap sources for tunneling and will allow for the tunneling shown in Figure 6.24; this trap is also associated with the barrier height reductions given in Table 6.1. The tunneling current can be described by the overall leakage current through the tunneling/emission rate R(Φ) in general as (Sathaiya and Karmalkar, 2006):

$$J = \frac{q}{E}\int_{-\Phi}^{0} R\,(\Phi)\,d\Phi \qquad (6.12)$$

Trap assisted tunneling (TAT) has been well described by (Petrosky et al, 2009; Sathaiya and Karmalkar, 2006) and known to be a source of leakage current in AlGaN/GaN HEMT's. Figure 6.25 shows the where traps are located, whether bulk or surface states (which includes the interface states).

Using a basic AlGaN/GaN band structure, a possible scenario for the tunneling is shown below in Figure 6.24. The traps are below the AlGaN surface at energies of ~ 1eV, and with a density of $2\text{x}10^{12}$ cm^{-2} (Look et al, 1997; Look, 2001; Fang et al, 2009). At a

temperature in the vicinity of 400-500 K for the DLTS measurement, for passivated samples as well as unpassivated, and the main trap H_1, is intrinsic and thought to be due to threading dislocations (Fang et al, 2009). The effects of these hole like traps and their variation with Si_3N_4 thickness, is shown in Figure 6.26.

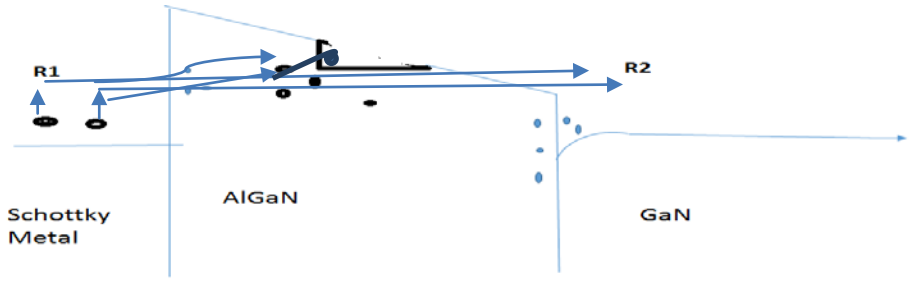

Figure 6.24. Band diagram of the tunneling from surface states.

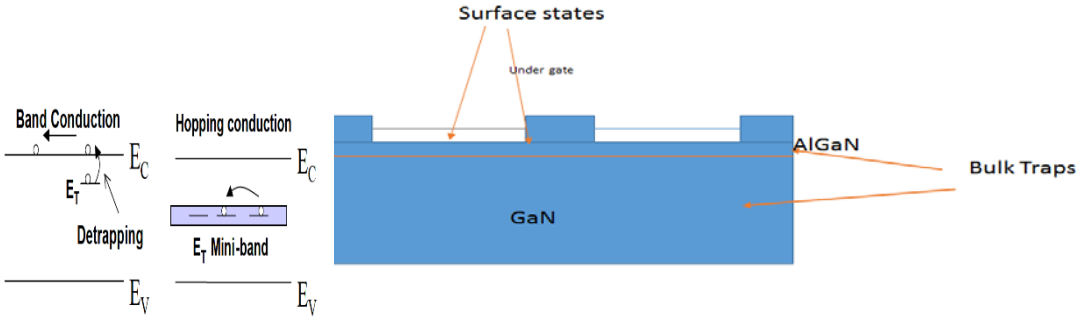

Figure 6.25. Trap sites and hopping in AlGaN/GaN.

The previously shown Schottky (gate) leakage and capacitance currents in this chapter can be attributed to mechanisms such as trap assisted tunneling and defect assisted tunneling, that are accomplished through hopping mechanisms as in Figure 6.25 (right) (Kim et al, 2006). It is thought that GaN layer threading dislocations, as well as traps within the AlGaN barrier facilitate tunneling through the barrier. The threading

dislocations are associated with the YL shown in the PL in Chapter 5. The extended defects (Sathaiya and Karmalkar, 2006) shown in the DLTS traps are identified through the trap dependence of t_p as seen in Figure 6.32. It is the reverse bias leakage current that is associated with tunneling, where Kim *et al.* (Kim et al, 2006), further attributes it to the metal contact Ni on the AlGaN's dislocation interface states and perhaps to nitrogen vacancies, V_N. The nitrogen vacancies complex with Mg to form the BL at 3.0 eV in the PL. The main radiation induced defect is the V_N. Its radiation induced increase is shown in the post radiation BL increase in peak (Figure 5.46). From DLTS data, it will be shown in Figures 6.30 through 6.32 that increases in post radiation leakage current and threshold voltage shifts result. For samples such as the ones in the study with Ni/Au Schottky barrier diodes and an AlN/$Al_{0.25}Ga_{0.75}N$ structure, Huang et al. (Huang et al, 2009), has attributed leakage current to threading dislocations.

Figure 6.26 shows trap H_1 persists through all Si_3N_4 passivation layer thickness as well as changes in applied bias from -2.0 to 0.5 V. This is an indicator of hole like traps and is in agreement with the hole traps found previously (Meneghinni, 2008; Fang and Look, 2005). As an edge dislocation, found in n-GaN that is grown nitrogen rich, it is believed to cause a line dislocation terminating as an acceptor type defect or the V_{GA} that is part of DAP in the YL at 2.2 eV

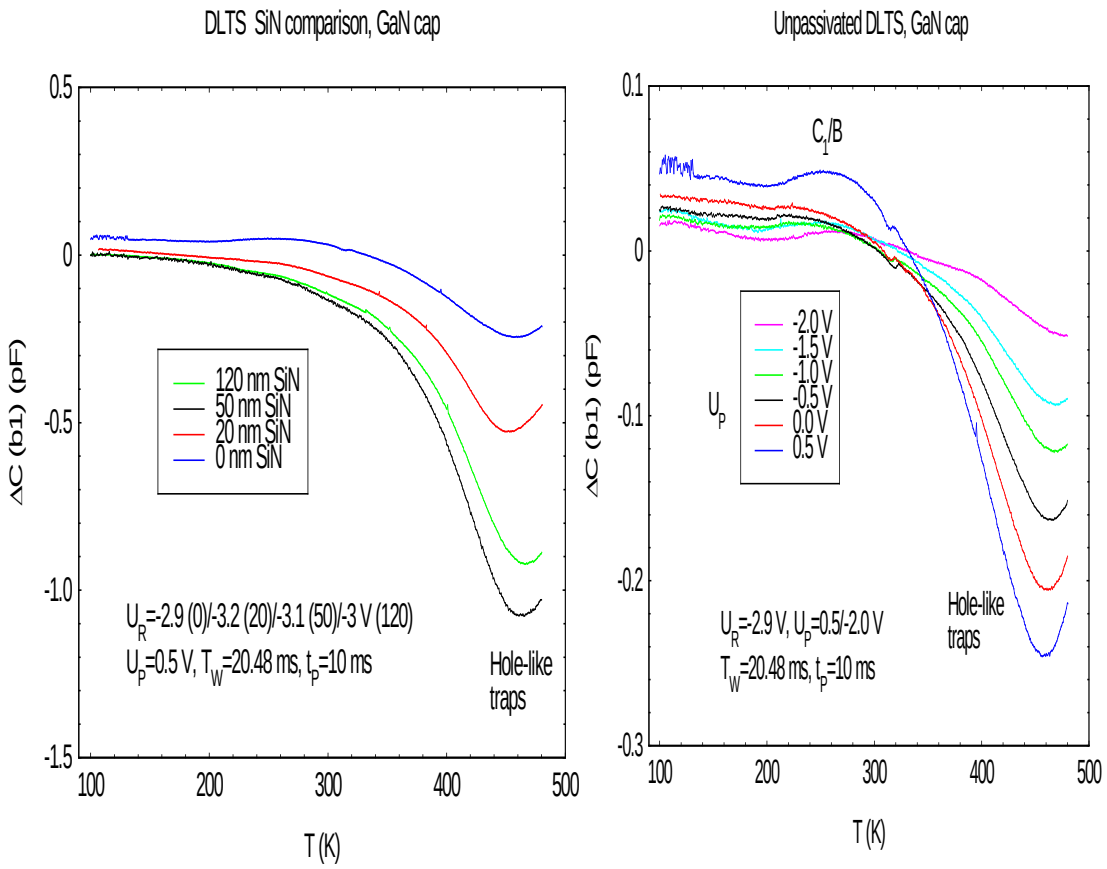

6.26. Left: Temperature dependent GaN /AlGaN/GaN DLTS as a function of Si_3N_4, showing the persistence of "hole like" traps. Right: Temperature dependent GaN/AlGaN/GaN DLTS spectra as a function of a filling pulse for an unpassivated sample with variation of the applied field from 0.5 V to -2.0 V.

in the photoluminescence. The transition is believed to be V_{GA} –>O, or V_{GA} ->Si_N , the latter transition the most likely. The effect of the Si_3N_4 passivation layer thickness, as previously discussed, brings additional trapping. In Figure 6.27, perhaps the reservoir of hole like traps has not been depleted. A stronger reverse bias defines the" hole-like" traps better, at around 450 K. These are thought to be intrinsic and due to threading dislocations.

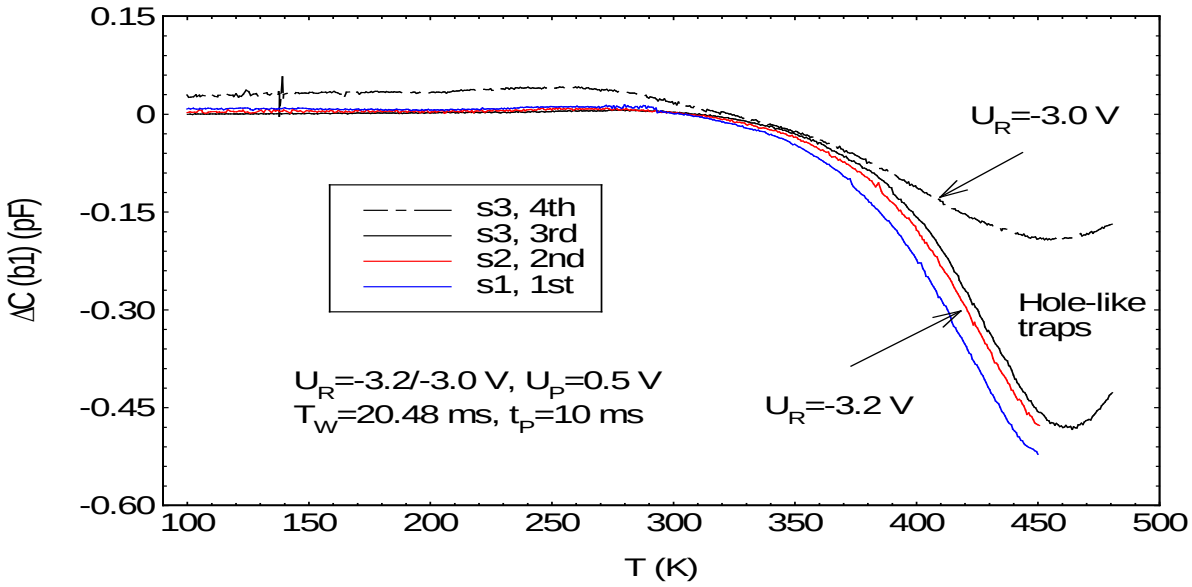

Figure 6.27 Pre –irradiated, unpassivated DLTS GaN/AlGaN/GaN structure for which the contacted ohmics where varied, as well as the reverse bias.

The persistence of a negatively going DLTS signal, thought to be due to hole like traps, is shown in both the AlN structure and the GaN cap structure, again believed to be of intrinsic nature due to threading dislocations. While this is n-GaN being looked at, if it was grown nitrogen rich as opposed to gallium rich, we could expect to see such traps in the lattice. Figure 6.28 is a comparison from Saadaoui et al. (Saadaoui et al, 2011) on "hole like traps". This defect is ~ 0.75 eV below the Fermi level.

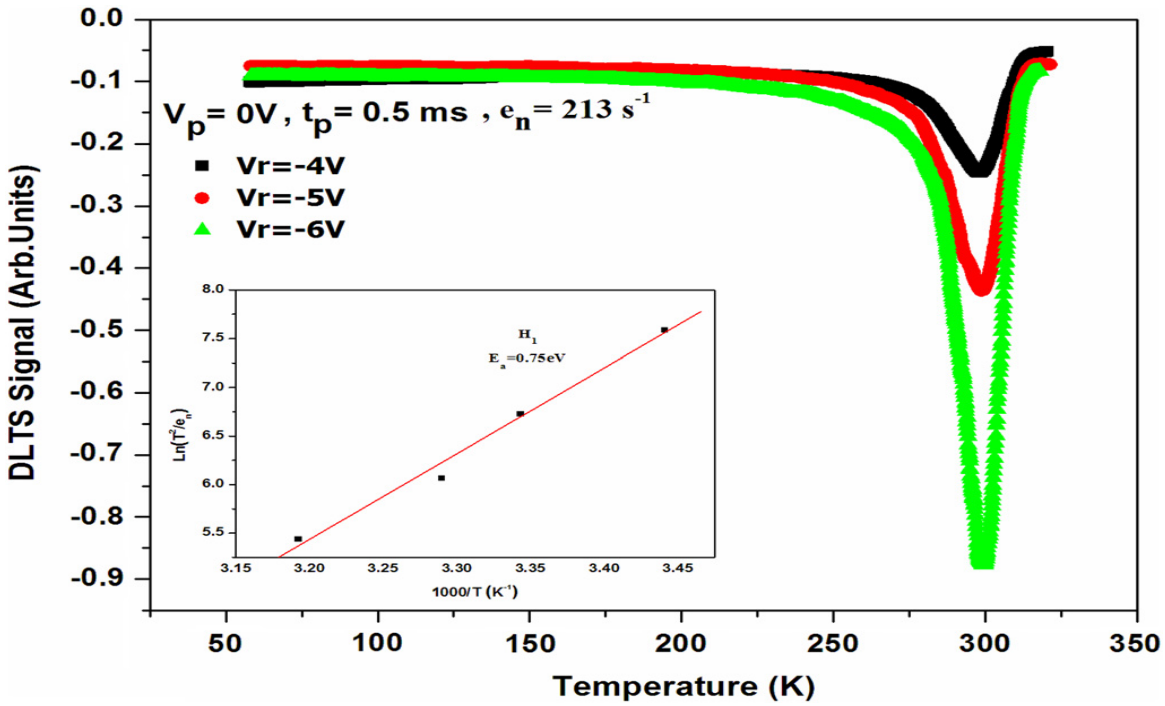

Figure 6.28 . H_1 hole trap that is believed to be the cause of tunneling at the Schottky Ni/AlGaN interface (from Saadaoui et al, 2011).

This H_1 trap at the Ni/Au interface exists intrinsically in the AlGaN and is linked to V_{GA}. As discussed previously, tunneling through traps at the metal/SC interface is a source of intrinsic leakage current in AlGaN/GaN devices. Post radiation, as it does pre irradiation, it complexes with the Si_N that forms the YL. The radiation induced PL peak change is not as great as that for the BL, associated with V_N, because the radiation produces more V_N than $V_{GA.}$

Trap A_x is associated with the nitrogen interstitial, N_I, a radiation induced deep acceptor trap with energy ~1.2 eV; this trap is attributed to leakage current and negative threshold voltage shifts. It is believed to exist in the AlGaN region. The C traps are in the area attributed to N vacancies (V_N) and are believed to be associated with the complexes formed with V_N. 1 MeV electron irradiation produces a Frenkel pair, mentioned earlier.

The next two DLTS figures show other V_N complexes described in the PL models in Chapters 5 and 7.

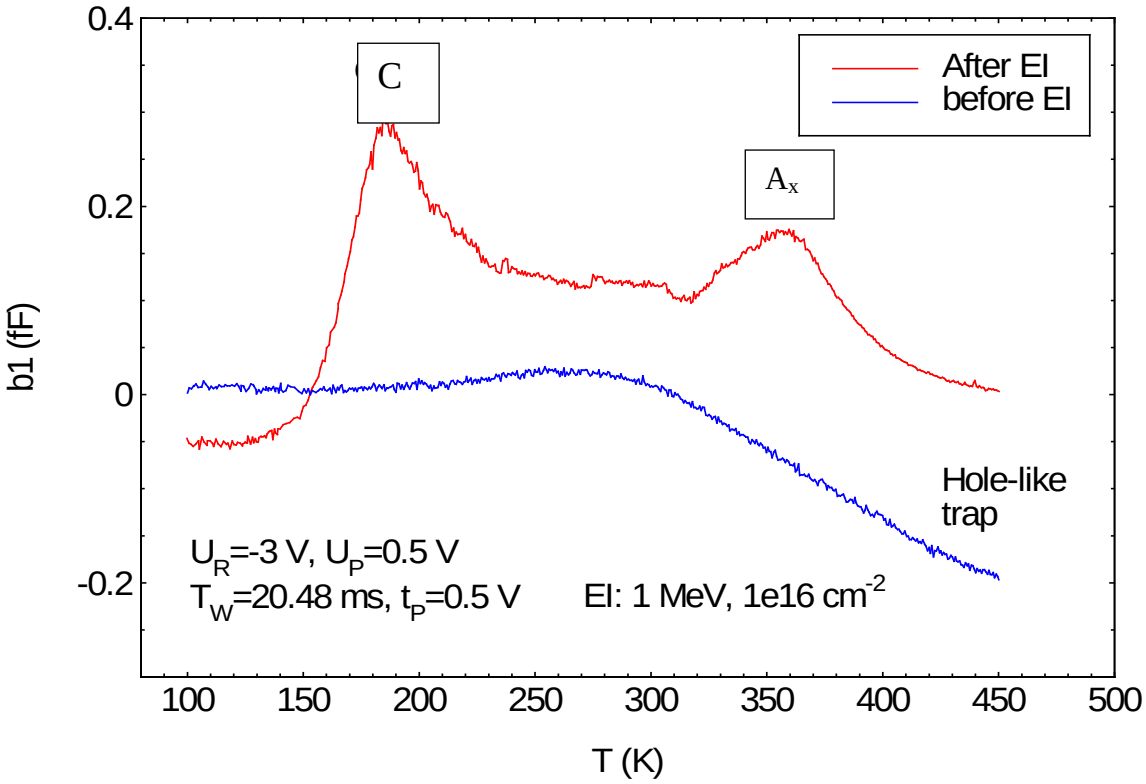

Figure 6.29. AlGaN/AlN/GaN Pre-irradiation (E0) vs. post irradiation (E1) DLTS for 50 nm Si_3N_4 passivation showing radiation induced traps. EI=electron irradiation.

Trap E, V_N, is in the GaN buffer region and has an activation energy of ~ 0.13 eV. It will be shown in Chapter 7 that it is a combination of two traps of 0.06 and 0.07 eV activation energies. As a radiation induced shallow donor, it is likely the cause of the 300 K positive interface charge build up given in TAT models. It can be linked to the positive threshold voltage shift seen in many of the samples and by the research of others such as J. McClory. Trap D, with an activation energy of ~0.25 eV, is also in the buffer region. Traps E and D are believed to cause leakage current and threshold voltage shifts. Traps that are in close proximity to each other can be linked to associated complexes. These

traps have correspondence in PL and likewise impurities in close proximity can be involved in a known complex in a PL transition, such as the transitions associated with the YL and BL. This can further be verified with their formation energy E_T. If the DLT capture cross section is included, the then these trap energies are the equivalent those in the PL for V_N. With traps E and Ax, the DLTS may be showing the radiation induced DAP or the N-Frenkel pair.

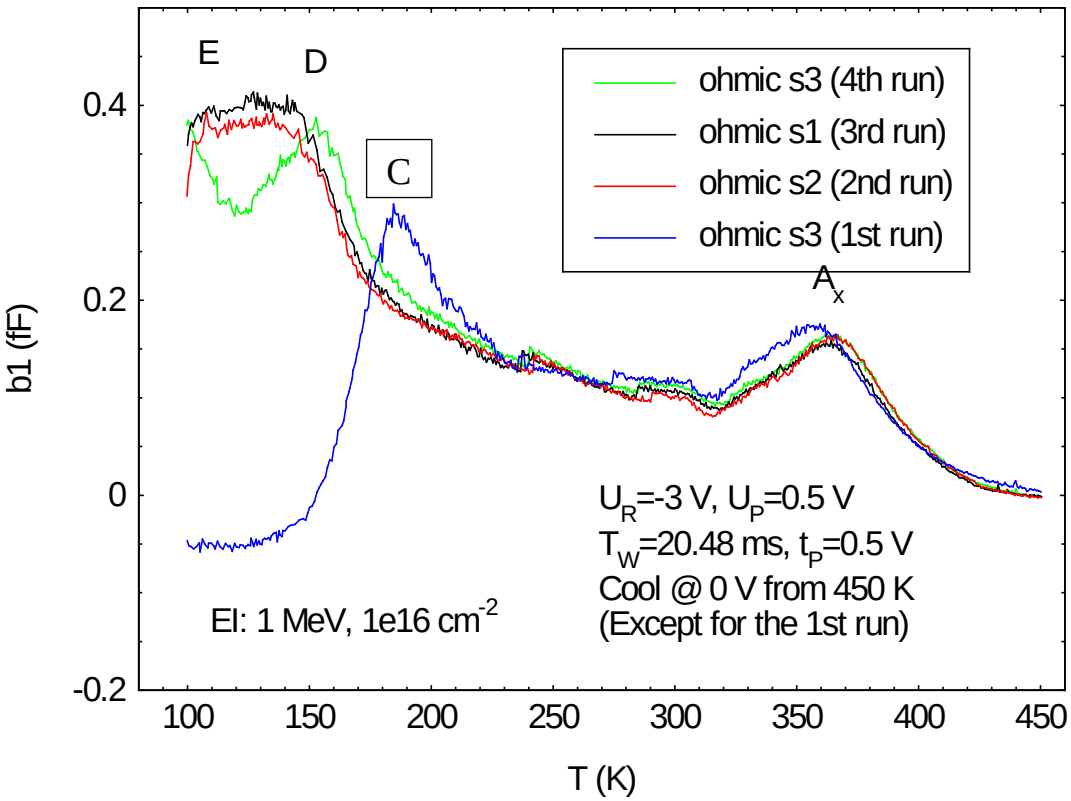

Figure 6.30 Same sample as above, E1, 50 nm, RT annealed, showing observation of traps is affected by starting conditions. Change in DLTS features at low temperature (4^{th} run), showing clear D trap and part of E trap.

Figure 6.31 shows that traps A, D and E from the previous Figure 6.30 have not annealed out after 1 week at room temperature. Trap E and all peaks in that area are

associated with V_n. The other peaks in that E trap area are associated with the complexing with V_n, as discussed in the previous paragraph. The V_n complexing is shown and explained in the Pl results in chapter 5 and analysis in chapter 7. Figure 6.32 is the same as Figure 6.31, but shows the observed traps A, E and D as a function of variation of tp, resulting in settlement of defects in the sample. It can be concluded that these traps have some association with extended defects, for which there are references to in the literature (Saadaoui et al, 2011).

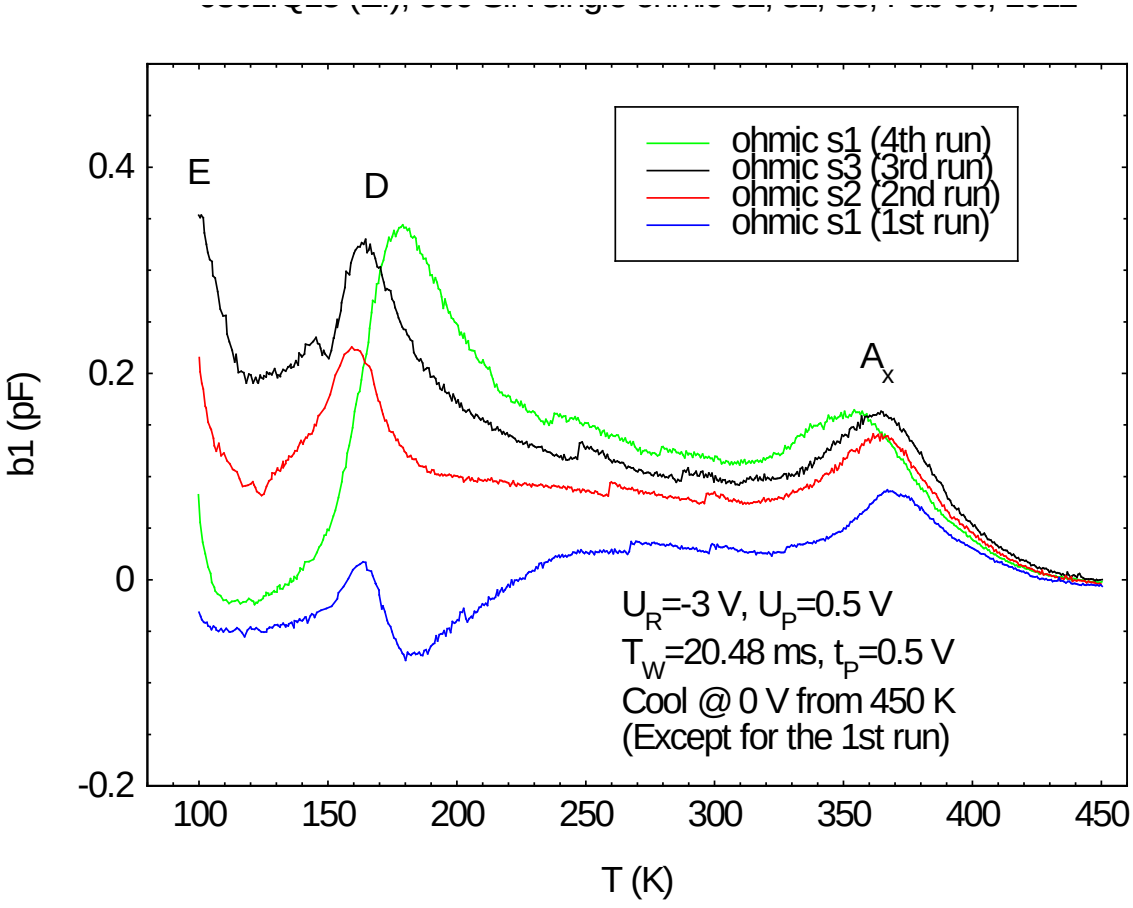

Figure 6.31**.** The persistence of the A and D trap in irradiated 50 nm passivated after a 1 week room temperature anneal for AIN sample, through multiple runs and ohmic configurations**.**

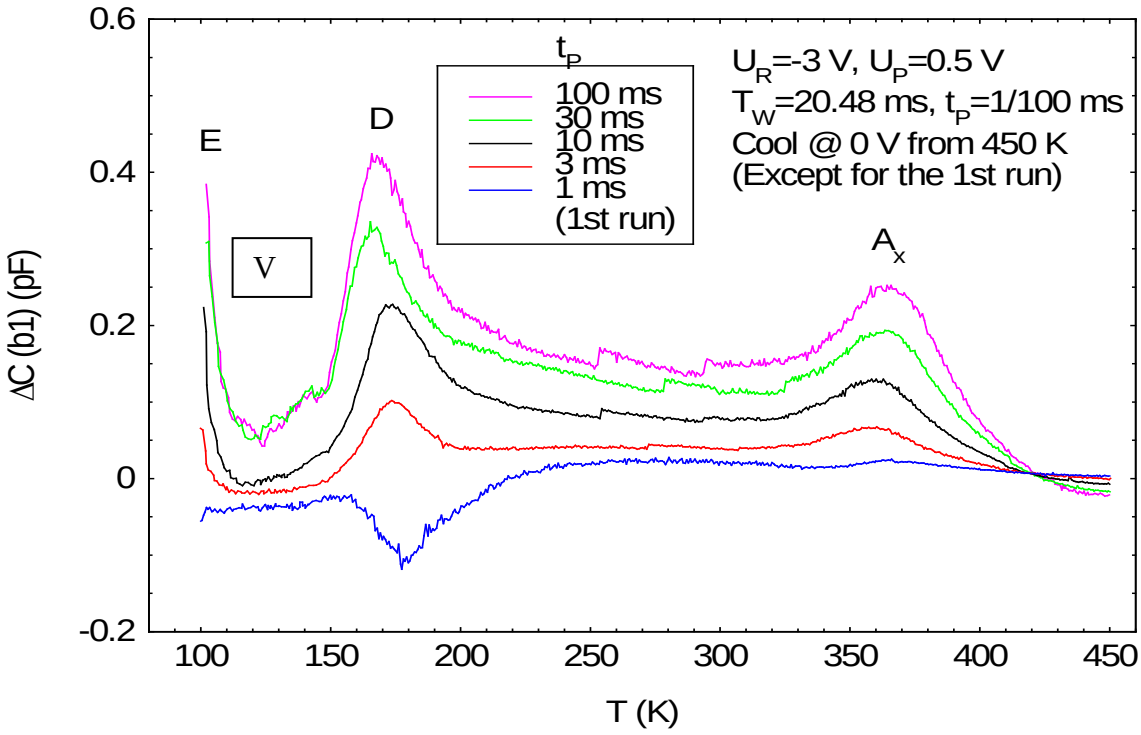

Figure 6.32. Dependence of DLTS signal on the tp, which indicates an association of these traps (A_x and D) with extended effects**.**

The unpassivated GaN cap sample shows fewer of the trap features, but in general, the traps shown are due to a number of measurement parameters. If the reasons are other than variation of measurement parameters, the observed traps could be due to radiation induced compensation, more likely to happen in the unpassivated GaN cap sample. It is also possible that the unpassivated samples encounter more damage to the SB metal, and some of the SB modulation that is needed to get good DLTS peak formation is lost due to radiation damage. Certainly the Casino models in Figure 5.51 show the unpassivated samples encountering more radiation intensity than the unpassivated samples. Notice that the unpassivated GaN cap has the radiation induced nitrogen interstitial but not the V_N that was shown for the previous AlN sample DLTS.

This could be due to the reasons just stated, or the fact that there is less V_N formation with a cap structure without the extra Si_3N_4 passivation. The AlN samples show more post radiation leakage current traceable to their associated DLTS. Figure 6.34 shows that N_I is radiation induced.

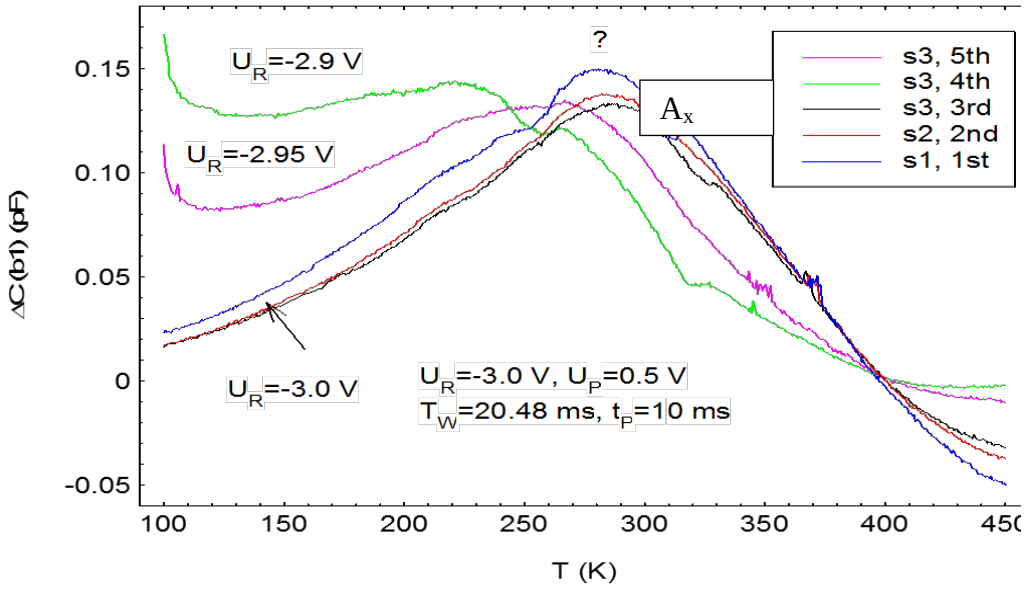

Figure 6.33. Unpassivated GaN/AlGaN/GaN E1 showing what is believed to be the radiation induced nitrogen interstitial at A_x. The various sx runs are for changing the probe location on the corner ohmics, where x =1, 2, 3 and the order of the run is indicated also. U_R is the reverse bias current.

.

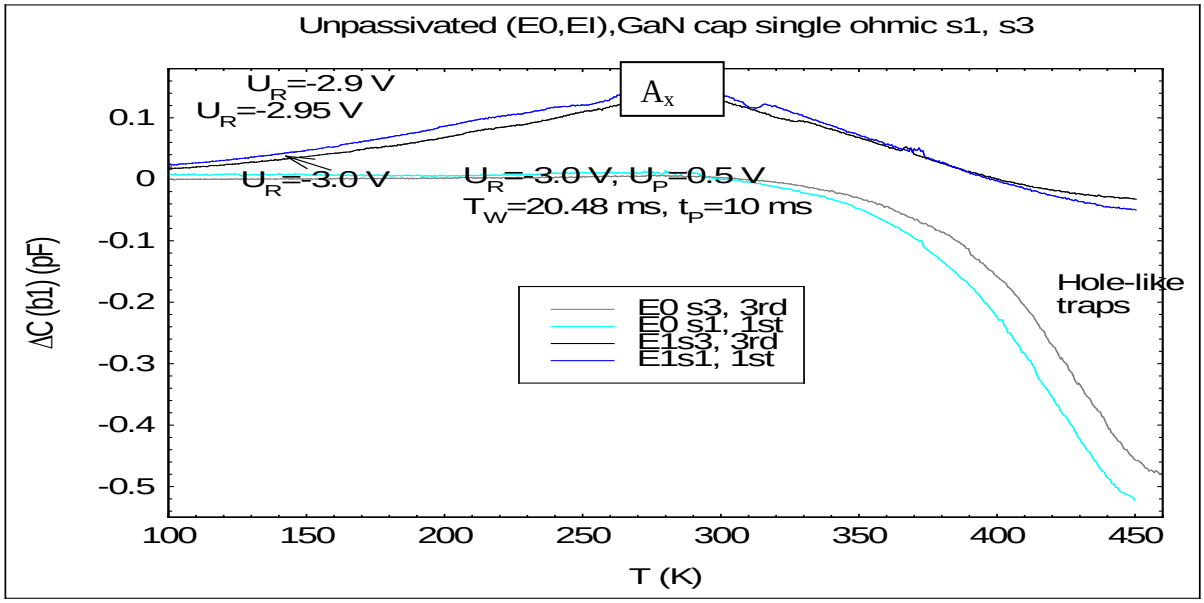

Figure 6.34. Unpassivated GaN cap E0 and E1 comparison showing radiation induced nitrogen interstitial at A_x.

VII. Analysis and Discussion

This results shown in chapters 5 and 6 reported the damage due to 1.0 MeV electron irradiation as a variation of Si_3N_4 passivation layers on two AlGaN/GaN HEMT structures. The fluence was $1x10^{16}$ electrons/cm^2 .The change in transport properties, photoluminescence, leakage current and capacitance voltage was studied to see how they affected these structures.

For the electrical transport mechanisms as measured by a Hall system, the use of Si_3N_4 prior to electron irradiation, the results and effect depended on the Si_3N_4 thickness layer and the particular device structure. The questions addressed where what was the effect of the Si_3N_4 layer and what was the effect of radiation. It was determined that electrons populating the 2DEG are from surface donors, according to the charge balance equation, now restated:

$$\sigma_{surface} + \sigma_{AlGaN} = q\, n_s \qquad (7.1)$$

Consequently, passivation will affect the balance as shown in equations 5.6 through 5.10. 1 MeV affects both the sheet charge density and alters the doping profile by changing the acceptor and donor populations, but introduces scattering centers that bring the mobility down.

With both the sheet charge density n_s and the mobility μ_n degraded as shown in the experimental results throughout chapter 5, the channel conductivity goes down and resistivity increases. Based on the results of this study, the Si_3N_4 changes some aspects of device performance positively and some negatively. The passivation can prevent virtual gate formation, but it also introduces more scattering defect centers and Schottky metal/

semiconductor interface traps that provide pathways to facilitate hopping conduction across the barrier and thus leakage current. It also has an effect on the electric field, due to the total charge balance changes .Given a fully functional transistor, a tradeoff can be made as to leveraging the protection provided by the passivation versus the additional gate leakage current introduced. Well-designed HEMTs will not has as much leakage current in baseline characterization measurements. However, even with transistors that measure as having much better n factors, intrinsic and radiation induced defects limit their lifetime and reliability. An analysis of the interrelationships between the intrinsic and extrinsic factors can facilitate a move toward achieving the balance for more reliable and efficient devices.

Even with a well-designed structure, there are still material and thermal limiting factors to performance, lifetime and reliability. This was shown in chapter 3, Figures 3.2 through 3.7. The as grown traps, defects and impurities change the way the device is ideally designed to operate. An analysis of the radiation induced damage in terms of how these traps and defects affect the observed changes as already been shown in the altered charge balance equations.

AlGaN/GaN HEMTs are field effect devices exhibiting strong fixed polarization charge at the AlGaN/GaN interface. Using Gauss's equation to examine the regional charge distributions by region of the device, as in Figure 2.3, the electric field change by region be seen and how it changes with passivation and radiation. Changes in the charges that sum this net charge brought about by the passivation and radiation induced traps, which carry their own differing charges and energies can help explain the radiation induced changes that degrade or preserve. Reducing or preventing virtual gates and

current collapse, is one of the reasons why Si_3N_4 is currently used. Varying the thickness of the Si_3N_4 on AlGaN/GaN HEMTs under 1 MeV electron irradiation is novel research which gave insight as to whether the thickness of the passivation layer made a difference or was important.

Previous references were given on studies which show how structural parameters affect the 2DEG; and this has been shown throughout the results in this study. The two structures used were AlGaN/AlN/GaN and GaN/AlGaN/GaN. The use of a GaN cap as in GaN/AlGaN/GaN has shown to prevent current collapse. The cap acts as a surface - charge control layer. It screens the 2DEG from surface traps by reducing the effect of surface polarization whereas an AlN interlayer adds to polarization. With the AlN structure, since the polarization vectors associated with the charge from the AlN are in the same direction as the AlGaN, the induced field that produces the 2DEG is greater relative to a structure without an AlN interlayer. As a result, there will be more transfer of charge and thus more electrons in the 2DEG. Additionally when Si_3N_4 is added as a passivation layer, this increases the sheet charge density.

The monotonic increments of carrier density with passivation thickness indicates that Si_3N_4 does affect surface states and that these surface states are donors. The change in the saturation capacitance as it relates to the change in the corresponding carrier density further verifies the effect of Si_3N_4 on the surface states. The effects are Si_3N_4 thickness dependent.

The radiation interacts with the shallow impurities in the E_D level under the conduction band and brings about a post radiation changes in the Pl. The post radiation changes result from transitions that involve complexing with these impurities.These

impurites are believed to be the source of the unintentional doping in n-AlGaN/GAN. Another conclusion is that the displacement damage, or more specifically radiation induced acceptors, are the main source of the device degradation and is verified by the various methods of characterization.

Chapter 5 results relate to chapter 6 results. The results that report the type of changes occurring with the 2DEG as a function of Si_3N_4 layer thickness post radiation that show the radiation response is Si_3N_4 layer thickness dependent. They correspond to but differ from changes in the schottky leakage current and capacitance measurements. When measuring the 2DEG channel, the increased passivation provides a sheild against radiation, and Casino models shows in Figure 5.44 that at least for 50 nm passivation the range of hits is reduced. The increase in passivation layer thickness however, with the extra radiation induced defects, as shown in Table 5.4.

Studying the variation of passivation layer thickness can give an insight of the surface states as well as interface states and their associated traps that can degrade performance prior to irradiation. Studying this the post irradiation changes show changes in doping density that electrically change the device. With the results from the 1.0 MeV irradiaton damage, ,a template can be derived for the performance limiting traps and defects in a spaceborn, radiation intense environment. Trapping effects keep a device from functioning in the manner for which it was designed to perform. They divert current from its intended path by mechanisms such hopping conduction and then tunneling that increase the gate leakage current, and then furhter change the power requirements for switching the device off and/or on.

Hall measurements show the GaN becoming more p type in the AlN structure at room temperature, due to the radiation induced creation of acceptors. There is then both a decrease the 2DEG sheet charge density and mobility, mitigated to some degree with an optimun passivation layer thickness.

Analyis and conclusions for each method of characterization for which results were given in chapters 5 and 6 will be given and which include analysis and discussion to the investigative questions to be anwered by this dissertation research. The investigative questions to be answered are: how do the response of the transport characteristics (such as the mobility and carrier density) and gate current measurements under 1.0 MeV electron irradiation depend on the particular device structure and the Si_3N_4 passivation thickness layer.

7.1. Conclusions on the Radiation Effects and Si_3N_4 Thickness on Hall Transport Mechanisms

The analysis of the effect of Si_3N_4 layer thickness and post irradiation observed results will be given in this section. For both structures, this will include an analysis of the carrier sheet density, pointing out the differences in the electric field, the mobility models, mobility as relates to sheet carrier density, the charge balance model, and then the overall Hall carrier transport analysis.

7.1.1. Modeled Sheet Carrier Density and Electric Field Height

In chapter 5 the conduction band diagrams and electron 2DEG densities were modelled for each structure and then with changes with 50 nm passivation layer thickness

.The differences in 2 DEG sheet charge densities are structure dependent, as was shown throughout chapter 2. This was defined in equations 5.6 through 5.10 charge balance equations that gave the sum of the charges that cause population of the 2DEG. Other factors leading to the change in sheet charge density due to structure are the change in ϕ_s , ΔEc , and the changes in σ that change the electric field effect shown in equations 2.33 thorough 2.36.

Along with the variation of carrier density due to structure there are changes in the fixed electric field the either the AlN/GaN interface or AlGaN/ GaN interface. This is shown in the modelled differences in electric field, Figure 7.1. The AlN structure on the left shows a higher field, as would be expected due, to the additive polarization vectors effect of the interlayer. The GaN caps lower field is due to the polarization vectors going in opposite direction.

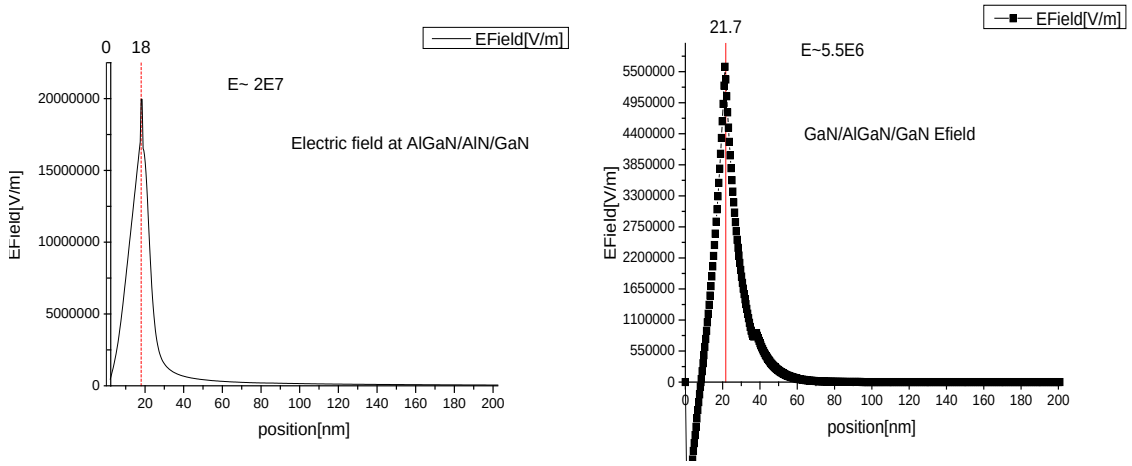

Figure 7.1. Modeled electric field is higher at the AlGaN/GaN interface for the AlN structure on the left and the GaN cap structure on the right resulting in a higher 2DEG sheet charge density.

The differences in sheet charge density were shown in chapter 5, Figures 5.4 through 5.14, for the changes in structure. Applying Gauss' law, equation 2.8, to the interface areas, and applying equations 2.9 and 2.10, the observed differences in carrier density can be explained. Figure 7.1 shows that the field and thus the effect is different at the 2DEG interface when the structures are different.

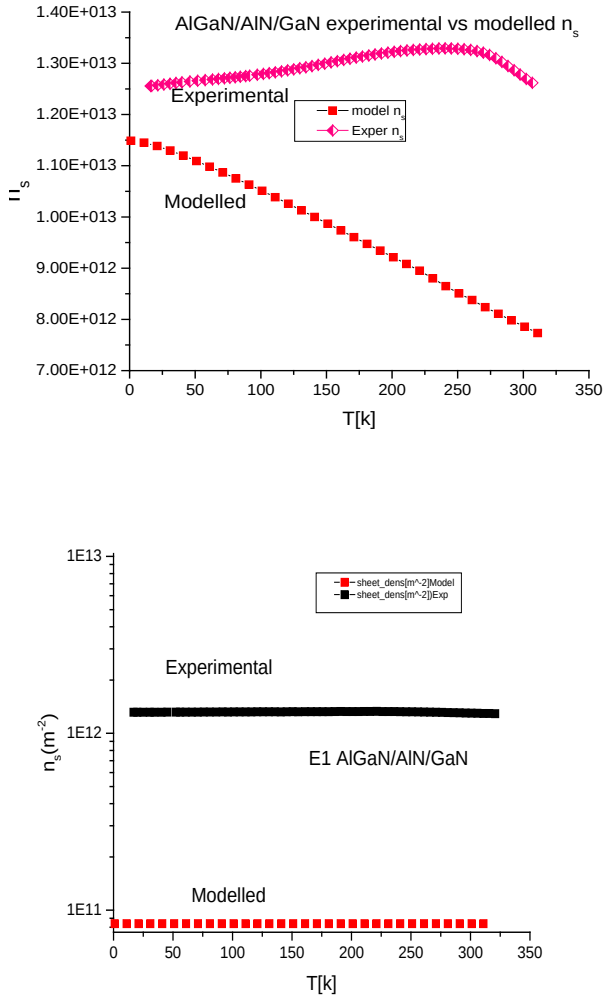

Figure 7.2. Carrier density as a function of temperature before (E0) experimental and modeled on the left the post irradiation (E1) on the right.

As opposed to the modeled, the experimental temperature dependent carrier density shows little temperature dependence until 300 K, where the Fermi distribution function for impurities and defects has a temperature dependence, in equation 2.38. At 300 K the thermal velocity of electrons contributing to the Hall measurement are thermally activated and can travel distances of tens of nanometers, thereby changing the density of the channel electrons.

Since the source of the 2 DEG electrons are the AlGaN surface states, then a corresponding decrease in the 2DEG sheet charge density would mean a decrease in surface donor states that could be the result of a large amount of acceptor states being created by the radiation. Effectively, the doping density for an n-GaN structure is changed by the radiation.

For the cap structure, the decrease in 2DEG sheet density with the comparatively greater separation between it and the 2DEG interface may be a factor that modifies the electron scattering mechanisms, and thus the mobility, as compared to the ALN structure. For the the temperature dependent sheet carrier densities shown in Figures 5.26 and 5.27 the GaN cap in GaN/AlGaN/GaN cap lowers the 2DEG as compared to the AlGaN/AlN/GAN for some of the reasons just stated . Since the scale on which the results is plotted is very fine, the changes in carrier density are not as large as the accompanying mobilities discussed in the next section. There is dependence of the 2DEG in the GaN/AlGaN/GaN heterostructure on both the GaN cap and the Si_3N_4 thickness. Looking at Figure 5.12 and the carrier density given by equation 2.39 in chapter 2, a conclusion can be drawn about effect of the cap in lowering the sheet carrier density; it is due to the ϕ_s term being subtracted in the sheet charge n_s equation. The ϕ_s in the GaN cap

structure is a result of the oppositely aligned polarization vectors at the GaN/AlGaN interface.

Post radiation DLTS defect analysis shows the beam is both destroying and creating donors (E trap) and creating acceptors (A traps). If it is creating acceptors in GaN, the 2DEG competes with acceptors and the $\sigma_{surface,E1}$ term is equation 5.12 decreases. Or if it is destroying surface donors, the $\sigma_{Buffer,E1}$ term in equation 5.12 increases; this would be destroying donors that are providing electron carriers for the 2 DEG.

7.1.2. Charge Balance Model for Sheet Carrier Density

Using equations 2.35 and 5.13, a model for the 2 DEG sheet charge for a structure with AlN is:

$$\sigma_{pz,AlGaN} + -\sigma_{pz,\,AlGaN} + {}^{+}\sigma_{AlGaN} + \sigma_{Buffer} + \sigma_{\,surface} + -\sigma_{\,AlGaN} + {}^{+}\sigma_{AlN} + \sigma_{pz,\,AlN} + -\sigma_{pz,AlN} = q\, n_{s,AlGaN/AlN} \tag{7.2}$$

Which is combined equation in 2.37 that incorporates the conduction band offset of AlN /GaN:

$$n_{s,AlGaN/AlN} = \frac{\sigma_{AlGaN} * t_{AlGaN} + \sigma_{AlN} * t_{AlN} \;\; -\frac{\varepsilon\,\varepsilon_0\,\varphi_B}{q} + \frac{\varepsilon_0 \varepsilon\,(\,\Delta E_{c,AlGaN}\,)}{q^2}}{t_{AlGaN} + t_{AlN} + d_0}$$

$$= \frac{\sigma_{AlGaN} * t_{AlGaN} - \;\; \frac{\varepsilon\,\varepsilon_0\,\varphi_B}{q} + \frac{\varepsilon_0 \varepsilon\,(\,\Delta E'_{c,eff}\,)}{q^2}}{t_{AlGaN} + t_{AlN} + d_0} \tag{7.3}$$

Using 5.14 correspondingly for the structure with the GaN cap, which has less of a sheet carrier density compared to the AlN structure:

$$\sigma_{pz,AlGaN} + -\sigma_{pz,\,AlGaN} + {}^{+}\sigma_{AlGaN} + \sigma_{Buffer} + \sigma_{\,surface} + -\sigma_{\,AlGaN} + {}^{-}\sigma_{Cap} + \sigma_{pz,\,Cap} + -\sigma_{pz,Cap}$$

$$= q\, n_{s,Cap(\varphi_B)} \tag{7.4}$$

With setting the right hand side of the equation to the calculated sheet carrier density in equation 2.39:

$$n_{s,cap} = \frac{\sigma_{AlGaN} * t_2 + t_1 - \frac{\varepsilon\, \varepsilon_0\ \varphi_B}{q}}{t_1 + t_2\ d_0} \tag{7.5}$$

A distinction can be made based on how equation 7.3 changes with a conduction band offset and equation 7.4 changes with its surface potential. After irradiation, from equation 5.11 the charges most affected by radiation are:

$$\sigma_{AlGaN} + \sigma_{Buffer} + \sigma_{surface} + -\sigma_{AlGaN} \tag{7.6}$$

Using the calculations leading up to equation 5.13, the post irradiation irradiated charge balance equation for a passivated AlN structure will be:

$$q\, n_{s,AlN} - \Delta\sigma_{AlN,E1} = q\, n_{s,AlN,P,E1} = q\, n_{s,AlGaN/AlN} \tag{7.7}$$

which would include the ΔE_c as well changes in ϕ_B

For the GaN cap structure, the post radiation passivated sheet carrier density can be expressed as:

$$q\, n_{s,Cap} - \Delta\sigma_{Cap,E1} = q\, n_{s,\,Cap(\varphi_s),P,E1} \tag{7.8}$$

Equations 7.7 and 7.8 would include the donor and acceptor population changes. N_A and N_D shift in the charge balance relationship in equation 7.6 due to irradiation and are incorporated in the charges. The increased acceptor charges would be negative and thus decrease the sheet charge density qn_s as well as all observed results that contribute to $q\, n_s$.

7.1.3. Mobility Analysis

As has been cited in previously in Chapters 3 and 5, the high energy electron irradiation experiments by D.Look et al (Look, 2001) that revealed the creation of shallow donors as well as deep shallow acceptors. These defects create scattering centers and thus decrease the net mobility. The scattering is coulombic and occurs mostly outside the 2 DEG region, which is very thin and won't contain many defects.

Referring back to Figures 5.24 and 5.25, the decrease in mobility for all passivation thicknesses is due to fact that the acceptor type defects (charged) that are created by the 1.0 MeV electron irradiation scatter more than the donor type (which are neutral). More acceptors than donors are created. The just discussed carrier density decreases with irradiation because of the creation of these acceptors which compete with the 2DEG carriers. The post radiation reduction in mobility should be linked to post radiation carrier scattering mechanisms by way of equation 5.16. The additional radiation induced scattering in equation 5.16 is due to increased ionized impurity scattering (Look, 2001) and displacement scattering. The defects are created mostly in the AlGaN (McClory, 2008) where thought to be acceptor type or N vacancies V_N, as the minimum displacement energy for N is lower than Ga. However, the V_{GA} acceptor defects are the ones created in the bulk and that take away from the 2DEG. The N interstitials are the other part of the Frenkel pair resulting from the displacement of a nitrogen lattice atom and form the deep traps that increase trap assisted tunneling of the gate currents through the Schottky and AlGaN barriers and lead to a leakage current. This will be discussed further in section7.5.The photoluminescence and DLTS will further identify these defects.

In the room temperature results in Figures 5.1 and 5. 4 in chapter 5, the GaN cap in GaN/AlGaN/GaN raises the mobility at 300 K relative to the same structure with no GaN cap, as Figure 2.10b. It is believed that because the 2DEG wave function lies very close to the AlGaN/GaN interface, Figure 7.3b, the electrons are susceptible to any physical processes occurring at the interface, such as roughness scattering. The AlN separates the 2DEG wave function from the interface to a greater degree 7.3a, but the cap yields less electrons Figure 2.11 and equation 2.35, and thus less electron-electron scattering within the 2DEG quantum well. The comparison can be made a structure with AlN vs no AlN structure, as in Figure 7.3.

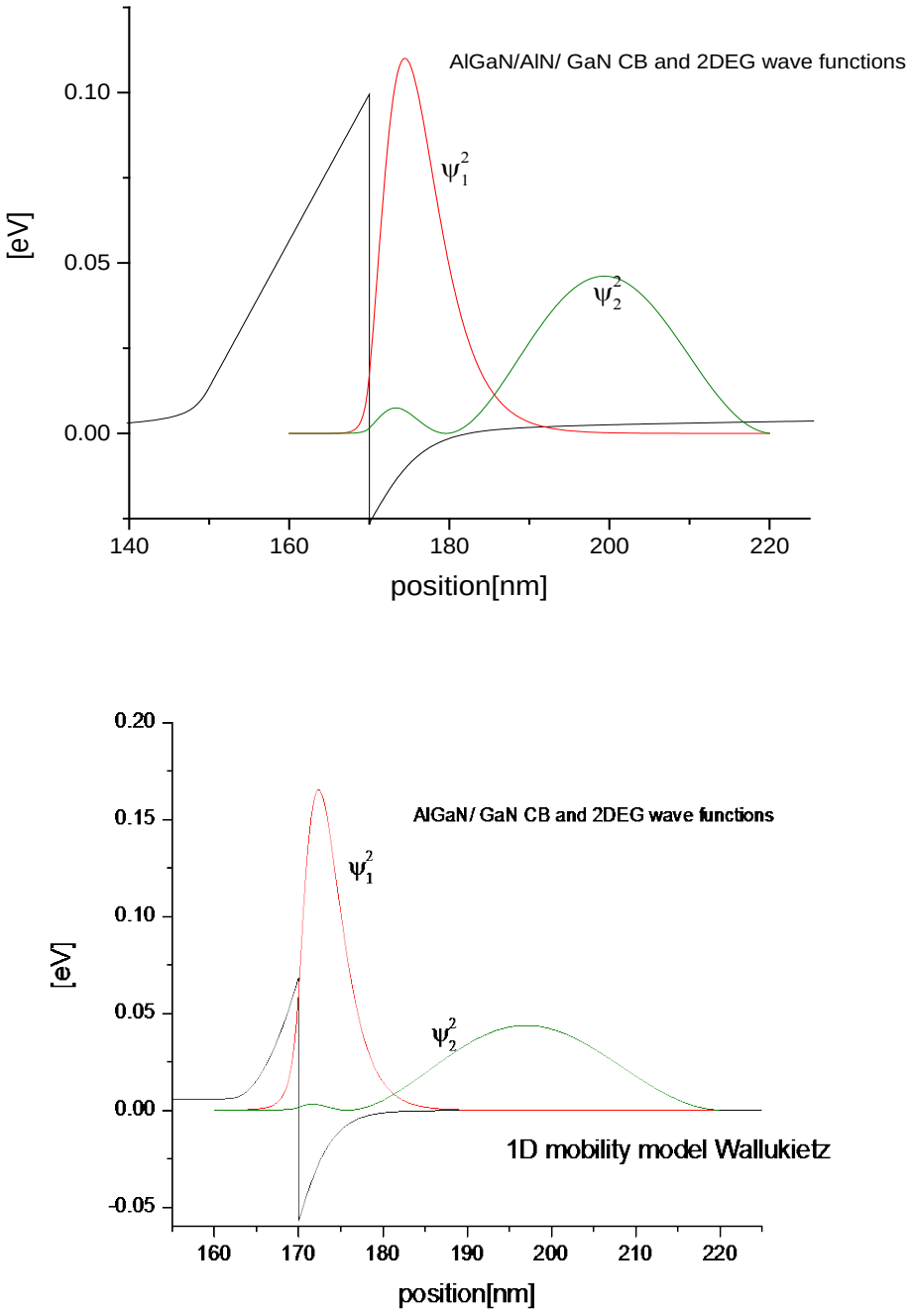

Figure 7.3. The first and second modeled 2DEG wavefunctions. The left side has a spacer which is equivalent to an AlN, and the right side has no spacer and therefore its first wave function touches the barrier and introduces additional scattering.

In Figure 5.1, the mobility decreases at 20nm, is approximately the same at 50nm and increases for 120 nm with the use of a GaN cap as compared with samples without a cap. The increase or saturation level effect may be explained by the number of fully occupied or partially occupied subbands. Sheet carrier density saturation occurs at 50nm with an AlN structure and due to processing variability's, as early as 20 nm of Si_3N_4 passivation, for a GaN cap structure. With the GaN structure, shown again in Figure 7.4, with 50 nm passivation thickness, there is a combined 52nm above the AlGaN. As shown in the GaN cap carrier density data, in going over 50 nm passivation layer thickness, saturation occurs.

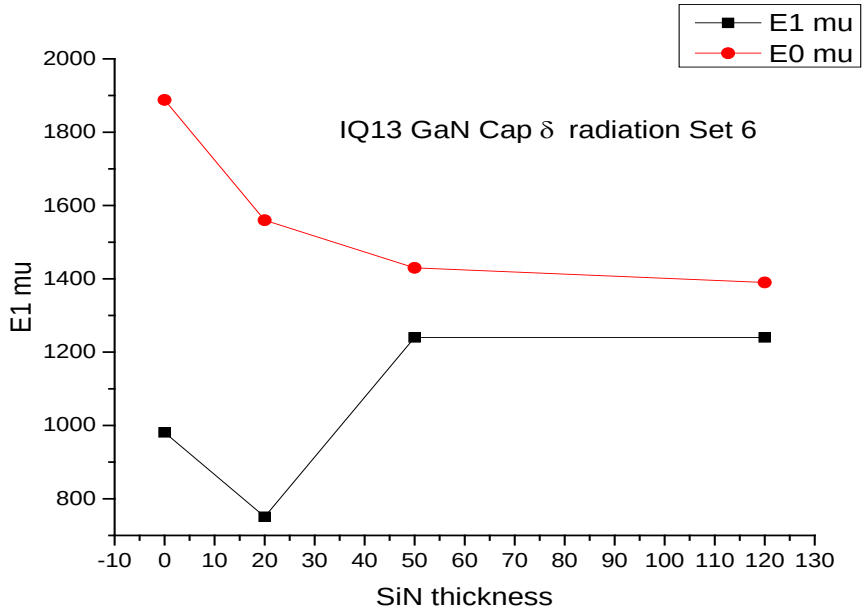

Figure 7.4. The comparison between pre and post radiation in a GaN cap sample, showing at 50 nm passivation thickness the sample has mobility of ~1500 cm^2/V-S post radiation.

7.1.3.1. Mobility Fits and Modeled Scattering

The dominant scattering mechanism at 300 K is phonon scattering, in particular polar optical, whatever the structure is, Figures 5.5 through 5.9. For the capped structure, only the intrasub-band scattering within the 1st sub-band is important in the room temperature polar optical phonon scattering mechanism. In addition to increasing the sheet carrier density, increasing of the thickness of the S_3iN_4, which may also be increasing tensile strain, leads to decreasing mobility.

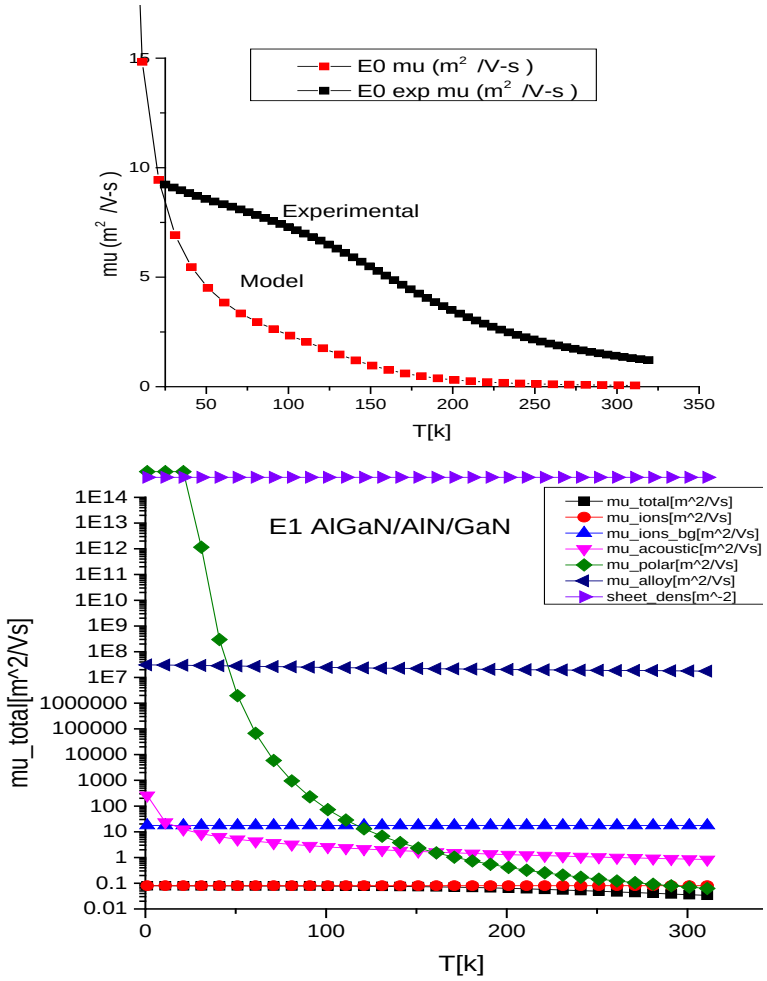

Figure 7.5. E0 mobility, modelled vs. experimental mobility for AlGaN/AlN/GaN on the top, the E1 total mobility as a function of scattering mechanisms on the bottom.

In Figure 7.5 (top), the modeled mobility incorporated the scattering mechanisms given in Table 5.1. The modeled mobility is lower and more temperature dependent than the experimental because it assumes a higher contribution from the scattering mechanisms. In Figures 5.5 through 5.9 the modelled changes in scattering mechanisms as a function of structure variation was shown. In Figures 5.5 and 5.7, because of the m^{-2} relationship these scattering mechanisms have to the total mobility, alloy scattering in the structures with an AlN is only a fraction of its contribution as compared to the GaN cap structures in Figures 5.10 and 5.11, where it is a large contribution. With passivation on the AlN structure it nearly disappears until 310 K is reached, but it continues to be a large contribution to the scattering in the passivated GaN cap structure. The passivation layer eliminates much of the ionized background scattering both structures. Ionized impurity scattering is decreased with passivation for the AlN structure but changes only slightly for the GaN cap structure. Acoustic phonon scattering is greater in the AlN structure than the GaN cap structure, but passivation reduces it for the former and increases it for the GaN cap structure. So knowing how passivation changes selected scattering mechanisms and thus the total mobility, one can determine how to engineer a structure to control the mobility.

Post irradiation, taking into consideration the additional scattering centers created by the radiation, the components of the total mobility μ_c given in equation 5.1, $\tau^{-1}{}_{dis}$ as well as $\tau^{-1}{}_{ii}$, would be increased and therefore the mobility decreased. Figure 7.5 (bottom), for an AlGaN/AlN/GaN structure shows that now ionized impurity scattering the biggest contribution to the modeled post irradiation mobility. The ionized background scattering has also increased.

The post irradiation Pl measurements can explain the post irradiation Hall measurements. The post irradiation photoluminescense spectra qualitatively show the increase in V_N and V_{Ga}, acceptor scatterers, and the Hall data quantitatively verifies this by showing a decreased sheet carrier density as well as decreased mobility. There is more post radiation scattering since the acceptor type defects (charged) that are created by the 1.0 MeV electron radiation scatter more than the donor type defects (which are neutral). More defects are likely to be created in the AlGaN. The minimum displacement energy is E_d = 66 eV for nitrogen and E_d = 38 eV for gallium so more gallium vacancies are created. In addition to changing the Hall measurements, radiation induced acceptors form the deep traps that increase trap assisted tunneling in the Schottky (gate) currents and lead to leakage current. This will be discussed in the I_g-V_g and DLTS analysis.

7.1.4. Overall Hall Carrier Transport Measurement Analysis

In the previous chapters it was shown that the 2DEG gets its electrons from the AlGaN surface, and that Si_3N_4 increases the net positive charge that populates the 2DEG in the charge balance equation. This is because more donor electrons are available to be transferred to the channel. Studies (Kordos et al, 2006) have shown the effect of increases in tensile strain are equal to the increases in sheet carrier density. This would fit into the charge balance model, because strain translates into piezoelectric charge.

So the observed conclusions for carrier density changes due to passivation layer thickness are compounded with the tensile strain; there appears to be a linear increase in the carrier density for thicknesses over 50 nm pre radiation. Post radiation there is a significant loss of electrons due to the creation of acceptor sites in the unpassivated

sample, while there is a preservation of the carrier density for the passivated samples. There are polarization induced fields in the GaN cap, AlN, AlGaN and the Si_3N_4 that can be additive if parallel or that can be anti-parallel, which all effect the charge balance equation model.

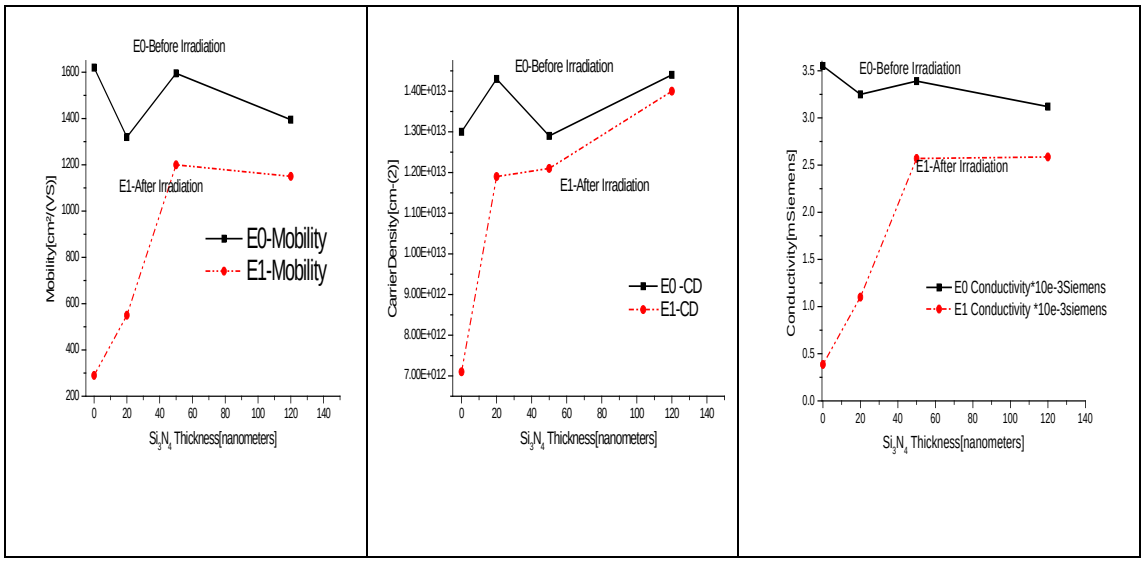

Figure 7.6. RT Changes in (a) mobility, (b) carrier density and (c) conductivity as a function of silicon nitride thickness before (E0) and after 1 MeV electron radiation (E1).

The unpassivated sample in Figures 7.6 shows the degradation of the transport properties of the AlGaN/GaN structure under 1 MeV electron irradiation (E1) at a fluence of 10^{16} cm^{-2} at room temperature. In Figure 7.6a, with a 300 % improvement in mobility for the 120 nm sample and a 314% improvement for the 50 nm sample over the unpassivated sample, a *claim* can be made for substantial improvement and preservation of the device. Figure 7.6 c shows that the conductivity improvement is approximately a factor of 8 in the 120 nm over the unpassivated sample. A silicon nitride thickness of at least 50 nm is needed to gain the improvement in conductivity, whereas for carrier

density a 20 nm thickness brings about improvement. Figure 5.26 shows the decrease in mobility due to irradiation in the unpassivated E1 at low T is a factor 31 while that in 1200 E1 (120nm) passivated is less than 2. The Table 7.1 below are the source of the data for the conclusions shown in Figures 7.6.

Table 7.1. Summarized averaged Hall system results radiation effects on the AlN structure.

Sample	position	Nitride thickness	Irradiation dose	Mobility at 300 K	Concentration at 300 K	Conductivity
0E0	(07,06)	0 Å	0	1620	1.30×10^{13}	3.54
0E1	(07,06)	0 Å	10^{16} cm^{-2}	290	0.71×10^{13}	.387 ↓89%
200E0	(05,06)	200 Å	0	1320	1.43×10^{13}	3.25
200E1	(05,06)	200 Å	10^{16} cm^{-2}	550	1.19×10^{13}	1.09↓66%
500E0	(05,02)	500 Å	0	1595	1.29×10^{13}	3.39
500E1	(05,02)	500 Å	10^{16} cm^{-2}	1200	1.21×10^{13}	2.37↓30%
1200E0	(07,04)	1200 Å	0	1355	1.44×10^{13}	3.2
1200E1	(07,04)	1200 Å	10^{16} cm^{-2}	1150	1.40×10^{13}	2.49 ↓22%

Table 7.2 Summarized averaged Hall system results radiation effects on the GaN cap structure.

Sample	Wafer = IQ13/quadrant /Sample count	Nitride thickness	Irradiation dose	Mobility at 300 K	Concentration at 300 K	Conductivity at 300 K
0E0	0	0 Å	0	1830	1.150×10^{13}	3.365
0E1	0	0 Å	10^{16} cm^{-2}	1016, ↓ 45%	1.071×10^{13} , ↓ 24%	1.425 ↓ 57%
200E0	200	200 Å	0	1547	$1.42x\ 10^{13}$	3.5
200E1	200	200 Å	10^{16} cm^{-2}	695 ↓ 55%	1.23×10^{13}	.865 ↓ 75%
500E0	500	500 Å	0	1423	1.45×10^{13}	3.31
500E1	500	500 Å	10^{16} cm^{-2}	1096 ↓ 23 %	1.31×10^{13} 10% , ↓	2.383 ↓ 28%
1200E0	1200	1200 Å	0	1410	1.37×10^{13}	3.145
1200E1	1200	1200 Å	10^{16} cm^{-2}	1007.6 ↓13.7%	1.29×10^{13} , ↓6%	2.1 ↓33%

Summarizing averaged Hall system results radiation effects on the GaN cap structure.

1. Number of defects created based on changes in carrier density before and after radiation are: From $1.150\ x10^{13}cm^{-2}$ to $1.071\ x10^{13}cm^{-2}$ means there was an electron loss of $0.079 \times 10^{13}cm^{-2}$ or defects created in GaN (2DEG).
2. This is $1.343\ x10^{10}$ cm^{-1} for 1.7 μm GaN buffer or 13430000 10^{10} nm^{-1} ,1.343×10^{7} nm^{-1} or in the GaN buffer 1.343 nm^{-1} to produce the given sheet change density

The fitted donor and acceptor concentrations have been shown to be 6.7 x10^{15} and 1.7 x 10^{15} cm^{-3} respectively. V_{GA} is often the dominant acceptor in undoped GaN.

Table 7.3 Loss of sheet carrier concentration post radiation

Si3N4 thickness	Δn_s
0	-.079 x E13cm^{-2}
20	.019 x E13cm^{-2}
50	.014 x E13cm^{-2}
120	.008 x E13cm^{-2}

Effect of electron irradiation is summarized in the following model:

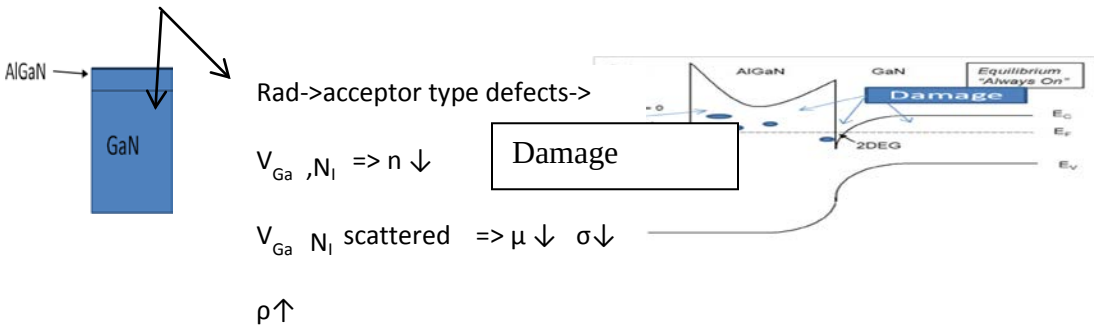

Figure 7.7. Simplified damage model for electron irradiation effects on AlGaN\GaN.

The production of Gallium vacancies and Nitrogen interstitials is at a rate of 1- 10 cm^{-1}, and the densities of these point defects would be 10^{16} – 10^{17} cm^{-3}. If the GaN buffer

layer is 1 μm, then 10^{17} cm^{-3} acceptor-type defects would produce a sheet acceptor charge of 10^{13} cm^{-2}, which is comparable to the 2DEG charge of 10^{13} cm^{-2}. The defect production algorithm in chapter 5, section 5.4, calculated a production rate of 23.9 $x10^{8}$ nm^{-3} for defects in the GaN with N and Ga. These defects would be the ones created by the primary 1MeV electrons and do not account for the secondary electrons or the backscattered electrons. So the total radiation induced defect population is actually the value stated by D. Look (Look, 2001).

7.2. Conclusions and Model for Radiation Effects Shown in Photoluminescence

The Si_3N_4 passivation layer shows a monatomic variation with PL intensity prior to 1MeV radiation, but not so for Hall system characterization. The post radiation Pl gives a 50nm peak and a 20 nm minimum in the deep center range, but then reverses to monatomic variation in the near band edge range. There is a shift in the main D^0 X center in the rear band edge do to mismatch lattice constants which results from tensile strain.

The Pl gives the spatial localization of impurities such as oxygen and silicon, which are precursors to the D^0 X centers, deeper impurities like magnesium, and V_n and V_{Ga} donor information.

The model that follows accounts for the observed changes in the Pl results shown in the Chapter 5 due to 1 MeV irradiation. The changes with Si_3N_4 thickness pre-irradiation were previously explained as due to the attenuation of the PL laser beam going through the material, and corresponded linearly to the thickness of the Si_3N_4 pre-irradiation, but not post irradiation.

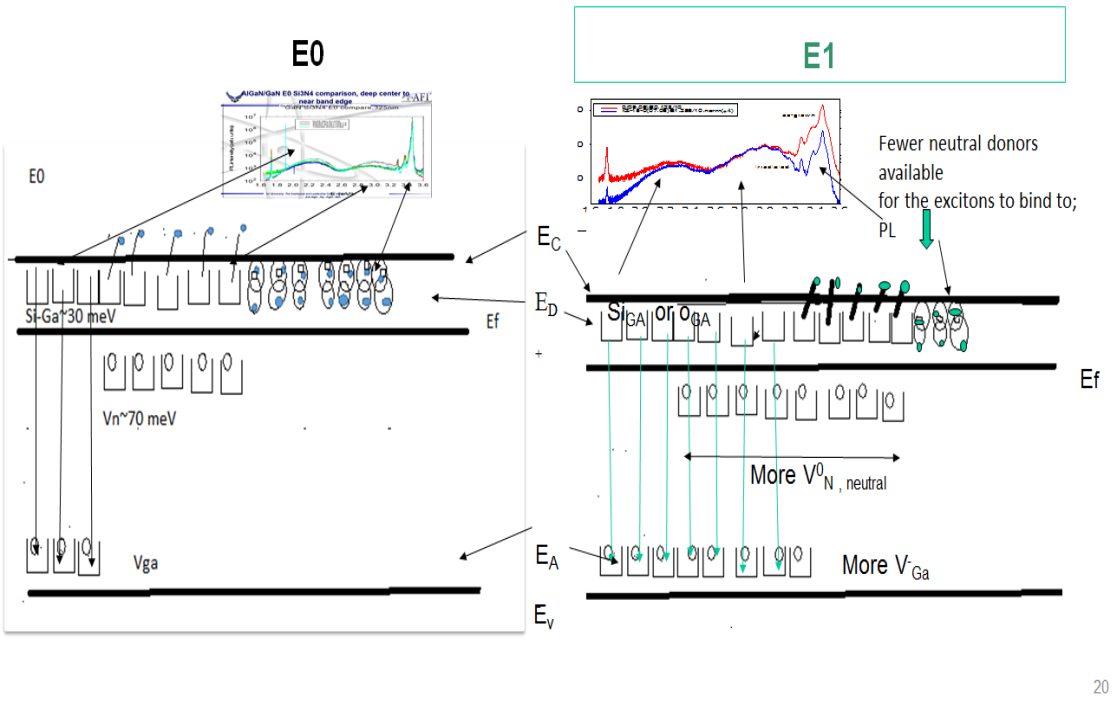

Figure 7.8. Model for radiation damage explaining PL peak changes and change in the Nitrogen and Gallium donor and acceptor populations.

The model in Figure 7.8 summarizes the PL radiative peak production events before and after 1.0 MeV electron. The diagram on the left is for pre-irradiation (E0), and on the right is for post irradiation (E1). For E0, below the conduction band, there is the donor, E_D level, which starts at approximately 30 meV; the donors here would be shallow donors. Above the valence band is the acceptor level E_A. Silicon is a known impurity in AlGaN/GaN, as well as oxygen. So at about 30meV, a positively charged Si^+_{Ga} will drop to E_A, according to temperature dependence. There are also Si^+_{Ga}, just below the conduction band in energy in the E_D level and V_{GA} just above the conduction band in

energy in the E_A level; the V_N which are closer to mid-state will retain their electrons because they are below the Fermi level, at about 70 meV.

Excitons, shown as the upper circle of the pairs on the right on the E_D level, bind to neutral donor, which are shown as the circle attached to them. Here the Si atom is neutral on Ga, Si^0_{Ga} ; excitons seek out and bind to neutral donors as described in chapter 2 sections 2.3.1.1 and 2.3.1.2 .Here it is proposed one is observing Si^0_{Ga} because the donors with the paired excitons are neutral as revealed in the near band edge PL peak, Figure 5.33. There are many neutral donor with which excitons can bind to in this area, so the PL peak is high in the near band edge area in the insert plot for E0 in Figure 7.8. While this model is showing Si as the neutral donor, but both silicon and oxygen peaks show up in the NBE peaks; oxygen (3.46 eV) and silicon (3.466 eV). Other models may propose oxygen as the neutral donor. The Pl signal in general is proportional an E_D-E_A model.

For the post irradiation, E1, shown on the right side of Figure 7.8, the near band edge centers are much lower and have degraded as was shown in Figures 5.35 through 5.38. With shallow center peaks, due to the collapse of exciton –bound to neutral donor, less of these pairs are available. The model indicates fewer neutral Si, and fewer centers that the excitons can attach themselves to. So the PL signal is lower. Post irradiation, there is still a large amount of silicon and/or oxygen atoms, although their electrons may have excited to a higher state; some will be remain neutral. Looking deeper in energy, when the sample is irradiated- the result is the creation of many V_{Ga} and V_N vacancies. For the V_{GA} in E_A, they now all may have electrons. The electrons from the Si^0_{Ga} and

Si^{+}_{Ga} all transition to additional acceptors created in the E_A level. With the V_N electrons, they drop down to form V_{Ga}- , negatively charged. Now $V_N \rightarrow V_N^{+}$,as electrons have been emitted.

In chapter 2 it was shown that the deep centers are Ga (YL) or nitrogen (BL) vacancy relate. In the case for the YL, the electron radiation is creating more V_{Ga}, but not enough to effect the intensity of the PL illumination, as can be seen in the E1 plot inset on the right side of Figure 7.8, which is also Figure 5.35. This indicates either saturation occurring at 2.2 eV or there are now less of the other atoms in the complex that form the transition, given in section 5.3.2 of chapter 5. The models shows V_{Ga} taking electrons from the Si, but it could also be a $V_{Ga} \rightarrow$O transition.

Post irradiation, the amount of silicon in the GaN may not be changing, but there are V_{Ga}, because 1 MeV electrons create $V_{Ga.}$, as well as V_N. While actually more nitrogen vacancies are created-they are electrically neutral so the creation of the V_{Ga} will have more of an effect.

This models analysis of the BL area is that the transition $V_{N->}Mg_{Ga}$, which creates the PL peak at ~3.0 eV, may not lead to a decrease in peak height because the radiation may not be affecting the Mg. Mg is needed in the transition, and the radiation is not creating more Mg, but it is creating more V_N. So the BL in the plot insert on the right of Figure 7.8 for E1 is not changed. These plots have been normalized relative to the near band edge peaks.

If $V_{Ga ->}O_N$, or $V_{Ga ->}Si_N$ is producing the YL, there is enough O or Si for PL peak formation post irradiation in the 2.2 eV area, and peak doesn't change as significantly. The Pl peak intensity won't change as much if the donor population is not strongly

affected by the radiation; the subsequent complexing centers necessary for the transition to occur at that energy are not strongly reduced.

The model in Figure 7.8 for the effects of 1.0 MeV electron irradiation on the PL can be summarized by the energy conservation equation, which also gives insight into the DAP changes occurring post radiation that effect other device characteristics:

$$E_{Donors,\,E1} + E_{Acceptors\,E1} + E_{Dxo,\,E0} = E_{Donors,\,E0} + E_{Acceptors,\,E0} + E_{Vn,\,E1} + E_{NI,\,E1} + E_{VGa,\,E1} + E_{GaI,\,E1} \pm E_{\hbar\Omega} + E_{formation} + E_{Dxo,\,E0\text{-}E1}$$

Table 5.3 in chapter 5 summarizes observed traps found by various methods including Pl and DLTS. For each observed change in PL peak, the results are summarized below.

Table 7.4. Pl Peaks for AlGaN/AlN/GaN, summary of the defect peaks. * If donor population not strongly affected by E1, PL won't change much.

	E0 0 to 120 nm Si_3N_4	**E1** 0 to 120 nm Si_3N_4
Si (shallow donor)	3.466 eV /(30meV below CB)	Exciton collapse –pairs ↓PL↓
Si^{+}_{Ga} or O_{Ga}	NBE-E_D /(30meV below CB)	PL↓ donor electrons to E_A
Si^{0}_{Ga}	E_D /(30meV below CB)	Electrons excited to CB amount↓ PL ↓
O (shallow donor)	NBE-3.46 eV/(30meV below CB)	Electrons excited to CB amount↓ PL ↓
BL	3.0 eV	E1 increasing V_N
V^{+}_{N}	70 meV –below E_f	E1 increasing
YL	2.2 eV (shallow acceptor)	*E1 increasing V_{Ga} So Pl not changing
Phonon peaks	~93 meV from DX	Shifted, degraded due to E1 displacement damage
Free exciton	3.478 eV	collapsed
V_{Ga}	E_A	Increased due to E1

7.3. Radiation Effects on Variation of Si_3N_4 Thickness on Schottky Leakage Current and Related Measurements

The forward bias in the AlN structure has some temperature dependence; post irradiation there is no temperature dependence of forward or reverse bias, indicating there is tunneling. The lack of temperature dependence pre irradiation in the reverse bias in Figures 6.1 through 6.3 in chapter 6 indicates there could be intrinsic material defect mechanisms causing the leakage current in the unpassivated structure. Additionally, the device design is a factor in leakage current. Other measurement techniques tie into the leakage current results. The DLTS in Figures 6.26 through 6.28 indicates a hole like trap H_1, a deep trap, in as grown material for unpassivated as well as passivated ,thought to be associated with threading dislocations which in turn can cause leakage current in the un-irradiated structure, explained in chapter 5. Leakage current in intrinsic as grown material is also associated with threading dislocations. One such example is identified in the Pl spectra for the YL at 2.2 eV. The PL reveal pre –irradiation defects that can be trapping centers, particularly due to their level in the band gap.

While passivation in general has been proven to be beneficial, for the sample set used in this research, AlGaN surface passivation with Si_3N_4 causes an increase of reverse bias leakage current and threshold voltage shifts left.

Post irradiation there is an increase in leakage current, but much less with the GaN cap structure as shown in Figure 6.7 in chapter 6. With this structure, since the defects introduced by Si_3N_4 are on the GaN cap passivation layer, there is less tunneling that leads to leakage current. All test structures showed a significantly high leakage current leakage current before passivation and irradiation, so all data measurements are

evaluated accordingly. To the contrary, Hall data showed with 50 nm passivation thickness the unmodulated channel current is preserved.

After electron irradiation, the Si_3N_4 improved the post radiation unmodulated channel conductivity over the un-passivated structures, but the tradeoff is that it caused increased Schottky leakage currents in I_g-V_g. The Schottky leakage current increase was more severe after irradiation in passivated HEMTs due to extra trapping in the Schottky area for the samples with an AlN interlayer. Due to the processing of the test structures in this research, it is believed that this extra trapping due to passivation exceeds that of commercially grown and fabricated devices.

In conclusion, the gate leakage current increase was more severe after irradiation in passivated HEMTs because of the added trapping centers due to both the passivation and radiation. Post radiation the lack of temperature dependence in the forward and reverse bias currents increased implying that the tunneling conduction contributing to leakage current increased. The effects of post radiation degradation are shown to be passivation interface dependent as opposed to Si_3N_4 passivation layer thickness dependent as in Figure 6.8 of chapter 6, but also as in Figure 6.7 of chapter 6, device structure dependent.

7.4. Radiation Effects on Si_3N_4 Thickness Variation on Capacitance Voltage and Related Measurements

The 300 k C_g-V_g for the 2 structures indicate a post raditaion V_{th} shifts ;the Hall carrier density data shows there are less carriers.The post radiation V_{th} shift for the GaN cap structure is less than for the AlN structure, indicating either the relative loss of

carriers is less or less trapping is occuring, even though it started with less carriers. The stretch out of the AlN sample C_g-V_g curves post irradition with passivation indicate the Si_3N_4 is introducing more interface traps in the Schottky area. The increase in Si_3N_4 passivation thickness when there is a GaN cap does not directly correspond to a linear increase in sheet carrier density because of the polarization/stress combinations that are not always additive for the components of equations 7.2 through 7.7 that account for n_s. Additionally, with a cap structure, the Si_3N_4 does not interface with the AlGaN, so while the passivation can change the field effect it will not passivate the surface donor traps. The however the GaN cap acts as a passivation layer, without contributing to an increase of 2DEG.

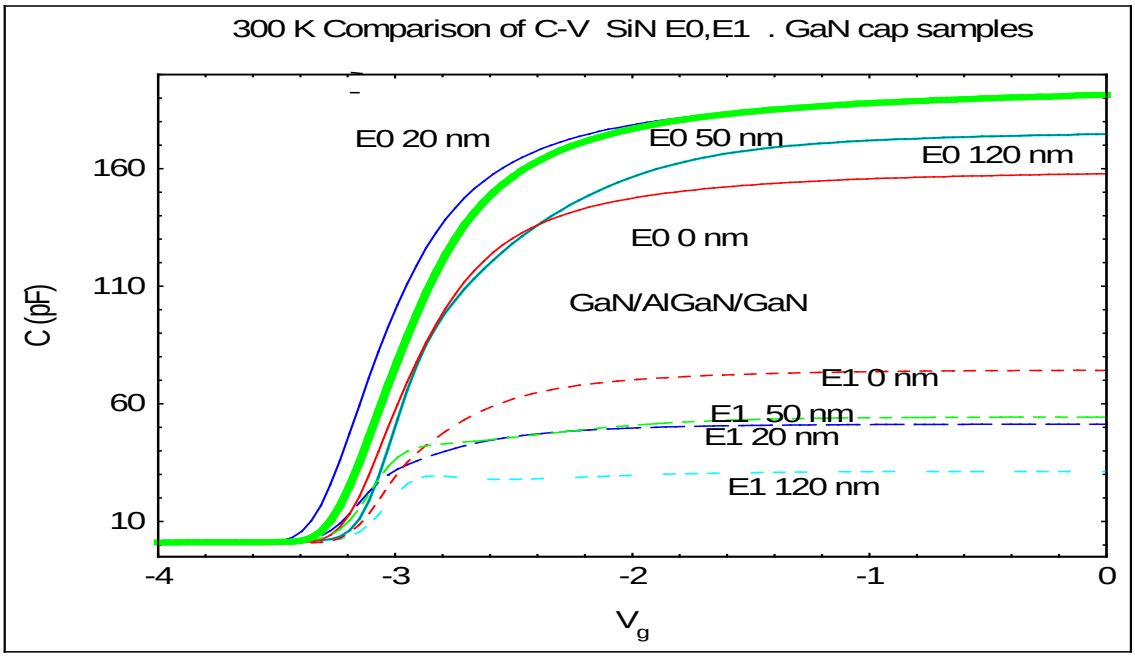

Figure 7.9. C_g-V_g showing threshold voltage shifts due to both radiation (dashed lines) and passivation thickness in GaN/AlGaN/GaN.

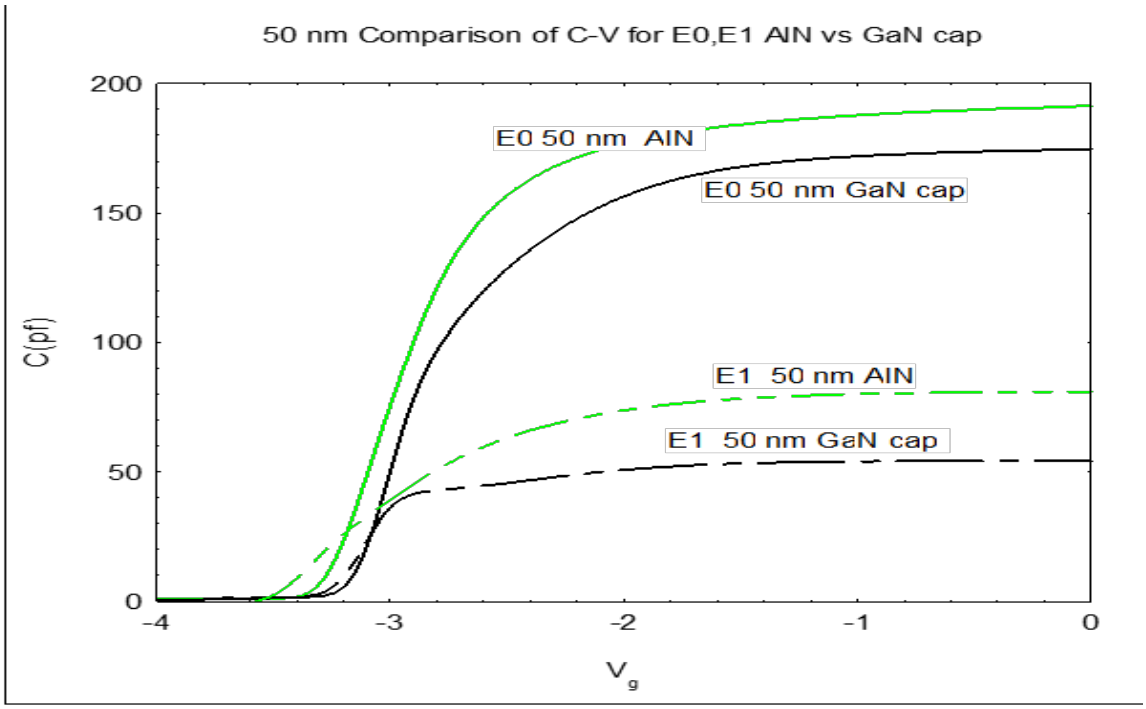

Figure.7.10. For these 50nm passivated samples, there is a threshold voltage shift right the GaN cap structure E1, corresponding to a decrease in carrier density, but for the AlN there is first right and as it stretches out in the depletion area due to N_{it} more of a negative bias is required for depletion.

The AlN structure has the highest saturation or "on" capacitance prior to irradiation, which is defined as the flat part of the curve in Figure 6.10 of chapter 6. Post irradiation, the decreased saturation capacitance in Figures 7.9 and 7.10 can be attributed to the decrease in carriers due to radiation induced acceptors and traps in the channel. The Hall data in Figures 7.6b and 6.19 of chapter 6 correlate to the saturation capacitance. The C_g-V_g curves stretch out in the depletion area (Schottky area) due to the radiation induced interface traps N_{iT}, which increase in density with Si_3N_4 thickness. As explained in the previous section on I_g-V_g, there is less tunneling with the GaN cap and there is not the stretch out of the C_g-V_g curves with higher passivation thickness in Figure 7.9. The passivation is performing a different role post irradiation when there is a GaN cap, but

there is a slight stretch out in the depletion region in the unpassivated and 20 nm thickness Si_3N_4. The increased passivation of 50 and 120 nm appears to decrease the interface trap buildup. The beneficial effects are further concurred in Figure 6.7 of chapter 6 for the use of a GaN cap with Si_3N_4 passivation. The measurements done for the C_g-V_g give results that are passivation layer thickness dependent, wherein a reverse bias is applied, which also resemble the thickness dependence shown in the reverse bias portion of the I_g-V_g in Figure 6.8 of chapter 6.

For the cap structure, the decrease in capacitance with Si_3N_4 passivation layer can be explained by the fact that GaN has a higher dielectric constant than Si_3N_4 in equation 6.4 b for which C_{tot} has a 1/ C relationship. Here there are 3 layers in series that contribute to the total capacitance. The distance between the Schottky metal and the peak waveform "d" is increased in the relationship $C = \varepsilon_0 A/d$ with a GaN cap, as in Figure 6.4b of chapter 6 can also explain the lower capacitance of a GaN cap structure as opposed to the structure with the AlN interlayer.

Si_3N_4 has the ability to passivate acceptors or donors, so a V_{th} shift left seen in Figure 6.12 of chapter 6 would be attributed to this. This can be observed in all samples with increasing passivation, with the exception of the AlN" 20 nm anomaly".

Post irradiation for the GaN cap structure, there is a V_{th} right in all the samples except 50nm of passivation thickness in Figures 7.9 and 7.10. The 50 nm of passivation in the AlN sample brings additional trapping that stretches out the depletion area left and requires more of a negative bias for depletion. For the GaN cap, 50 nm of thickness has no shift. The post radiation Hall carrier density shows a decrease in sheet carrier density for all samples except for the unpassivated GaN cap sample. With a lower amount of

carriers in the channel, less of a negative bias is required for the sample to reach depletion so V_{th} shifts right. With radiation induced traps, there can be hole-like trapping, and holes have a slower mobility, which in turn can lead to a positive charge buildup in the Schottky metal area.

Passivation generally improves device performance pre-irradiation. It creates higher carrier concentrations in the 2DEG, as shown in the carrier density data in chapter 5 section 5.2.3. Consistently, the chapter 5 results shows Si_3N_4 passivation preserves the channel mobility under 1.0 MeV electron irradiation with a minimum 50 nm passivation layer. The area of the channel, under the Schottky and controlled by the Schottky suffers decreased performance due to the trapping effects at the interfaces which are due to the extra trap centers brought about with the passivation and then radiation, just as in the Ig-Vg results. Some of this can be mitigated by better transistor design, as the results shown are for a HEMT epistack with limited transistor properties. In the post irradiation measurements, the passivation decreases the effect of changes in gate currents for GaN cap structures but has a somewhat reverse effect for the AlN structure, showing over all the GaN structure had less leakage current. Since the barrier height ϕ_B shown in Figure 7.11 is proportional to the inverse of the capacitance squared, C^{-2}, the lower capacitances of the GaN cap structures would imply a higher barrier height [Sze, p 230]. The relationships between V_{th}, ϕ_B, and the carrier density (via N_D) is shown in equations 7.10 and 7.11 and Figures 7.14 and 7.15 (in arbitrary units).

The Vth can be defined as:

$$V_{th} = \phi_B - \frac{\Delta E_c}{q} - \frac{q\, N_D\, d_d}{\varepsilon} \tag{7.10}$$

And the post radiation changes in ΔV_{th} should correspond to the post radiation changes in the sheet carrier density:

$$\Delta n_s = \frac{\varepsilon(x)}{qd}(-\Delta V_{th}) \tag{7.11}$$

The shifts are all left and give positive values for ΔV_{th}, which would mean the sheet carrier density decreases.

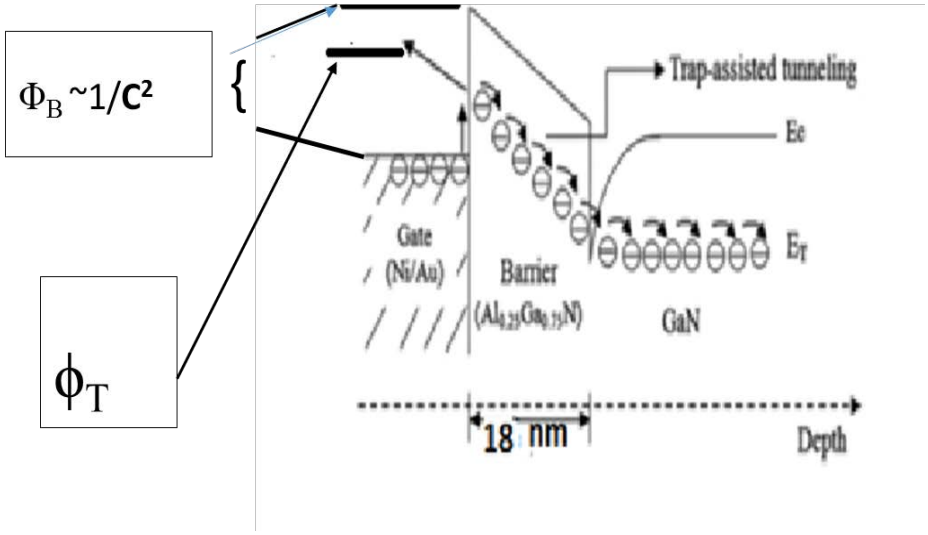

Figure 7.11. Figure showing the decrease in barrier height due to trap assisted tunneling, ϕ_B.

7.4.1. Changes in Threshold Voltage and Barrier Height and Tunneling Effects

The changes in barrier height in the Figures 7.12 and 7.13 show the passivation layer thickness and structure relationships, given in arbitrary units. Lower barrier heights can allow for more tunneling as demonstrated in Figure 7.11 above. Pre-irradiation, 50 nm and over increases the barrier height for the AlN structure, while for the GaN cap it appears to do statistically little accept for a slight lowering. The traps introduced by way

of radiation and or passivation lower the barrier, allowing for leakage current due to hopping conduction from trap to trap.

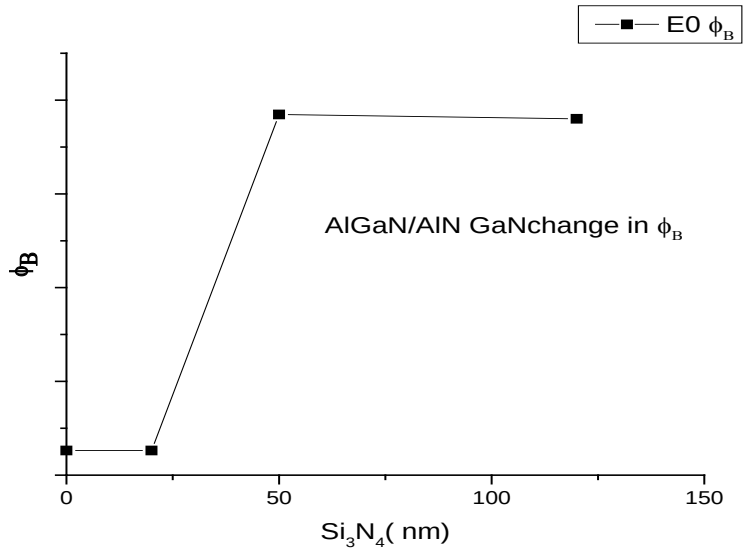

Figure 7.12 Si_3N_4 changes barrier height for AlGaN/AlN/GaN pre irradiation.

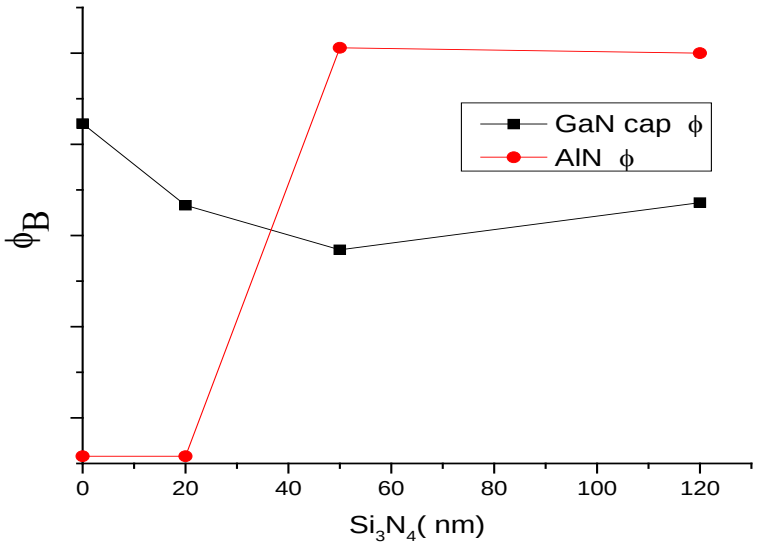

Figure 7.13. The barrier height differences due to structure as a function of passivation thickness, showing that before irradiation 50 nm and above increase the barrier height in AlGaN/AlN/GaN but first decrease it in GaN/AlGaN/GaN and then it climbs back up.

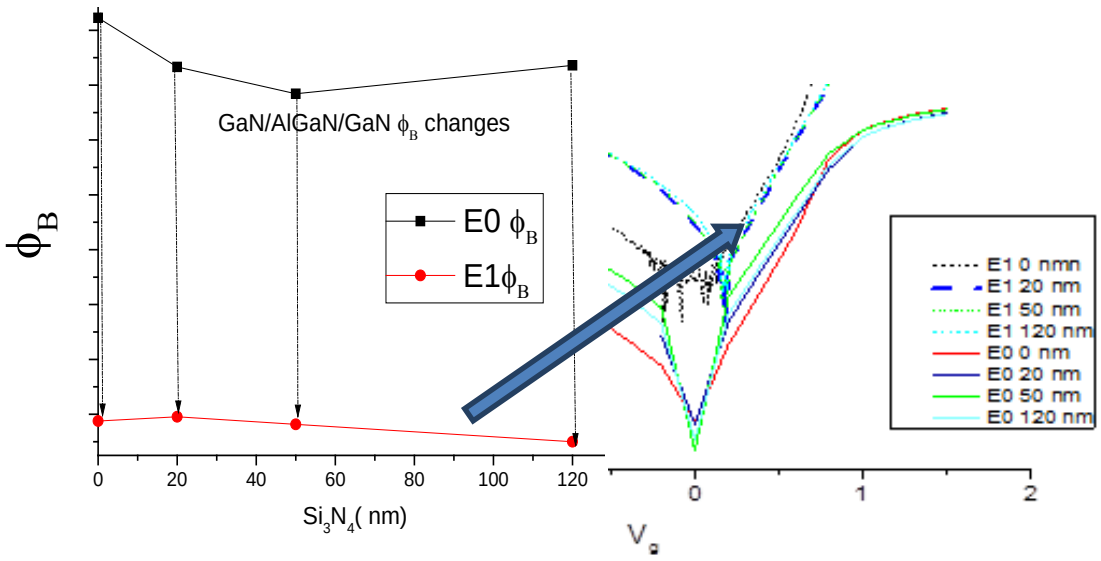

Figure 7.14. The degradation in barrier height with 1 MeV radiation for GaN/AlGaN/GaN, showing it is least for 50 nm passivation thickness. The enlargement of the forward bias in Figure 6.8, chapter 6 is on the right.

Post radiation, the relative decrease in barrier height for the GaN/AlGaN/GaN structure is slightly less with 50 nm passivation, although the effect of passivation seems more interface dependent than thickness, as in shown in the E1 forward bias in Figure 6.8, chapter 6. The highest leakage currents post irradiation can be linked to the highest degradation in barrier heights on the left. The 20 and 50 nm E1 leakage currents are statistically equal, as are their E1 barrier heights, although 50 has the lowest percentage of change.

Table 7.5. Experimental changes in pre and post radiation threshold voltage shift, carrier density and barrier heights.

Si_3N_4 Thickness	ΔVth	Δn_s	$\Delta\phi_B$
0	0.138 positive	-.079 x $10^{13}cm^{-2}$ $\downarrow$	2.93987$\downarrow$
20	0.718 positive	-.019 x $10^{13}cm^{-2}$ $\downarrow$	2.55084$\downarrow$
50	-0.03938 negative	.014 x $10^{13}cm^{-2}$ $\downarrow$	2.41042$\downarrow$
120	0.0848 positive	.008 x $10^{13}cm^{-2}$ $\downarrow$	2.74491$\downarrow$

Table 7.5 summarizes the changes in post irradiation sheet carrier density, threshold voltage shift and barrier height in Figure 7.15. The decrease in carrier densities are 24%, 13%, 10%, and 6 % for the 0, 20, 50 and 120 nm samples. The decrease in barrier heights are 29%, 26%, 25% and then 28%. The changes in ΔVth, Δn_s , and $\Delta\phi_B$ that go into equations 7.8 and 7.9 can begin to explain the observed post radiation changes seen the in I_g-V_g, C_g-V_g and Hall carrier density in this dissertation research as well as inter-relate them.

Compared to the un-irradiated sample, the 50 nm passivation sample has the least amount of barrier height decrease, while it suffers a 10 % loss in carriers, which could mean there is less tunneling at this thickness. The Vth is shifting right as equation 7.9 would imply, due to the negative change in carriers.

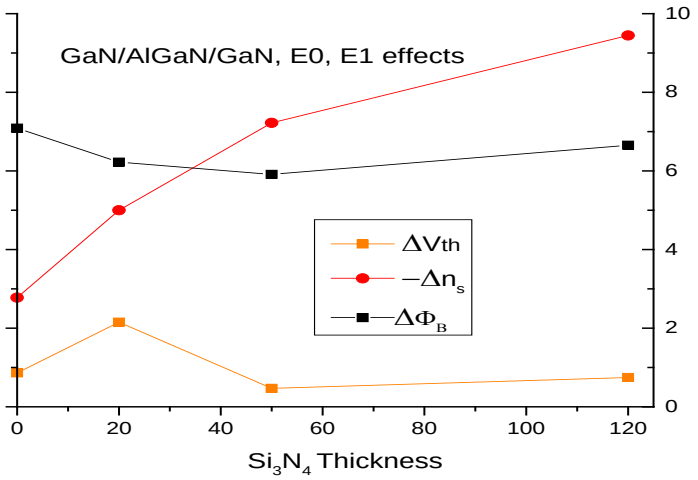

Figure 7.15. The relative effects of the changes due to 1.0 MeV irradiation on barrier height, carrier density and threshold voltage shifts as a function of Si_3N_4 thickness. The negative sheet carrier density change means the change in carriers is decreasing with increasing Si_3N_4 thickness. The units are arbitrary.

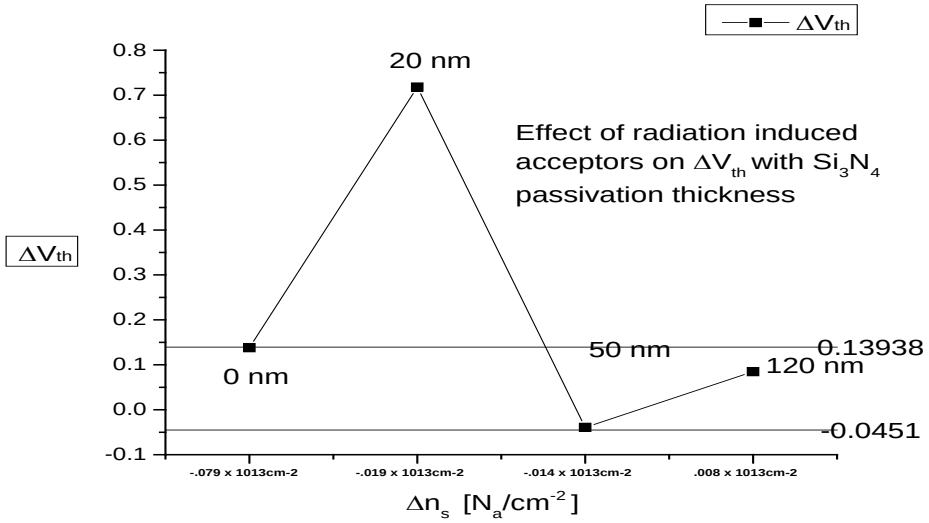

Figure 7.16 Effect of radiation induced N_A to the change in threshold voltage per thickness of Si_3N_4.

Figure 7.16 shows the uniqueness of the GaN cap with 50 nm thick passivation layer by bringing about a negative change in Vth as compared to the other thicknesses. An enlargement of Figures 7.9 and 7.10 is shown in Figure 7.17.

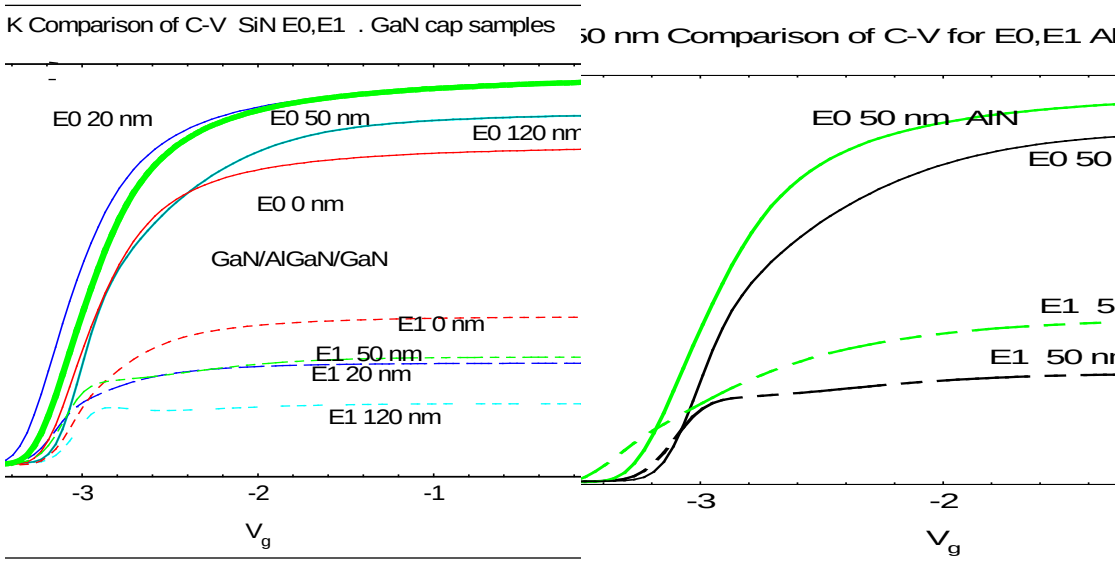

Figure 7.17. Correspondence to Figure 7.16 changes in E0E1 threshold voltage shift as a function of passivation layer thickness.

7.5. Trap analysis and Radiation effects from Deep Level Transient Spectroscopy

A number of deep centers in the activation range between 0.18 to 0.85 eV have been identified and characterized by the deep level transient spectroscopy results shown in chapter 6. The DLTS results show intrinsic traps as well as radiation induced defects that contribute to the observed leakage current results as well as decrease in carrier density in the Hall results. The intrinsic defects due to the high dislocation density in the GaN lattice can act as traps or recombination centers.

The electron irradiation induced center associated with V_N, the nitrogen vacancy trap E, shown in Figures 6.30, 6.31 and 6.32, are believed to have an activation energy, from Hall data analysis of E_T = 0.06 eV. The center for the nitrogen interstitial trap A_2, shown in 6.29 through 6.34, has E_T = 0.85 eV. For trap E, however, there is a measured E_T = 0.18 eV. The discrepancy was resolved by those getting similar results (Fang et al, 2005; Polenta et al, 2000; Look et al, 2005). It was shown that trap E was found to consists of 2 traps, ED1 and ED2, each with activation energies E_T ~ 0.06 eV, but different capture cross sections (σ=1-3 x 10^{-20} cm^2 for ED1 and σ=5-8 x 10^{-19} cm^2 for ED2). Both ED1 and ED2 are V_N associated. Figure 7.18 below, is taken from the analysis done by Fang et al (Fang et al, 2005), and describes the association.

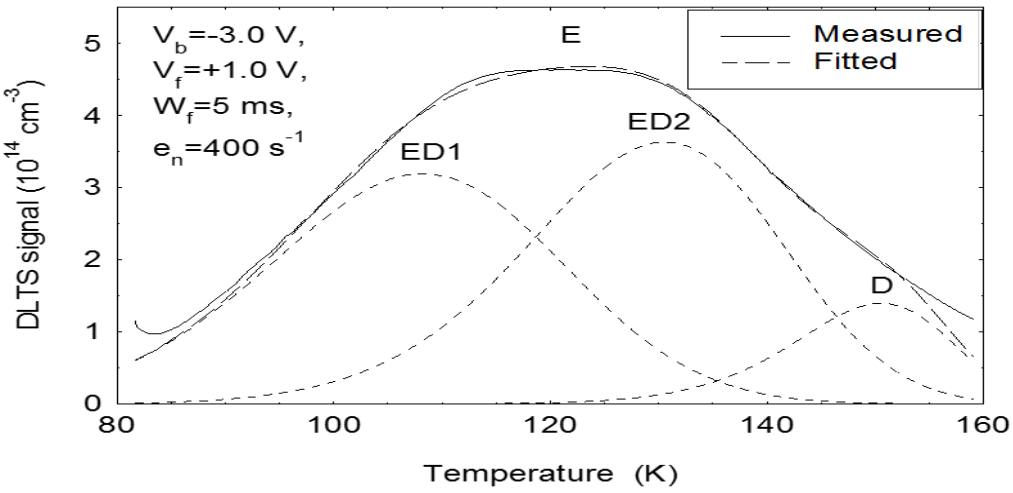

Figure.7.18. Figure showing the 2 separate traps ED1 and ED2 that make up trap E.

EI-induced deep center A_2, could be a Ga_I-related defect, if it is associated with the 0.85 eV center found by photoluminescence on electron-irradiated GaN, however, A_2

could be a N_I or V_{Ga}-N_I-related defect, as suggested by Auret et al. (Auret et al, 2002). Other 0.85 eV and 0.93 eV centers have been observed by optical detection of magnetic resonance in photoluminescence (PL-ODMR) on 2.5-MeV electron-irradiated MOCVD-GaN, with a dose of 1×10^{18} cm^{-2}, and these centers are believed to be Ga_I-related (Look et al, 2001; McClory, 2008). Another theory is since A_2 shows a production rate close to that of E, a V_N-related center, it is possible that A_2 might be an N_I-related defect, created by the reaction $N_N \rightarrow V_N + N_I$. While there is no absolute consensus of exactly what each of the A traps are in Figures 6.29 through 6.34, they are for certain believed to be the acceptors created when radiation creates Frenkel pairs, such a N_I or V_{Ga}-N_I-related defect.

The vacancy trap E is thought to be V_N, a N vacancy that explains the post irradiation decrease in Hall sheet carrier density. This was discussed in the introduction in chapter 3. It is a shallow donor and discussed in the PL model in section 7.2 which shows it increasing post irradiation in Table 7.4 as well as in the E1 model. The post irradiation BL at ~ 3.0 eV, which is formed in a Mg $\rightarrow V_N$ transition, does not decrease, and non-normalized data shows it increasing in peak intensity post irradiation in Figure 5.39. V_N is also known to be a cause of leakage current.

In section 7.3 the H_1 hole like trap was discussed and is believed to be an intrinsic cause of leakage current. The C trap in Figure 6.29 and 6.30 is radiation induced while the C_1 trap in Figure 6.26 is intrinsic. The trap D did not RT anneal out in Figure 6.31. It is associated with extended defects and leakage current and can complex with V_N. Table 7.5 summarizes the observed DLTS traps and their effects.

Table 7.6. Observed DTLS traps and their possible effects in samples

Trap	0 nm Si_3N_4 (energy/ eV)		Effects/correlations
	E0	E1	
A_2 Ga related defect		E_T = 0.85 eV	V_{th} shifts, seen in PL
A		A (E_T=0.66 eV , σ_T=1.3 x 10^{-15} cm^2 t)	Negative V_{th} shifts
A_x		E_T = 1.2 eV	acceptor trap Leakage current ,Negative V_{th} shifts
E(production rate of ~0.2 cm^{-1})		E_T =0.13 eV	V_N a shallow donor V_N ->Leakage current, V_{th} shifts
C_1	E_T =0.44 eV		line defect associated with dislocations (line defects)
C	E_T=0.34 eV and σ_T=8.6 x 10^{-16} cm^2		Near surface, penetration ~ 300 nm into GaN
D not affected by irradiaion	E_T=0.25 eV and σ_T=9.0 x 10^{-16} cm^2		Leakage current, V_{th} shifts
H_1	E_T = 0.75 eV		Threading dislocations, leakage current
V_N complexes	ED1, ED2		Pl transitions

7.6. Bethe Bloche Electron Damage Models

Over all Bethe Bloche defect damage algorithm results point to majority of displacement damage from the incident 1.0 MeV electron irradiation being to nitrogen lattice atom. The more massive gallium nucleus is able to deflect more of the incident radiation particles and should suffer less damage percentage wise. However, Look and

Farlow (Look et al, 2003) showed that 1 MeV irradiation creates more gallium vacancies by way of: $V_{GA} \rightarrow Ga_I$, where a beam energy of ~530 keV would be needed. This would mean that there would be more radiation induced V_{GA} acceptors created at this energy. The V_N created would not have as a significant effect on the carrier density decrease as the V_{GA}. The E1 PL model shows this, as E_A donor atoms electrons will lose electrons to these acceptors. The charged acceptors, the V_{GA}'s, can also explain the decrease post irradiation in mobility, which in section 7.1.4.

According to Casino simulations, the Si_3N_4 passivation should reduce the amount of damage in the AlGaN. The experimental results show that the passivation does shield or offset damage in the channel. The sheet charge density is a function of the field effect from the charges in the AlGaN primarily, so when the field is changed due to the donor and acceptor densities changes, the sheet charge density should also.

The defects have been analyzed in the PL and DLTS. Not just the location of the defects is important in analyzing radiation induced damage, but the volume. Table 5.4 of chapter 5 summarized the amount of defects nm^2. This information can be combined with Casino hits and backscattering information compared with the carrier removal rate in the experimental post radiation sheet carrier density results. Figure 7.19, obtained from one of the defect production algorithms used in this research, shows that the cross section for damage is higher for gallium at higher energies.

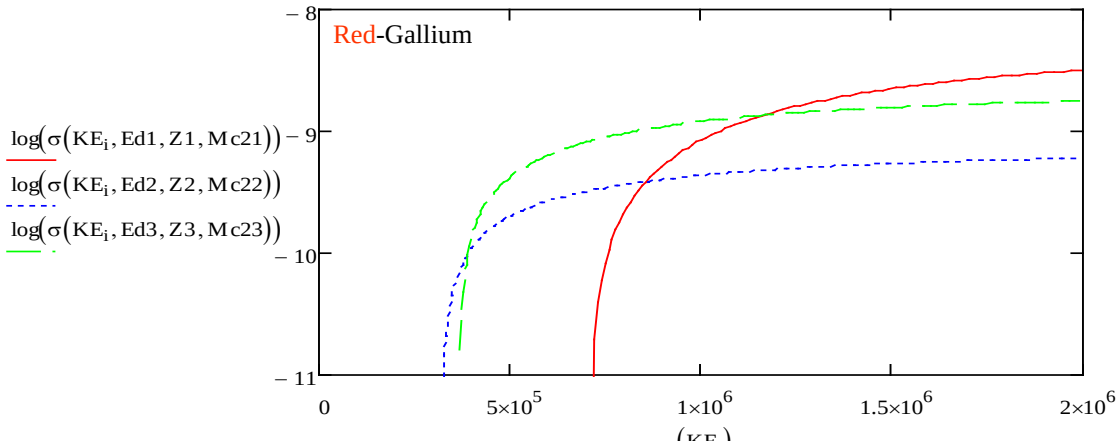

Figure 7.19. Cross section as a function of kinetic energy in AlGaN for Gallium (red), Nitrogen (blue) and Aluminum (green). The log of the cross section times the dose and density will give a defect production rate. Acceptors will be Gallium vacancies, while the nitrogen defects can be donors or acceptors.

7.7. Summary of Damage Path by 1 MeV Electron Irradiation Area Models for Radiation Damage with Variation of Si_3N_4

Figure 7.20 pictorially summarizes the path and components of damage due to passivation and 1.0 MeV irradiation on the AlGaN/GaN HEMT structures in this study.

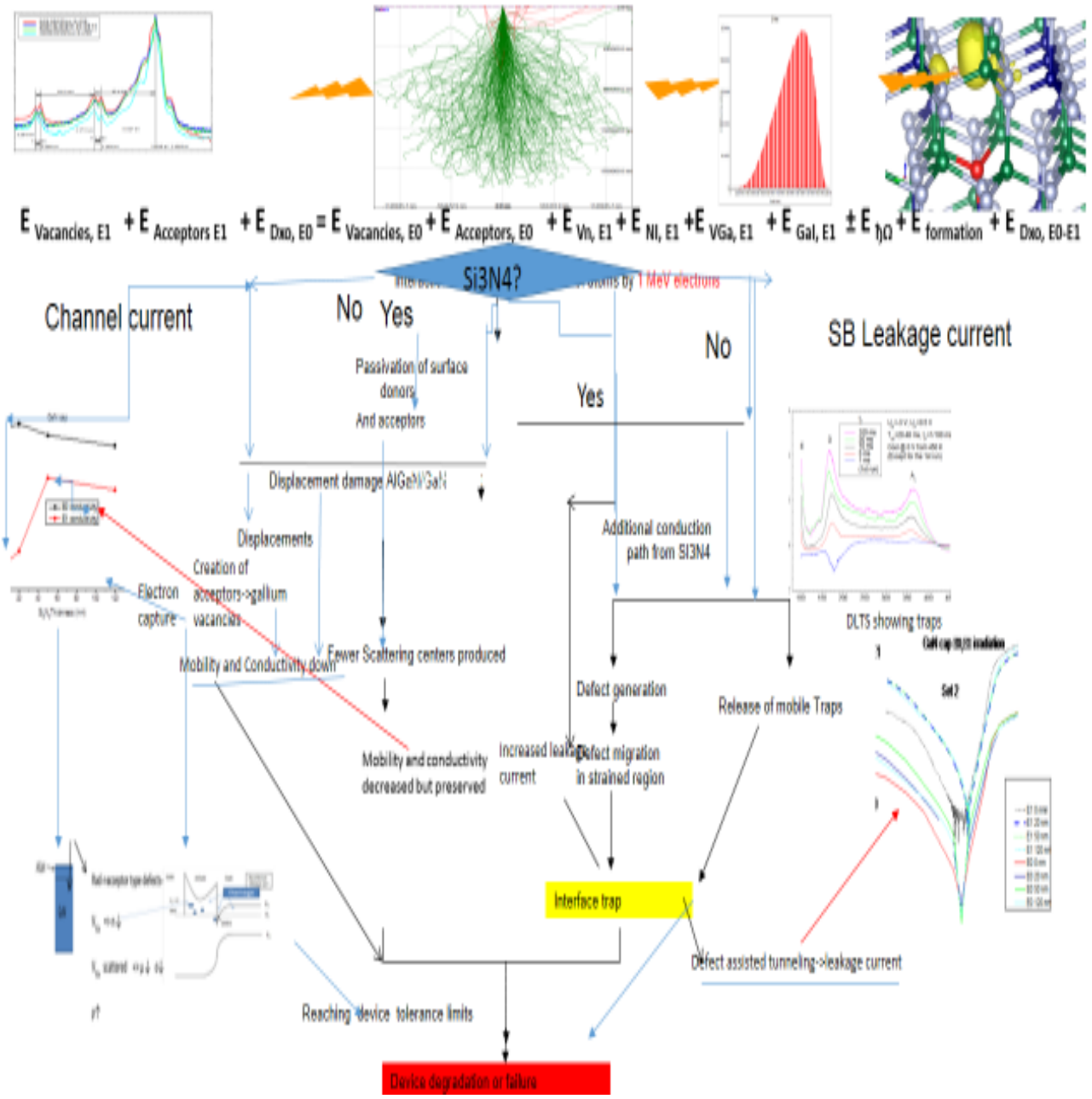

Figure 7.20. Pictorial model that summarizes the 1 MeV electron irradiation damage in the channel and in with the Schottky controlled measurements.

7.8. Conclusions and Investigative Questions Answered

Unpassivated GaN/AlGaN/GaN and 50nm passivated AlGaN/AlN/GaN C_g-Vg -T showed an initial Vth shift left at 300 and 400 K as compared to 100 K, in Figures 6.15 and 6.16. As the device goes deeper into depletion, the stretch out in the Vth increases due to N_{IT}.

For the GaN/AlGaN/GaN structure, in Figures 7.9 and 7.10, post irradiation at 300k, there is a decrease in saturation capacitance and Vth shifts right. The eventual negative Vth shift for 50nm passivation post radiation for AlGaN/AlN/GaN seen in Figure 7.10 has been observed previously for 1 MeV electron irradiated Schottky diodes. In Figure 3.7, the C_g-V_g curves at high electron irradiation go more negative as fluence goes up. Fang et al (Fang et al, 2009) reported a Vth negative shift post radiation with 1 MeV electron irradiation. The irradiation causes a significant increase in leakage current, which is dominated by tunneling, which can be traced to irradiation-induced traps. The DLTS A_x trap has been shown to cause negative Vth shifts.

In the study by A. Polyakov, after the electron irradiation, the capacitance in the depletion area was decreased to the values close to parasitic capacitance, indicating that the buffer was rendered insulating. His findings point to part of the E trap complex, which is also shown in the DLTS in this research. The E trap, which is believed to be the V_N, showed an activation energy which was that of the main compensating center in GaN. This would mean that all shallow donors that were undercompensated in the initial samples were compensated by irradiation. They showed that the main compensating agent in electron irradiated n-GaN films is the ~1 eV acceptor related to nitrogen interstitials N_I which shows up in this research as the trap A_x trap. He suggests negative

broad hole traps band due to dislocations and are modulated by positive peaks from electron traps like the ones in this study's E trap group. Therefore electron irradiation of AlGaN/GaN HEMTs can be used to "correct" the technology when it fails to produce semi-insulating buffers, but only in cases when the concentration of residual donors is not much higher than 10^{15} cm^{-3}. So their explanation of the positive threshold voltage shift was explained as due to increased compensation of conductivity in AlGaN barriers.

The interface traps are positively charged and are drawn to the metal/AlGaN interface (or if an GaN/AlN/GaN structure, the metal/GaN interface, which should have lower piezo-induced field) and thus creates interface traps. As shown also with radiation there is an increase of N_{IT} with Si_3N_4 thickness and temperature under negative bias direction and depending on structure. At 300 K, the radiation produced traps become more mobile.

The defect algorithm shows the nm^{-3} rate of defects produced is highest for the lower atomic number/weight nitrogen, which is less able to deflect the oncoming 1 MeV electrons. The post radiation Hall measurements decrease due to acceptor type defects. The defect production algorithm shows there is a thickness dependent introduction of defects with Si_3N_4 (Table 5.4.) Casino results show that the AlGaN in an unpassivated sample receives the greatest amount of damage; the defect production algorithm shows the greatest amount of damage to be to the nitrogen lattice atoms, but the greatest cross section of damage due to 1.0 MeV electrons is to the gallium lattice atom.

Decades of research indicate that the incident radiation creates a nitrogen Frenkel pair, evidenced by the above described trap E and traps Ax and A; the 1^{st} being the V_n and the A and Ax being N_I or V_{Ga}-N_I-related defect. Both DLTS and PL show evidence of

their associated complexes. Acceptor type traps such as the E traps are known to cause scattering, and they scatter coulombicly; and if they are in 2DEG, they will reduce the mobility. E traps reside either in the GaN buffer or the 2DEG. “A“ traps are thought to reside in the bulk. The simplified space charge model of the Nd/N_a radiation induced changes in Figure 7.7 summarizes the E0-E1 Hall channel measurements and is tied to the accumulation region of Schottky measurements. Unlike low energy electron radiation damage, 1 MeV irradiation does not room temperature anneal well, as shown in Figure 6.16. DLTS room temperature annealed results show in Figure 6.31 and 6.32 show the persistence of A and D and E traps; and it has been concluded traps A and D are associated with extended defects.

It was shown that radiation creates donors and acceptors from the DLTS, as well as in the Hall measurements and PL. Due to the radiation induced increase in N_A concentration. There is assumed to be a an increase of the trapped interface charges at the metal/SC interface, thus lowering of the barrier height post irradiation, which in turn facilitates trap assisted tunneling and then increased Schottky leakage current. The experimental results show a lowering of the barrier height, summarized in Table 7.5. The ΔV_{th} change is related to the Δn_s change via equation 7.9; with this research, there was a decrease in n_s which is correlated to increase in acceptors (shown in the PL, DLTS). The corresponding Vth change is in Figure 7.16.

It is believed that the V_N are created uniformly throughout the AlGaN; the V_N can act as a donors or acceptor. V_N is verified in the DLTS as trap E and is radiation induced. It is also identified the Pl BL and explained in the chapter 5 deep center PL figures and persists through all the Si_3N_4 thickness range. The YL, is attributed to an intrinsic

threading dislocation and pre irradiation leakage current. The acceptor in the YL transition is $V_{GA,}$ thought to be DLTS trap Ax that is also created post irradiation and further contributes to E1 leakage current. The concentration of V_{GA} is greatest in n rich GaN.

Charge balance has been addressed throughout this dissertation research. The piezoelectrically induced field and the charge balance changes after radiation has been given in equations 7.6 and 7.7. These equations take into account the ΔE_c and ϕ_s structure differences explained in chapter 2.2.3 and the experimental differences in the 2DEG electron density was shown in sections 5.2.3 and 5.2.4 of chapter 5. With 1.0 MeV electron irradiation, since the doping density is changed by the radiation, the charge balance equation for donors and acceptors gives specific values for the changes donor and acceptor densities:

$$n_H + N_A = N_D / (1 + n/\phi_D) \tag{7.12}$$

where in equation 7.12 n_H is the experimentally obtained carrier density, N_A is the acceptor density, N_D is the donor density and $\phi_D = (\frac{g_0}{g_1})N'_c \exp (\alpha_D /k)T^{3/2} \exp (-E_{D0} /kT)$. The term $\frac{g_0}{g_1}$, which here is ½ and $N'_c = 2(2\pi m_n^* k)^{3/2} /h^3$ .With knowing the radiation increased acceptor concentration, this can be compared to the experimental post radiation n_H. Gauss's law tells us that the changes in the field equal changes in the charge. This is how the charge balance relationships in equations 7.6 and 7.7 where obtained, which give the source of the 2DEG due to the additional charges from a passivation layer and reduction after electron irradiation. The results are a lower 2DEG sheet charge density

post radiation. The reduction in mobility has already be shown to be due to the increase in scattering from τ^{-1}_{dis} as well as τ^{-1}_{ii} in equation 5.1, and thus lowering it.

So as a final analysis, the post radiation Hall carrier density results confirm that the radiation induced Frenkel pair causes an acceptor increase, which in turn shows up in the Hall measurement results. The radiation induced donors and acceptors affect C_g-V_g and I_g-V_g degradation results. The post radiation Pl points to donors and acceptors created, as well as the surface state ionization occurring that collapses some of the post radiation NBE Pl peaks. A Pl damage model is summarized in Table 7.4. The DLTS traps, which are summarized in Table 7.6, are from the results shown in chapter 6, section 6.4. They have been related to the observed Vth shift changes and increases in leakage current; they also tie into the Hall post radiation results and correspond to the PL results. The experimental barrier heights in Table 7.5 and plotted in Figure 7.12 through 7.15 explain how the Si_3N_4 and radiation can cause a virtual lowering of the barrier that allows for trap and or defect assisted tunneling. Within the framework of the structures studied, there appears to be a better or more optimum thickness based on the 2 structures for radiation hardness, which is the 50 nm passivated GaN cap.

The following summarizes the DLTS, PL, Hall, C_g-V_g and I_g-V_g inter-relationships for this study:

- $[V_{GA}] \rightarrow *[V_{GA} - Si_{GA}]$ is occurring at 2.2 eV in E0 PL. H_1 trap associated with PL YL and intrinsic leakage current.

- $[V_{GA}] \rightarrow [V_{GA} - Si_{GA}]$ is occurring at 2.2 eV in E1 PL, more E1 $V_{GA.}$ Hall measurements decrease.

- $[V_N]$ increase has occurred, where E trap (V_N) is the radiation induced a defect that is causing a threshold voltage shift right in the C_g-V_g. It is in the PL BL transition

  $[V_{N->} Mg_{Ga}]$

- For The E1 increase in the 3.0 eV BL, as shown in the post irradiation PL, the increase in V_N can account for more BL transitions.

- The acceptors created in E1, A_2 (V_{GA}) and Ax(N_I)which show up in the DLTS in GaN, near or in the 2DEG , and can lower the Hall channel carrier density , because an acceptor is competing with the positive charges producing the 2DEG density, as in in the charge balance equation ;acceptors also lower the mobility. A traps are radiation induced and causing a threshold voltage shifts in the C_g-V_g.

- The other part of the nitrogen Frenkel pair N_I, an acceptor defect, which is believed to be in the GaN, near or in the 2DEG is , lowers both the Hall channel carrier density , because it is competing with the positive charges producing the 2DEG density, as in in the charge balance equation ;it also lowers the mobility. In the E1 leakage I_g-V_g, there may have been compensation by way of $[V_{GA}] \rightarrow [V_{GA} - V_N] + N_I$

The investigative questions, the response of the transport characteristics (such as the mobility and carrier density) to radiation depends on the particular device structure and the Si_3N_4 passivation thickness, and yes, the leakage current response to radiation depends on as well Si_3N_4 passivation thickness as well as the device structure.

VIII. Conclusion

The post radiation results due to the 1.0 MeV electron irradiation show the creation of shallow donors as well as deep and shallow acceptors. These defects create scattering centers and thus decrease the net mobility. The scattering is Coulombic and can be in both the GaN (affecting the 2DEG) and the AlGaN.

There is pre-irradiation gate leakage because of the existing intrinsic material defects that provide preferential pathways for hopping conduction. Post-radiation induced traps are introduced at the Schottky metal/AlGaN interface as well as throughout the structure. There are effects from ionization, but the damage of concern for AlGaN/GaN is nitrogen vacancies and interstitials, and gallium vacancies. The Ga vacancies occur when the incident electron irradiation has enough energy to move the atom from its normal lattice position, which results in more damage in the nitrogen sub-lattice. For the structures with an AlGaN/AlN/GaN, there is a linear dependence on Si_3N_4 thickness in the saturation region C_g-V_g results. With both structures, the passivation thickness dependence is correlated to carrier density. The GaN cap in GaN/AlGaN/GaN changes the surface potential at the metal interface; as compared to the AlGaN/AlN/GaN, which then changes the net piezo-electric induced charge at the 2DEG interface and thereby the 2DEG sheet charge density. Carrier-density saturation occurs with a 50-nm passivation layer with a GaN cap, but peaks at 120-nm passivation without the cap. It is theorized that the Si_3N_4 can produce or enhance the surface donors, resulting in higher carrier density, but with the added centers and defects brought about with this increased

passivation layer, mobility goes down. Its fixed positive charge increases the net charge at the 2DEG interface that attracts carriers into the triangular quantum well.

Since Si_3N_4 eliminates (or reduces) the surface donor and/or acceptor states, which cause trapping, in the presence of irradiation it can offset the damage. The incident radiation beam creates acceptors as well as donors, but it can also be destroying donors species. When creating acceptors in GaN, the 2DEG competes with these acceptors. It is thought that part of the ability of Si_3N_4 to passivate is due to the way it is processed, which is in a very hydrogen-rich environment. There is extensive research showing radiation induced traps are affected by hydrogen. Due to the migration of hydrogen related species, devices using Si_3N_4 have a lower sensitivity or radiation response than those using other passivation materials such as silicon carbide or other deposited oxides or no passivation.

The presence of either a 50- or 120-nm Si_3N_4 passivation layer preserves the channel transport for both structures under 1.0 MeV electron irradiation, which appears to be an optimum range of passivation thickness. The structure with the GaN cap shows better post radiation Schottky measurements. The purpose of the cap is to reduce surface charge buildup. Additionally, if the decrease in barrier height is related to the increase in acceptor type defects can be related, then 50 nm passivation for this structure is most effective against radiation damage, as it experiences the lowest barrier height reduction.

It can be concluded that Si_3N_4 preserves the surface donor states in the presence of irradiation, thus offsetting the damage. And it can be concluded that the use of a GaN cap as used in this study, as compared a structure without a GaN cap, makes a structure more radiation hard.

8.1. Significance of Research

This research gives the materials characterization of performance and reliability limiting factors such as traps as a result of 1.0 MeV radiation on test structures with varying thickness of silicon nitride passivation. This information can be used to identify some of the intrinsic radiation-induced material defects which will enable design of better AlGaN/GaN HEMTs.

While these were test structures in this research, the information obtained from Hall carrier density, mobility, conductivity, PL, Cg-Vg, Ig-Vg, and DLTS provide as well as structure/effect and radiation damage models presented as a function of Si_3N_4 layer thickness can be used and combined with other modes of characterization such as stress and thermal analysis to better understand the intrinsic and radiation induced material defect limiting defects and traps that affect AlGaN/GaN HEMT lifetime and reliability. This, in turn, may be applied to optimize the device critical performance.

Even though there are a number of limiting design constraints with these samples in determining gate current measurements (in this case Schottky measurements), the observed Hall results that show peak device performance with 50 nm Si_3N_4 passivation layer thickness can be used as a template to polarization engineer more rad hard structures.

8.2. Recommendations for Future Research

Future research should include a comprehensive model of damage that includes all of the contributions to device failure in radiation intense environments and study them

as a function of Si_3N_4 layer thickness. Emphasis should be put on analyzing the stress changes with Si_3N_4 thickness in relation to other device characteristics. Configurations should first be modeled to reduce the parameter set of contributions. Then, experimentally, with a reduced parameter set, and well-designed transistors, test to determine how performance varies with increments in the range of 50- through 120-nm Si_3N_4 thickness with electron, proton and neutron irradiation since the present study reveals that is a useful range for improving device metrics.

Bibliography

Agullo-Lopez, F., Catlow, C. R. A., Townsend, P. D.. *Point Defects in Materials.* Waltham, MA: Academic Press, 1988.

Aktas, O., Kuliev, A., Kumar, V., Schwindt, R., Toshkov, S., Costescu, D., Stubbins, J., and Adesida, I.. "^{60}Co gamma radiation effects on DC, RF, and pulsed *I-V* characteristics of AlGaN/GaN HEMTs." *Solid-State Electronics,* 48 (2004): 471-475.

Ambacher, O., Foutz, B., Smart, J., Shealy, J. R., Weimann, N. G., Chu, K., Murphy, M., Sierakowski, A. J., Schaff, W. J., Eastman, L. F., Dimitrov, R., Mitchell, A., and Stutzmann, M.. "Two dimensional electron gases induced by spontaneous and piezoelectric polarization in undoped and doped AlGaN/GaN heterostructures." *Journal of Applied Physics,* 87 (2000): 334.

Arulkumaran, S., Egawa, T., Ishikawa, H., Jimbo, T., and Sano, Y.. "Surface Passivation effects on AlGaN/GaN high electron mobility transistors with SiO_2 , Si_3N_4, and silicon oxynitride." *Applied Physics Letters,* 84, no. 4 (2004): 613.

Asgari, A., Kalafi, M., and Faraone, L.. "Effects of partially occupied sub-bands on two-dimensional electron mobility in $Al_xGa_{1-x}N$/GaN heterostructures." *Journal of Applied Physics,* 95 (2004): 1185.

Asgari, A., Kalafi, M., and Faraone, L.. "The effects of GaN capping layer thickness on two-dimensional electron mobility in GaN/AlGaN/GaN heterostructures." *Physica E: Low-dimensional Systems and Nanostructures,* 25 (2005): 431-437.

Asgari, A., Babanejad, S., and Faraone, L.. "Electron mobility, Hall scattering factor, and sheet conductivity in AlGaN/AlN/GaN heterostructures." *Journal of Applied Physics,* 110 (2011): 113713.

Atwater, H. A.. *Si Passivation and Chemical Vapor Deposition of Silicon Nitride: Final Technical Report, March 18, 2007.* Subcontract NREL/SR-520-42325. Golden, CO: National Renewable Energy Laboratory, November 2007.

Auret, F. D., Goodman, S. A., Legodi, M. J., Meyer, W. E., and Look, D. C.. "Electrical characterization of vapor-phase-grown single-crystal ZnO." *Applied Physics Letters,* 80 (2002): 1340.

Binari, S. C., Klein, P. B., and Kazior, T. E.. "Trapping effects in GaN and SiC microwave FETs." *Proceedings of the IEEE,* 90, no. 6 (2002): 1048-1058.

Borchi, E., Bruzzi, M., Dezillie, B., Lazanu, S., Li, Z., and Pirollo, S.. "Hall Effect Analysis in Irradiated Silicon Samples with Different Resistivities." *IEEE*

Transactions on Nuclear Science, 46, no. 4 (1999): 834.

Calleja, E., Sánchez, F. J., Basak, D., Sánchez-García, M. A., Muñoz, E., Izpura, I., Calle, F., Tijero, J. M. G., Sánchez-Rojas, J. L., Beaumont, B., Lorenzini, P., and Gibart, P.. "Yellow luminescence and related deep states in undoped GaN." *Physical Review B*, 55 (1997): 4689.

Cho, H. K., Kim, K. S., Hong, C.-H., and Lee, H. J.. "Electron traps and growth rate of buffer layers in unintentionally doped GaN." *Journal of Crystal Growth*, 223 (2001): 38-42.

Chou, Y. C., Lai, R., Li, G. P., Nam, P., Kim, H. K., Ra, Y., Grundbacher, R., Alers, E., Biedenbender, M., and Oki, A.. "Novel Nitride Passivation on 0.15 μm Pseudomorphic GaAs HEMTs Using High-Density Inductively Coupled Plasma CVD (HD-ICP-CVD)." *Proceedings of the International Conference on Gallium-Arsenide Manufacturing Techniques*, 2002.

Christian, de Brida. *Gallium Nitride Simulations using Sentaurus Software.* PhD dissertation. University of Padova, Padova, Italy, 2010.

Colton, John S.. *Selective Excitation of the Yellow and Blue Luminescence in n and p doped Gallium Nitride.* PhD Dissertation. University of California Berkeley, Berkeley, CA, 2000.

Condito, V., Lambert, N., Schwartz, T. J., and Dodge, S.. "The effects of Nitride passivation on the total dose radiation resistance of a precision operational amplifier." *IEEE Transactions on Nuclear Science*, 28, no. 6 (1981): 4325-27.

Fagerlind, M., Allerstain, F., Sveinbjornsson, E. O., and Rorsman, N. R.. "Investigation of the Interface between silicon nitride passivations and AlGaN/AlN/GaN heterostructures by C(v) characterization of metal insulator semiconductor heterostructure capacitors." *Journal of Applied Physics*, 108 (2010): 014508.

Fang, Z.-Q., Look, D. C., Kim, D. H., and Adesida, I.. "Traps in AlGaN/GaN/SiC heterostructures studied by deep level transient spectroscopy." *Applied Physics Letters*, 87 (2005): 182115.

Fang, Z.-Q., Farlow, G. C., Claflin, B., Look, D. C., and Green, D. S.. "Effects of electron-irradiation on electrical properties of AlGaN/GaN Schottky barrier diodes." *Journal of Applied Physics*, 105 (2009): 123704.

Fang, Z.-Q., Claflin, B., Look, D. C., Green, D. S., and Vetury, R.. "Deep Traps in AlGaN/GaN heterostructures studied by deep level transient spectroscopy: Effect of carbon concentration in GaN buffer layers." *Journal of Applied Physics*, 108 (2010): 063706.

Fang, Z.-Q., Claflin, B., and Look, D. C.. "Deep Traps in AlGaN/GaN Heterostructure Field Effect Transistors Studied by Current-Mode Deep-Level Transient Spectroscopy: Influence of Device Location," *Journal of Electronic Materials,* 40, no. 12 (2011): 2337-43.

Farvacque, J.-L., Bougrioua, Z., Carosella, F., and Moerman, I.. "Free carrier mobility in AlGaN/GaN quantum wells." *Journal of Physics: Condensed Matter,* 14 (2002): 13319.

Georgievich, K. N.. *Radiation Effects in Semiconductor III-Nitrides, Final Project Technical Report*. ISTC Project No. 3029. Moscow, Russia: International Science and Technology Center (ISTC), May 2008.

Goodman, S. A., Auret, F. D., Legodi, M. J., Myburg, G., Beaumont, B., and Gibart, P.. "Electron irradiation induced defects in n-GaN." *Semiconducting and Insulating Materials Conference 2000,* SIMC-XI International (2000): 43-46.

Govarkov, A. V., Smirnov, N. B., Polyakov, A. Y., Markov, A. V., Voss, L., and Pearton, S. J.. "Microcathodoluminescence and electrical properties of GaN epitaxial layers grown on thick freestanding GaN substrates." *Journal of Vacuum Science and Technology B,* 24, no. 2 (2006): 790-794.

Green, K.. *Electron Paramagnetic Resonance Spectroscopy and Hall Effect Studies of Low Electron Irradiation on GaN*. PhD dissertation. Air Force Institute of Technology, Wright-Patterson AFB, OH, September 2003.

Hogsed, M. R., Yeo, Y. K., Ahoujja, M., Ryu, M.-Y., Petrosky, J. C., and Hengehold, R. L.. "Radiation-induced electron traps in $Al_{0.14}Ga_{0.86}N$ by 1 MeV electron radiation." *Applied Physics Letters*, 86 (2005): 261906.

Hsu, L., and Walukiewicz, W.. "Electron mobility in $Al_xGa_{1-x}N$/GaN heterostructures." *Physical Review B,* 56 (1997): 1520.

Hu, X., Koudymov, A., Simin, G., Yang, J., Asif Khan, M., Tarakji, A., Shur, M. S., and Gaska, R.. "Si_3N_4/AlGaN/GaN-metal-insulator-semiconductor heterostructure field-effect transistors." *Applied Physics Letters,* 79, no. 17 (2001): 2832-2834.

Hu, W. D., Chen, X. S., Quan, Z. J., Zhang, X. M., Huang, Y., Xia, C. S., Lu, W., and Ye, P. D.. "Simulation and optimization of GaN-based metal-oxide-semiconductor high-electron-mobility-transistor using the field-dependent drift velocity model." *Journal of Applied Physics*, 102 (2007): 034502.

Huang, S., Shen, B., Xu, F.-J., Lin, F., Miao, Z.-L., Song, J., Lu, L, Cen, L.-B., Sang, L.-W., Qin, Z.-X., Yang, Z.-J., and Zhang, G.-Y.. "Study of the leakage current mechanism in Schottky contacts to $Al_{0.25}Ga_{0.75}N$/GaN heterostructures with AlN interlayers." *Semiconductor Science and Technology*, 24, no. 5 (2009): 055005.

Hwang, Y.-H., Li, S., Hsieh, Y.-L., Ren, F., Pearton, S. J., Patrick, E., Law, M. E., and Smith, D. J.. "Effect of proton irradiation on AlGaN/GaN high electron mobility transistor off-state drain breakdown voltage." *Applied Physics Letters,* 104 (2014): 082106.

Ibbetson, J. P., Fini, P. T., Ness, K. D., DenBaars, S. P., Speck, J. S., and Mishra, U. K.. "Polarization effects, surface states, and the source of electrons in AlGaN/GaN heterostructure field effect transistors." *Applied Physics Letters*, 77 (2000): 250.

International Commission on Radiation Units and Measurements. *Stopping Power for Electrons and Positrons.* ICRU Report No. 37. Bethesda, MD: ICRU, 1984.

Jackson, H., Petrosky, J., Farlow, G., and Hengehold, R.. "Effect of Optimum Silicon Nitride Passivation Thickness on Electron Irradiated AlGaN\GaN." *Proceedings of the 2013 Materials Research Society Spring Conference,* 2013.

Jackson, John David. *Classical Electrodynamics,* 3 ed.. Hoboken, NJ: John Wiley & Sons, 1999.

Jarzen, T.. *Capacitance-Voltage Study on The Effect of Low Energy Electron Radiation on AlGaN/GaN High Electron Mobility Transistors*. MS thesis. Air Force Institute of Technology, Wright-Patterson AFB, OH, May 2005.

Jeon, Chang Min, and Lee, Jong-Lam. "Effects of tensile stress induced by silicon nitride passivation on electrical characteristics of AlGaN/GaN heterostructure field effect transistors." *Journal of Applied Physics*, 86 (2005): 172101.

Jogai, B.. "Influence of surface states on the two-dimensional electron gas in AlGaN/GaN heterojunction field-effect transistors." *Journal of Applied Physics,* 93 (2003): 1631.

Joh, Jungwoo, and del Alamo, Jesus A.. "A Current-Transient Methodology for Trap Analysis for GaN High Electron Mobility Transistors." *IEEE Transactions on Electron Devices*, 58, no. 1 (2011): 132-140.

Johnston, Allan. "Space Radiation Effects and Reliability Considerations for Micro-and Optoelectronic Devices." *IEEE Trans. on Device and Material Reliability*, 10, no. 4 (2010): 449-459.

Kalavagunta, A., Touboul, T., Shen, L., Schrimpf, R. D., Reed, R. A., Fleetwood, D. M., Jain, R. K., and Mishra, U. K.. "Electrostatic Mechanisms Responsible for Device Degradation in AlGaN/AlN/GaN HEMTs." *IEEE Transactions on Nuclear Science*, 55, no. 4 (2008): 2106.

Kalavagunta, A.. *Understanding the Impact of Bulk Traps on GaN HEMT DC and RF Characteristics*. PhD dissertation. Vanderbilt University, Nashville, TN, 2009.

Karmarkar, A. P., White, B. D., Buttari, D., Fleetwood, D. M., Schrimpf, R. D., Weller, R. A., Brillson, L. J., and Mishra, U. K.. "Proton-induced damage in gallium nitride-based Schottky diodes." *IEEE Transactions on Nuclear Science,* 52 (2005): 2239-2244.

Khan, M. A., Kuznia, J. N., Olson, D. T., Schaff, W. J., Burm, J. W., and Shur, M. S.. "Microwave performance of a 0.25 μm gate AlGaN/GaN heterostructure field effect transistor." *Applied Physics Letters,* 65 (1994): 1121.

Kim, H., Schuette, M., Jung, H., Song, J., Lee, J, Lu, W., and Mabon, J. C.. "Passivation effects in Ni/AlGaN/GaN Schottky diodes by annealing." *Applied Physics Letters,* 89 (2006): 05351.

Klein, P. B., Henry, R. L., Kennedy, T. A., and Wilsey, N. D.. *Defects in Semiconductors*. Edited by H. J. Bardeleben. Materials Science Forum 10-12 (1986): 1259.

Kocan, Martin. *AlGaN/GaN MBE 2DEG Heterostructures: Interplay between Surface-, Interface-, and Device-Properties.* PhD Dissertation. Rheinisch-Westfälischen Technischen Hochschule Aachen (Technical University of Aachen), Aachen, Germany, 2003.

Kordos, P., Kudela, P., Gregusova, D., and Donoval, D.. "The Effect of Passivation on the Performance of AlGaN/GaN Heterostructure Field-Effect Transistors." *Semiconductor Science and Technology,* 21 (2006) 1592-1596.

Kuang, W.. *TCAD Simulation and Modeling of AlGaN/GaN HFETs.* PhD Dissertation. University of North Carolina, Chapel Hill, NC, 2008.

Kwon, Y.-H., Shee, S. K., Gainer, G. H., Park, G. H., Hwang, S. J., and Song, J. J.. "Time-resolved study of yellow and blue luminescence in Si- and Mg-doped GaN." *Applied Physics Letters,* 76 (2000): 840.

Lee, I.-H., Choi, I.-H., Lee, C. R., and Noh, S. K.. "Evolution of stress relaxation and yellow luminescence in GaN/sapphire by Si incorporation." *Applied Physics Letters,* 71 (1997): 1359.

Lenka, T. R., and Panda, A. K.. "Effect of structural parameters of 2DEG and C~V characteristics of AlGaN/AlN/GAN-based HEMT." *Indian Journal of Pure & Applied Physics,* 49 (2011): 416-422.

Leo, W. R.. *Techniques for Nuclear and Particle Physics Experiments*. Berlin, Germany: Springer-Verlag, 1987.

Lu, L., Zhang, J.-C., Xue, J.-S., Ma, X.-H., Zhang, W., Bi, Z.-W., Zhang, Y., and Hao, Y.. "Neutron irradiation effects on AlGaN/GaN high electron mobility transistors." *Chinese Physics B,* 21, no. 3 (2012): 037104.

Look, David C.. *Electrical Characterization of GaAs Materials and Devices.* Hoboken, NJ: John Wiley & Sons, 1989.

Look, D. C., Reynolds, D. C., Hemsky, J. W., Sizelove, J. R., Jones, R. L., and Molner, R. J.. "Defect Donor and Acceptor in GaN." *Physical Review Letters,* 79 (1997): 2273-2276.

Look, D. C.. "Defect-Related Donors, Acceptors, and Traps in GaN." *Physica Status Solidi B,* 228, no. 1 (2001): 293-302.

Look, D. C., Farlow, G. C., Drevinsky, P. J., Bliss, D. F., and Sizelove, J. R.. "On the nitrogen vacancy in GaN." *Applied Physics Letters,* 83 (2003): 3525.

Look, D. C., Fang, Z., and Claflin, B.. "Identification of donors, acceptors and traps in bulk-like HVPE GaN." *Journal of Crystal Growth,* 281, no. 1 (2005): 143-150.

Look, D. C.. *Donors, Acceptors, and Traps in AlGaN and AlGaN/GaN Epitaxial Layers: Final Technical Report, July 31, 2006.* Grant AFOSR/F49620-03-1-0197. Arlington, VA: Air Force Office of Scientific Research, July 2006.

Luo, B., Johnson, J. W., Ren, F., Allums, K. K., Abernathy, C. R., Pearton, S. J., Dwivedi, R., Fogarty, T. N., Wilkins, R., Dabiran, A. M., Wowchack, A. M., Polley, C. J., Chow, P. P., and Baca, A. G.. "DC and RF performance of proton-irradiated AlGaN/GaN high electron mobility transistors." *Applied Physics Letters,* 79 (2001): 2196-2198.

Marino, F. A., Faralli, N., Palacios, T., Farry, D. K., Goodnick, S. M., and Saraniti, M.. "Effects of Threading Dislocations on AlGaN/GaN High-Electron Mobility Transistors." *IEEE Tranactions on Electron Devices,* 57, no. 1 (2010): 353.

Mattila, T., and Nieminen, R. M.. "Point-defect complexes and broadband luminescence in GaN and AlN." *Physical Review B,* 55 (1997): 9571.

McClory, J. W., Petrosky, J. C., Sattler, J. M., and Jarzen, T. A.. "An Analysis of the Effects of Low-Energy Electron Irradiation of AlGaN/GaN HFETs." *IEEE Transactions on Nuclear Science,* 54, no. 6 (2007): 1946-1952.

McClory, J. W.. *The Effect of Radiation on Electrical Properties of Aluminum Gallium Nitride/Gallium Nitride Heterostructures.* PhD dissertation. Air Force Institute of Technology, Wright-Patterson AFB, OH, June 2008.

McKelvey, James. *Polymer Processing.* Hoboken, NJ: John Wiley & Sons, 1962.

Meneghesso, G., Zanon, F., Uren, M. J., and Zanoni, E.. "Anomalous Kink Effect in GaN High Electron Mobility Transistors." *IEEE Electron Device Letters,* 30, no. 2 (2009): 100-102.

Meneghinni, Matteo. *Analysis of the Physical processes that limit the reliability of GaN based opto-electronic devices.* PhD dissertation. University of Padova, Padova, Italy, 2008.

Meyer, David J.. *Surface Passivation Studies of AlGaN/GaN High Electron Mobility Transistors.* PhD dissertation. University of Pennsylvania, Philadelphia, PA, 2008.

Mizutani, T., Ito, S., Kishimoto, S., and Nakamura, F.. "AlGaN/GaN HEMTs With Thin InGaN Cap Layer for Normally Off Operation." *IEEE Electron Device Letters,* 28, no. 7 (2007): 549.

Moran, J.. *The Effects of Temperature and Electron Radiation on the Electrical Properties of AlGaN/GaN Heterostructure Field Effect Transistors*. MS thesis. Air Force Institute of Technology, Wright-Patterson AFB, OH, March 2009.

Moran, J. T., McClory, J. W., Petrosky, J. C., and Farlow, G. C.. "The Effects of Temperature and Electron Radiation on the Electrical Properties of AlGaN/GaN HFETs." *IEEE Transactions on Nuclear Science,* 56, no. 6 (2009): 3223-28.

Neugebauer, J., and Van de Walle, C. G.. "Gallium vacancies and the yellow luminescence in GaN." *Applied Physics Letters,* 69 (1996): 503.

Ng, H. M., Doppalapudi, D., Moustakas, T. D., Weimann, N. G., and Eastman, L. F.. "The role of dislocation scattering in n-type GaN films." *Applied Physics Letters,* 73, no. 6 (1998): 821.

Norton, Matthew S.. "Numerov's Method for Approximating Solutions to Poisson's Equation." Unpublished paper, February 20, 2009. Available online at http://www.siue.edu/~mnorton/Numerov.pdf (accessed 29 May 2014).

NIST Website. http://www.nist.gov/pml/div683/hall_effect.cfm (accessed 29 May 2014).

Ogino, T., and Aoki, M.. "Mechanism of Yellow Luminescence in GaN." *Japanese Journal of Applied Physics,* 19 (1980): 2395.

Ohno, Y., Nakao, T., Kishimoto, S., Maezawa, K., and Mizutani, T.. "Effects of Surface Passivation on breakdown of AlGaN/GaN high electron mobility transistors." *Applied Physics Letters,* 84, no. 12 (2004) 2184.

Palmer, D. W.. "Electronic Energy Levels in Group III Nitrides," in Bhattacharya, P., Fornari, R., and Kamimura, H. (editors). *Comprehensive Semiconductor Science and Technology*, Vol. 4. Amsterdam: Elsevier, 2011.

Petrosky, J. C., McClory, J. W., Gray, T. E., and Uhlman, T. A.. "Trap Assisted Tunneling Induced Currents in Neutron Irradiated AlGaN/GaN HFETs." *IEEE Transactions on Nuclear Science*, 56, no. 5 (2009): 2905-09.

Polenta, L., Fang, Z.-Q., and Look, D. C.. "On the main irradiation-induced defect in GaN." *Applied Physics Letters,* 76 (2000): 2086.

Polyakov, A. Y., Smirnov, N. B., Govorkov, A. V., Markov, A. V., Pearton, S. J., Dabiran, A. M., Wowchak, A. M., Cui, B., Osinsky, A. V., Chow, P. P., Kolin, N. G., Boiko, V. M., and Merkurisov, D. I.. "Electron Irradiation of AlGaN/GaN and AlN/GaN heterojunctions." *Applied Physics Letters,* 93 (2008): 152101.

Prunty, T. R., Smart, J. A., Chumbes, E. M., Ridley, B. K., Eastman, L. F., and Shealy, J. R.. "Passivation of AlGaN/GaN heterostructures with Silicon Nitride for Insulated Gate Transistors." *Proceedings of the 2000 IEEE/Cornell Conference on High Performance Devices,* (2000).

Reshchikov, M. A., and Markoc, H.. "Luminescence properties of defects in GaN." *Journal of Applied Physics,* 97 (2005): 061301.

Saadaoui, S., Ben Salem, M. M., Gassoumi, M., Maaref, H., and Gaquiere, C.. "Electrical Characterization of (Ni/Au)/$Al_{0.25}Ga_{0.75}N$/GaN/SiC Schottky barrier diode." *Journal of Applied Physics,* 110 (2011): 013701.

Sathaiya, D. M., and Karmalkar, S.. "Thermionic trap-assisted tunneling model and its application to leakage current in nitrided oxides and AlGaN/GaN high electron mobility transistors." *Journal of Applied Physics,* 99 (2006): 093701.

Sattler, J. M.. *An Analysis of the Effects of Low Energy Electron Radiation on AlxGa1-x N/GaN Modulation-Doped Field-Effect Transistor*. MS thesis. Air Force Institute of Technology, Wright-Patterson AFB, OH, March 2004.

Shealy, J. R., Prunty, T. R., Chumbes, E. M., and Ridley, B. K.. "Growth and passivation of AlGaN/GaN heterostructures." *Journal of Crystal Growth*, 250 (2007): 7-13.

Shen, Likun. *Advanced Polarization–Based Design of AlGaN/GaN HEMTs*. PhD Dissertation. University of California Santa Barbara, Santa Barbara, CA, 2004.

Suharsanan, S., and Karmalkar, S.. "Modeling of the reverse gate leakage in AlGaN/GaN high electron mobility transistors." *Journal of Applied Physics*, 107 (2010): 0645501.

Sze, S. M., and Ng, Kwok K.. *Physics of Semiconductor Devices.* Hoboken, NJ: John Wiley & Sons, 2007.

Tsai, Y. S., and Whitis, V. *Thick Target Bremsstrahlung and Target Consideration for Secondary Particle Production by Electrons*. Publication SLAC-PUB-184. Stanford, CA: Stanford Linear Accelerator Center, March 1966.

Tsurumi, N., Uemoto, Y., Sakai, H., Ueda, T, Tanaka, T, and Ueda, D. "GaN transistors for Power Switching and High Frequency Applications." *Digest of Papers from the 2008 Compound Semiconductors and Circuits Symposium,* (2008): 1-5.

Van Vechten, J. A.. "Activation enthalpy of recombination-enhanced vacancy migration in Si." *Physical Review B,* 38 (1988): 9913.

Vertiatchikh, A. V., Eastman, L. F., Schaff, W. J., and Prunty, T.. "Effect of surface passivation of AlGaN/GaN heterostructure field-effect transistor." *Electronics Letters,* 38, no. 8 (2002): 388-389.

Vetury, R., Zhang, N. Q., Keller, S., and Mishra, U. K.. "The Impact of Surface States on the DC and RF Characteristics of AlGaN/GaN HFETs." *IEEE Transactions on Electron Devices,* 48, no. 3 (2001): 560.

Warren, W. L., Rong, F. C., Poindexter, E. H., Gerardi, G. J., and Kanicki, J.. "Structural identification of the silicon and nitrogen dangling-bond centers in amorphous silicon nitride." *Journal of Applied Physics,* 70 (1991): 346.

Weimann, N. G., Eastman, L. F., Doppalapudi, D., Ng, H. M., and Moustakas, T. D.. "Scattering of electrons at threading dislocations in GaN." *Journal of Applied Physics,* 83 (1998): 3656.

White, B. D., Bataiev, M., Goss, S. H., Hu, X., Karmarkar, A., Fleetwood, D. M., Schrimpf, R. D., Schaff, W. J., and Brillson, L. J.. "Electrical, spectral, and chemical Properties of 1.8 MeV proton irradiated AlGaN/GaN HEMT structures as a function of proton fluence." *IEEE Transactions on Nuclear Science,* 50 (2003): 1934-1941.

Wolfe, Charles M., Holonyak, Nick, Jr., and Stillman, Gregory E.. *Physical Properties of Semiconductors.* Upper Saddle River, NJ: Prentice Hall, 1989.

Wright, D. N.. *Optical and Passivating Properties of Hydrogenated Amorphous Silicon Nitride Deposited by Plasma Enhanced Chemical Vapor Deposition for Application on Silicon Solar Cells.* PhD Dissertation. Institute for Energy Technology, Kjeller, Norway, 2008.

Zanoni. E., Meneghesso, G., Meneghini, M., and Stocco, A.. "GaN HEMT reliability from time dependent gate degradation to On-state failure mechanisms." *Proceedings of the 2012 Materials Research Society Spring Conference,* 2012.

REPORT DOCUMENTATION PAGE

Form Approved
OMB No. 0704–0188

1. REPORT DATE (DD–MM–YYYY)	2. REPORT TYPE	3. DATES COVERED *(From — To)*
19-06-2014	Dissertation	September 2009 – June 2014

4. TITLE AND SUBTITLE
Effect of Variation of Silicon Nitride Passivation Layer on Electron Irradiated Aluminum Gallium Nitride/Gallium Nitride HEMT Structures

5a. CONTRACT NUMBER
5b. GRANT NUMBER
5c. PROGRAM ELEMENT NUMBER

6. AUTHOR(S)
Jackson, Helen C., GG-11, AFRL/RXAN

5d. PROJECT NUMBER
AN102002
5e. TASK NUMBER
5f. WORK UNIT NUMBER

7. PERFORMING ORGANIZATION NAME(S) AND ADDRESS(ES)
Air Force Institute of Technology
Graduate School of
2950 Hobson Way
WPAFB OH 45433-7765

8. PERFORMING ORGANIZATION REPORT NUMBER
AFIT-ENP-DS-14-J-17

9. SPONSORING / MONITORING AGENCY NAME(S) AND ADDRESS(ES)
Air Force Research Laboratory
Donald L. Dorsey
3005 Hobson Way, Bldg. 600, Rm. 2BK 422
Wright-Patterson AFB, OH 45433-7707
Donald.Dorsey@us.af.mil
312-798-8739

10. SPONSOR/MONITOR'S ACRONYM(S)
AFRL/RXAN
11. SPONSOR/MONITOR'S REPORT NUMBER(S)

12. DISTRIBUTION / AVAILABILITY STATEMENT
Distribution Statement A. Approved for Public Release; Distribution Unlimited

13. SUPPLEMENTARY NOTES
This work is declared a work of the U.S. Government and is not subject to copyright protection in the United States.

14. ABSTRACT
Silicon nitride passivation on AlGaN/GaN heterojunction devices can improve performance by reducing electron traps at the surface. This research studies the effect of displacement damage caused by 1.0 MeV electron irradiation as a function of the variation of passivation layer thickness and heterostructure layer variation on AlGaN/GaN HEMTs. The effects of passivation layer thickness are investigated at thicknesses of 0, 20, 50, and 120 nanometers on AlGaN/GaN test structures with either an AlN nucleation layer or a GaN cap structures which are then measured before and immediately after 1.0 MeV electron irradiation at fluences of 10^{16} cm^{-2}. Hall system measurements are used to observe changes in mobility, carrier concentration and conductivity as a function of Si_3N_4 thickness. Models are developed that relate the device structure and passivation layer under 1.0 MeV radiation to the observed changes to the measured photoluminescence and deep level transient spectroscopy. A software model is developed to determine the production rate of defects from 1.0 MeV electrons that can be used for other energies and materials. The presence of either a 50 or 120 nm Si_3N_4 passivation layer preserves the channel current for both and appears to be optimal for radiation hardness.

15. SUBJECT TERMS
AlGaN/GaN; Passivation Layer; High Electron Mobility Transistors; Deep Level Transient Spectroscopy; Radiation Hardness

16. SECURITY CLASSIFICATION OF:			17. LIMITATION OF ABSTRACT	18. NUMBER OF PAGES	19a. NAME OF RESPONSIBLE PERSON
a. REPORT	b. ABSTRACT	c. THIS PAGE			Nancy C. Giles, AFIT/ENP
U	U	U	UU	282	19b. TELEPHONE NUMBER (Include Area Code) (937)255-3636 x4601 nancy.giles@afit.edu

Standard Form 298 (Rev. 8–98)
Prescribed by ANSI Std. Z39.18